Fluvial inorganic carbon cycling across divergently evolving permafrost landscapes (Yukon and Northwest Territories, Canada)

by

Scott Zolkos

A thesis submitted in partial fulfillment of the requirements for the degree of

Doctor of Philosophy

in

Ecology

Department of Biological Sciences
University of Alberta

ABSTRACT

Across the circumpolar north, rapid warming and intensifying hydrologic cycles are accelerating permafrost thaw and strengthening land-freshwater linkages. Among the most significant implications of this change is the mobilization of large amounts of previously sequestered organic and inorganic substrate from thawing permafrost into modern aquatic biogeochemical cycles. While microbial oxidation of permafrost organic carbon can produce carbon dioxide (CO_2) and methane (CH_4) upon thaw, current understanding about the sources and transformation (cycling) of carbon – and thus potential climate feedbacks – in permafrost thaw-affected freshwaters is driven by research in relatively organic-rich terrains. Much less is known about carbon cycling in permafrost terrains containing a relatively greater proportion of inorganic substrate, where the chemical weathering of minerals may shift the direction and magnitude of permafrost carbon-climate feedbacks. This work investigates the summertime (2014–2017) magnitude, drivers, and regional variability in inorganic carbon cycling in a series of northern watersheds in diverse permafrost terrains across the Yukon and Northwest Territories (Canada). Much of this work occurred on the Peel Plateau (Northwest Territories), where terrain subsidence following permafrost thaw (thermokarst) releases tills into fluvial networks.

Measurements of dissolved inorganic carbon (DIC, $\Sigma[CO_2, HCO_3^-, CO_3^{2-}]$) showed that the thaw and chemical weathering of carbonate- and sulfide-bearing tills on the Peel Plateau reshaped fluvial inorganic carbon cycling across watershed scales. The substantial thermokarst-driven increase in weathering was reflected by a 100-fold increase in bicarbonate (HCO_3^-) concentrations between non thermokarst-affected headwaters and the Stony Creek outlet into the Peel River. Ions and stable isotopes of DIC ($\delta^{13}C_{DIC}$) and CO_2 ($\delta^{13}C_{CO2}$) indicated that carbonate weathering was primarily driven by sulfuric acid from sulfide oxidation, which contributed to

CO_2 supersaturation within thermokarst features. This CO_2 was rapidly effluxed to the atmosphere in headwaters, while the downstream evolution of HCO_3^- and other ions, $\delta^{13}C_{DIC}$, and $\delta^{13}C_{CO2}$ along transects spanning nested watersheds reflected inputs from RTS-affected tributaries and revealed a modest increase in biotic CO_2 production. Our finding that H_2SO_4 carbonate weathering is traceable across watershed scales aligns with our hydrochemical modeling results, which show a multi-decadal increase in H_2SO_4 carbonate weathering products within the Peel River from ca. 1975–2015, in conjunction with accelerating thermokarst activity.

While our estimates of CO_2 and CH_4 efflux from within thermokarst features indicate these fluxes are currently modest contributions to the atmosphere, results from our abiotic mineral weathering experiment are consistent with observations that intensifying thermokarst – which exposes deeper, previously unthawed tills – will amplify H_2SO_4 driven carbonate weathering and HCO_3^- export and increase atmospheric CO_2 over geological timescales via HCO_3^- transformation within marine precipitation reactions. Trends in fluvial carbon cycling in nearby permafrost terrains revealed that inorganic carbon cycling and export (as HCO_3^-) dominated in mountainous terrain with carbonate bedrock, and dissolved organic carbon (DOC) export and CO_2 and CH_4 efflux dominated in low-relief terrains with a relatively greater proportion of organic matter. Fluvial carbon cycling was intermediate on the Peel Plateau, except where thermokarst enhanced carbonate weathering and sediment release by unearthing mineral-rich tills. From an ecosystem carbon balance perspective, fluvial C export was equivalent to 8% of CO_2 uptake by terrestrial vegetation, except in the watersheds affected by thermokarst (~1% by area), where fluvial C export was equivalent to roughly 40% of CO_2 uptake by vegetation.

Consistent with observations elsewhere, our results show that the magnitude and drivers of fluvial carbon cycling can vary considerably across proximal yet diverse landscapes. This

research is among the first to document the effects of thermokarst on fluvial carbon cycling in a relatively inorganic-rich permafrost terrain. We conclude that the regional variability in the mineral composition of permafrost, and thus the degree to which carbonate weathering is coupled with sulfide oxidation, will moderate CO_2 consumption or release via chemical weathering of thawed minerals. Although we show that carbonate- and sulfide-bearing thermokarst terrains span the circumpolar north, carbonate and silicate weathering by carbonic acid (H_2CO_3*, including CO_2) will consume CO_2 and be carbon neutral or a sink over geological timescales. Determining the effects of thermokarst on fluvial inorganic carbon cycling in northern permafrost terrains is a top research priority for refining models of the Arctic carbon cycle and constraining permafrost carbon-climate feedbacks.

PREFACE

Science is a collaborative endeavor, especially in the Arctic. Each chapter in this thesis reflects a team effort involving many colleagues including those listed below, resulting in manuscripts published in or in preparation for submission to peer-reviewed journals, as detailed below. For all chapters, S.Z. and S.E.T. designed the study with input from co-authors and led fieldwork; S.Z. led data analysis and manuscript writing; all co-authors contributed to writing.

Chapter 2: Zolkos, S., Tank, S.E., & Kokelj, S.V. (2018). Mineral Weathering and the Permafrost Carbon-Climate Feedback. *Geophysical Research Letters*, *45*(18), 9623-9632.

Chapter 3: Zolkos, S., Tank, S.E., Striegl, R.G., & Kokelj, S.V. (2019). Thermokarst Effects on Carbon Dioxide and Methane Fluxes in Streams on the Peel Plateau (NWT, Canada). *Journal of Geophysical Research: Biogeosciences, 124*(7), 1781-1798.

Chapter 4: Zolkos, S., Tank, S.E., Estop-Aragonés, C., & Olefeldt, D. Experimental Evidence for the Role of Mineral Weathering within Permafrost Carbon-Climate Feedbacks. Under revision for resubmission to *Geochimica et Cosmochimica Acta*.

Chapter 5: Zolkos, S., Tank, S.E., Striegl, R.G., Kokelj, S.V., Estop-Aragonés, C., Olefeldt, D. Thermokarst Effects on Inorganic Carbon Cycling and Export Across Watershed Scales (Peel Plateau, Canada). In preparation for submission to *Earth and Planetary Science Letters*.

Chapter 6: Zolkos, S., Tank, S.E., Striegl, R.G., Kokelj, S.V., Shakil, S. Divergent Landscape Evolution Shapes Fluvial Chemistry and Carbon Balance in the Western Canadian Arctic. In preparation for submission to *Global Biogeochemical Cycles*.

ACKNOWLEDGEMENTS

An immense thank you to my advisor, Dr. Suzanne Tank. Briefly working with Suzanne in 2011 exposed me to her contagious enthusiasm for science, commitment to training young scientists, and endless energy. Needless to say, I was correct in thinking that these qualities would make Suzanne a wonderful supervisor. Suzanne's dedicated engagement in my graduate research, her encouragement to pursue ideas and knowledge, and her foresight and wisdom to keep me from wandering too astray have made me a better scientist.

I thank my supervisory committee, Dr. Robert Striegl and Dr. Vincent St. Louis, for sharing their expertise in carbon cycling and gas efflux. Their insights into my early study designs, help with laboratory analyses, and conversations about results greatly strengthened this research. I also thank Dr. Steve Kokelj for insightful conversations about permafrost environments and advice on the study region and sampling designs. I am grateful to Steve for many thoughtful comments, which helped to inspire my intellectual growth. I also thank the members of my candidacy exam (Dr. Duane Froese and Dr. David Hik) and defense committee (Dr. Scott Lamoureux and Dr. Alberto Reyes) for generously sharing their time and scientific expertise.

Funding support from UAlberta North (Northern Research Award), the Aurora Research Institute (Research Fellowship Program), and the Arctic Institute of North America (Grant-in-Aid) helped to make this work possible. I am grateful to these organizations and their wonderful staff, and also to the University of Alberta for providing me with teaching assistantships during my graduate studies, which made my stay in Canada both legal and financially possible.

I thank my fellow lab mates and graduate cohort for their friendship, collegiality, and encouragement of my homebrewing pursuits. Our long and ranging conversations and adventures made my time in Canada a wonderful experience. I also thank the many friends and mentors who have inspired my growth as a scientist and person. From those at the Woods Hole Research Center to the International Arctic Science Committee Fellowship Program and beyond, listing everyone I wish to thank would lengthen this thesis significantly.

Thank you to the northern residents of Fort McPherson and Inuvik for generously sharing your land and companionship. Learning how truly beautiful the land, culture, and people are in northern Canada is among the most important personal outcomes of my work. While climate

change has no geographical boundaries, its consequences are an immense burden to northern communities. Thus, I hope the findings of this work may help the efforts to mitigate this burden.

Most importantly, thank you to my family, especially my parents, Cate and Timm, and my brother, Brett, for unending love and supporting my dreams. Since an early age, my parents inspired my passion for science by releasing Brett and I into the outdoors to explore with (we presumed) limited supervision. The freedom and support to explore the natural world, our trips to museums, and their shared excitement for science are a modest reflection of their mastery in parenting and eternal love. Both my immediate and extended family is the foundation on which these efforts are built. I am grateful for your love and support. To my wife, Anya: thank you for enduring five years of being separated by anywhere from two to fourteen time zones for much of the time. This work is as much a testament to your resolve and support as it is to our ability to plan our future while in different countries and continents. Like the discharge of the great Arctic rivers, our love knows no boundaries and historical trends suggest that it will increase in the coming decades. I am so grateful to be on this journey with you.

TABLE OF CONTENTS

LIST OF TABLES

LIST OF FIGURES

CH. 1: General Introduction

1.1. Background

1.1.1. Mineral Weathering and the Carbon Cycle

Biogeochemical cycles describe the movement and transformation of chemical elements within and between the biosphere, geosphere, and atmosphere (Schlesinger & Bernhardt, 2013). In essence, they detail the processes which give rise to the chemical structure and composition of Earth's ecosystems. Tracing the biogeochemical cycles of elements through ecosystems allows for an accounting of the flow and transformation of chemical compounds, with important ramifications for Earth's climate. In this regard, the carbon cycle is particularly important, because carbon dioxide (CO_2) and methane (CH_4) in the atmosphere warm the global climate by trapping infrared energy radiated from Earth's surface (Stocker et al., 2013). Over geological timescales, atmospheric CO_2 levels are moderated by the chemical weathering of silicate and carbonate minerals, which is enhanced by vegetation productivity (Berner, 1998), resulting in the transformation of CO_2 into HCO_3^-, its riverine export, and ultimately its sequestration in sedimentary carbonates via precipitation reactions within the marine carbon cycle (Berner, 1999). Mineral weathering is thus a critical link between the short- and long-term carbon cycles and, over geological timescales, it is one of the Earth's great thermostats.

The degree to which mineral weathering represents a CO_2 sink depends on the acid responsible for weathering and the mineral composition of the substrate exposed to weathering. HCO_3^- represents a CO_2 sink if generated from carbonic acid (H_2CO_3*, including dissolved CO_2) weathering of carbonates (short-term sink) or silicates (long-term sink). In contrast, the coupled weathering of carbonate and sulfide minerals – which weather more readily than silicates (Stumm & Morgan, 1996) – generates HCO_3^- without consuming CO_2, resulting in net CO_2 release to the atmosphere. Indeed, CO_2 release from sulfuric acid (from sulfide oxidation) weathering of carbonates likely inhibited the complete glaciation of Earth's surface in the geological past (Torres et al., 2017). Mineral weathering is well known to influence climate over long timescales, yet, in environments with relatively high rates of mineral weathering, HCO_3^- production can be rapid. For instance, in glacial foreground environments, the retreat of glaciers and chemical weathering of finely-ground carbonate rock flour by H_2CO_3* during fluvial transport is known to produce substantial amounts of dissolved inorganic carbon (DIC, $\Sigma[CO_2, HCO_3^-, CO_3^{2-}]$) (Anderson, 2007) and can consume dissolved CO_2 to below atmospheric levels

(St. Pierre et al., 2019; Striegl et al., 2007). The cryosphere – particularly glaciated terrains across the circumpolar north – protects large quantities of mineral-bearing tills, which are increasingly vulnerable to climate warming (Kokelj, Lantz, et al., 2017; St. Pierre et al., 2019). While intensified mineral weathering can be expected to influence carbon cycling across the circumpolar north, regional variability in the mineral composition of tills, the magnitude of mineral weathering, and implications for carbon cycling and climate feedbacks remain unknown.

1.1.2. Global and Arctic Climate Change

The rate and magnitude of global warming during the last few centuries is unprecedented within the last 50 million years (Burke et al., 2018), resulting in profound biogeochemical and ecological changes at a global scale (Scholze et al., 2006; Walther et al., 2002). These changes are particularly striking at northern latitudes (Post et al., 2009, 2013), where mean annual air temperatures are warming at twice the global rate (Serreze & Barry, 2011). Disproportionately fast warming in the Arctic results from a complex series of feedbacks, which, at a basic level, are associated with a reduction in the reflectivity of Earth's surface (albedo) owing to diminishing snow and ice cover (Serreze & Barry, 2011). The increase in relatively darker surfaces on the land and in the Arctic Ocean results in greater absorption of incoming solar energy, thereby amplifying warming and further reducing snow and ice cover. More than half of the global warming in the past 60 years was associated with anthropogenic activities including the release of the greenhouse gases CO_2 and CH_4 (Stocker et al., 2013). Future warming and intensifying precipitation at northern latitudes (+8˚C and +40% by 2100; Stocker et al., 2013) are expected to drive a suite of environmental changes that will fundamentally alter ecosystems both in the north (AMAP, 2019) and at a global scale (Stocker et al., 2013).

Among the most significant implications of rapid northern warming are the degradation of the cryosphere (Biskaborn et al., 2019; Gardner et al., 2011), increasing vegetation productivity (Myers-Smith et al., 2011; Pearson et al., 2013), intensifying hydrologic cycles (Bring et al., 2016; Rawlins et al., 2010), and strengthening land-freshwater linkages (Vonk et al., 2015; Walvoord & Kurylyk, 2016). Together, these changes are reshaping northern biogeochemical cycles. Notably, increasing solute fluxes in major northern rivers in recent decades reflect a thickening of the active layer, deepening hydrologic flow paths, and enhanced mineral weathering occurring in concert with climate warming and intensifying precipitation (Drake,

Tank, et al., 2018; Tank et al., 2016; Toohey et al., 2016). Warming-induced changes to the carbon cycle are of particular concern in the Arctic, where perennially frozen ground (permafrost) acts as a structural foundation for many northern ecosystems (AMAP, 2017) and communities (Hjort et al., 2018), and also contains Earth's largest terrestrial store of organic carbon (Ciais et al., 2013; Hugelius et al., 2014).

1.1.3. Northern Permafrost Carbon and Climate Feedbacks

Roughly 24% of the exposed land surface area in the northern hemisphere is underlain by permafrost (Schaefer et al., 2012) and mostly at latitudes above 60˚N (Obu et al., 2019), where climate conditions have enabled permafrost to persist for millennia (Froese et al., 2009; Lacelle et al., 2013; Murton et al., 2017). At a global scale, permafrost last reached its maximum extent roughly 20,000 years ago (kybp), during the late Pleistocene (French, 2018). The presence of geologic features once associated with permafrost extend to 45˚N in the upper United States (French, 2018), suggesting that permafrost in North America extended considerably farther south during the last glacial maximum (~21 kybp) (Slaymaker, 2017). Despite the northward retreat and ultimate disappearance of the former Laurentide Ice Sheet (LIS) in concert with climate warming (French, 2018; Slaymaker, 2017), the LIS left a lasting legacy. The comminution of bedrock during the LIS expansion and the climate and vegetative protection of tills in the wake of its retreat endowed former glacial margins across northwestern Canada with relatively ice- and sediment-rich permafrost (Kokelj, Lantz, et al., 2017; Kokelj, Tunnicliffe, et al., 2017).

The modern-day distribution of northern permafrost is organized into four categories of areal coverage which broadly follow a latitudinal climate gradient from cold, high latitudes to relatively warmer, lower latitudes: continuous (90-100%), discontinuous (50-90%), sporadic (10-50%), and isolated (0-10%) (Brown et al., 1997). In essence, permafrost is a condition which can affect a broad compositional spectrum of earthen material. In other words, the composition of northern permafrost soils varies considerably with respect to ground ice content (Brown et al., 1997), organic carbon (Hugelius et al., 2014), nutrients (Fuchs et al., 2018; Harden et al., 2012), and sediments (Schuur et al., 2015). To a degree, regional variability in the composition of permafrost is influenced by glacial history (see above). Compared with North America, much of modern-day Siberia, Alaska, and the Yukon Territory (Canada) were not glaciated during the Pleistocene (Clark et al., 2009; Ehlers et al., 2011). This region, Beringia, was home to the

mammoth steppe-tundra ecosystem, where a relatively dry climate during the late Pleistocene suppressed the development of continental glaciers (Hopkins, 1982) and enabled a large amount of aeolian and fluvial organic carbon to accumulate within aggrading permafrost (Zimov et al., 2006). These yedoma deposits are rich in organic carbon (2–5% C) and extend across large swaths of Siberia, Alaska, and the Yukon Territory (Froese et al., 2009; Strauss et al., 2017).

As a whole, soils in the northern circumpolar permafrost region contain more carbon (1,307 ± 170 PgC) (Hugelius et al., 2014) than is in the atmosphere (830 PgC), global vegetation (520 PgC), or fossil fuel reserves (1,100 PgC) (mean values from Ciais et al., 2013). Consequently, the release and biogeochemical transformation of even a small portion of the permafrost carbon pool has significant implications for CO_2 release to the atmosphere and climate feedbacks (Schuur et al., 2015). Model predictions estimate that ~15% of the carbon currently locked away in northern permafrost soils (92 ± 17 PgC under RCP 8.5) will thaw by 2100 and produce enough CO_2 to warm global temperatures an additional ~0.2˚C (Schuur et al., 2015). However, the transformation of permafrost carbon into fluvial CO_2 and CH_4 within fluvial networks and the effects of mineral weathering on fluvial CO_2 remain unaccounted for in current models of permafrost carbon-climate feedbacks.

1.1.4. Northern Streams and Rivers: Indicators and Integrators of Change

Building on early estimates of the permafrost carbon-climate feedback, which were driven by observations in terrestrial and lacustrine environments (Zimov et al., 2006), recent experiments and measurements in the field show that permafrost dissolved organic carbon (DOC) can be relatively labile and rapidly transformed into CO_2 within fluvial network headwaters (Drake et al., 2015; Drake, Guillemette, et al., 2018; Littlefair & Tank, 2018; Vonk et al., 2013; Ward et al., 2017). These findings together with observations of increasing export of DOC and alkalinity (reflective of the acid neutralizing capacity, includes HCO_3^-; Stumm & Morgan, 1996) in major Arctic rivers (Drake, Tank, et al., 2018; Tank et al., 2016; Toohey et al., 2016) indicate an acceleration of carbon cycling across the vast pan-Arctic watershed. This is expected to have strong effects in the Arctic Ocean (AMAP, 2018; Tank et al., 2012), which contains 1% of the global ocean volume and receives more than 10% of global river discharge (Shiklomanov, 1998). Together, long-term monitoring of river chemistry – which captures biogeochemical signals of change integrated across the pan-Arctic watershed (Drake, Tank, et al., 2018; Holmes et al.,

2012; Li Yung Lung et al., 2018; McClelland et al., 2016; Tank et al., 2012; Wild et al., 2019) and efforts to trace the downstream evolution of fluvial carbon cycling (Drake, Guillemette, et al., 2018; Murphy et al., 2019; Serikova et al., 2018) are revealing the effects of permafrost thaw across watershed scales. However, these dynamics remain understudied in the headwaters of fluvial networks in relatively inorganic-rich permafrost terrains spanning the circumpolar north, where the rapid transformation of permafrost substrate may intensify mineral weathering and reshape inorganic carbon cycling across watershed scales.

1.2. Research Questions, Objectives, and Study Region

Broadly, this thesis aims to constrain the effects of thermokarst on freshwater carbon cycling. To accomplish this, this research investigated fluvial chemistry and carbon fluxes across scales and diverse permafrost-affected landscapes, ranging from immediately downstream of thermokarst features to a series of watersheds in terrains with varying hydrology, geology, topography, vegetation, and thermokarst activity. Much of this work (Chapters 2–5) occurred on the Peel Plateau (NT), where intensifying precipitation and warming air temperatures are accelerating the thaw and mobilization of large amounts of ice- and sediment-rich tills into fluvial networks (Kokelj et al., 2013; Segal et al., 2016a). The final data chapter (Chapter 6) was undertaken across diverse terrains along a 300-km stretch of the Dempster Highway in the Yukon and Northwest Territories, including the Peel Plateau, to understand how the evolution of regional permafrost landscapes and contrasting glacial legacies have given rise to divergent trends in modern-day carbon cycling and ecosystem carbon balance.

This work aims to answer the questions: How will climate change reshape inorganic carbon cycling in northern environments? What is the magnitude of this change, and how and why do the drivers vary across diverse permafrost landscapes? The objectives of each data chapter are as follows:

1. **Chapter 2:** Characterize the effects of thermokarst on mineral weathering and DIC production within headwater streams on the Peel Plateau;
2. **Chapter 3:** Quantify CO_2 and CH_4 concentration and efflux in thermokarst-affected streams, characterize the geochemical controls on CO_2 and CH_4 production, and estimate the magnitude of CO_2 and CH_4 efflux in thermokarst relative to watershed-scale efflux;

3. **Chapter 4:** Experimentally determine the relative influence of permafrost mineral composition and thaw history on DIC production and speciation;
4. **Chapter 5:** Quantify how thermokarst effects on inorganic carbon cycling propagate through fluvial networks and determine the fate of inorganic permafrost constituents;
5. **Chapter 6:** Constrain the magnitude and drivers of fluvial carbon cycling and export across diverse permafrost terrains, and fluvial contributions to ecosystem carbon balance.

Chapter 7 provides general conclusions and offers insight on future research directions to better constrain the role of thermokarst and mineral weathering within emerging models of the Arctic carbon cycle and permafrost carbon-climate feedbacks. While the main findings of this work are presented within separate, thematically-oriented chapters, the common thread that weaves them together is the goal to quantify and track the effects of thermokarst on inorganic carbon cycling across the land to freshwater continuum and across spatial scales.

CH. 2: Mineral Weathering and the Permafrost Carbon-Climate Feedback

Summary

Permafrost thaw in the Arctic enables the biogeochemical transformation of vast stores of organic carbon into carbon dioxide (CO_2). This CO_2 release has significant implications for climate feedbacks, yet the potential counterbalance from CO_2 fixation via chemical weathering of minerals exposed by thawing permafrost is entirely unstudied. We show thermokarst in the western Canadian Arctic enables rapid weathering of carbonate tills, driven by sulfuric acid from sulfide oxidation. Unlike carbonic acid-driven weathering, this caused significant and previously undocumented CO_2 production and outgassing in headwater streams. Increasing riverine solute fluxes correspond with long-term intensification of thermokarst and reflect the regional predominance of sulfuric acid-driven carbonate weathering. We conclude that thermokarst-enhanced mineral weathering has potential to profoundly disrupt Arctic freshwater carbon cycling. While thermokarst and sulfuric acid-driven carbonate weathering in the western Canadian Arctic amplify CO_2 release, regional variation in sulfide oxidation will moderate the effects on the permafrost carbon-climate feedback.

2.1. Introduction

Arctic warming is intensifying permafrost thaw (Overpeck et al., 1997) and mobilizing significant amounts of sediment (Kokelj et al., 2013), solutes (Malone et al., 2013), and organic carbon (Vonk et al., 2015) to inland and coastal waters. The transformation of these thawed materials fundamentally alters biogeochemical cycles (Drake et al., 2015), with profound ecological implications from local (Chin et al., 2016) to global scales (Schuur et al., 2015). By 2100, greenhouse gas emissions from thawing permafrost – mostly as CO_2 – are projected to add ~0.2˚C to global warming (Schuur et al., 2015). However, Arctic carbon cycle models do not yet account for the interaction of two critical processes: extreme permafrost thaw across landscapes (thermokarst), and CO_2 transformation via chemical weathering of minerals exposed by thawing permafrost. These processes may influence the permafrost carbon-climate feedback (Schuur et al., 2015), but have received little attention.

Mineral weathering by carbonic acid (H_2CO_3; dissolved CO_2) regulates climate over geological timescales (Berner, 1999) and is a globally-significant CO_2 sink (~0.4 PgC y^{-1})

(Stocker et al., 2013). By converting CO_2 to bicarbonate (HCO_3^-), H_2CO_3-driven carbonate weathering reduces CO_2 susceptiblity to atmospheric exchange (Tank et al., 2016) and enables the HCO_3^- in dissolved inorganic carbon (DIC, $\Sigma[CO_2, HCO_3^-, CO_3^{2-}]$) to represent a carbon sink (Tank et al., 2012):

$$CaCO_3 + H_2CO_3 \rightarrow Ca^{2+} + 2HCO_3^- \quad (2\text{-}1)$$

Limited research shows carbonate weathering across the circumpolar north may consume significant CO_2 (Tank et al., 2012). Intensification of this process is expected to counterbalance rising atmospheric CO_2 levels (Beaulieu et al., 2012) and should thus temper the permafrost-carbon climate feedback. However, the strength of this CO_2 sink depends on the acid responsible for weathering. In contrast to equation (2-1), carbonate weathering by sulfuric acid (H_2SO_4) – commonly from sulfide oxidation – generates HCO_3^- without consuming CO_2 (Calmels et al., 2007; Li et al., 2008; Stallard & Edmond, 1983; Torres et al., 2017; Turchyn et al., 2013):

$$2CaCO_3 + H_2SO_4 \rightarrow 2Ca^{2+} + SO_4^{2-} + 2HCO_3^- \quad (2\text{-}2)$$

Riverine fluxes of the products from equations (2-1) and (2-2) link Arctic carbon cycling from headwaters to coastal waters (Calmels et al., 2007; Tank et al., 2012). Along this continuum, HCO_3^- transformation can generate CO_2 via carbonate precipitation in the ocean (Calmels et al., 2007), or by neutralizing protons from H_2SO_4 (Ali & Atekwana, 2011) (equation 2-3).

$$H^+ + HCO_3^- \rightleftharpoons H_2CO_3 \rightleftharpoons H_2O + CO_{2(aq)} \rightleftharpoons H_2O + CO_{2(g)} \quad (2\text{-}3)$$

The presence of sulfides in permafrost may therefore alter the balance between H_2CO_3- and H_2SO_4-driven weathering, with fundamental implications for climate feedbacks (Burke et al., 2018; Torres et al., 2017). Along with carbonate lithologies, shale – which often contains sulfides (Clarke, 1924) – occurs across the Arctic and within Pleistocene glacial limits (Hartmann & Moosdorf, 2012; Kokelj et al., 2017). This suggests extensive glacial comminution of carbonates and sulfides which have been preserved within vast stores of weatherable tills (Bjornson, 2003). These tills are associated with some of the most ice-rich and rapidly thawing

permafrost terrain in the Arctic. Here, we use ions and stable isotopes to characterize thermokarst-driven weathering and quantify its effects on CO_2 in headwater streams on the Peel Plateau (NWT, Canada). We tracked these effects across scales by modeling riverine solute fluxes and conducted geospatial analyses to evaluate how intensifying thermokarst and mineral weathering could reshape the Arctic carbon cycle and influence climate feedbacks.

2.2. Materials and Methods

2.2.1 Study Area

The Peel Plateau provides the ideal environment for testing novel hypotheses that explore the effects of extreme thaw on inorganic carbon cycling in Arctic fluvial networks. It is a fluvially-incised, glaciogenic landscape with ice-rich, Pleistocene-aged permafrost tills up to 100 m thick (Kokelj et al., 2017; Lacelle et al., 2013). The sediments within these tills derive from bedrock extending eastward to the Canadian Shield (Lacelle et al., 2013), across carbonate- and sulfide-bearing units (Stott, 1991), and contain carbonates, sulfides, and silicates (Bjornson, 2003) (Table A1-1). Early Holocene warming 14–8.5 kybp (Lacelle et al., 2010) promoted near-surface thaw of these tills and enabled weathering, leaching of solutes, and sequestration of organic matter within the top few meters of soil (Burn, 1997; Lacelle, 2004; Malone et al., 2013). Holocene cooling and upward aggradation of the permafrost table preserved these modified soils as a relatively organic-rich, paleo-thaw layer above the underlying, ice-rich Pleistocene tills (Kokelj et al., 2017; Lacelle et al., 2013). Today, climate warming and intensifying precipitation in the western Canadian Arctic are driving permafrost thaw, resulting in retrogressive thaw slump (RTS) development across the Peel Plateau (Brooker et al., 2014; Kokelj et al., 2013; Segal et al., 2016a) (Fig. 2-1). RTS occur in ice-rich terrain throughout the Arctic and, on the Peel Plateau alone, mobilize millions of cubic meters of mineral and organic permafrost substrate into modern biogeochemical cycles (Kokelj et al., 2017; Littlefair et al., 2017). The magnitude of this disturbance regime is reflected by rising solute concentrations in the Peel River, which comprises a ~70,000 km^2 watershed (Kokelj et al., 2013) (Fig. 2-1).

2.2.2 Sample Collection and Analysis

We sampled dissolved ions, dissolved CO_2, DIC, and isotopes from 24 sites across eight RTS-affected streams (Fig. 2-1). Dissolved CO_2 was collected using headspace equilibration

(Hesslein et al., 1991) and measured by infrared gas analyzer. pCO_2 was calculated using Henry's constants corrected for water temperature (Weiss, 1974). DIC was preserved in serum bottles with KCl (Striegl et al., 2012) and measured by gas chromatography following Stainton (1973). DIC species were calculated in CO2sys (v.2.3) (Pierrot et al., 2006) using freshwater constants for K1 and K2 (Millero, 1979; Millero, 2010). We used equivalent ratios of ions in stoichiometric proportion to the products in equations (2-1), (2-2), (A1-5), (A1-7), and (A1-8) to evaluate dominant mineral weathering reactions.

$\delta^{13}C_{CO2}$ and 0.45-µm filtered samples for carbon ($\delta^{13}C_{DIC}$, $\delta^{13}C_{DOC}$) and sulfate ($\delta^{34}S_{SO4}$, $\delta^{18}O_{SO4}$) isotopes were analyzed by isotope ratio mass spectrometry. End-member $\delta^{13}C_{DIC}$ ranges for equilibrium and kinetically-controlled reactions (Kendall & Caldwell, 1998) were calculated following Jin et al. (2009) and Lehn et al. (2017). Biogenic and geogenic $\delta^{13}C_{CO2}$ end-member ranges were derived for DOC respiration and H_2SO_4- and H_2CO_3-driven carbonate weathering, respectively (Clark & Fritz, 1997; Kendall et al., 2014; Mook et al., 1974; Zhang et al., 1995), with corrections for atmospheric $\delta^{13}C_{CO2}$ (Hamilton & Ostrom, 2007; Kendall et al., 2014). We constrained $\delta^{34}S$ end-members using values from the literature (Calmels et al., 2007; Stott, 1991; Strauss, 1997) and $\delta^{34}S$ we measured on sulfides from regional tills. We calculated the range of $\delta^{18}O_{SO4}$ expected from sulfide oxidation, with corrections for isotopic fractionation (van Everdingen & Krouse, 1985), using $\delta^{18}O_{H2O}$ measurements for regional permafrost (Lacelle et al., 2013; Michel, 2011), rain and snow (IAEA/WMO, 2017). Finally, we used X-ray diffraction (XRD) and RockJock11 (Eberl, 2003) to determine minerals present in RTS runoff, first sieving and analyzing organic content to confirm low potential interference with XRD (Heiri et al., 2001; Mandile & Hutton, 1995).

2.2.3 Statistical and Geospatial Analyses

RTS effects on stream chemistry were assessed using linear mixed effects models in the R package *lme4* (Bates et al., 2015), and RTS solutes in streams using a two end-member mixing model (Malone et al., 2013) assuming constant end-member conductivities (Laudon & Slaymaker, 1997; Pellerin et al., 2007). We analyzed long-term trends in Peel River ion fluxes by pairing long-term water chemistry from Environment Canada and historical discharge data from the Water Survey of Canada in LoadRunner software, which automates runs of the U.S. Geological Survey constituent load-modeling software LOADEST (Runkel et al., 2004). Trends

were evaluated with the non-parametric Mann-Kendall test in R (R Core Team, 2015), using the trend pre-whitening approach (Yue et al., 2002) in the *zyp* package (Bronaugh & Werner, 2013) to account for serial correlation. Geospatial data for lithology (Hartmann & Moosdorf, 2012), glacial limits (Kokelj et al., 2017), hillslope thermokarst (Olefeldt et al., 2016), and observations of carbonates in permafrost (Biskaborn et al., 2013; Fritz et al., 2012; Hyatt, 1992; Keller et al., 2007; Lauriol et al., 2010; Schirrmeister et al., 2011; Stutter & Billett, 2003) characterized regions where thermokarst could disrupt Arctic carbon cycling. Detailed methods for all analyses are provided in the supporting information.

2.3. Results and Discussion

2.3.1 Thermokarst Effects on Mineral Weathering in Fluvial Network Headwaters

This study builds on previous work that identified increasing solute fluxes downstream of RTS (Kokelj et al., 2013; Littlefair et al., 2017; Malone et al., 2013). To examine how the intensity of permafrost thaw and thus the composition of thawed permafrost material affects aquatic inorganic carbon cycling, we compared stream chemistry upstream and downstream of eight RTS features of varying sizes on the Peel Plateau, in addition to the highly turbid rillwater "runoff" streams within RTS (Fig. 2-1a; Table A1-2). Across sites, the chemistry of RTS runoff and affected streams was consistent with the weathering of carbonate and sulfide minerals (Fig. 2-2, 2-3a) that were likely integrated into local tills from regional dolomite and shale bedrock by the Laurentide Ice Sheet (LIS) (Calmels et al., 2007; Norris, 1985; Stott, 1991). Ca^{2+}+Mg^{2+} and SO_4^{2-} were substantially higher in RTS runoff (> ~2,000 μmol L^{-1}; $p < 0.01$) and downstream of RTS ($p < 0.03$) than in pristine streams (Fig. 2-2; Table A1-3). The downstream increase in DIC was primarily as HCO_3^-, which increased ~40% between pristine and RTS-affected reaches (Fig. 2-2a). In comparison, pristine streams were characterized by lower HCO_3^-, Ca^{2+}+Mg^{2+}, and SO_4^{2-} (~500 μmol L^{-1}). Analysis of minerals in runoff confirmed the presence of carbonates (dolomite, calcite) and sulfide (pyrite), in addition to silicates, gypsum, and anatase (Table A1-1).

Ions derived from carbonate and sulfide minerals – which weather more readily than silicates (Blum et al., 1998; Hercod et al., 1998; Stumm & Morgan, 1996) – characterized the solute pool in RTS runoff. Ion ratios suggest carbonate weathering in RTS runoff was driven by H_2SO_4 (Fig. 2-3a) rather than H_2CO_3 (Fig. 2-3b). Similarly, DIC stable isotopes implicate carbonate weathering by H_2SO_4 as a major source of solutes in runoff (Fig. 2-3c, end-member 1). This

signature of H_2SO_4-driven carbonate weathering persisted from runoff into affected streams, following some dilution by pristine streams, and appeared to be coupled with enhanced sulfide oxidation. Isotopically, the SO_4^{2-} in runoff resembled sulfide exposed by an RTS (Fig. 2-3d) and subject to oxidation by oxygen in water molecules from rainfall or melting permafrost ice (equation A1-10), with greater contributions from atmospheric O_2 under drier conditions (equation A1-11). Although the LIS may have also eroded gypsum-bearing units (Stott, 1991), a limited amount of gypsum appears to contribute to SO_4^{2-} in fluvial networks on the Peel Plateau. The strong isotopic signal of sulfide oxidation extends from permafrost soils to RTS runoff, and across stream orders to the Stony Creek outflow and Peel River (Fig. 2-3d). Evidently, these effects originate in headwaters, where fluvial incision of permafrost-preserved ice-rich tills promotes RTS development (Kokelj et al., 2017) (Fig. 2-1). These striking changes in mineral weathering reflect major thermokarst-enabled alteration to the downstream inorganic carbon cycle. Similar biogeochemical disruption is likely characteristic of circumpolar glaciated terrains (Kokelj et al., 2017), where ice- and mineral-rich substrate is susceptible to rapid thaw and weathering.

Thermokarst intensity – measured here as headwall height – controls the depth of materials thawed and thus the composition of substrate transported to streams. As thermokarst intensifies on the Peel Plateau, larger RTS with "deeper" headwalls expose greater proportions of sulfide and mineral carbon preserved in previously unthawed Pleistocene soils than smaller, "shallower" disturbance features (Fig. 2-1; Table A1-2) (Littlefair et al., 2017; Malone et al., 2013). Accordingly, we hypothesized RTS morphology would be a key driver of mineral carbon transformation. Deeper RTS enabled weathering of Pleistocene tills, leading to an increasing signature of H_2SO_4-driven carbonate weathering in RTS runoff (Fig. 2-3c); higher concentrations of HCO_3^- in runoff (supporting information Fig. A2-1a); and consistent transport of HCO_3^- to affected streams via runoff (supporting information Fig. A2-1b, Table A1-4). In comparison, runoff from the shallowest RTS features (SD, HD) appeared more influenced by H_2CO_3 from biogenic and atmospheric CO_2, or perhaps silicate weathering by H_2CO_3 (Fig. 2-3c; supporting information Fig. A2-2 end-members 2 and 4). This shift in the composition of mineral substrate exposed by intensifying thermokarst – to greater proportions of previously unthawed sulfides and carbonates – signals a future of increasing H_2SO_4-driven

carbonate weathering on the Peel Plateau as thaw accelerates (Kokelj et al., 2015; Segal et al., 2016a) (supporting information Fig. A2-3).

2.3.2 Carbonate Weathering as a CO_2 Source on the Peel Plateau

In contrast to HCO_3^-, pCO_2 did not differ significantly between pristine and RTS-affected streams (1,041 ± 112 vs. 889 ± 103 µatm, mean ± SE, respectively), despite being consistently supersaturated in runoff (4,437 ± 643 µatm; Table A1-3, Fig. 2-3e). Although RTS contributed a substantial proportion of solutes to affected streams (supporting information Fig. A2-1), the limited contribution of CO_2 appears to be driven by a combination of rapid CO_2 loss to the atmosphere and some consumption by mineral weathering. Across all features, $\delta^{13}C_{CO2}$ in runoff was more consistent with HCO_3^- protonation following H_2SO_4-driven carbonate weathering (equations 2-2 and 2-3) than with biogenic or atmospheric CO_2 (Fig. 2-3f, end-member 2). This suggests HCO_3^- protonation, which appears to neutralize H_2SO_4 in RTS features on the Peel Plateau, has contributed to the significant CO_2 supersaturation in runoff. Weathering in regional headwaters thus amplifies rather than counterbalances the permafrost carbon-climate feedback. In shallow RTS, which are characterized by a larger proportion of organic substrate from the active layer and early Holocene thaw layer, more CO_2-rich runoff (21-72% of DIC, on average) and lower pH (supporting information Fig. A2-4) partly reflects greater contribution from microbial respiration to the DIC pool, which may promote H_2CO_3-driven carbonate weathering.

These findings suggest H_2SO_4-driven carbonate weathering and rapid loss of geogenic CO_2 in headwaters are widespread in this region. Indeed, the conditions are suitable: the Peel River and its tributaries flow through regions of abundant thermokarst (Kokelj et al., 2017) and exposed shale bedrock (Norris, 1985). Long-term trends in Peel River solute yields can provide insight into the regional ubiquity and intensification of these processes across the 70,000 km^2 Peel River watershed.

2.3.3 Multi-Decadal Trends in H_2SO_4-driven Carbonate Weathering

Previous work has shown that SO_4^{2-}:Cl^- concentration ratios have more than doubled in the Peel River since 1960, in conjunction with intensifying RTS activity driven by increasing air temperatures and precipitation (Kokelj et al., 2013; Segal et al., 2016a). Here, we show that Ca^{2+}, Mg^{2+}, and SO_4^{2-} fluxes increased significantly from 1979 to 2015, by 32%, 52%, and 125%,

respectively (Fig. 2-4a; Table A1-5). In comparison, alkalinity fluxes – largely reflective of HCO_3^- in this region (Tank et al., 2016) – increased marginally (by 10%; $p = 0.09$; Fig. 2-4b). While silicate weathering perhaps generated some Mg^{2+}, the presence of dolomite and sulfide in RTS (Table A1-1); the relatively faster weathering rate of carbonates compared to silicates (Stumm & Morgan, 1996); and the lack of change in Peel River discharge over this period (Fig. 2-4c) suggests accelerating thermokarst activity enhanced carbonate weathering following sulfide oxidation, and drove the striking increase in these solute fluxes. Furthermore, the increase in SO_4^{2-} relative to Ca^{2+} and Mg^{2+} largely reflects H_2SO_4-driven carbonate weathering (Fig. 2-4d), which may temper the alkalinity response (equations 2-2, A1-5 and A1-8).

Following the stoichiometry in equation (A1-8), if carbonate weathering by excess H_2SO_4 generates one mole of CO_2 for every mole of SO_4^{2-}, we estimate up to ~240 Gg of geogenic CO_2 loss from fluvial networks in the Peel River watershed during 2015, given a calculated SO_4^{2-} flux of 19.9 Gmol y^{-1}. While this estimate spans the Peel River watershed, RTS-affected headwaters may contribute disproportionately because this geogenic CO_2 is rapidly produced and lost in the vicinity of thermokarst. The corresponding CO_2 yield across the Peel River watershed (3.4 gC m^{-2} y^{-1}) is nearly one order of magnitude greater than recent estimates for Alaskan streams (0.4 gC m^{-2} y^{-1}) (Crawford et al., 2013). Additionally, this geogenic CO_2 flux in the Peel River watershed offsets a significant fraction (>20%) of estimated CO_2 consumption by mineral weathering across the larger 1.8M km^2 Mackenzie River watershed (Beaulieu et al., 2012).

These Peel River trends align with riverine signatures of intensifying physical erosion and chemical weathering across the Mackenzie River watershed (Calmels et al., 2007; Tank et al., 2016), where carbonate (rather than silicate) weathering dominates contributions to HCO_3^- flux (Beaulieu et al., 2012; Tank et al., 2012). Both the Peel (this work) and Mackenzie (Tank et al., 2016) Rivers exhibit increasing Ca^{2+}+Mg^{2+} and SO_4^{2-} yields from ~1975–2015. However, in the Peel River, absolute increases in yield (total change normalized to watershed area) were far greater for both Ca^{2+}+Mg^{2+} (152 vs. 41 kmol km^{-2}) and SO_4^{2-} (132 vs. 29 kmol km^{-2}), reflecting differences in geomorphology and watershed geology. In the Peel, where a significantly greater proportion of watershed area is underlain by ice-rich RTS-affected permafrost, hydrochemical trends reveal intensifying thermokarst as a key driver of enhanced sulfide and carbonate weathering across a range of watershed scales. These findings suggest that disruption to aquatic

inorganic carbon cycling at the circumpolar scale will be strongest where thermokarst and carbonate-bearing terrains coincide.

2.3.4 Pan-Arctic Thermokarst Effects on Inorganic Carbon Cycling

Broadly overlapping distributions of carbonate-bearing permafrost and thermokarst-sensitive terrains indicate that perturbations to the aquatic inorganic carbon cycle may be pronounced across vast swaths of the circumpolar north (Fig. 2-5). These effects seem likely to manifest within and outside of former glacial limits across northern Canada and Alaska. These conditions are also present through much of the Yedoma region in northeast and north-central Siberia, but may be dampened for syngenetic permafrost if mineral weathering occurred during deposition and permafrost aggradation. Recent work shows sulfide oxidation to be more widely distributed at the global scale than previously understood (Burke et al., 2018). In permafrost regions where sulfides are prevalent, we document that the release of minerals into active biogeochemical cycles will enhance the permafrost carbon-climate feedback. Elsewhere, thaw-enhanced mineral weathering is still likely to be pronounced. However, in the absence of sulfides, H_2CO_3-driven weathering will sequester CO_2 (Dornblaser & Striegl, 2015). The balance between these processes at the pan-Arctic scale remains entirely undocumented.

2.4. Conclusions

To date, biotic-organic interactions have been the focal point for permafrost-carbon research. Here, we show abiotic feedbacks – which are strong enough to drive glacial-interglacial cycles (Foster & Vance, 2006; Torres et al., 2017) – can rapidly alter contemporary carbon cycling across broad spatial scales. Quantifying permafrost mineral and inorganic carbon stocks, their vulnerability to weathering, and subsequent chemical weathering reactions is critical for bringing inorganic processes into our conceptualization of the permafrost carbon-climate feedback (Schuur et al., 2015), and constraining the changing carbon cycle across diverse Arctic landscapes.

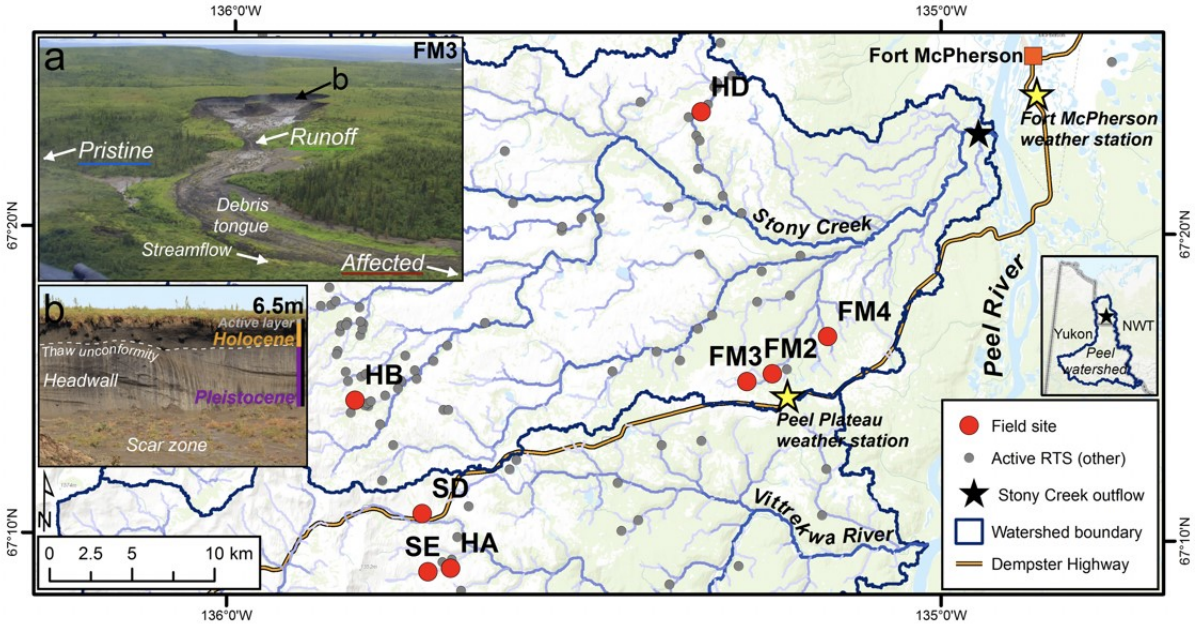

Figure 2-1. Field sites in stream networks, Peel Plateau, Canada. (a) Stream sampling locations (pristine, runoff, RTS-affected). Sediment-laden, solute-rich runoff from thawing permafrost flows via the scar zone and debris tongue into the stream. Ablation and thawing of exposed ground ice drive RTS growth. Rainfall helps maintain a permafrost "headwall" (b) and perpetuates upslope growth by accelerating downslope flow of thawed, collapsed material into the debris tongue, which can grow hundreds of meters long and tens of meters thick. See location of (b) in (a). Basemap: Esri ArcGIS Online; "Active RTS": Segal et al. (2016b).

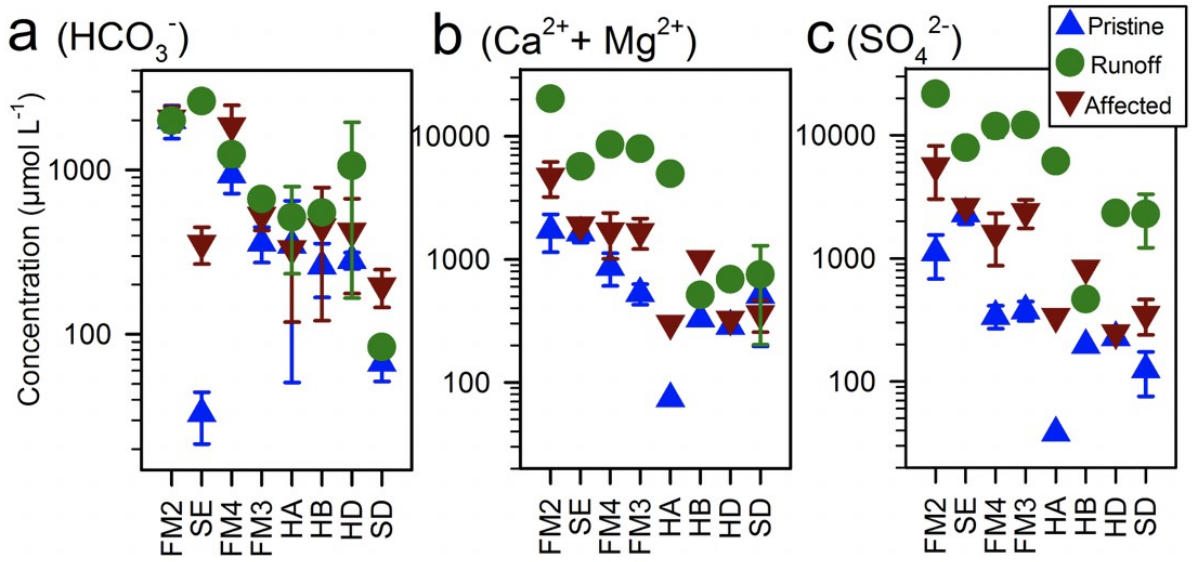

Figure 2-2. RTS impacts on (a) HCO_3^-, (b) Ca^{2+}+Mg^{2+}, and (c) SO_4^{2-}. RTS are ordered left to right by decreasing maximum headwall height. Error bars indicate standard error.

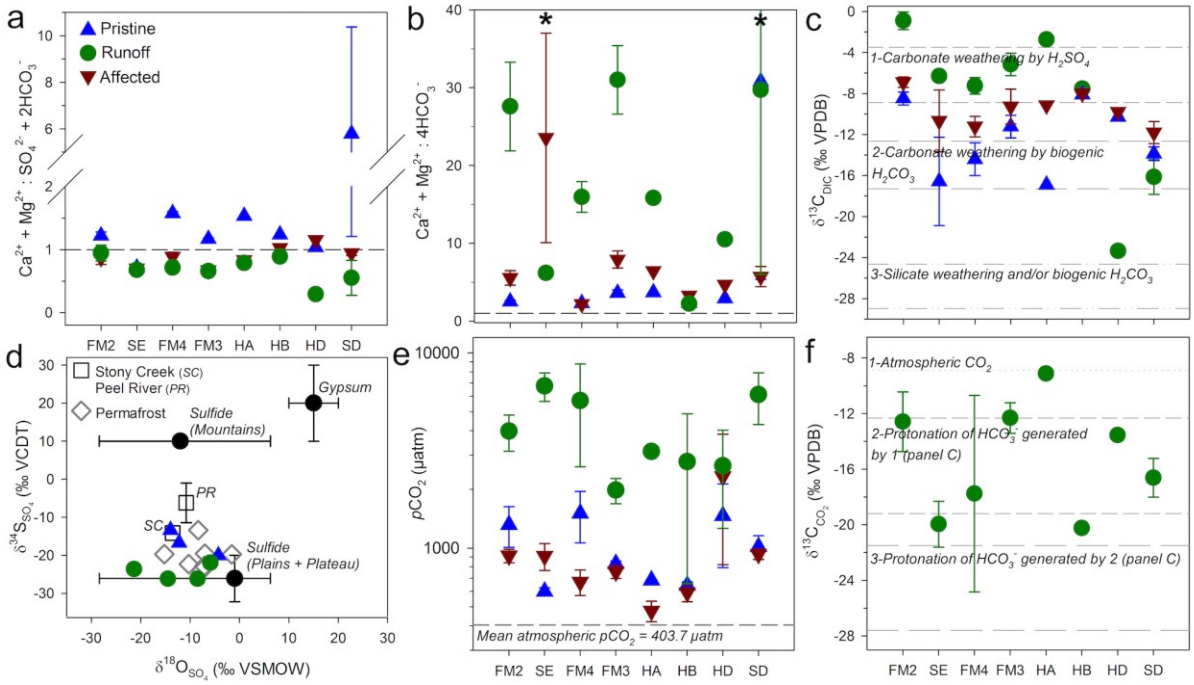

Figure 2-3. (a,b) Ratios of solute equivalent concentrations in streams. Dashed lines indicate carbonate weathering by H_2SO_4 (a) or H_2CO_3 (b). (c) Composition of stable DIC isotopes in streams. End-members (area between lines with same dash) derived from the literature. (d) Sulfur isotope composition of streams and permafrost; published Peel River values (open squares) (Calmels et al., 2007; Hitchon & Krouse, 1972); published regional sulfide (plains, mountains) and gypsum end-members (Calmels et al., 2007); and $\delta^{18}O_{SO4}$ range expected from oxidation of regional sulfides (van Everdingen & Krouse, 1985). Whiskers for sulfide end-members denote range, calculated following details in supporting information. (e) pCO_2 by RTS. (f) Composition of stable CO_2 isotopes in RTS runoff. (a, b, c, e, f) Sites ordered left to right by decreasing headwall height (whiskers represent standard error). For all, see supporting information for derivation of end-members and ranges.

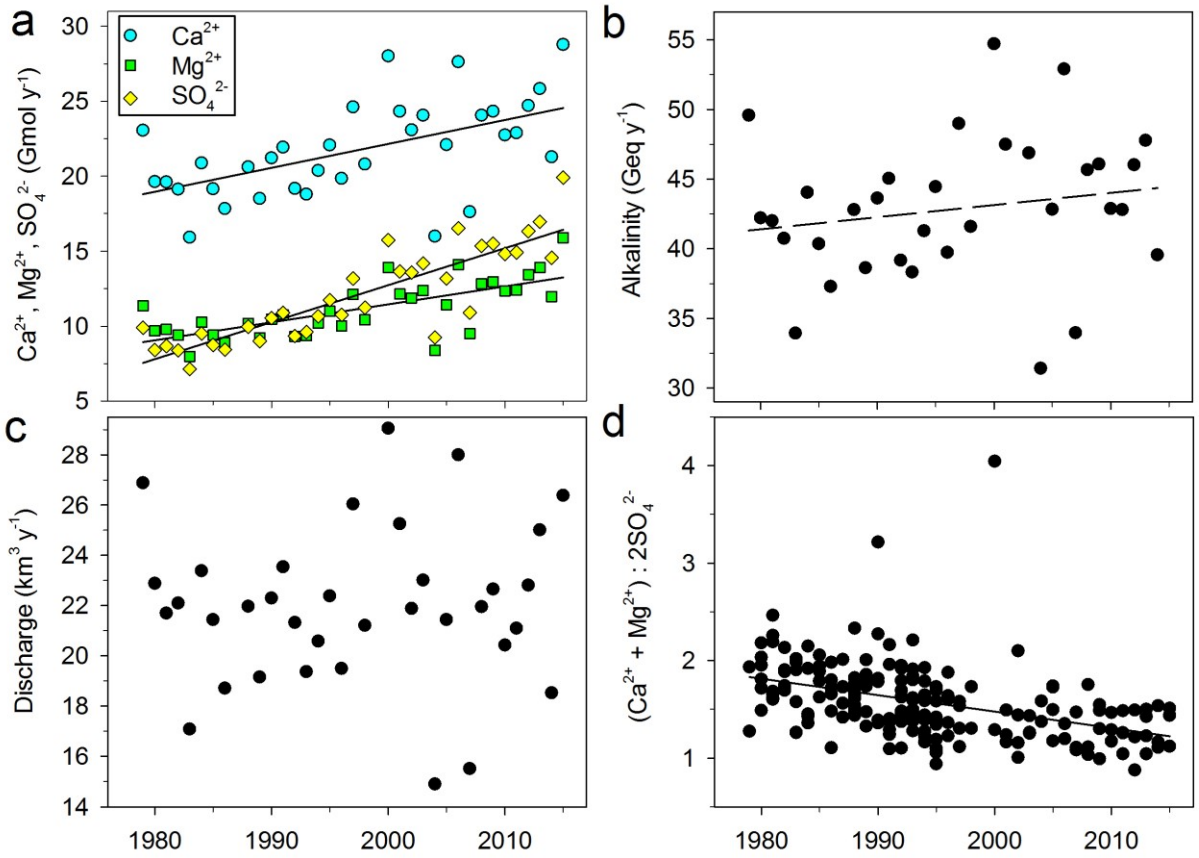

Figure 2-4. Modeled annual fluxes of (a) Ca^{2+}, Mg^{2+}, and SO_4^{2-} and (b) alkalinity. (c) Modeled annual discharge. (d) Ratio of solute equivalent concentrations; values near one indicate H_2SO_4-driven carbonate weathering (equation A1-8). For all, solid and dotted regression lines indicate significant and marginal trends, respectively (supporting information Table A1-5; see Methods).

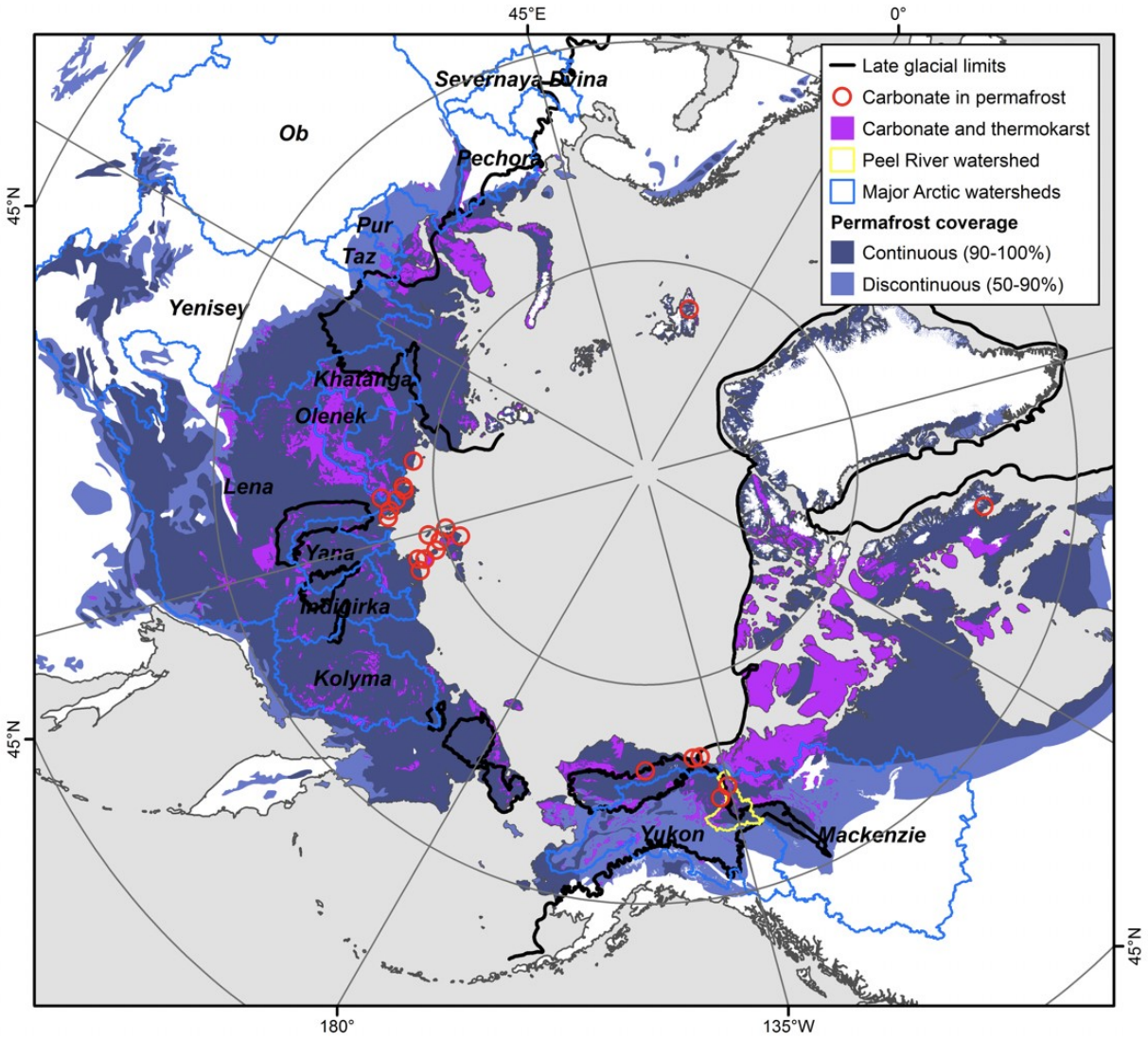

Figure 2-5. Pan-Arctic hillslope thermokarst terrains, carbonate-bearing lithologies, late glacial limits, and observations of carbonate-bearing permafrost from this study and the literature (see Methods for data sources). Basemap, major Arctic river watersheds, and permafrost coverage from ESRI ArcGIS Online.

CH. 3: Thermokarst Effects on Carbon Dioxide and Methane Fluxes in Streams on the Peel Plateau (NWT, Canada)

Summary

Thermokarst can rapidly mobilize vast amounts of sediment, solutes, and organic carbon previously maintained in frozen soils to inland waters. Streams provide a critical pathway for transforming these materials into carbon dioxide (CO_2) and methane (CH_4), yet the direct effects of thermokarst on fluvial C gas efflux from streams to the atmosphere are largely unknown. Working on the Peel Plateau in the western Canadian Arctic, we show that CO_2 efflux in rill runoff thaw streams (runoff) within retrogressive thaw slumps (RTSs) was four times greater than in adjacent streams and contributed modestly but disproportionately to efflux at the landscape scale. In contrast, CH_4 efflux was generally greater in adjacent streams than in RTS runoff and, overall, was within the range of values reported for other northern streams. While RTS occurrence was a primary driver of CO_2 efflux, CH_4 efflux was more strongly associated with conditions reflective of biological activity. Transects downstream of two RTSs revealed that CH_4 consistently and rapidly degassed to the atmosphere, while elevated CO_2 was sustained downstream of one RTS feature. At the watershed scale, streams adjacent to RTSs rather than runoff streams within RTSs dominated fluvial CO_2 and CH_4 efflux. Intensifying thermokarst activity in the western Canadian Arctic will likely amplify contributions from runoff streams in RTSs to watershed-scale fluvial C gas efflux.

3.1. Introduction

Perennially frozen soils (permafrost) contain more carbon (800 Pg) (Hugelius et al., 2014) than is currently in the atmosphere. From a climate perspective, the microbial oxidation of organic carbon in thawing permafrost stands to amplify climate warming by releasing the greenhouse gases carbon dioxide (CO_2) and methane (CH_4) (Schuur et al., 2015). As rapid northern warming and intensifying precipitation (Lique et al., 2016) strengthen hydrologic connectivity between thawing permafrost and aquatic ecosystems (Walvoord & Kurylyk, 2016), streams may be primary sites of permafrost transformation into CO_2 and CH_4 (C gas) (Vonk, Tank, Bowden, et al., 2015) and potentially of C gas efflux to the atmosphere.

In fluvial networks, CO_2 concentrations are typically most pronounced in headwaters (Butman & Raymond, 2011, Crawford et al., 2013, Hutchins et al., 2019), owing to relatively

strong hydrologic connectivity between streams and soils (Hope et al., 2004; Hotchkiss et al., 2015) and to CO_2 production within streams from processing of organic and mineral substrates (Drake et al., 2015; Zolkos et al., 2018). In regions with organic-rich yedoma permafrost, for instance, dissolved organic carbon (DOC) is relatively biolabile and readily oxidized by microbes following thaw, resulting in rapid aquatic CO_2 production (Drake et al., 2015, 2018). In regions with more sediment- and mineral-rich permafrost, such as in ice-rich glaciated terrain, the chemical weathering of minerals exposed by thaw can consume or produce CO_2 in streams (Tank et al., 2012; Zolkos et al., 2018). Fluvial CH_4 concentrations can be highly heterogeneous across short distances because of variability in the environmental conditions that are conducive to methanogenesis (Crawford, Loken, et al., 2017). CH_4 production in streams can be enhanced by nutrients (e.g. DIN; Stanley et al., 2016), or limited by the presence of alternate terminal electron acceptors (e.g. DIN, SO_4^{2-}) that enable non-methanogenic archaea to outcompete methanogens for organic substrate (Abbott et al., 2015; Schade et al., 2016; Stanley et al., 2016). Permafrost thaw is well-known to cause profound changes to stream geochemistry (Abbott et al., 2015; Drake et al., 2018; Rudy et al., 2017; St. Pierre et al., 2019), yet the implications for fluvial C gas production are not well understood (but see Abbott et al., 2015).

The effects of permafrost thaw on streams are particularly striking in ice-rich landscapes, where terrain subsidence following thaw can lead to the formation of thermokarst (Kokelj & Jorgenson, 2013). Thermokarst-susceptible terrains span ~20% of the northern permafrost region (Olefeldt et al., 2016) and are characterized by a suite of disturbance types strongly conditioned by factors including ground ice content, topography, and climate (Kokelj et al., 2015; Kokelj & Jorgenson, 2013; Segal et al., 2016a). For instance, climate-driven thermokarst is transforming ice-rich glaciated landscapes, making them amongst the most dynamic permafrost environments in the circumpolar north (Kokelj et al., 2013; Kokelj, Lantz, et al., 2017; Lacelle et al., 2015; Lewkowicz & Way, 2019). Thermokarst in ice-rich glaciated landscapes can release a substantial amount of solutes and sediments (Kokelj et al., 2013; Rudy et al., 2017) containing carbon (Hugelius et al., 2014; Lamoureux & Lafrenière, 2014; Vonk et al., 2013) and nutrients (Bowden et al., 2008; Walvoord & Striegl, 2007) into freshwater systems. However, the effects of thermokarst on fluvial CO_2 and CH_4 concentration and efflux to the atmosphere remain poorly constrained (Vonk, Tank, Bowden, et al., 2015).

In this study, we characterize the effects of thermokarst on C gas production and quantify its efflux from a series of northern streams in an ice-rich glaciated landscape. Our objectives were to quantify CO_2 and CH_4 concentration and flux in thermokarst-affected streams; characterize the geochemical controls on C gas production; and determine the contribution of thaw streams within thermokarst features to fluvial C gas efflux at the watershed scale. We hypothesized that the release of mineral and organic substrate from permafrost would enhance CO_2 production and efflux within and downstream of thermokarst features, but that terminal electron acceptors from thawing permafrost would suppress CH_4 production and efflux. These findings advance understanding of the biogeochemical effects of permafrost thaw on aquatic ecosystems and the potential significance of these effects in moderating Earth's climate.

3.2. Methods

3.2.1 Study Area

The Peel Plateau (NWT, Canada) is an ideal setting to test the direct effects of thermokarst on fluvial C gas efflux. It is a fluvially-incised, glaciated landscape comprising a 60 to 80 km band along the eastern margins of the Richardson Mountains and northeastern Mackenzie Mountains, with ice-rich permafrost extending up to 50 m in thickness (Kokelj, Tunnicliffe, et al., 2017). The Peel Plateau is predominantly comprised of glacial till, glaciofluvial, and glaciolacustrine deposits (Duk-Rodkin & Hughes, 1992a; Kokelj, Tunnicliffe, et al., 2017) emplaced at the western margin of the Laurentide Ice Sheet (LIS). These deposits contain carbonates and sulfides (Zolkos et al., 2018) that were likely incorporated into the basal ice and diamicton by the LIS during its westward expansion across regional carbonate and shale bedrock (Norris, 1985; Stott, 1991). Following retreat of the LIS, rapid climate warming during the early Holocene (12–8.5 kybp) resulted in regional thermokarst, including an increase in thaw depth and an acceleration of thaw slumping (Lacelle et al., 2014), enabling mineral weathering and the accumulation of solutes and organic matter (Burn, 1997; Lacelle, 2004; Malone et al., 2013). Subsequent cooling through the mid- to late-Holocene caused upward aggradation of permafrost and preservation of the solute- and organic-rich Holocene layer above deeper ice- and sediment-rich Pleistocene tills (Kokelj et al., 2013; Lacelle et al., 2013). Modern climate warming and intensifying regional precipitation are accelerating thermokarst activity across the Peel Plateau and in other ice-rich, glacigenic terrains across the Canadian Arctic (Kokelj et al., 2015; Kokelj,

Lantz, et al., 2017; Lewkowicz & Way, 2019; Rudy et al., 2017; Segal et al., 2016a). Thermokarst in these environments often manifests as retrogressive thaw slump (RTS) features. RTSs develop due to ablation of exposed, ice-rich permafrost, causing rapid thaw of thick layers of frozen ground and transport of large volumes of saturated thawed materials from slopes to fluvial systems (Kokelj et al., 2015) (Fig. 3-1). In addition to mobilizing previously sequestered material into modern biogeochemical cycles, RTS can temporarily alter hydrology if the debris tongue (Fig. 3-1) partially dams the impacted stream, creating a transient upstream reservoir (Kokelj et al., 2013; St. Pierre et al., 2018).

3.2.2. Sample Collection and Analysis

3.2.2.1. Sampling Design

Our work occurred in the Stony Creek and Vittrekwa River watersheds of the Peel Plateau (Fig. 3-1). We sampled streams from June to August 2015, at five sites accessed by foot from the Dempster Highway and at three sites accessed by helicopter (Fig. 3-1). Sites accessed by foot were visited five or six times each (roughly every two weeks) and sites accessed by helicopter were visited twice (mid-June, late July). Following Littlefair et al. (2017), we evaluated thermokarst effects on C gas concentrations and potential geochemical drivers in streams by collecting paired samples upstream and downstream of RTSs, from the unimpaired and affected reaches, respectively. To characterize the geochemistry of thawed permafrost material entering streams, we sampled thaw streams flowing from the RTS headwall and within the debris tongue (Fig. 3-1a,b), after the streams merged into channelized rill runoff and prior to the runoff entering the stream adjacent to the RTS (Fig. 3-1a,c). To test how the composition of thawed permafrost material influences C gas efflux, we sampled streams affected by RTSs with varying headwall exposures, because the proportion of exposed Pleistocene permafrost typically increases with headwall height (Fig. 3-1b; Table 3-1). At two RTSs, we also sampled 25, 50, 100, and 200 m downstream of RTS runoff to investigate the evolution of C gas in affected stream reaches (Fig. 3-1c). Transects were established for one shallow RTS (i.e. shorter headwall) (SD) and one deeper RTS (SE) (Table 3-1).

3.2.2.2. Stream Sampling

Water temperature, pH, and dissolved oxygen (D.O.) were measured using a precalibrated YSI Professional-Plus sonde. pH and temperature were measured with an Oakton pHTestr 30 (accuracy ± 0.01 pH units) on the rare occasion when the YSI was not working. C gases were collected and sonde measurements were made at all sampling points (Fig. 3-1). Ions and nutrients were measured upstream and downstream of RTSs, in RTS runoff streams, and, for transect sampling at RTSs SD and SE, also at 50 and 200 m downstream. Ions, dissolved organic carbon (DOC), and UV-visible absorbance were collected in sample-rinsed 1L HDPE bottles and refrigerated (4˚C, dark) for 24h to allow sediments to settle prior to filtering through precombusted (450˚C, 4h) 0.7-µm glass fiber filters (Whatman GF/F). Filtered subsamples were stored in filtrate-rinsed, acid-washed bottles (10% HCl, 24h), except anions and absorbance, which were stored in non-acid-washed bottles. All subsamples were refrigerated prior to analysis, except dissolved inorganic nitrogen (DIN, $\Sigma[NH_3^+, NO_3^-, NO_2^-]$), which was stored at –15˚C. Filtrate for DOC was acidified to below pH 2 with 8M trace metal-grade HCl (Vonk, Tank, Mann, et al., 2015). Dissolved inorganic carbon (DIC = $\Sigma[CO_2, HCO_3^-, CO_3^{2-}]$) was collected and analyzed following Zolkos et al. (2018). Briefly, DIC samples were filtered (0.45-µm polyethersulfone [PES]) and preserved in sealed glass bottles with KCl (Striegl et al., 2012), and measured by gas chromatography following Stainton (1973).

Dissolved C gases were measured upstream and downstream of RTSs and in runoff streams, and, for transect sampling at RTSs SD and SE, also at 25, 50, 100, and 200 m downstream. Samples were collected using the headspace equilibration method (Hesslein et al., 1991) and stored in an airtight 60 mL syringe (CO_2) or with positive pressure in pre-evacuated serum bottles sealed with pre-baked (60˚C, 12h) butyl rubber stoppers (CH_4) (Spawn et al., 2015). One atmospheric CO_2 sample was collected per site and average monthly atmospheric CH_4 concentrations were obtained from the National Oceanic and Atmospheric Administration (http://www.esrl.noaa.gov/) for Barrow, Alaska. Gas samples were stored in the dark and at ~20˚C prior to analysis within 10h (CO_2) or four months (CH_4). Water and air temperatures, atmospheric pressure, and the volumetric ratio of sample to atmospheric headspace was recorded for correcting later calculations of CO_2 and CH_4 partial pressures (pCO_2 and pCH_4). DIC species were calculated in CO2sys (v.2.3; Pierrot et al., 2006), using DIC concentration and pCO_2 and the temperature-dependent freshwater constants for K1 and K2 (Millero, 1979; Millero, 2010).

These constants describe the equilibrium distribution of aqueous carbonate species (Stumm & Morgan, 1996), which can be summarized as:

$$H_2O + CO_{2(g)} \rightleftharpoons H_2CO_3^* \rightleftharpoons H^+ + HCO_3^- \rightleftharpoons 2H^+ + CO_3^{2-} \quad (3\text{-}1)$$

Where $H_2CO_3^*$ includes dissolved CO_2 and K2 is defined as $HCO_3^- = H^+ + CO_3^{2-}$.

Stable isotopes of DIC ($\delta^{13}C_{DIC}$) were collected upstream and downstream of RTSs and in runoff streams without headspace in polycarbonate bottles. Stable isotopes of DOC ($\delta^{13}C_{DOC}$) in permafrost ice were collected from above the Holocene thaw unconformity at depths of 0.5 m beneath the land surface at RTS SD and 0.8 m at RTS SE, and from Pleistocene till at a depth of 2 m (RTS FM3) (Fig. 3-1). Permafrost samples were collected using a mallet and stainless-steel chisel and thawed in plastic bags upon returning from the field. Water for $\delta^{13}C$ was filtered (0.45-µm PES) within 10 hours into precombusted 40 mL borosilicate vials with no headspace and sealed with two silicone-teflon septa. Stable water isotopes ($\delta^{18}O$) were collected in the runoff streams of RTS features FM2, FM3, SE, HA, and HB once during the summer, to estimate within-RTS streamflow (see below). Samples were collected without headspace or air bubbles in 30 mL HDPE bottles and sealed with electrical tape to prevent atmospheric exchange, refrigerated, and filtered (0.45-µm cellulose acetate) prior to analysis.

3.2.2.3. Geochemical Analyses

Cations were analyzed by Inductively-Coupled Argon Plasma Optical Emission Spectrometer (Thermo ICAP-6300) and anions by Ion Chromatography (Dionex DX-600) at the University of Alberta Biogeochemical Analytical Services Laboratory (BASL). DIN was analyzed at BASL by flow injection analysis (Lachat QuickChem QC8500 FIA Automated Ion Analyzer), using automated colorimetry to determine NO_3^- and NO_2^-. DOC was measured by high-temperature combustion (Shimadzu 5000A TOC analyzer), using solutions prepared from a 1,000 ppm KHP standard (ACCUSPEC) to create a four-point standard curve. An in-house caffeine standard (10 mg L^{-1}) was run every 20 samples to monitor instrument drift.

UV-visible absorbance was analyzed in a field lab at room temperature within one week of collection. Samples were analyzed in duplicate using a Genesys 10 UV spectrophotomer and 1 cm quartz cuvette. MilliQ water blanks were analyzed at the beginning and end of each run to

monitor machine drift and the absorbance at 750 nm was used to correct each sample for offset due to scattering (Stubbins et al., 2017). Using corrected spectra, we calculated specific UV absorbance at 254 nm ($SUVA_{254}$, L mgC^{-1} m^{-1}) as the Decadic absorption coefficient at 254 nm (A_{254}, m^{-1}) divided by DOC concentration (Weishaar et al., 2003), first correcting for Fe interference (Poulin et al., 2014). We use $SUVA_{254}$ as an index of relative DOC aromaticity (Weishaar et al., 2003), to assess potential organic carbon reactivity.

CO_2 of the equilibrated headspace was measured by infrared gas analyzer (IRGA; PP Systems EGM-4) upon returning from the field. IRGA machine drift was checked monthly using a 1,010 ppm CO_2 standard (Scotty Gases). CH_4 of the equilibrated headspace was measured in duplicate injections using a gas chromatograph (GC; Varian CP-3800) equipped with a Flame Ionization Detector. Concentration was calculated from four-point calibration curves, built daily from commercial standards (Praxair), and a CH_4 standard was analyzed every 10 samples to monitor GC drift. We calculated pCO_2 using Henry's constants corrected for *in situ* water temperature (Weiss, 1974) and pCH_4 following Wiesenburg & Guinasso (1979), accounting for the ratio of sample volume to headspace during equilibration.

$\delta^{13}C$ (DIC, DOC) was analyzed at the University of Ottawa Stable Isotope Laboratory by isotope ratio mass spectrometry (IRMS), using an OI Analytical Aurora Model 1030W Total Organic Carbon Analyzer interfaced to a Finnigan Mat DeltaPlusXP IRMS. $\delta^{18}O$ were analyzed by cavity ringdown spectroscopy (Picarro L2130-i) at BASL. Calibration curves for water isotopes were built from U.S. Geological Survey secondary standards (USGS45 and USGS46) and in-house tap water, and calibrated by an International Atomic Energy Agency standard as a quality control.

3.2.3. Water Discharge and Channel Slope

During each site visit, water discharge (Q) was measured upstream and downstream of RTSs and, for transect RTSs SD and SE, additionally at 50 m and 200 m downstream. Discharge was calculated from measurements of stream velocity (RedBack Model RB1, PVD100) and stream cross-sectional area (Gordon, 2004) measured at increments equal to 10% of stream width (Lurry & Kolbe, 2000), except in small streams (increments ≥ 8 cm). Stream velocity was additionally used in calculations of the gas transfer velocity (discussed below). Following Gordon (2004), we used a clinometer to measure stream channel slope ($m\ m^{-1}$) along three reaches comprising one

full meander amplitude at each site. The meander was centered on the sampling site and slope was calculated as the mean of the three measurements.

In order to quantify discharge of runoff streams, we first calculated the proportion of runoff in the downstream (i.e. RTS-affected) reach (f_{runoff}), using stable water isotopes in a two end-member mixing model:

$$f_{runoff} = (\delta^{18}O_{down} - \delta^{18}O_{up}) / (\delta^{18}O_{runoff} - \delta^{18}O_{up}) \quad (3\text{-}2)$$

where "up" and "down" are the upstream (i.e. unaffected) and downstream reaches. f_{runoff}, and thus C gas efflux from RTS runoff (Sec. 3.2.4), could not be calculated where $\delta^{18}O_{down} \geq \delta^{18}O_{up}$. This occurred at RTSs that were smaller (SD, HD) or less active (FM4), likely owing to a relatively low proportion of ^{18}O-depleted meltwater from permafrost ice in the downstream reach. We then calculated discharge from RTSs (Q_{runoff}) as the product of f_{runoff} and the measured downstream discharge (Q_{down}):

$$Q_{runoff} = f_{runoff} \times Q_{down} \quad (3\text{-}3)$$

We paired Q_{runoff} with gas measurements to estimate C gas efflux from runoff streams within RTSs (described below).

3.2.4. C Gas Efflux from Streams to the Atmosphere

We empirically derived models for the gas transfer velocity (k) from CO_2 and CH_4 efflux measurements made during summer 2016. Using an IRGA, we measured efflux as the change in CO_2 concentration within the headspace of a stationary, streamlined chamber (designed following Crawford et al., 2013). The chamber was submerged 2 cm below the stream surface using a tripod assembly and connected to the IRGA by 2 m of inert Bev-a-line tubing. CO_2 was recorded every 15 seconds for five minutes and efflux was calculated from the net change in concentration upon reaching a constant slope of change in concentration versus time, which typically occurred within the first minute. Discrete CH_4 samples were collected every five minutes for twenty minutes, stored in the same fashion as dissolved CH_4 samples (above), and concentrations were measured within eight months using a GC (Sec. 3.2.2). Atmospheric CO_2

was measured from the IRGA with the chamber suspended above the stream and atmospheric CH_4 was collected and stored in 10 mL vials. CO_2 and CH_4 efflux (J) were derived from triplicate and single measurements, respectively, following Duc et al. (2013):

$$J = PH\Delta C / RT\Delta t \times c \quad (3\text{-}4)$$

Where units for CO_2 and CH_4 efflux are μmol m^{-2} s^{-1} and nmol m^{-2} s^{-1}, respectively ; P is atmospheric pressure (atm); H is the height of the flux chamber (m); ΔC is the change in headspace gas volume fraction (ppmv); R is the ideal gas constant (82.0562 mL atm K^{-1} mol^{-1}); T is the air temperature (˚K); Δt is the measurement duration (s); and c is a factor that converts from mol to μmol or nmol for CO_2 and CH_4. The gas transfer velocity k (m d^{-1}) was calculated using J and the concentrations (mol m^{-3}) of dissolved gas in the stream (c_{water}) and in equilibrium with the atmosphere (c_{sat}) (Cole & Caraco, 2001). Based on gas efflux and stream flow measurements from 2016, the best predictor model for k of CO_2 (kCO_2) was stream velocity (V), while water discharge (Q) was the best predictor of kCH_4:

$$kCO_2 = 12.207V + 1.505 \quad (df = 12, p < 0.00, R^2 = 0.64) \quad (3\text{-}5)$$
$$kCH_4 = 0.272\ln Q + 1.811 \quad (df = 7, p < 0.01, R^2 = 0.61) \quad (3\text{-}6)$$

These models were validated for streams with diverse flow conditions (velocity = 0.03–0.74 m s^{-1}, Q = 0.001–0.168 m^3 s^{-1}) and morphology (width = 0.34–1.49 m). Flux data were quality-checked prior to developing the k models and five CH_4 efflux measurements were omitted, owing to poor linearity (n = 4) and CH_4 loss from the chamber (n = 1) (Table A2-1). These models were then used to calculate the k values and instantaneous water-to-air efflux associated with our 2015 measurements of V, Q, [CO_2], and [CH_4] (Cole & Caraco, 2001; MacIntyre et al., 1995; Raymond et al., 2012)(MacIntyre et al., 1995):

$$J = k(c_{water} - c_{sat}) \quad (3\text{-}7)$$

We followed this approach to estimate instantaneous efflux of CO_2 and CH_4 from runoff, using equations (3-5) and (3-6), measurements of runoff c_{water} and c_{sat}, and estimates of runoff stream

velocity constrained by Q_{runoff} and field estimates of runoff channel depth (5–20 cm) and width (20–30 cm). To provide context for our estimates of C gas efflux, we compare them with a compilation of published C gas efflux values from diverse locations and environments.

3.2.5. C Gas Persistence and Contributions to Watershed-Scale Fluvial Efflux

We used excess C gas (Striegl et al., 2012) calculated as a proportion (c_{water} : c_{sat}) to evaluate the persistence of C gas along transects in two downstream reaches (RTSs SD and SE). Normalizing by c_{sat} facilitated comparison by controlling for variation in C gas saturated concentrations between streams. To quantify C gas loss along these transects, we used a simple mass balance equation:

$$\text{C gas loss} = \Delta c_{water} \times Q / V \times d \quad (3\text{-}8)$$

Where Δc_{water} is the change in CO_2 or CH_4 (μmol L^{-1}); Q is discharge converted to L s^{-1}; V is velocity (m s^{-1}); and d is the distance (200 m). Estimates of C gas loss were converted to mgC for reporting.

We evaluated RTS effects on C gas efflux at the landscape scale (mol d^{-1}) by separately upscaling efflux estimates in streams outside of RTSs and in runoff (Fig. 3-1). For streams outside (i.e. upstream and downstream) of RTSs, we summed the product of mean C gas efflux and fluvial surface area for each stream order (Campeau et al., 2014). C gas efflux was upscaled for stream orders one to three (accounting for 86% of total stream length; Table A2-2), because higher-order streams were not sampled. Field measurements of mean stream width and GIS estimates of stream length were used to estimate fluvial surface area. Stream length was derived from stream networks that were delineated from the Natural Resources Canada Canadian Digital Elevation Model (NRCan CDEM) using ArcHydro software in ArcGIS 10.5. We first reconditioned the CDEM using the NRCan National Hydro Network, which we modified as needed to match streams visible in satellite imagery (European Space Agency Copernicus Sentinel data 2017). Similarly, for RTS runoff streams, we multiplied mean C gas efflux by runoff fluvial surface area. The surface area of RTS runoff was constrained by field estimates of the depth and width of runoff channels, and multiplied by the number of active RTSs in the Stony Creek and Vittrekwa River watersheds (n = 129; Segal et al. 2016b) (Fig. 3-1).

3.2.6. Statistical Analyses

Following Littlefair et al. (2017), we compared stream chemistry and discharge upstream and downstream of RTSs to test thermokarst effects on possible geochemical controls on C gas (see next paragraph). We also compared stream chemistry upstream and in RTS runoff to characterize the composition of runoff streams. We used linear mixed effects regression models in the R package *lme4* (Bates et al., 2015) for both types of comparisons (e.g. Hutchins et al., 2019). Models included sampling location (i.e. upstream, within, downstream) as a fixed effect, RTS feature as a random effect, and Julian Day nested within RTS feature to pair samples collected on the same day.

We used a second linear mixed effects model design to explore geochemical controls on pCO_2 and pCH_4 across gradients of thermokarst disturbance. The geochemical controls we evaluated using these models included organic matter (DOC); carbon quality and source ($SUVA_{254}$, $\delta^{13}C_{DOC}$, $\delta^{13}C_{DIC}$) (Striegl et al., 2007; Tanski et al., 2017; Weishaar et al., 2003); nutrient and terminal electron acceptors (DIN, SO_4^{2-}) (Abbott et al., 2015; Stanley et al., 2016); mineral weathering (conductivity, DIC) (Tank et al., 2012; Zolkos et al., 2018); and stream temperature and D.O.. The models included fixed effects for these geochemistry variables (FE_{chem}) and also for sampling location (FE_{Loc}), to capture variability upstream, downstream, and in RTS runoff streams (equations 3-9 and 3-10). We included random intercept terms for RTS site (RE_{RTS}; FM2, SE, etc.) and sampling date (RE_{Date}) to capture variation between RTSs during the summertime. To evaluate variability in the strength of RTS effects on C gas, we specified a random slope term ($RE_{Loc\sim RTS}$) in a second model (equation 3-10) for comparison with the random intercept model (Harrison et al., 2018):

$$gas_1 = gas_2 + FE_{chem1} \ldots FE_{chem\,n} + FE_{Loc} + RE_{RTS} + RE_{Date} \quad (3\text{-}9)$$

$$gas_1 = gas_2 + FE_{chem1} \ldots FE_{chem\,n} + FE_{Loc} + RE_{Loc\sim RTS} + RE_{Date} \quad (3\text{-}10)$$

For these equations, gas_1 is pCO_2 when gas_2 is pCH_4, and vice-versa. We first determined whether a random intercept or slope model was more parsimonious, based on the lowest Akaike information criterion (AIC) score. Next, we trimmed the full model using the *step* function in the R package *lmerTest* (Kuznetsova et al., 2018) to eliminate non-significant fixed and random

effects. We then used Variance Inflation Factor (VIF) to identify highly collinear covariates (VIF > 3; Zuur et al., 2010), which were removed from the trimmed models. Random effects were evaluated using likelihood ratio tests and fixed effects using restricted maximum likelihood, and models were refit with maximum likelihood as needed for comparison. Model fits were inspected visually using quantile-quantile and residual plots and covariates were transformed as needed to meet assumptions of independent and homoscedastic residuals (Zuur, 2009). We additionally used Principal Component Analysis (PCA) to qualitatively expound on the mixed effects regression results by including these same geochemistry parameters in a broad assessment of C gas drivers. All statistics were performed using R software v.3.4.4 (R Core Team, 2015) and data below the detection limit (DL) were analyzed as DL/2 (EPA, 2000).

3.3. Results

3.3.1. RTS Effects on C Gas Concentrations and Fluxes

Compared to upstream sites, pCO_2 was significantly greater in RTS runoff (df = 43, t = –8.2, $p < 0.001$) and was marginally lower immediately downstream of RTSs (df = 37, t = 1.95, p = 0.06), but greater downstream of RTSs SE and HD (Table 3-2, Table 3-3). pCH_4 was supersaturated in most streams yet was variable among sites. pCH_4 values were higher upstream of some RTSs (FM4, FM3, HA, HD) and higher downstream of others (FM2, SE, HB, SD) (Table 3-2). In contrast to the notable increase of pCO_2 within RTS runoff relative to upstream and downstream sites, pCH_4 was higher in RTS runoff at some sites (SE, HA, HB, SD), but much lower in runoff in others, reflecting the overall variability of pCH_4 across this landscape.

Instantaneous CO_2 efflux from RTS runoff (mean = 8.32 μmol m^{-2} s^{-1}) was, on average, four times greater than in streams outside of RTSs (i.e. upstream and downstream), for sites having flux measurements both in runoff and also upstream and downstream of RTSs. Instantaneous CO_2 efflux (1.96 ± 1.69 μmol m^{-2} s^{-1}, mean ± SD) was not significantly different upstream and downstream of RTSs, while CH_4 efflux varied considerably among sites (9.89 ± 16.3 nmol m^{-2} s^{-1}) (Fig. 3-2). Runoff CH_4 efflux (mean = 1.4 nmol m^{-2} s^{-1}) was, on average, roughly half that of streams outside of RTSs, and was in the lower range of values reported for streams elsewhere (Fig. 3-2, Table 3-4).

3.3.2. Geochemical Controls on pCO_2 and pCH_4

Common geochemical controls of pCO_2 and pCH_4 were significantly affected by RTS activity. Compared to upstream, RTS runoff and downstream had significantly higher concentrations of DIC, SO_4^{2-} and DIN, and showed lower values of $SUVA_{254}$ and D.O. (Table 3-2, Table 3-3; see also Kokelj et al., 2013; Littlefair et al., 2017; Zolkos et al., 2018). DOC concentrations were also significantly lower downstream than upstream (Table 3-3). Stable isotopes reveal that runoff DOC ($\delta^{13}C_{DOC}$ –25.8‰ ± 0.7, mean ± SD) was more similar to Peel Plateau permafrost DOC (–26.0‰ ± 0.4; $n = 3$) than upstream or downstream waters (Table 3-2, Table 3-3). $\delta^{13}C_{DIC}$ values were highest (most ^{13}C-enriched) in runoff streams and were significantly higher downstream than upstream.

The pCO_2 linear mixed effects model revealed that higher levels of pCO_2 were associated with greater concentrations of DOC and DIC, and lower D.O. and water temperature. The most parsimonious pCO_2 model included a fixed effect for sampling location (FE_{Loc}) but no random effects:

$$\ln(pCO_2) = 0.32\ln(\text{DOC}) - 0.17(\text{D.O.}) + 0.10\ln(\text{DIC}) - 0.07(T) + FE_{Loc} + 6.83 \quad (3\text{-}11)$$

Modeled estimates of pCO_2 derived from equation (3-11) corresponded well with measurements from the field ($p < 0.001$, df = 39, $R^2 = 0.89$; Fig. 3-3a).

The pCH_4 linear mixed effects model indicated that pCH_4 was positively associated with DIC, pCO_2, and DIN, and negatively with $\delta^{13}C_{DIC}$ (Table 3-5). The most parsimonious pCH_4 model included random effects that suggest the strength of RTS effects on pCH_4 varied by feature ($RE_{Loc\sim RTS}$):

$$\ln(pCH_4) = 0.85\ln(\text{DIC}) - 0.20(\delta^{13}C_{DIC}) + 0.11\ln(pCO_2) + 0.02\ln(\text{DIN}) + RE_{Loc\sim RTS} \quad (3\text{-}12)$$

Modeled estimates of pCH_4 derived from equation (3-12) also corresponded well with measurements from the field ($p < 0.001$, df = 44, $R^2 = 0.76$; Fig. 3-3b).

RTS effects on C gas were also revealed in the PCA analysis of C gas drivers, in which the first principal component (PC1 = 49%) was broadly reflective of an RTS effect. PC1 separated

permafrost thaw-derived inorganic solutes (SO_4^{2-}, DIN) and carbon quality ($SUVA_{254}$) along axis one from variables related to organic processes (DOC, CH_4) in the second axis (PC2 = 16%) (Fig. 3-4). The pCO_2 and pCH_4 linear mixed effects regression models (equations 3-11, 3-12) and the PCA indicated that pCH_4 was less consistently associated with RTS effects (i.e. the first PCA axis) than was pCO_2.

3.3.3. C Gas Persistence in RTS-Affected Streams

In RTS SE, a deeper feature exposing substantial mineral-rich Pleistocene permafrost (Fig. 3-5a), pCO_2 was supersaturated in RTS runoff (~5,240 ± 610 µatm, mean ± SD) and immediately downstream (910 ± 320 µatm), and increased along the 200 m transect, sustaining excess CO_2 throughout this reach (Fig. 3-5b). Mass balance (equation 3-8) reveals this CO_2 production added ~330 mM of C-CO_2 to the water column along the transect length (mean for n = 5 summertime transects), precluding a reliable estimate of CO_2 efflux to the atmosphere. Given mean downstream velocity was 0.51 m s^{-1} and the transect was 200 m in length, CO_2 increased by ~0.84 mM s^{-1}, not accounting for loss to the atmosphere. In contrast, pCH_4 was generally at equilibrium with the atmosphere and slightly greater in RTS SE runoff (mean excess C gas ~4) than at upstream and downstream sites (Fig. 3-5c). CH_4 varied along the downstream transect and was characterized, on average (n = 5 transects), by minor production of ~0.5 mM of C-CH_4 (Fig. 3-5b).

In the shallow RTS (SD; Fig. 3-5d), pCO_2 in runoff (~6,110 ± 3,620 µatm, mean ± SD) and upstream (1,090 ± 360 µatm) were similar to SE, but rapidly diminished within 200 m to near equilibrium with the atmosphere (excess C gas ~1) (Fig. 3-5e). In contrast to RTS SE, pCH_4 in runoff (mean excess C gas >200) was substantially greater than upstream (570 ± 590 µatm) and was also elevated immediately downstream (150 ± 120 µatm), but was in equilibrium with the atmosphere within 200 m downstream (Fig. 3-5f). Mass balance shows the C gas efflux along the 200 m transect at SD was ~370 mM C-CO_2 and ~90 mM C-CH_4 (mean, n = 5 transects).

3.3.4. The Effect of RTSs on CO_2 Flux at the Watershed Scale

Daily CO_2 efflux to the atmosphere from RTS runoff streams in the Stony Creek and Vittrekwa River watersheds was estimated at 1–2 kmol C-CO_2 d^{-1}, equivalent to 0.25% of the CO_2 efflux from first- to third-order streams (490 kmol C-CO_2 d^{-1}), despite a fluvial surface area

that was equivalent to 0.07% of the area of first- to third-order streams (Table A2-2). Daily CH_4 efflux from RTS runoff ($1x10^{-4}$–$3x10^{-4}$ kmol C-CH_4 d^{-1}) was equivalent to < 0.01% of the CH_4 efflux from first- to third-order streams (2.9 kmol C-CH_4 d^{-1}).

3.4. Discussion

3.4.1. C Gas in Streams Across a Glaciated Permafrost Landscape

These observations of stream C gas efflux, which are among the first in any thermokarst region (Crawford et al., 2013; Striegl et al., 2012), quantify that fluvial C gas efflux can be a substantial component of the carbon cycle in a till-dominated, ice-rich glaciated landscape. On the Peel Plateau, pCO_2 and CO_2 efflux were substantially greater within RTSs than in adjacent streams and at the upper range of values reported for Arctic, boreal, and temperate streams (Table 3-4). In streams outside of RTSs, pCO_2 and CO_2 fluxes were similar to values reported for streams in other northern regions. In comparison, CH_4 efflux was variable and generally smaller in runoff than in streams outside of RTSs, and was similar to streams in other northern regions. Measurements of C gas together with stream geochemistry reveal different primary controls on CO_2 and CH_4 in streams on the Peel Plateau.

3.4.2. Degrading Permafrost as a CO_2 Source

Our mixed effects models and PCA results show that RTS effects on pCO_2 were consistent during the summertime and across features, such that pCO_2 was typically greatest within RTSs and often lower downstream than upstream (Table 3-5). This aligns with a growing number of observations that the exposure of permafrost material can stimulate significant CO_2 production (Drake et al., 2018; Vonk, Tank, Mann, et al., 2015; Zolkos et al., 2018). Some of the primary geochemical controls on pCO_2 (equation 3-11) were characteristic of RTS runoff (greater DIC, lower oxygen; Table 3-5), where carbonate weathering generates substantial DIC and H_2SO_4 from sulfide oxidation promotes geogenic CO_2 production (Zolkos et al., 2018). pCO_2 was also generally associated with greater DOC concentrations and cooler stream water (equation 3-11), perhaps reflecting contributions from biogenic CO_2 production (e.g. Littlefair & Tank, 2018) and greater solubility of $CO_{2(g)}$ at lower water temperatures (Stumm & Morgan, 1996). However, DOC concentration was not a strong predictor of pCO_2 ($t_{51} = 2.8$, $p < 0.01$, $R^2 = 0.12$), as indicated by the relatively weak association between pCO_2 and DOC in the PCA. Rather than

DOC, higher pCO_2 was more strongly associated with lower $SUVA_{254}$ values ($t_{47} = -7.3$, $p < 0.001$, $R^2 = 0.52$) – and pCO_2 was negatively associated with $SUVA_{254}$ in the PCA (Fig. 3-4) – suggesting that carbon composition (i.e. less aromatic DOC) was a stronger control than DOC concentration on pCO_2 (e.g. Drake et al., 2015; Littlefair & Tank, 2018; Wickland et al., 2012). Yet, there was no discernible relationship between pCO_2 and $SUVA_{254}$ in runoff streams within deeper RTS (>10 m; Table 3-1) ($t_8 = -1.1$, $p = 0.31$), where abiotic processes (e.g. mineral weathering) are also known to generate some CO_2 (Zolkos et al., 2018). Across broader permafrost landscapes, this indicates that thermokarst will enhance fluvial CO_2 production, and that regional variability in the composition of permafrost may be a strong control on the source of this CO_2 (Drake et al., 2018; Zolkos et al., 2018).

The release of solutes and intensification of mineral weathering by RTSs are reflected at broader scales by increasing riverine solute loads (Malone et al., 2013; Zolkos et al., 2018), yet the effects of RTS on pCO_2 and fluvial inorganic carbon cycling at intermediate scales remains unexplored. For instance, the interaction between relatively mineral-rich sediments and organic matter may subdue biogenic CO_2 production farther downstream, if DOC adsorption to RTS sediments (e.g. Littlefair et al., 2017) protects carbon from being mineralized by microbes (Gentsch et al., 2015). While regional variability in the composition of permafrost may influence thermokarst effects on fluvial inorganic carbon cycling, this work reveals a common thread between relatively mineral-rich and organic-rich permafrost regions: a large component of permafrost C can be rapidly converted to CO_2 and degassed following thaw (Drake et al., 2018; Zolkos et al., 2018). This points to the need for coupled terrestrial and aquatic C gas flux measurements at and near thermokarst features, to better constrain carbon cycling across thermokarst landscapes (Cassidy et al., 2016).

3.4.3. The Influence of Landscape Conditions on CH_4 in Thermokarst-Affected Streams

In contrast to pCO_2, the pCH_4 linear mixed effects model and the PCA indicate that variability in pCH_4 was more strongly controlled by landscape conditions other than the occurrence of RTSs ($RE_{Loc\sim RTS}$, equation 3-12; Fig. 3-4). pCH_4 in streams was broadly associated with conditions reflective of biological activity, including more negative $\delta^{13}C_{DIC}$, elevated pCO_2, and greater nutrient (DIN) availability (fixed effects, equation 3-12), and DOC (Fig. 3-4). While greater concentrations of terminal electron acceptors (e.g. DIN; Abbott et al.,

2015) and cooler water temperatures (Campeau & del Giorgio, 2014) may reduce methanogenesis in some northern streams, we found limited evidence that these variables influenced pCH_4 in streams on the Peel Plateau, contradictory to our hypothesis. Although DOC was not significant in the pCH_4 model (equation 3-12), it was significantly correlated with pCH_4 ($t_{46} = 3.3$, $p < 0.01$, $R^2 = 0.17$) and strongly associated with pCH_4 in the PCA (Fig. 3-4). Given that the importance of nutrients and water temperature for regulating CH_4 varies among study locations (Stanley et al., 2016), these results indicate that CH_4 production in streams was more strongly coupled with organic carbon availability across the Peel Plateau landscape than with the exposure of permafrost material by RTSs. This aligns with the general understanding that CH_4 in streams is often associated with conditions that promote the accumulation of organic matter and enhance hydrologic connectivity between streams and C gas-rich soil porewaters in the surrounding landscape (Campeau et al., 2018; Crawford et al., 2013; Crawford, Stanley, et al., 2017; Jones & Mulholland, 1998; Wallin et al., 2014).

Although RTSs on the Peel Plateau were more strongly associated with fluvial CO_2 than CH_4, thermokarst could alter aquatic CH_4 flux by modifying stream conditions (e.g. hydrology, sediments, organic material). For instance, although we found no consistent relationship between stream slope and pCH_4 in streams outside of RTSs ($t_{34} = -1.5$, $p = 0.16$, $R^2 = 0.03$), some streams partly impounded by RTS debris tongues had substantial pCH_4 (e.g. upstream of RTS FM4). This corresponds with observations that sedimentation in low-energy stream reaches can enhance streambed anoxia and CH_4 production (Stanley et al., 2016), and that impoundments promote anaerobic decomposition of organic substrate and methanogenesis (e.g. St. Louis et al., 2000). To our knowledge, this is the first reported observation of thermokarst enhancing dissolved CH_4 concentrations via stream impoundment. While impoundments may enhance CH_4 ebullition, the fairly rapid flow and moderately steep stream slopes which we observed in un-impounded reaches upstream and downstream of RTSs (Table A2-3) are not typically conducive to CH_4 bubble formation. Such interactions between thermokarst, stream hydrology, and C gas will likely become increasingly common, yet are seldom considered within the framework of Arctic carbon cycling.

3.4.4. C Gas Persistence in Thermokarst-Affected Streams

Lower pCO_2 downstream than upstream of most RTSs suggests that runoff stream inputs of DIN, less aromatic DOC, and warmer water (Table 3-3) – which are considered amenable to aquatic CO_2 production (Campeau & del Giorgio, 2014; Crawford et al., 2013; Wickland et al., 2012) – likely did not stimulate substantial CO_2 generation downstream of most RTSs. This could be partly due to the rapid loss of some labile organic matter via mineralization within RTSs (Littlefair & Tank, 2018), or perhaps the protection of permafrost carbon from microbes via adsorption to RTS sediments (Gentsch et al., 2015; Littlefair et al., 2017). Both discharge and pH were significantly greater downstream of RTS compared to upstream (Table 3-3), suggesting that stream turbulence and degassing (MacIntyre et al., 1995), and/or downstream pH buffering by inputs of HCO_3^- from carbonate weathering within RTSs (Zolkos et al., 2018) enhanced CO_2 loss to efflux and/or dissociation. To elucidate these potential controls on downstream pCO_2, we used a linear model to assess the change in pCO_2 as a function of the changes in HCO_3^- and Q (as downstream : upstream ratios). While the model had fairly low predictive power ($p = 0.03$, $R^2 = 0.16$), it showed that Q was relatively more significant to the downstream decrease in pCO_2 ($t_{29} = -2.1$, $p = 0.05$) than was HCO_3^- ($t_{29} = 0.9$, $p = 0.38$). This suggests that, immediately downstream of thermokarst, CO_2 loss was more strongly driven by turbulence and degassing than by mineral weathering effects on pH and DIC speciation (equation 3-1).

The stream reaches affected by RTSs HD and SE were notable exceptions to the trend of lower downstream pCO_2. At RTS HD, low downstream pH (mean = 6.07) may have enabled high levels of pCO_2 from runoff to persist (Table 3-2). In contrast, pH downstream of SE was closer to neutral (mean = 6.77) and excess CO_2 values > 2 indicates that CO_2 production sustained elevated pCO_2 for at least 200 meters downstream (Fig. 3-5b). The source of this CO_2 remains somewhat ambiguous. The relatively stable SO_4^{2-} concentrations along the transect downstream of SE (mean change = –10 µM, $n = 3$; Fig. A3-1) suggests that H_2SO_4 carbonate weathering and geogenic CO_2 production are relatively greater in RTS runoff (Zolkos et al., 2018). Less aromatic DOC downstream of RTS SE (mean $SUVA_{254}$ = 2.14 versus 3.68 L mgC^{-1} m^{-1} at other RTS) possibly enhanced microbial CO_2 production (Littlefair & Tank, 2018). Yet, we did not consistently observe increasing $SUVA_{254}$ coupled with decreasing DOC along the transect, as might be expected if microbial oxidation of less aromatic DOC were driving CO_2 production (Drake et al., 2015). Inputs from groundwater, if present, could further complicate

these trends by contributing CO_2 (Kling et al., 1992). Clearly, elucidating pCO_2 dynamics downstream of RTSs on the Peel Plateau is an important step to advance understanding of thermokarst effects on C cycling at the land-freshwater interface.

Similarly, C gas trends downstream of RTS SD revealed that CH_4 inputs from thermokarst were rapidly fluxed to the atmosphere and not replenished. While these contributions were transient, they resulted in moderate overall CH_4 efflux along a short stream reach (~1,090 mgC-CH_4 over 200 m). Although elevated pCH_4 and CH_4 efflux were not always coupled in RTS runoff, the high levels of pCH_4 in RTS SD runoff suggest greater contributions to fluvial CH_4 efflux compared to most of the other RTSs. Broadly, the high CH_4 production in RTS SD, which exposed a relatively greater proportion of organic-rich active layer and Holocene permafrost sediments, indicates that the composition of thawed substrate may influence fluvial CH_4 on the Peel Plateau and elsewhere (e.g. Abbott & Jones, 2015). In comparison, pCH_4 within SE runoff was slightly elevated (CH_{4water} : CH_{4sat} = 4) and the effects were negligible downstream, where CH_4 varied around atmospheric levels (~1.8 ppm). These findings reveal that stream pCH_4 on the Peel Plateau is less associated with RTSs than pCO_2 and, similar to other fluvial networks, can be challenging to predict (Crawford, Loken, et al., 2017).

3.4.5. Fluvial C Gas Flux in Thermokarst Landscapes

In the context of the broader Peel Plateau landscape, our results demonstrate that RTSs currently make a modest contribution to CO_2 efflux in headwater streams. However, this contribution will likely increase as thermokarst activity accelerates in this region (Segal et al., 2016a). While streams outside of RTSs dominate CH_4 efflux at the watershed scale, RTSs may enhance fluvial pCH_4 where thawing permafrost exposes a greater proportion of organic substrate and sedimentation of fine materials promotes anoxic streambed conditions (Vonk, Tank, Bowden, et al., 2015). Exploring these effects may yield new insights on the role of thermokarst in C gas production and an evolving Arctic aquatic carbon cycle.

Efforts to refine these watershed-scale flux estimates should include larger stream orders and new RTSs; characterize the effects of impounded streams (St. Pierre et al., 2018) and sedimentation (Kokelj, Tunnicliffe, et al., 2017) on C gas; explore pCO_2-pCH_4 dynamics across the soil-stream interface (Campeau et al., 2018); and also work to understand the effects of thermokarst on fluvial C gas efflux in regions where permafrost contains a greater proportion of

organic carbon (e.g. Hugelius et al., 2014; Olefeldt et al., 2016). Integrating terrestrial processes that can affect C gas in soils (e.g. vegetation-nutrient dynamics, active layer deepening, mineral weathering) (Berner, 1999; Schuur & Mack, 2018; Striegl et al., 2005) into studies of fluvial C gas dynamics will also help to advance understanding of the northern C cycle. While thermokarst effects on C gas flux are likely to be strongly coupled with regional variability in the composition of permafrost and intensity of thaw, we contend that thermokarst will amplify fluvial C gas efflux and accelerate C cycling across diverse Arctic ecosystems.

Table 3-1. Study site locations, retrogressive thaw slump (RTS) headwall heights, and number of site visits.

RTS	Lat (DD)	Lon (DD)	Headwall height† (~m, max)	*n* site visits
FM2	67.257	-135.236	25	6
SE	67.148	-135.718	23	5
FM4	67.277	-135.159	17	6
HD	67.400	-135.334	11.7	2
FM3	67.253	-135.273	10.3	6
HA	67.150	-135.688	7.3	2
HB	67.240	-135.823	7.1	2
SD	67.179	-135.726	2	5

†Headwall heights from the literature (FM2; Kokelj et al., 2013); field measurements in 2015 (FM4, SD); estimated from photo with known scale (SE); estimated from the ArcticDEM Explorer (www.pgc.umn.edu/data/arcticdem/) (FM3 and HD [imagery date = May 6, 2015], HA [June 18, 2016], HB [July 27, 2016]).

Table 3-2. Measurements of gas and stream chemistry variables (means reported).

RTS	Loc	pCO_2 (µatm)	pCH_4 (µatm)	kCO_2 (m d^{-1})	kCH_4 (m d^{-1})	Cond (µS cm^{-1})	SO_4^{2-} (µM)	DIC (µM)	DOC (µM)	$\delta^{13}C_{DIC}$ (‰VPDB)	$\delta^{13}C_{DOC}$ (‰VPDB)	$SUVA_{254}$ (L mgC^{-1} m^{-1})	DIN (µg L^{-1})	Temp (˚C)	pH	D.O. (mg L^{-1})	Q (m^3 s^{-1})
FM2	UP	1317	7.4	5.49	0.31	312	1118	2088	952	–8.48	–26.74	3.61	33.5	6.8	6.64	13.0	0.009
	IN	3013	7.6	–	–	2120	21626	2160	418	–0.91	–26.26	1.00	70.9	15.2	7.10	7.5	–
	DN	912	33.1	6.38	1.06	994	5611	2116	775	–6.89	–26.68	2.65	30.5	12.0	7.69	11.3	0.099
SE	UP	600	1.0	8.95	1.09	338	2314	66	252	–16.57	–27.91	2.75	7.8	9.0	6.17	11.9	0.075
	IN	5238	6.2	–	–	897	7881	2952	1182	–6.30	–24.80	1.25	115.9	10.9	6.67	5.5	–
	DN	909	2.1	7.69	1.12	391	2635	407	285	–10.66	–27.20	2.14	49.8	10.3	6.77	10.7	0.100
FM4	UP	1446	143.8	5.32	0.64	133	339	1051	1582	–14.42	–27.16	4.14	5.0	9.3	7.16	11.7	0.030
	IN	5030	22.0	–	–	1681	11819	1519	2175	–7.25	–25.50	1.29	370.9	12.3	6.38	5.5	–
	DN	652	39.4	9.02	0.74	343	1598	1919	1338	–11.22	–27.29	3.93	15.1	9.8	7.25	12.3	0.032
FM3	UP	816	27.4	4.78	0.71	101	376	411	1130	–11.22	–27.29	4.21	7.6	9.5	6.78	11.6	0.041
	IN	1979	6.5	–	–	1514	11999	717	975	–5.16	–25.81	1.19	173.7	13.5	6.90	8.8	–
	DN	756	16.7	7.77	0.86	363	2380	571	963	–9.26	–27.35	3.07	38.2	10.3	6.93	11.9	0.070
HA	UP	684	6.6	5.81	1.04	22	38	395	788	–16.91	–27.80	3.99	1.6	4.8	5.83	17.7	0.059
	IN	3122	11.6	–	–	1067	6122	666	929	–2.74	–25.12	1.05	121.1	13.1	6.42	9.1	–
	DN	476	5.4	7.37	1.04	93	337	361	595	–9.14	–27.92	3.84	11.7	6.3	6.98	18.2	0.064
HB	UP	643	6.4	5.36	0.95	66	196	218	555	–8.10	–28.02	4.06	1.2	5.3	7.03	17.4	0.045
	IN	2770	20.8	–	–	514	461	695	322	–7.53	–26.60	3.34	12.9	12.5	7.11	12.5	–
	DN	591	9.8	5.92	1.03	187	833	484	441	–7.98	–28.04	3.99	6.1	9.1	7.15	14.6	0.068
HD	UP	1465	10.2	8.13	1.66	113	228	366	1115	–10.27	–27.71	4.33	1.0	7.3	6.00	17.1	0.566
	IN	2638	9.1	–	–	1347	2327	1197	1316	–23.37	–26.57	NA	146.7	8.6	5.45	14.9	–
	DN	2329	8.0	8.13	1.37	304	248	551	988	–9.79	–28.68	4.77	2.8	7.7	6.07	16.8	0.368
SD	UP	1364	0.5	4.60	0.74	36	124	181	751	–13.87	–27.43	3.46	2.6	6.6	5.99	12.8	0.030
	IN	6109	567.8	–	–	348	2279	390	1229	–16.15	–25.96	1.91	60.3	8.6	5.21	9.6	–
	DN	1086	145.2	5.20	0.75	101	350	278	653	–11.81	–27.09	3.53	6.4	8.2	6.02	12.3	0.030

nd = no data. D.O. = dissolved oxygen. UP = upstream of retrogressive thaw slump (RTS), IN = within RTS runoff stream, DN = downstream of RTS.

Table 3-3. Results from linear mixed effects regression models comparing C gas and stream chemistry upstream, downstream, and in retrogressive thaw slump (RTS) runoff.

Downstream				*Runoff*			
Variable	**df**	**t**	***p***	**Variable**	**df**	**t**	***p***
$1/pCO_2$	36.5	1.95	0.06	$1/pCO_2$	43.3	-8.19	0.00
ln pCH_4	58.8	2.24	0.03	ln pCH_4	56.3	1.54	0.13
ln CO_2 flux	41.8	0.80	0.43	CO_2 flux	–	–	–
CH_4 flux	–	–	–	CH_4 flux	–	–	–
ln Cond	35.5	9.18	0.00	ln Cond	48.8	16.74	0.00
ln SO_4^{2-}	17.6	7.54	0.00	ln SO_4^{2-}	26.1	10.03	0.00
$1/\delta^{13}C_{DIC}$	16.8	-5.70	0.00	$\delta^{13}C_{DIC}$	–	–	–
$\delta^{13}C_{DOC}$	20.8	0.61	0.55	ln $\delta^{13}C_{DOC}$	18.8	7.17	0.00
ln DIC	30.6	3.74	0.00	ln DIC	58.6	5.53	0.00
DOC	17.0	-5.40	0.00	ln DOC	26.6	0.60	0.56
$SUVA_{254}$	17.6	-3.43	0.00	$SUVA_{254}$	19.4	-8.80	0.00
ln DIN	25.0	5.69	0.00	ln DIN	25.2	7.27	0.00
√Temp	36.8	4.12	0.00	Temp	55.7	5.82	0.00
ln D.O.	16.9	-2.24	0.04	D.O.	22.1	-7.46	0.00
pH	34.9	3.14	0.00	pH	34.3	-1.02	0.32
ln *Q*	31.6	3.01	0.01	*Q*	–	–	–

"Downstream" = comparison upstream and downstream of RTSs; "Runoff" = between RTS runoff and the upstream reach. Data transformed as indicated to meet assumptions of linear mixed effects regression. df = degrees of freedom, D.O. = dissolved oxygen, *Q* = discharge. CO_2 and CH_4 flux and discharge omitted for runoff streams because of low *n*. Runoff $\delta^{13}C_{DIC}$ and downstream CH_4 flux omitted because transformation of values to meet regression assumptions was unattainable. Note: where an inverse transformation was applied (i.e. "1/"), negative t indicates that the variable's values were lower upstream (opposite for positive t-values).

Table 3-4. Carbon gas concentrations and fluxes from this study and other selected sites. Means (range) reported for this study.

Location	Biome	Environment	pCO_2 (µatm)	CO_2 flux (µmol m^{-2} s^{-1})	pCH_4 (µatm)	CH_4 flux (nmol m^{-2} s^{-1})	Study
NWT, Canada	Arctic	Streams	1,085 (529–3,186)	1.92 (0.5–5.8)	33.1 (0.04–318.9)	7.30 (-16–87.5)	This study (pristine streams)
NWT, Canada	Arctic	Streams	903 (418–3,837)	2.01 (0.1–12.8)	38.8 (0.04–340)	12.33 (-1.2–68.4)	This study (RTS-affected streams)
NWT, Canada	Arctic	Small streams in RTSs	3,897 (658–16,593)	8.2 (0.5–28.5)	83.1 (0.04–1,357)	1.41 (-0.4–4.6)	This study (RTS runoff)
Alaska, USA	Arctic	Streams	1,417	5.21	4	7.3	Crawford et al. (2013)
N.E. Siberia, Russia	Arctic	Streams	3,336	8.29	–	–	Denfeld et al. (2013)
N.E. Siberia, Russia	Arctic	Rivers	412	0.01	–	–	Denfeld et al. (2013)
N.E. Siberia, Russia	Arctic	Major river (Kolyma)	613	0.48	–	–	Denfeld et al. (2013)
Québec, Canada	Boreal	Streams and rivers	2,959	0.86	1,781	94.2	Campeau et al. (2014)
Ontario, Canada	Boreal	Streams connected to peatlands	~3,200–9,300	3.99	–	10.8	Billett & Moore (2008)
Québec, Canada	Boreal	Streams	1,858	3.00	–	–	Teodoru et al. (2009)
Sweden	Boreal	Streams	1,349	4.89	–	–	Humborg et al. (2010)
Sweden	Boreal	Streams	~700–24,000	3.84–16.93	–	–	Wallin et al. (2013)
Sweden	Boreal	Streams	~800–13,000	_	~75–26,000	_	Wallin et al. (2014)
Northern Sweden	Boreal	Streams	–	7.41	–	–	Jonsson et al. (2007)
Tibetan Plateau	Alpine/ temperate	Rivers (Yellow, Yangtze, Yarlun Tsangpo, and Indus)	864	2.0–6.1	6.30	2.3–46.4	Qu et al. (2017)
New Hampshire, USA	Temperate	Streams	537–878	0.24–0.92	5.7–24.4	0–0.04	Schade et al. (2016)
Mississippi, USA	Temperate	Rivers (Missouri, Ohio, and Upper and Lower Mississippi)	1,335	3.12	–	–	Dubois et al. (2010)
USA (Contiguous)	Temperate	Streams	3,120	6.26	–	–	Butman & Raymond (2011)

China	Subtropical	Rivers (Xijiang and its tributaries, Guijiang and Hejiang)	600–11,000	2.2–4.1	–	–	Yao et al. (2007)
Amazon basin	Tropical	Rivers	4,350	–	–	–	Richey et al. (2002)
NWT, Canada	Arctic	Polygonal peatland melt ponds	–	3.5	–	0.1	Martin et al. (2017)
Québec, Canada	Boreal	Thaw ponds	–	0.04–0.23	–	1.4–5.4	Matveev et al. (2018)
Alaska, USA	Arctic/Boreal	Small streams in RTSs	~2,000–5,000	–	~100	–	Abbott & Jones (2015)
Alaska, USA	Arctic/Boreal	Thermokarst gully	~4,000–6,000	–	~100–1,000	–	Abbott & Jones (2015)
Alaska, USA	Arctic/Boreal	Active layer detachment	~1,500	–	~100	–	Abbott & Jones (2015)
Alaska, USA	Arctic/Boreal	Terrestrial flux	–	0.13–0.22	–	–	Natali et al. (2015)
Ellesmere Island, Canada	Arctic	Terrestrial flux (disturbed tundra)	–	0.55	–	–	Cassidy et al. (2016)
Ellesmere Island, Canada	Arctic	Terrestrial flux (undisturbed tundra)	–	1.04	–	–	Cassidy et al. (2016)

Data from the literature were converted into instantaneous C gas flux, as needed.

Table 3-5. Results of the linear mixed effects models exploring geochemical controls on pCO_2 and pCH_4 upstream and downstream of retrogressive thaw slumps (RTSs), and in RTS runoff.

	Fixed effects				*Random effects*	
Model	**Variable**	**df**	***t***	***p***	**Variance**	**Std Dev**
pCO_2	DOC	34	3.45	0.00		
	D.O.	34	-7.98	0.00		
	DIC	34	1.90	0.07		
	Temp	34	-3.95	0.00		
	Within	34	4.84	0.00		
	Downstream	34	-0.51	0.61		
pCH_4	DIC	11.4	3.74	0.00		
	$\delta^{13}C_{DIC}$	21.7	-3.97	0.00		
	pCO_2	23.8	0.39	0.70		
	DIN	23.9	0.14	0.89		
	Within				3.96	1.99
	Downstream				5.28	2.30
	Residual				0.52	0.72

See text for description of linear mixed effects regression models and fixed and random effects, and Fig. 3-3 for model results.

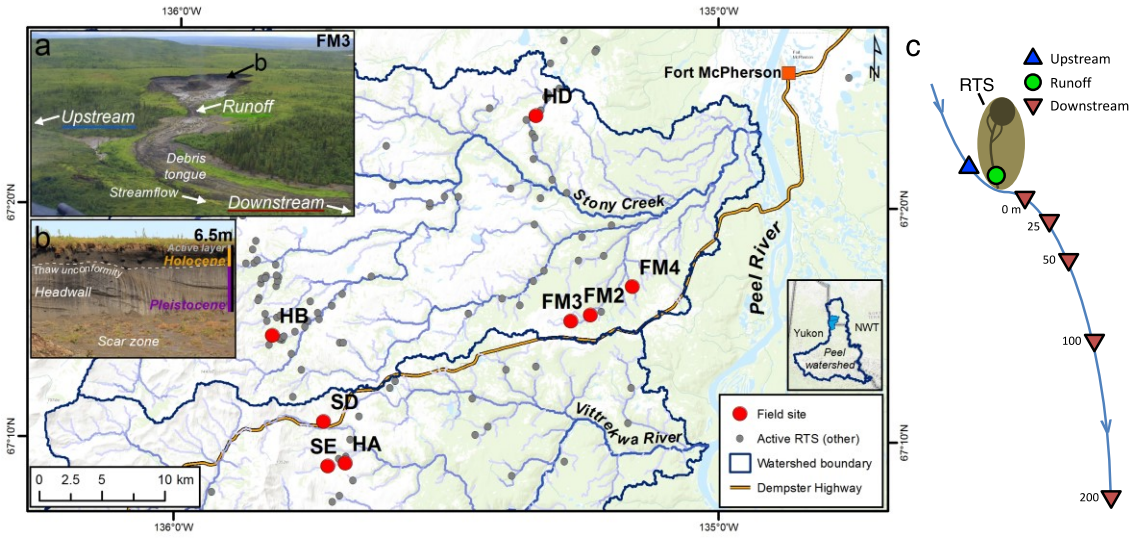

Figure 3-1. Study sites on the Peel Plateau (NWT, Canada). (a) Sampling locations along a typical RTS-affected stream. (b) RTS headwall (see location in inset photo (a)). RTS growth is sustained by headwall ablation and downslope evacuation of collapsed material via fluidized flow, which is enhanced by rainfall (Kokelj et al., 2015), creating a sediment- and solute-rich runoff stream, which flows through the scar zone and debris tongue and into streams. (c) Sampling locations for the transect sampling design. Note location of Stony Creek and Vittrekwa River watersheds (light blue) in inset map above legend.

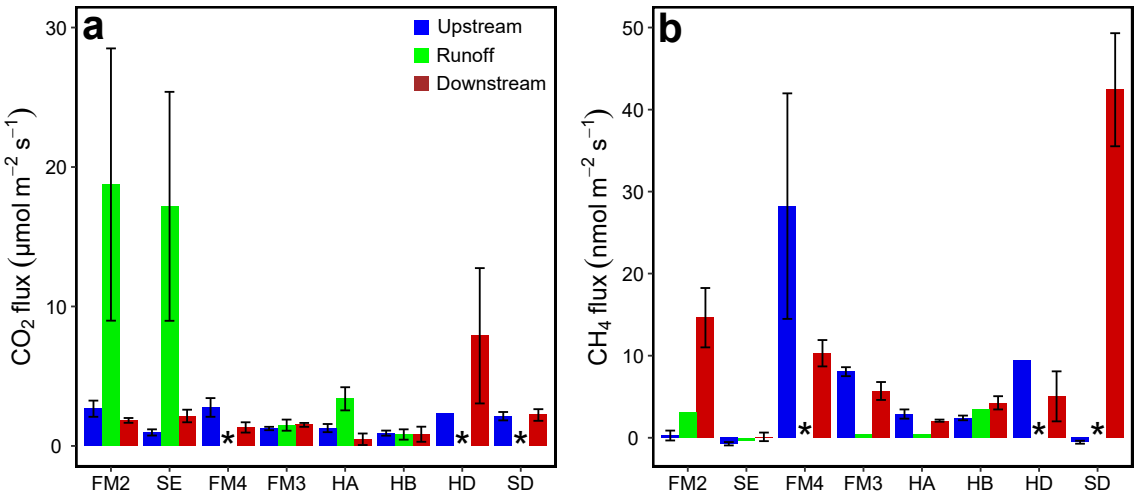

Figure 3-2. Mean CO_2 (a) and CH_4 (b) flux upstream and downstream of retrogressive thaw slumps (RTSs), and in RTS runoff. Runoff fluxes could not be estimated for RTSs FM4, HD, and SD (*; see Sec 2.3). Error bars represent standard error for upstream and downstream, range for CO_2 flux from RTS runoff, and are not included where $n = 1$.

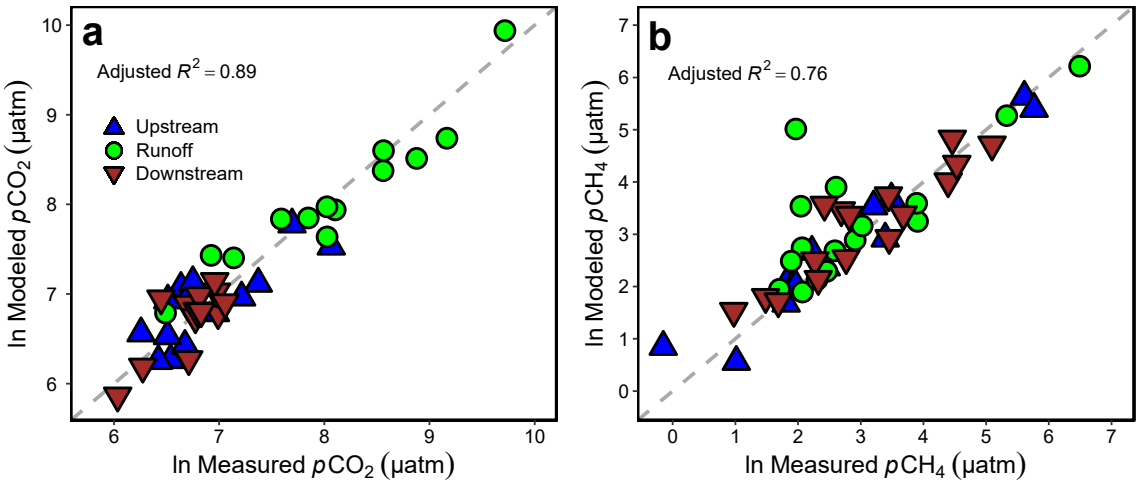

Figure 3-3. Modeled versus measured (a) pCO_2 (n = 36) and (b) pCH_4 (n = 31) in streams on the Peel Plateau. Dashed line = 1:1. For pCH_4, five measurements were excluded where CH_4 < DL.

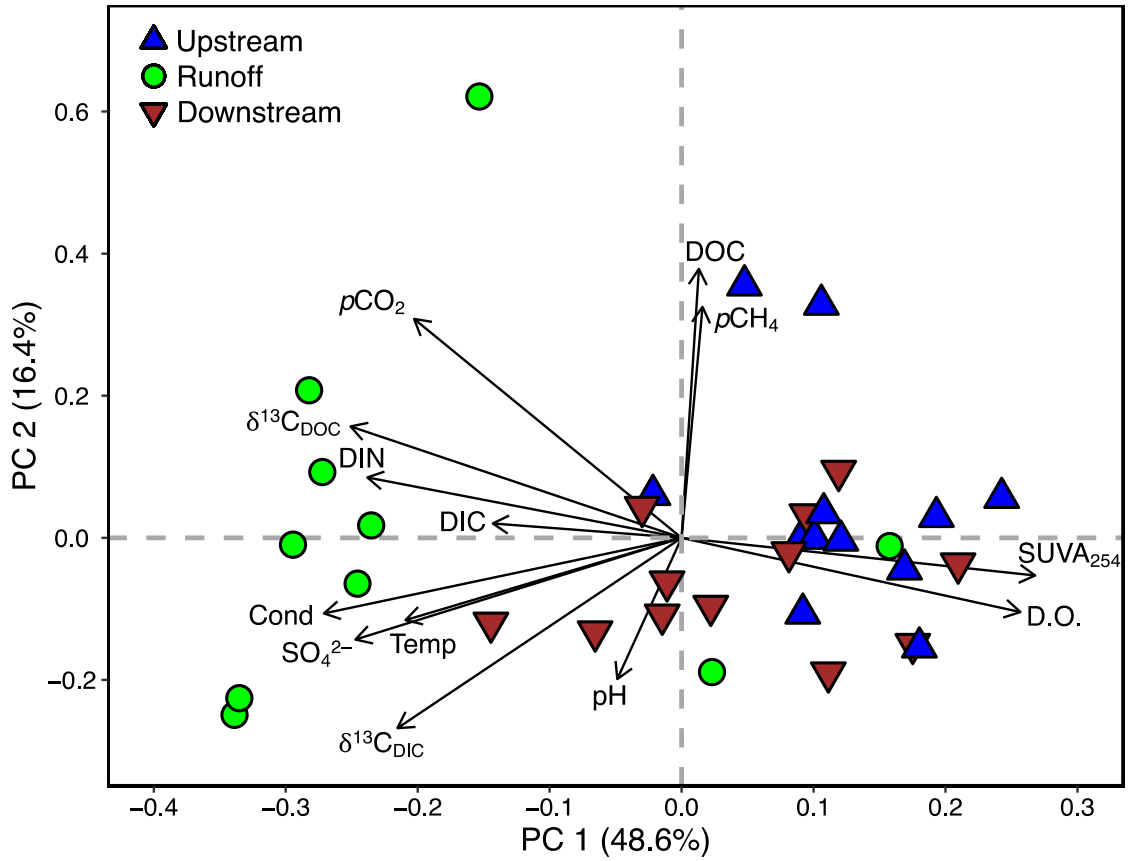

Figure 3-4. Principal component (PC) analysis of stream chemistry variables showing the first two PCs and the percent of the dataset variance explained by PC1 and PC2. Proximal vectors are more strongly associated (e.g. conductivity, SO_4^{2-}) than orthogonal vectors. Alignment with the x or y axis reflects a greater association with PC1 or PC2, respectively.

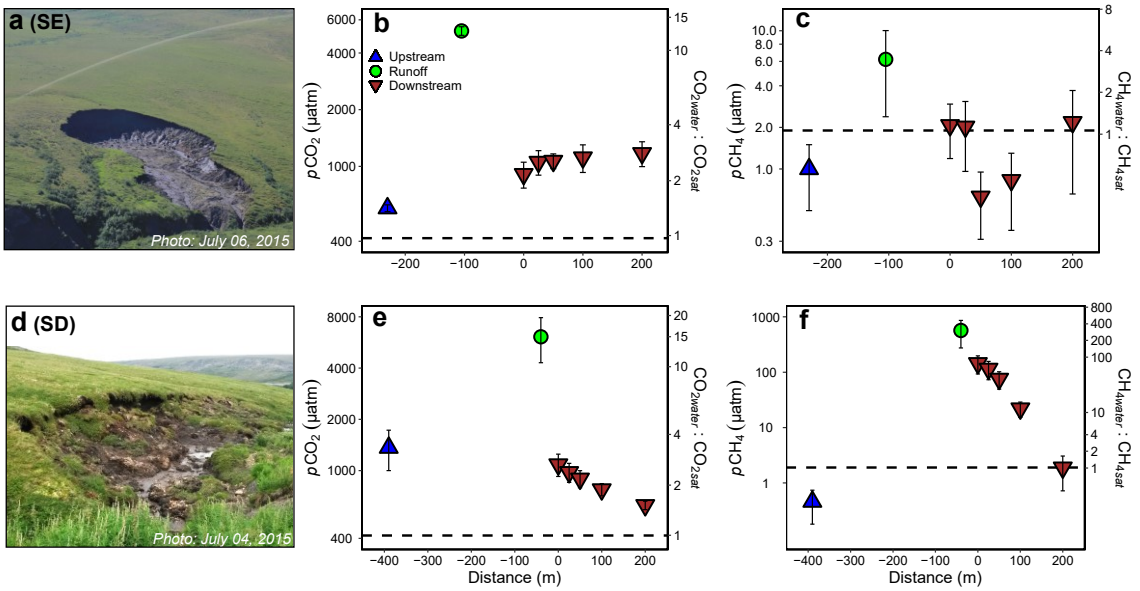

Figure 3-5. pCO_2 (b,e) and pCH_4 (c,f) trends in streams at RTSs SE (a–c) and SD (d–f). Primary y-axis is C gas partial pressure and secondary y-axis is excess C gas (c_{water} : c_{sat}). Dotted line represents mean atmospheric C gas concentration. Distances on x-axis denote sampling locations relative to the start of the downstream reach at 0 m. Error bars represent standard error. The headwalls of SE and SD were ~23 m and 2 m, respectively (Table 1).

CH. 4: Experimental Evidence for the Role of Mineral Weathering within Permafrost Carbon-Climate Feedbacks

Summary

Mounting evidence suggests that biogeochemical processing of thawing permafrost carbon will amplify CO_2 release within Arctic fluvial networks, thereby strengthening the permafrost carbon feedback. These effects may be particularly strong in thermokarst terrains, where rapid permafrost thaw can release large quantities of sediment into streams. Yet, the weathering of thawed minerals may fix CO_2 and render it less susceptible to atmospheric exchange, provided weathering is driven by carbonic rather than sulfuric acid. Here, we determine the effects of mineral weathering on fluvial CO_2 by incubating permafrost sediments with varying degrees of prior exposure to thaw in stream-like conditions in the laboratory. Sediments were collected from three retrogressive thaw slump features on the Peel Plateau (NWT, Canada), where prehistoric warming and contemporary thermokarst exposed the sediments to varying degrees of thaw. We found that sediments that thawed within recent decades and previously un-thawed diamicton from deeper permafrost layers generated significant solutes and dissolved inorganic carbon. Further, the mineral composition of these sediments aligned with the strong geochemical signals of carbonate weathering coupled with sulfide oxidation. This weathering generated geogenic CO_2, yet 30%, on average, was consumed by buffering from carbonate weathering. In contrast, the mineralogy and geochemical trends associated with sediments from the modern and paleo-active layer, which were previously exposed to thaw over longer timescales, more strongly reflected silicate weathering. Minor carbonate and sulfide weathering resulted in minor dissolved inorganic carbon and CO_2 production, yet this CO_2 was not measurably diminished by carbonate buffering. These trends suggest that prior exposure to thaw and weathering on the Peel Plateau reduced carbonate and sulfide in upper soil layers, with critical implications for modern-day fluvial inorganic carbon cycling. We conclude that thermokarst unearthing deeper tills on the Peel Plateau will amplify regional inorganic carbon cycling for decades to centuries. However, previously-undocumented CO_2 consumption via carbonate buffering may partly counterbalance CO_2 release to the atmosphere. Across the circumpolar north, regional variability in thaw history, the mineral composition of permafrost, and the intensity of thermokarst are among the primary controls on mineral weathering within permafrost carbon-climate feedbacks.

4.1. Introduction

Mineral weathering is one of Earth's great thermostats, regulating climate by moderating the concentration of atmospheric CO_2 over geological timescales (Berner, 1998). Carbonate and silicate weathering by carbonic acid (H_2CO_3*, including dissolved CO_2) transforms biogenic CO_2 produced by plant root respiration and microbial oxidation of soil organic matter into bicarbonate (HCO_3^-; equations 4-1 to 4-3) (Berner, 1999), rendering it less susceptible to exchange with the atmosphere:

$$H_2O + CO_{2(g)} \rightleftharpoons H_2CO_3^* \rightleftharpoons H^+ + HCO_3^- \rightleftharpoons 2H^+ + CO_3^{2-} \quad (4\text{-}1)$$

$$H_2CO_3 + (Ca,Mg)CO_3 \rightarrow (Ca^{2+},Mg^{2+}) + 2HCO_3^- \quad (4\text{-}2)$$

$$2H_2CO_3 + 3H_2O + (Ca,Mg)Al_2Si_2O_8 \rightarrow (Ca^{2+},Mg^{2+}) + 2HCO_3^- + 2Al_2Si_2O_5(OH)_4 \quad (4\text{-}3)$$

In contrast, sulfide oxidation (equation 4-4) enables weathering by sulfuric acid (H_2SO_4) that either liberates mineral C without consuming CO_2 (equation 4-5; carbonate weathering) or generates no dissolved C (equation 4-6; silicate weathering) (Lehn et al., 2017):

$$FeS_2 + 15/4O_2 + 7/2H_2O \rightarrow Fe(OH_3) + 2H_2SO_4 \quad (4\text{-}4)$$

$$H_2SO_4 + 2(Ca,Mg)CO_3 \rightarrow 2(Ca^{2+},Mg^{2+}) + SO_4^{2-} + 2HCO_3^- \quad (4\text{-}5)$$

$$H_2SO_4 + H_2O + (Ca,Mg)Al_2Si_2O_8 \rightarrow (Ca^{2+},Mg^{2+}) + SO_4^{2-} + Al_2Si_2O_5(OH)_4 \quad (4\text{-}6)$$

Additionally, in the absence of sufficient carbonate buffering (equation 4-1), H_2SO_4 can lower pH and increase the CO_2 proportion of dissolved inorganic carbon (DIC = $\Sigma[CO_2, HCO_3^-, CO_3^{2-}]$) thereby facilitating CO_2 release to the atmosphere (Ali & Atekwana, 2011). Half of the HCO_3^- which persists from streams and rivers into the marine carbon cycle returns to the atmosphere as CO_2 over geological timescales (Calmels et al., 2007):

$$2Ca^{2+} + 2HCO_3^- + SO_4^{2-} \rightarrow Ca^{2+} + SO_4^{2-} + CaCO_3 + CO_2 + H_2O \quad (4\text{-}7)$$

Thus, the balance between H_2CO_3 and H_2SO_4 weathering controls the degree to which mineral weathering is carbon neutral (equation 4-2) versus a carbon sink (equation 4-3) or source (equation 4-5) (Calmels et al., 2007; Hindshaw et al., 2016; Tank et al., 2012) and acts as a

positive or negative feedback to climate warming (Berner, 1999; Gislason et al., 2009; Pogge von Strandmann et al., 2017; Torres et al., 2017).

At a global scale, the chemistry of major rivers indicates that carbonate and silicate weathering consume substantial CO_2 (~12 x 10^{12} mol CO_2-C y^{-1} each; Gaillardet et al., 1999). Yet, growing recognition of the global prevalence of sulfide oxidation suggests that mineral weathering is less of a CO_2 sink than was previously understood (Burke et al., 2018; Guo et al., 2015; Li et al., 2008; Ross et al., 2018; Soulet et al., 2018). At local and regional scales, the degree to which mineral weathering acts as a climate feedback is driven by variation in lithology and physical erosion (Gaillardet et al., 1999). For instance, riverine DIC can be relatively high in catchments with carbonate lithologies (Blum et al., 1998; Tank et al., 2012) as carbonates weather more readily than silicates (Stumm & Morgan, 1996) and can thus have a greater influence on climate over contemporary timescales (Beaulieu et al., 2012). River chemistry reveals that physical erosion enhances solute production by exposing previously un-weathered material (Calmels et al., 2007) and by increasing the potential reactivity of sediments (Anderson, 2007), for example where glacial activity generates finely-comminuted sediments (St. Pierre et al., 2019). In major Arctic rivers, modern-day ion yields suggest that carbonate weathering in northern catchments currently accounts for ~10% of the global CO_2 consumption by weathering (Gaillardet et al., 1999; Tank et al., 2012). In northern regions, regional variability in glacial activity and changes in the exposure of carbonate- and sulfide-bearing lithologies – and in the balance between H_2CO_3 and H_2SO_4 weathering – thus has significant implications for the role of mineral weathering and fluvial inorganic carbon cycling in climate feedbacks.

Rapid warming at northern latitudes stands to amplify weathering and inorganic carbon cycling by reactivating large stores of mineral and organic carbon sequestered within perennially frozen ground (permafrost) (Hugelius et al., 2014; Schuur et al., 2015; Walvoord & Striegl, 2007) into modern biogeochemical cycles (Vonk et al., 2015). This can occur via thickening of the seasonally-thawed active layer, resulting in deeper flowpaths and the exposure of a greater proportion of mineral substrate to weathering in the thawed state (Keller et al., 2010; Lehn et al., 2017; Walvoord & Striegl, 2007). In comparison, landscape subsidence following thaw (thermokarst) can rapidly reactivate permafrost substrate into biogeochemical cycles (e.g. Vonk et al., 2015) and potentially thaw larger amounts of sediments with more limited prior exposure to weathering. Roughly 900,000 km^2 (5%) of the northern permafrost region may be susceptible

to hillslope thermokarst like retrogressive thaw slumps (RTSs) (Olefeldt et al., 2016), which can expose and erode particularly large volumes of permafrost sediments (~$1x10^3$ m^3 y^{-1}) into fluvial networks (Kokelj et al., 2013). RTSs are known to alter stream geochemistry and aquatic ecosystems across broad scales (Chin et al., 2016; Malone et al., 2013), with critical implications for DIC cycling from headwaters to marine environments (Tank et al., 2016). While thermokarst may amplify DIC cycling and influence climate feedbacks, there is limited research detailing the effects of prior thaw on permafrost mineral composition and modern-day weathering regimes in thermokarst-affected fluvial networks.

Here, we refine understanding of mineral weathering contributions to the permafrost carbon-climate feedback on the Peel Plateau (NWT, Canada), where accelerating thermokarst activity is mobilizing millions of cubic meters of mineral-rich glacial tills with varying degrees of prior thaw into fluvial networks (Kokelj et al., 2013; Segal et al., 2016a; van der Sluijs et al., 2018). We build on previous research that investigated the effects of RTSs on solutes, sediments, and organic carbon in fluvial networks (Kokelj et al., 2013; Littlefair et al., 2017; Malone et al., 2013) by characterizing the mineral composition of RTS sediments that commonly enter streams on the Peel Plateau and experimentally weathering these sediments to determine how thermokarst and thaw history affect DIC concentration and speciation. Our results indicate that fluvial inorganic carbon cycling on the Peel Plateau is amplified by more intense thermokarst, which thaws deeper sediments containing a greater proportion of carbonate and sulfide. We conclude that thermokarst on the Peel Plateau and in similar Arctic environments may intensify inorganic carbon cycling in fluvial networks for centuries.

4.2. Materials and Methods

4.2.1. Study area and retrogressive thaw slump sites

The Peel Plateau is characterized by permafrost tills up to 50 m in thickness underlain by sandstone and siltstone bedrock (Kokelj, Tunnicliffe, et al., 2017; Norris, 1985). These tills are mainly comprised of carbonates, sulfides, and silicates (Zolkos et al., 2018) likely derived from regional carbonate and shale bedrock (Norris, 1985; Stott, 1991) that was integrated into the Laurentide Ice Sheet (LIS) during its westward expansion. The last glacial maximum in the Peel Plateau region at around 18500 cal yr BP (Lacelle et al., 2013) was followed by retreat of the LIS and early Holocene warming at 12000–8500 cal yr BP (Kokelj, Tunnicliffe, et al., 2017). This

warming promoted thaw of the ground surface, mineral weathering, and the accumulation of solutes and organic matter in the upper few meters of soil (Burn, 1997; Lacelle, 2004; Malone et al., 2013). A cooling climate 7000–5500 cal yr BP supported permafrost aggradation and the preservation of this solute- and organic-rich layer above the deeper, ice-rich Pleistocene sediments that have been isolated from thaw and exposure (Kokelj, Tunnicliffe, et al., 2017; Lacelle et al., 2013). This shallow Holocene and the deeper Pleistocene permafrost layers are geochemically distinct and distinguished stratigraphically by an undulating thaw unconformity typically encountered 1.5 to 3 m below the surface (Malone et al., 2013) (Fig. 4-1a).

The modern-day Peel Plateau is comprised of ice-rich hummocky moraine, glaciofluvial, glaciolacustrine, and colluvial deposits (Duk-Rodkin & Hughes, 1992a). Incised valleys and sloping terrain host hundreds of RTSs (Fig. 4-1; Kokelj et al., 2013; Lacelle et al., 2015). The upslope growth of RTS features is sustained by the ablation of a vertical permafrost headwall of exposed ground ice and the downslope evacuation of a thawed slurry of slumped materials via fluidized flows which are enhanced by rainfall (Kokelj et al., 2015) (Fig. 4-1a). Meltwater from the thawing headwall and its interaction with thawing substrate produce sediment- and solute-rich runoff often conveyed through rill channels in the scar zone (henceforth "runoff"), and into streams. The thawed materials that flow from thawing slopes via precipitation-induced mass-wasting events are deposited as debris tongues that can grow over time to reach >1 km in length and tens of meters in thickness (van der Sluijs et al., 2018). These features are reshaped by the addition of debris from thawing slopes and by the erosion of the adjacent streams (Kokelj et al., 2015) (Fig. 4-1b). Sediments unearthed by RTSs can be broadly categorized into five sources of material with varying degrees of prior exposure to thaw and weathering: (i) the seasonally-thawed *active layer*; (ii) the relatively organic- and solute-rich paleo-active layer contained in *Holocene-aged permafrost*; (iii) the un-thawed *Pleistocene-aged permafrost* sediments; and the composite of these three components, that are either recently mobilized and undergoing active transport in *runoff* (iv) or deposited via mass-wasting events in recent years to decades within the *debris tongue* (v) (Fig. 4-1). Active layer and Holocene permafrost sediments in RTSs on the Peel Plateau were exposed to thaw for decades to centuries, whereas debris tongue sediments were exposed for weeks to decades, runoff sediments for hours to days, and Pleistocene permafrost sediments have remained sequestered within permafrost for millennia.

The three focal RTSs in this study are situated within the ~1,100 km^2 Stony Creek watershed, west of Fort McPherson, NWT (Fig. 4-1, Table 4-1). The RTS FM2 is among the largest (Table 4-1) active RTS features on the Peel Plateau (Lacelle et al., 2015) and has persisted for at least 70 years (Kokelj et al., 2015; van der Sluijs et al., 2018). The RTS HC is moderately-sized and estimates from the field suggest it is likely at least several decades old. The RTS HD scar zone was <1 ha in 2017 and likely formed within recent years to decades.

4.2.2. Field sampling

During summer 2017, we collected active layer and permafrost sediments from the vertical headwall exposure, in addition to runoff and debris tongue sediments at RTS features FM2, HC, and HD (Fig. 4-1, Table 4-1). These three RTS features were selected to capture potential variability in sediment geochemistry associated with varying compositions of glacigenic materials (Duk-Rodkin & Hughes, 1992a). To characterize RTS morphology, we measured headwall height at the time of sampling using a Uineye HK1200 laser range finder (±30 cm/0.35˚ accuracy). Holocene and Pleistocene permafrost samples were collected in each RTS feature using a mallet and stainless-steel chisel. Permafrost layers were differentiated in the field based on cryostratigraphy (Lacelle et al., 2013) and later in the lab using stable isotopes of water ($\delta^{18}O$), to ensure isotopic values reflected previously published values for Holocene ($\delta^{18}O$ = –17 to 25‰) and Pleistocene ($\delta^{18}O$ = –26 to –32‰) ground-ice (Fritz et al., 2012; Lacelle et al., 2013; Michel, 2011). Active layer and debris tongue samples were collected using a stainless-steel trowel. Active layer material was composited from two roughly equal plugs of material from the A and B horizons (below the organic layer and above permafrost table). Debris tongue samples comprised of thawed, colluviated materials were collected near the adjacent stream, distant from the active headwall, reflecting sediments that have been thawed for years to decades. For active layer, permafrost, and debris tongue samples, the outer 5-10 cm of material was removed and discarded prior to sampling. Samples were stored in 5L Whirlpak bags. Runoff was collected in pre-cleaned, triple-sample-rinsed 2L HDPE bottles and stored chilled (4˚C). Sediments were allowed to settle and/or thaw in the laboratory, and sediments from all five sources were dried at 20˚C.

4.2.3. Sediment mineralogy and geochemistry

Prior to mineral analysis by X-ray diffraction (XRD), dried sediments were gently disaggregated with a mallet, sieved to < 250 μm, and visible organic matter was removed. Samples were not pretreated prior to analysis and XRD spectra were visually inspected to confirm minimal potential interference from organic matter (Mandile & Hutton, 1995). Sieved sediments were then finely ground with a ceramic mortar and pestle, and mineralogy was analyzed at the University of Alberta by XRD (Rigaku Ultimate IV), using Cobalt radiation at 0.6 s/step and 0.02˚ steps (detection limit = 3%). The geochemical composition of sediments was analyzed by inductively coupled plasma mass spectrometer (Perkin Elmer Elan 6000 Quadrupole ICP-MS) at the University of Alberta Canadian Centre for Isotope Microanalysis, following Cooper et al. (2008). Subsamples (0.2 ± 0.02 g) of the sieved sediments were dissolved via sequential digestions using $HF+HNO_3^-$ and then $HCl+HNO_3^-$. Sediments were mixed with five mL of each acid (trace metal-grade), heated to 130˚C, and digested overnight until dry. Finally, 10 mL 8N HNO_3^- was added, heated to 130˚C, and a 1 mL aliquot was mixed with 0.1 mL HNO_3^-, 0.1 mL of internal standards (In, Bi, and Sc), and 8.8 mL of MilliQ deionized water.

4.2.4. Mineral weathering experiment

To determine how varying degrees of prior thaw and biogeochemical alteration of glacigenic materials can influence DIC cycling on the Peel Plateau, we incubated active layer, Holocene, Pleistocene, runoff, and debris tongue sediments under controlled conditions (Fig. A4-1). Following collection and processing (see above), sediments were sterilized in precombusted aluminum trays at 200˚C for 24h in a forced-draft oven (Wolf & Skipper, 1994) to inhibit CO_2 production from microbial oxidation of organic matter. This likely inhibited microbial sulfide oxidation in our experiment (Singer & Stumm, 1970), thus constraining sulfide oxidation to the abiotic dissolved O_2 pathway (Calmels et al., 2007). However, this step was considered necessary to isolate the abiotic controls on DIC speciation. Sterilization was tested by mixing sterile MilliQ water (0.2 μm-filtered, ultraviolet light-treated) with the sterilized sediment, and extracting and incubating the supernatant on nutrient-rich agar plates (37˚C, 7d; Zuberer, 1994). Sterilization was confirmed by no observable growth compared to identical sediments that had not been sterilized.

Sediments were incubated at total suspended solid concentrations (1800 mg L^{-1}) and water temperatures (10˚C) representative of stream reaches immediately downstream of RTS features

during the 2015 sampling season (Zolkos et al., 2018). We inoculated 200 mL of MilliQ water with 3.6 g of sterilized sediment in acid-washed, precombusted (5h, 500˚C) 250 mL glass bottles and sealed them with two silicone-teflon septa (Skidmore et al., 2004). For each sediment source, twelve identical bottles were prepared and duplicate bottles were terminated at 0.17h, 1h, 6h, 24h, 72h, and 168h. Two control bottles containing only MilliQ water were also terminated at 168h. We enabled weathering to proceed under closed system conditions by replacing headspace in bottles with N_2 gas, enabling dissolved atmospheric CO_2 and O_2 to contribute to carbonate weathering and sulfide oxidation. For RTS HD runoff, we had only enough sediment to run duplicate bottles that were terminated at 168h and we had no replicates for the other time points. To induce sediment suspension, all bottles were incubated on a rotary shaker set to 250 rpm during the course of the experiment, following Skidmore et al. (2004).

At each time point, bottles were removed and water was filtered (0.45-µm, polyethersulfone, ThermoScientific) for DIC, pH, and conductivity measurements. Water was also equilibrated with nitrogen gas to extract dissolved gas for measurements of CO_2 concentration and stable carbon isotope analysis of CO_2 ($\delta^{13}C_{CO2}$) (see below). Filtrate for DIC was stored without headspace in precombusted 12 mL exetainers, sealed with butyl septa, and refrigerated until analysis within two weeks (Apollo SciTech DIC analyzer). DIC standard curves were built from certified reference material (Scripps Institution of Oceanography) and, when required for low-DIC samples, from 100 or 600 µM solutions prepared from a 1000 ppm Na_2CO_3-$NaHCO_3$ DIC standard (ACCUSPEC). pH and conductivity were analyzed within two hours of filtering. pH was analyzed with a Mettler Toledo FiveEasy benchtop meter calibrated daily using a two-point calibration curve (7.01 and 10.01 pH, NIST). The mean pH of replicate samples was calculated by first converting pH to H^+. Conductivity was analyzed with a Thermo Orion 115 A+ meter calibrated daily using 1413 µS cm^{-1} solution. Dissolved CO_2 was extracted by equilibrating 20 mL of sample with 40 mL of nitrogen gas in an air-tight polypropylene syringe (Hesslein et al., 1991) and measured immediately by infrared gas analyzer (IRGA; PP Systems EGM-4). IRGA drift was checked daily with 60 mL of 1010 ppm CO_2 standard (Scotty Gases). We calculated the partial pressure of CO_2 (pCO_2) using Henry's constants corrected for water temperature (Weiss, 1974), accounting for the ratio of sample volume to headspace during equilibration.

At the final time point of each experiment, water was also filtered (0.45-µm, cellulose acetate, Sartorius) to determine the concentrations of cations and anions. Cations were preserved

with trace metal-grade HNO_3 and all ions were refrigerated until analysis at the University of Alberta Biogeochemical Analytical Services Laboratory (BASL, ISO/EIC 17025) following standard procedures. Equilibrated headspace gas samples for $\delta^{13}C_{CO2}$ were stored over-pressurized in bottles that were sealed with baked (12h, 60˚C) butyl stoppers and pre-evacuated. $\delta^{13}C_{CO2}$ was analyzed within two months by a Picarro isotope analyzer (G2201-*I*; < 0.2‰ precision) equipped with an injection module for discrete samples (SSIM). The Picarro analyzer was checked for drift against commercial and in-house $\delta^{13}C_{CO2}$ standards during each run.

4.2.5. Data analysis

We used the proportions of solute equivalent concentrations in a Piper diagram (Piper, 1944) to characterize potential mineral weathering reactions (see also Lehn et al., 2017). Calculations were made using the concentrations of cations and anions in the experiment bottles at 168h, first correcting for the solute concentrations measured in the MilliQ control bottles. The concentrations of dissolved CO_2 measured at each time point were also corrected for dissolved CO_2 in the control bottles. For the Piper diagram, we calculated HCO_3^- as $\Sigma[HCO_3^-, CO_2]$, to correct for HCO_3^- hydrolysis to CO_2. To test for multivariate similarity (i.e. geochemical likeness) between treatments, we first performed a hierarchical cluster analysis using the R software package *pvclust* (Suzuki & Shimodaira, 2015), which employs the R base function *hclust* to generate a bootstrapped (n = 1,000 iterations), Euclidean distance-based estimate of a stable configuration of measurement clusters. Variables were selected for the *pvclust* to yield insight about DIC concentration and speciation (DIC, pH) and CO_2 source ($\delta^{13}C_{CO2}$); to help differentiate between silicate and carbonate weathering (Al^{2+}); and to evaluate contributions from sulfide oxidation and gypsum dissolution (SO_4^{2-}). We then evaluated the associations between these geochemical variables and the sample clusters defined by *pvclust* using the *metaMDS* function in the R software package *vegan* (Oksanen et al., 2018). *metaMDS* augments traditional nonmetric multidimensional scaling (NMDS) by running multiple MDS iterations to find a stable solution, whereby proximity of measurements indicates similarity and vectors reveal how variables correlate with measurements. All statistics were performed in R software v.3.4.4 (R Core Team, 2018), with significance interpreted at $\alpha = 0.05$.

4.3. Results

4.3.1. Sediment mineral and geochemical composition

Permafrost sediments, RTS runoff, and debris tongue deposits contained carbonates (calcite, dolomite, and rarely siderite), pyrite, gypsum, quartz, and various Na-, Mg-, and K-aluminosilicates (Table 4-2; note the XRD detection limit of 3%). Albite, clinochlore, muscovite, and quartz were detected in all sediment sources. The XRD detected carbonates, pyrite, and gypsum in at least half of the sediment sources and in at least one source at each RTS. Carbonates and sulfides were generally present in Pleistocene permafrost sediments (>3%) and absent from active layer sediments (below detection), whereas the presence of carbonates and sulfides in Holocene, runoff, and debris tongue sediments varied (Table 4-2). The presence of sulfide and/or carbonate varied among sediment sources, and there were no sediments where carbonate was detected by XRD and sulfide was not.

The geochemical composition of sediments was characterized by – in decreasing order of concentration – Al^{2+}, Fe^{2+}, K^{+}, Mg^{2+}, Ca^{2+}, Na^{+}, and Sr^{2+} (Table 4-3). Because carbonates have high concentrations of Ca^{2+} and low concentrations of Na^{+} and Sr^{2+}, and the opposite is generally true for silicates (Keller et al., 2007), we used molar ratios to discern the relative proportion of carbonates (high Ca/Na and Ca/Sr) versus silicates in sediments. Ca/Sr and Ca/Na were typically higher in sediments where carbonates were detected by XRD (Table 4-2, Fig. 4-2). Some sediments with sulfides but not carbonates also had relatively high Ca/Na and Ca/Sr (e.g. FM2 Holocene and Pleistocene, HD debris tongue), perhaps reflecting the presence of carbonates below the XRD detection limit.

4.3.2. Weathering experiment: trends in conductivity, DIC, CO_2, and pH

For all RTSs and sediment sources, conductivity increased most strongly during the first 10 minutes of the incubation, and increased marginally thereafter, indicating that the majority of weathering occurred by 168h (Fig. 4-3a-c). At 168h, conductivity in treatments with Pleistocene permafrost, runoff, and debris tongue sediments (mean = 264 $\mu S\ cm^{-1}$) was significantly higher than in treatments with active layer and Holocene permafrost sediments (mean = 138 $\mu S\ cm^{-1}$, excluding HC Holocene [552 $\mu S\ cm^{-1}$]) (t-test: $t_{18} = 3.26$, $p < 0.001$). Solutes at 168h broadly reflected sulfide oxidation and/or sulfate salt (e.g. gypsum) dissolution (SSD) and relatively greater contributions from silicate and carbonate weathering by H_2SO_4 than H_2CO_3 (Fig. 4-4).

For all treatments, DIC concentrations increased rapidly during the first 6h and more gradually after 24–48h. Treatments containing sediments with carbonates and sulfides detected by XRD generated more DIC (mean = 725 µM after 168h) than those in which only sulfides were detected (mean = 265 µM), or neither carbonates nor sulfides were detected (mean = 153 µM) (Fig. 4-3d-f, Table 4-4). Treatments with active layer and Holocene sediments generally had the lowest DIC at 168h (mean = 104 and 335 µM, respectively), whereas DIC in treatments with Pleistocene, runoff, and debris tongue sediments had higher values (579, 541, and 652 µM, respectively) (Table 4-4).

For all treatments, CO_2 increased rapidly within 6h (Fig. 4-3g-i) and, in treatments containing sediments with both carbonates and sulfides detected by XRD, decreased from 3–14 µM thereafter. The decrease in CO_2 was equivalent to 8–54% (mean = 28%) of the maximum CO_2 reached during the experiment for these treatments. At 168h, CO_2 in these treatments was lower (mean = 28 µM) than in other treatments. In contrast, CO_2 in treatments containing sediments with sulfides detected by XRD generally reached the highest concentrations of CO_2 by 168h (mean = 79 µM, excluding FM2 Holocene). Most of the treatments with active layer and Holocene sediments, which did not have carbonates or sulfides detected by XRD, had relatively moderate CO_2 (mean = 38 µM).

pH increased in all treatments except for those with FM2 active layer sediments, which decreased from 7.04 to 6.69 pH units after 24h. By 168h, pH was highest where carbonates and sulfides were detected by XRD (mean = 7.23 pH units), lower when sulfides but not carbonates were detected (mean = 5.89), and the most acidic in treatments with lower proportions of carbonates and sulfides (mean = 4.66) (Fig. 4-3j-l).

4.3.3. Statistical clusters of treatments based on geochemistry

The cluster analysis revealed that treatments grouped into three geochemical clusters which broadly reflected gradients of prior thaw and exposure to weathering, and also the intensity of sulfide oxidation relative to carbonate weathering (Fig. A4-2). Clusters one and two mostly included samples with more limited prior thaw compared to cluster three, which contained most of the active layer and Holocene permafrost sediments (Fig. 4-5). Cluster one was characteristic of a relatively balanced coupling between sulfide oxidation and carbonate weathering, whereas cluster two was more strongly reflective of carbonate weathering in the presence of excess

H_2SO_4. These statistical clusters help to describe the influence of prior exposure to thaw and the balance between carbonate weathering and sulfide oxidation on the evolution of DIC and CO_2 during the experiment.

4.3.3.1. Cluster 1 – High DIC and pH, low Al^{2+}

Treatments containing sediments with both carbonates and sulfides detected by XRD (Table 4-2) had consistently high DIC (mean = 725 µM), elevated pH (mean = 7.22 pH units), and low dissolved Al^{2+} (mean = 0.1 µM) (Fig. 4-3, Table 4-4). In this cluster, mineral weathering resulted in rapid geogenic CO_2 production early in the experiment followed by a decrease after ~24h, yet CO_2 was always higher than in the control bottles. $\delta^{13}C_{CO2}$ at 168h varied between treatments, but was relatively ^{13}C-enriched (–8.3 to –13.2‰, n = 7; Table 4-4). Treatments in this cluster include Pleistocene permafrost sediments or recently thawed/colluviated material (i.e., runoff or debris tongue sediments), but not sediments from the active layer or Holocene permafrost.

4.3.3.2. Cluster 2 – High SO_4^{2-} and CO_2, ^{13}C-enriched CO_2

Bottles with FM2 Pleistocene, HD runoff, and HD debris tongue sediments had the highest CO_2 concentrations (Table 4-4), with no measurable decrease in CO_2 during the 168h incubation. Generally, these treatments had ^{13}C-enriched CO_2 (–4.67 to –7.84‰), high concentrations of SO_4^{2-} (mean = 1,307 µM), and (except for HD runoff) had sulfides detected by XRD, but not carbonates. DIC concentrations were intermediate between clusters one and three (mean = 265 µM).

4.3.3.3. Cluster 3 – Low DIC and SO_4^{2-}, high dissolved Al^{2+}, and ^{13}C-depleted CO_2

Bottles with active layer and Holocene sediments (except HC Holocene) had high concentrations of dissolved Al^{2+} (mean = 20.3 µM), consistently lower conductivity, moderate to low DIC (mean = 129 µM), low SO_4^{2-} (mean = 202 µM), and ^{13}C-depleted CO_2 (–16.3 to –20.3‰, n = 5) at 168h (Fig. 4-3, Table 4-4). There were no Pleistocene permafrost, runoff, or debris tongue sediments in this cluster.

4.4. Discussion

Our findings reveal several interacting controls from thermokarst on fluvial inorganic carbon cycling on the Peel Plateau. Most importantly, we find that thaw history is an important control on the carbonate and sulfide content of permafrost in this region. Generally, previously-thawed sediments (active layer and Holocene permafrost) appear to have more limited carbonates and sulfides than materials comprised of Pleistocene permafrost or recently thawed and colluviated sediments (runoff and debris tongue). Given this apparent depletion of carbonates and sulfides in upper soil layers during prior thaw on the Peel Plateau, the degree to which thermokarst unearths Pleistocene permafrost sediments at depth appears to be a primary control on the degree to which thermokarst intensifies DIC cycling and geogenic CO_2 production. These findings help to contextualize the effect of permafrost thaw on mineral weathering and inorganic carbon cycling on the Peel Plateau (Fig. 4-6) and potentially in ice-rich, glaciated terrains elsewhere in northwestern Canada, Alaska, and Eurasia (Kokelj, Lantz, et al., 2017; Rudy et al., 2017; Segal et al., 2016a).

4.4.1. Implications of thaw history and prior sediment exposure to mineral weathering for inorganic carbon cycling

The lower conductivity observed in most treatments with active layer and Holocene sediments (except HC Holocene; Table 4-2, Fig. 4-5) suggests that prior thaw of the upper layers of permafrost on the Peel Plateau promoted chemical weathering and the reduction of readily-weathered minerals within the upper few meters of soil (e.g. Malone et al., 2013). Except for HC Holocene, active layer and Holocene sediments did not have carbonate detected by XRD and also often had lower Ca/Sr and Ca/Na ratios. The relatively high DIC production associated with HC Holocene sediments may reflect the local presence of colluviated materials from former debris flows that were integrated into permafrost during its upward aggradation. The more modest DIC generation associated with the other active layer and Holocene sediments suggests that carbonates were present, but in relatively minor amounts. This is consistent with observations of modern and paleo-active layer soils in Alaska (USA) and the central Yukon Territory (Canada), where thaw and exposure promoted weathering and a reduction in carbonates relative to silicates in upper soil layers (Burn et al., 1986; Keller et al., 2010). Thus, on the Peel Plateau, we contend that weathering of sediments

from the active layer and previously-thawed permafrost will be more strongly influenced by silicates, whereas Pleistocene permafrost sediments will have greater carbonate weathering.

4.4.2. Thermokarst sediment mineral composition as a driver of DIC speciation in streams

The grouping of treatments into distinct geochemical clusters reveals that the mineralogy of sediments is an overarching control on the abiotic component of inorganic carbon cycling in thermokarst-affected streams on the Peel Plateau. Sediments in cluster one, which contained the most carbonates and sulfides (both >3%) and had more limited prior exposure to thaw, yielded the highest DIC concentrations and showed a trend of decreasing CO_2 after ~24h (Fig. 4-3). The high DIC and elevated pH (mean = 7.2) associated with cluster one sediments (Fig. 4-5) suggests that buffering shifted some CO_2 to HCO_3^-, lowering CO_2 concentrations and also $\delta^{13}C_{CO2}$ values (ca. –11‰) via equilibrium fractionation (Clark & Fritz, 1997). Accounting for these fractionation effects, $\delta^{13}C_{CO2}$ values observed in treatments with sediments from cluster one (–8 to –13‰) align with $\delta^{13}C$ of marine carbonates that were likely incorporated from regional bedrock into tills on the Peel Plateau (–0.7 to –5.6‰; Hitchon & Krouse, 1972). In contrast, the relatively more ^{13}C-depleted $\delta^{13}C_{CO2}$ values in cluster three (–16 to –20‰) may partly reflect isotopic fractionation (–13‰ at 10˚C; Clark & Fritz, 1997) associated with the dissolution of secondary carbonates ($\delta^{13}C$ ca. –12‰; Zamanian et al., 2016). The environmental conditions conducive to secondary carbonate formation are well-documented in northern permafrost soils. For instance, ion exclusion in the freezing front of the active layer and reprecipitation associated with drying or increasing pH (e.g. via CO_2 loss) in soils can drive the supersaturation of solutes and precipitation of minerals, including carbonates (Marion, 1995; Zamanian et al., 2016). Climate and soil conditions during the Holocene warm interval were also likely conducive to the formation of secondary carbonates, some of which were likely to be preserved within permafrost as it aggraded during a cooling climate later in the Holocene (Kokelj, Tunnicliffe, et al., 2017).

The decrease in CO_2 in the cluster one treatments suggests that, when carbonates are sufficiently abundant, carbonate weathering by H_2CO_3 (equation 4-2) and pH buffering (equation 4-1) can fix some CO_2 as HCO_3^- and partially offset geogenic and/or biogenic CO_2 production within RTSs on the Peel Plateau. Although we did not observe it in our treatments,

sediments with abundant carbonate and limited or no sulfides would have even stronger CO_2 consumption. In contrast, the striking CO_2 production in treatments with a greater proportion of sulfide (cluster two) suggests that carbonate weathering was insufficient to noticeably temper dissolved CO_2 concentrations. Rather, more intense sulfide oxidation likely sustained a relatively low pH (mean = 5.9, Table 4-2) and enabled more complete dissolution of carbonates, resulting in $\delta^{13}C_{CO2}$ (–6.5‰) reflective of a geogenic CO_2 source. These findings support recent work that shows greater DIC production within RTSs exposing a greater proportion of Pleistocene permafrost sediments (Zolkos et al., 2018), by revealing that the balance between carbonate weathering and sulfide oxidation may be a primary control on CO_2 levels within RTS-affected streams on the Peel Plateau. At the inter-regional scale, these differences likely reflect local variation in the composition of tills that were deposited at the end of the last glacial maximum and continue to be preserved within permafrost.

4.4.3. Thermokarst intensity as a control on inorganic carbon cycling on the Peel Plateau

These findings build on previous research showing that deeper RTSs on the Peel Plateau expose more solute-rich permafrost and are therefore likely to have a stronger effect on stream chemistry than shallow thermokarst (Kokelj et al., 2013; Malone et al., 2013). Here, we show that deeper RTSs also expose a greater proportion of carbonate- and sulfide-bearing Pleistocene permafrost sediments, and are thus likely to enhance H_2SO_4 carbonate weathering following thaw (equation 4-1), resulting in greater DIC production (e.g. Zolkos et al., 2018). Further, the striking DIC production in treatments with runoff and debris tongue material reveals that Pleistocene permafrost sediments can remain weatherable for at least days to years following thaw. For debris tongue sediments, this is likely in part due to the reburial of thawed sediments within accumulating debris, where minerals are less exposed to the environment and thus relatively more protected from chemical weathering. These thawed sediments can augment fluvial inorganic carbon cycling by entering streams via runoff and via the erosion of debris tongues. Initially, we reasoned that debris tongue sediments would have a limited effect on DIC, because this material is thawed and exposed at the surface environment prior to burial by subsequent debris flows (Kokelj, Tunnicliffe, et al., 2017). Contrary to our hypothesis, RTS debris tongue sediments were associated with consistently strong DIC production, indicating more limited depletion of carbonate and sulfide relative to

the active layer and Holocene permafrost sediments, which were exposed to thaw and weathering over longer timescales (decades to centuries). From an inorganic carbon cycling perspective, this suggests that previously un-thawed sediments that are redistributed following thaw may be an important legacy of thermokarst on the Peel Plateau, particularly if increasing thaw and rainfall facilitate the exposure and the transport of RTS sediments into stream networks (Kokelj et al., 2015; van der Sluijs et al., 2018). These interpretations align with observations of increasing downstream geochemical signals of carbonate weathering and sulfide oxidation (Zolkos et al., 2018) in conjunction with intensifying regional thermokarst in recent decades (Segal et al., 2016a). As future warming and increasing rainfall on the Peel Plateau increase RTS activity, the thawing of minerals in deeper permafrost can thus be expected to accelerate inorganic carbon cycling for decades to centuries.

4.4.4. Implications for the role of mineral weathering within permafrost carbon feedbacks

Across the pan-Arctic, increasing riverine solute fluxes in recent decades signals a thickening of the active layer, deepening flow paths, and enhanced mineral weathering in concert with climate warming and intensifying precipitation (Tank et al., 2016; Toohey et al., 2016; Drake et al., 2018a; Zolkos et al., 2018). While increasing riverine alkalinity fluxes in North America (Peel, Mackenzie; Tank et al., 2016; Zolkos et al., 2018) and Siberia (Ob', Yenisey; Drake et al., 2018a) reflect a broad scale acceleration of inorganic carbon cycling, stronger coupling between carbonate weathering and sulfide oxidation in northwestern Canada diminishes the weathering CO_2 sink compared to other Arctic regions (Beaulieu et al., 2012). From an Arctic carbon cycling perspective, regional variability in lithology is an important control on the mineral weathering component of carbon-climate feedbacks. Recent work suggests that biogenic processes drive DIC cycling in ice- and organic-rich (yedoma) regions affected by thermokarst (Drake, Guillemette, et al., 2018). Working in a relatively more mineral-rich permafrost terrain, we show that intensifying thermokarst stands to amplify geogenic processes, but that the magnitude of sulfide oxidation is a primary control on the degree to which mineral weathering represents a CO_2 sink. Despite increasing recognition that mineral weathering is an important component of the northern carbon cycle (Beaulieu et al., 2012; Calmels et al., 2007; Tank et al., 2012, 2016), the contribution of thermokarst to carbon cycling remains poorly constrained. This work indicates that thermokarst will have strong

effects on inorganic carbon cycling where glaciated terrains coincide with carbonate lithologies (Zolkos et al., 2018) and perhaps most strongly where sediments remain unmodified at the near surface (e.g. (Lewkowicz & Way, 2019; Rudy et al., 2017; Ward Jones et al., 2019).

Although sediment release from thermokarst can be substantial (Kokelj et al., 2013), the degree to which it affects the balance of CO_2 across broad scales remains unanswered. These effects are likely to be particularly strong across glacial deposits, where carbonates and sulfides are often highly reactive (Anderson et al., 2000; Blum et al., 1998; Torres et al., 2017) and even trace amounts can profoundly affect inorganic carbon cycling. In Alaska and Canada, the dissolution of carbonate glacial flour can consume significant CO_2 during fluvial transport (Striegl et al., 2007, St. Pierre et al., 2019). In comparison, the downstream effects on DIC from thermokarst sediment propagation through stream networks is unknown. Resolving this will help to quantify CO_2 balance across broad scales and increase capacity for tracing the effects of permafrost thaw on inorganic carbon cycling (Drake et al., 2018a).

4.5. Conclusions

In this study, we found evidence to suggest that thermokarst activity on the Peel Plateau will amplify inorganic carbon cycling where RTSs facilitate the exposure of deeper carbonate- and sulfide-bearing permafrost sediments. Across the circumpolar north, future increases in inorganic carbon cycling will be strongest where thermokarst unearths carbonate-bearing tills with limited prior thaw and modification (Kokelj, Tunnicliffe, et al., 2017). In these regions, the progression of – and balance between – H_2CO_3 and H_2SO_4 weathering will determine the degree to which DIC in freshwaters represents a CO_2 sink (Calmels et al., 2007; Tank et al., 2012; Tank et al., 2016; Drake et al., 2018a). By investigating the composition and reactivity of mineral substrate in permafrost regions elsewhere, particularly where thermokarst may expose and mobilize vast stores of minerals into fluvial networks (e.g. Olefeldt et al., 2016), future work will advance understanding of the role of mineral weathering within permafrost carbon-climate feedbacks (Schuur et al., 2015; Zolkos et al., 2018).

Table 4-1. Characteristics of RTS features in this study. All headwall height measurements were made during July 2017. Stable water isotope ($\delta^{18}O$) values are reported in ‰ Vienna Standard Mean Ocean Water.

RTS	Lat (DD)	Lon (DD)	$\delta^{18}O$ (‰) Holocene	$\delta^{18}O$ (‰) Pleistocene	Height (m, max)	Debris tongue length (~m)*	Scar zone (~ha)*
FM2	67.257	-135.236	–20.3	–28.3	24.2	1600	27
HC	67.328	-135.900	–21.6	–29.2	18.3	180	2.5
HD	67.400	-135.334	–21.8	–30.3	13.6	150	0.6

*Estimated from satellite imagery and/or field photos; excludes area of debris tongue.

Table 4-2. Minerals detected by X-ray diffraction (x) in non-sterilized sediments. AL = active layer, HO = Holocene, PL = Pleistocene, RU = runoff, DT = debris tongue. Other minerals: *Siderite: $FeCO_3$; †Lepidolite: $KLi_2Al(Si_4O_{10})(F,OH)_2$.

RTS	Source	Cluster	Gypsum $CaSO_4 \cdot 2H_2O$	Pyrite FeS_2	Calcite $CaCO_3$	Dolomite $CaMg(CO_3)_2$	Albite $Na(AlSi_3O_8)$	Orthoclase/ Sanidine $K(AlSi_3O_8)$	Clinochlore $Mg_5Al(AlSiO_{10})(OH)_8$	Muscovite $KAl_2(AlSi_3O_{10})(OH)_2$	Quartz SiO_2	Other
FM2	AL	3							x	x	x	
FM2	HO	3		x					x	x	x	
FM2	PL	2	x	x			x	x	x	x	x	
FM2	RU	1	x	x	x	x	x	x	x	x	x	
FM2	DT	1	x	x	x	x	x	x	x	x	x	
HC	AL	3							x	x	x	
HC	HO	1	x	x		x	x	x	x	x	x	
HC	PL	1		x	x	x	x	x	x	x	x	
HC	RU	1		x		x	x	x	x	x	x	*
HC	DT	1	x	x		x	x	x	x	x	x	
HD	AL	3							x	x	x	
HD	HO	3							x	x	x	
HD	PL	1	x	x	x	x	x		x	x	x	
HD	RU	2							x	x	x	†
HD	DT	2	x	x			x	x	x	x	x	

Table 4-3. Geochemical composition of sediments, measured by ICP-MS. Concentrations are in μmol g^{-1} of dry sediment, except Sr^{2+} (nmol g^{-1}).

Site	Source	Cluster	Al^{2+}	Fe^{2+}	K^{+}	Mg^{2+}	Ca^{2+}	Na^{+}	Sr^{2+}
FM3	AL	3	1665	650	435	319	159	218	1149
FM3	HO*	3	1454	635	376	291	234	194	1215
FM3	PL*	2	2458	684	665	480	153	152	1600
FM3	RU**	1	1584	627	420	395	271	246	1311
FM3	DT**	1	1601	629	467	388	256	208	1341
HC	AL	3	1811	599	454	302	53	206	1080
HC	HO**	1	1722	594	495	396	240	207	1262
HC	PL**	1	1324	526	341	284	188	201	1168
HC	RU**	1	1560	556	430	359	175	237	1318
HC	DT**	1	1586	593	441	371	169	246	1243
HD	AL	3	1625	600	494	302	31	198	1149
HD	HO	3	2010	605	511	336	49	196	1374
HD	PL**	1	1986	646	519	402	202	195	1379
HD	RU	2	2330	752	651	479	113	181	1513
HD	DT*	2	1799	649	506	380	142	208	1362

Table 4-4. Measurements of water chemistry from the mineral weathering experiment at 168h. AL = active layer, HO = Holocene, PL = Pleistocene, RU = runoff, DT = debris tongue. See text for details. **Sulfides and carbonates detected by XRD; *Sulfides detected.

Site	Source	Cluster	pH	Cond (µS cm^{-1})	DIC (µM)	Ca^{2+} (µM)	Mg^{2+} (µM)	Na^{+} (µM)	K^{+} (µM)	SO_4^{2-} (µM)	Cl^{-} (µM)	Al^{2+} (µM)	$\delta^{13}C_{CO2}$ (‰VPDB)
FM2	AL	3	6.69	138.2	215.9	642.2	114.4	13.9	38.6	90.3	3.4	7.9	-16.25
FM2	HO*	3	6.68	202.2	392.1	1009.8	165.0	10.9	37.1	157.5	2.3	8.7	-16.31
FM2	PL*	2	6.65	357.7	244.4	1093.6	496.2	79.6	103.6	1476.0	2.3	0.1	-7.84
FM2	RU**	1	7.25	404.2	760.4	1649.5	308.6	52.2	49.1	1471.1	2.5	0.2	-12.24
FM2	DT**	1	7.39	286.2	851.0	1152.0	190.5	61.3	67.8	783.4	1.4	0.3	-13.21
HC	AL	3	4.89	94.8	53.8	177.2	90.9	23.5	27.1	102.6	2.0	25.6	-20.16
HC	HO**	1	7.13	552.5	552.8	1974.6	594.1	30.4	72.1	2349.8	0.3	0.1	-8.32
HC	PL**	1	7.31	231.0	596.6	738.8	240.7	31.3	34.0	702.0	0.0	0.1	-9.62
HC	RU**	1	7.34	180.1	710.0	510.8	243.2	51.3	43.2	384.3	0.6	0.1	-11.12
HC	DT**	1	7.31	213.5	708.4	607.6	286.8	55.2	48.1	555.4	0.3	0.1	-12.47
HD	AL	3	4.19	126.1	41.4	169.4	82.3	34.4	35.3	313.6	2.5	10.0	-20.25
HD	HO	3	4.49	158.5	61.6	283.7	102.9	75.3	35.0	381.1	2.8	49.5	-19.12
HD	PL**	1	6.98	337.9	896.7	1212.4	337.4	36.1	67.0	1041.6	1.4	0.1	-9.85
HD	RU	2	5.51	320.4	152.8	725.1	421.3	349.7	99.0	1153.0	3.4	16.1	-6.94
HD	DT*	2	6.28	363.9	396.6	1047.7	509.8	126.6	76.0	1291.3	1.7	2.9	-4.67
Cluster means (standard error, range for pH)													
		1	7.2 (0.2)	315 (49)	725 (47)	1121 (207)	314 (50)	45 (5)	54 (5)	1041 (256)	0.9 (0.3)	0.1 (0)	-10.98 (0.7)
		2	5.9 (0.6)	347 (14)	265 (71)	955 (116)	476 (28)	185 (83)	93 (9)	1307 (94)	2.4 (0.5)	6.4 (4.9)	-6.50 (0.9)
		3	4.7 (1.2)	144 (18)	153 (68)	456 (163)	111 (15)	32 (12)	35 (2)	209 (59)	2.6 (0.2)	20.3 (8)	-18.40 (0.9)
Source means (standard deviation, range for pH)													
	AL		4.6 (1.2)	120 (22)	104 (97)	330 (271)	96 (17)	24 (10)	34 (6)	169 (125)	2.6 (0.7)	14.5 (9.6)	-18.89 (2.3)
	HO		5.0 (1.3)	304 (216)	335 (250)	1089 (848)	287 (268)	39 (33)	48 (21)	963 (1206)	1.8 (1.3)	19.4 (26.4)	-14.58 (5.6)
	PL		6.9 (0.3)	309 (68)	579 (326)	1015 (246)	358 (129)	49 (27)	68 (35)	1073 (388)	1.2 (1.1)	0.1 (0)	-9.10 (1.1)
	RU		6.0 (0.9)	302 (113)	541 (337)	962 (605)	324 (90)	151 (172)	64 (31)	1003 (559)	2.2 (1.4)	5.5 (9.2)	-10.10 (2.8)
	DT		6.7 (0.6)	288 (75)	652 (232)	936 (289)	329 (164)	81 (40)	64 (14)	877 (377)	1.1 (0.7)	1.1 (1.6)	-10.12 (4.7)

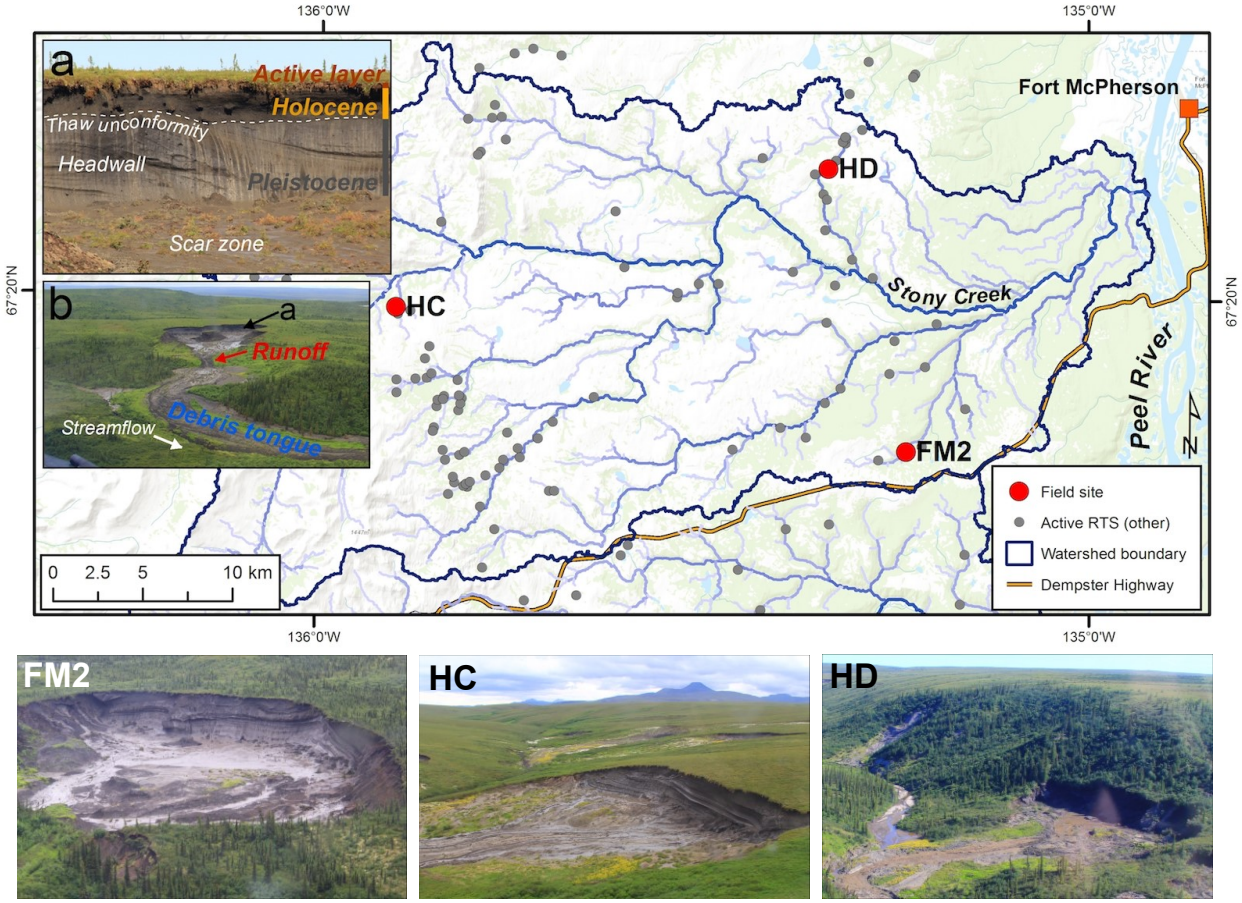

Figure 4-1. Map of retrogressive thaw slump (RTS) study sites (n = 3) on the Peel Plateau (NWT, Canada) from which sediments for the experiment were collected. Sediments were collected from RTS FM2, HC, and HD (see photos below and locations on map). Photos were taken in 2014 (FM2) and 2017 (HC, HD). The photo of FM2 captures its southern lobe only. Note orange-tint of iron from sulfide oxidation in RTS HD scar zone. Insets (a) and (b) depict sampling locations of the five sediment sources (i.e. treatments) detailed in the text. Note location of inset (a) shown in (b). Inset photos depict sediment sources common to all RTS that were sampled for the experiment (RTS in inset photos from this region but not study). Basemap from Esri ArcGIS Online; "Active RTS" points on map from Segal et al. (2016b).

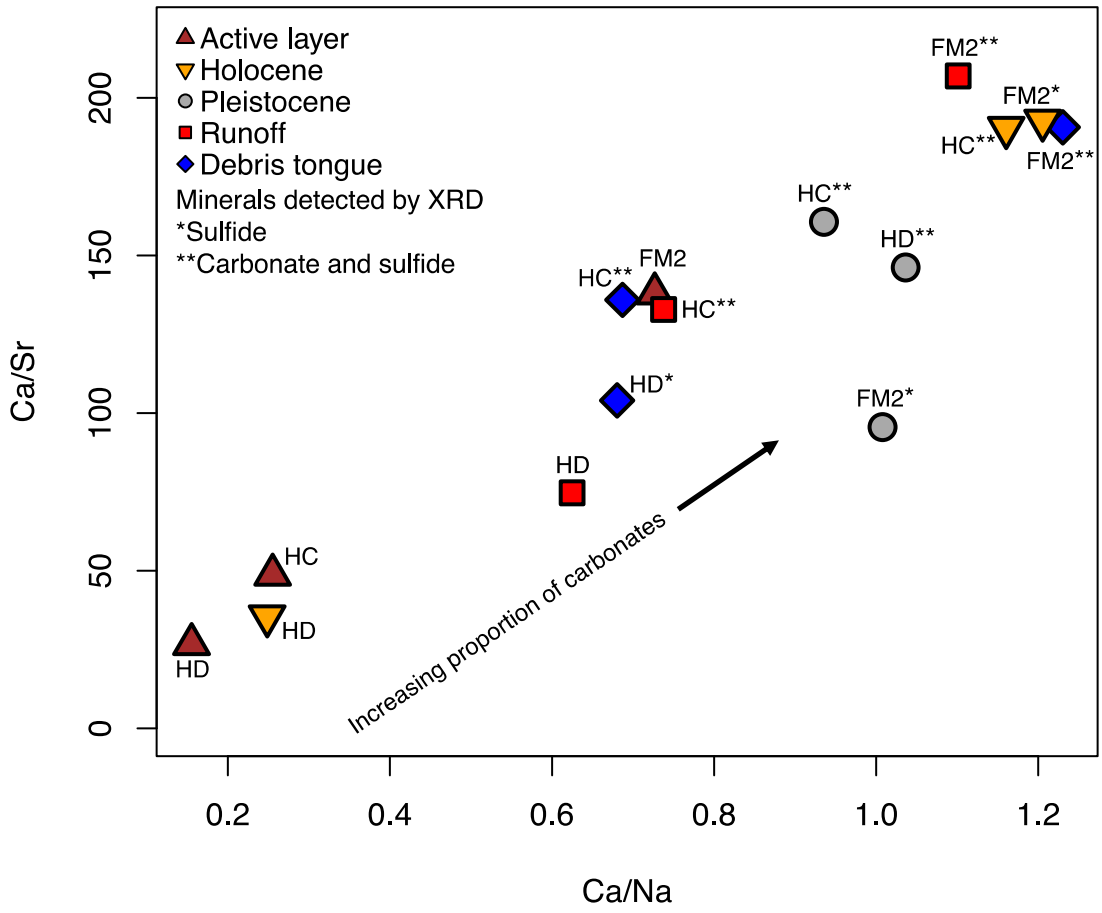

Figure 4-2. The relationship between Ca/Sr and Ca/Na of sediments used in the mineral weathering experiment.

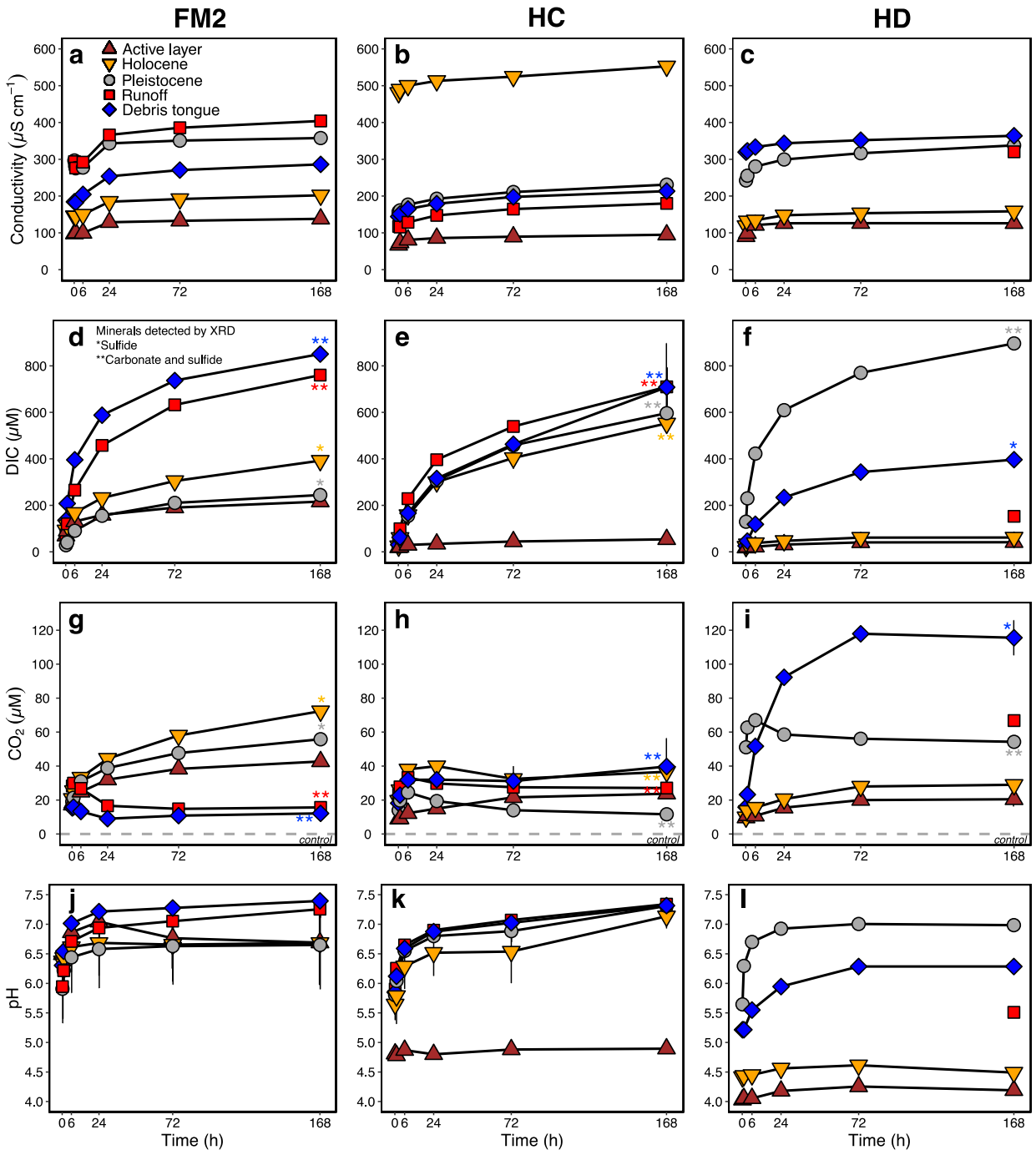

Figure 4-3. Weathering experiment trends in conductivity, dissolved inorganic carbon (DIC), dissolved CO_2, and pH by RTS and sediment source. Error bars represent ± standard deviation for conductivity, DIC, and CO_2, and range for pH (bars not shown where smaller than symbol). See Fig. 4-1 for locations and Table 4-1 for site characteristics. (**g-i**) Dashed lines represents CO_2 equilibrium in control bottles.

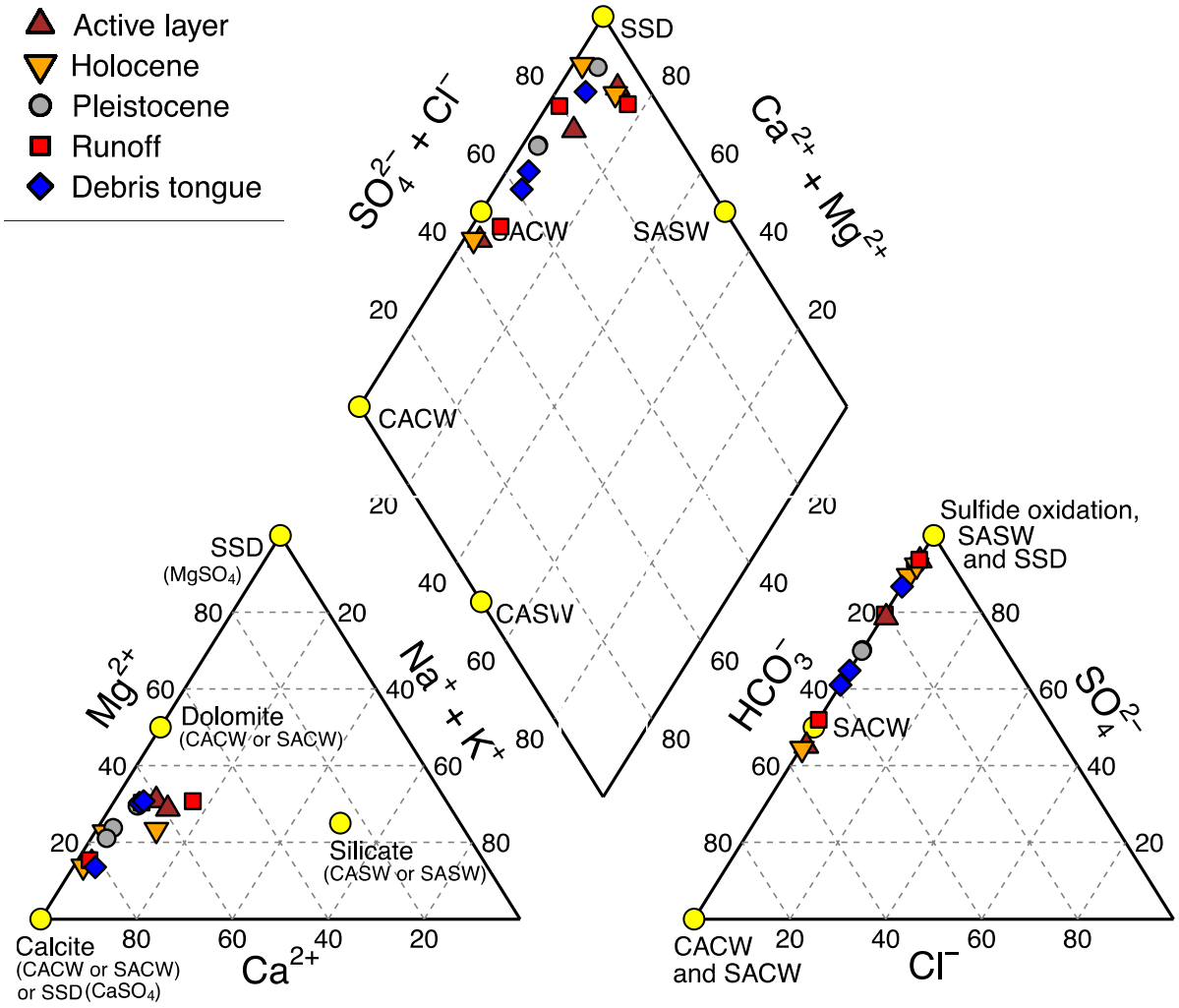

Figure 4-4. Piper diagram showing the chemical composition of MilliQ water treated with five different retrogressive thaw slump sediments (see legend) with varying degrees of prior thaw. CACW = H_2CO_3 carbonate weathering, SACW = H_2SO_4 carbonate weathering, CASW = H_2CO_3 silicate weathering, SASW = H_2SO_4 silicate weathering, SSD = sulfate salt (gypsum) dissolution. Values on axes represent the concentrations of ions as a proportion.

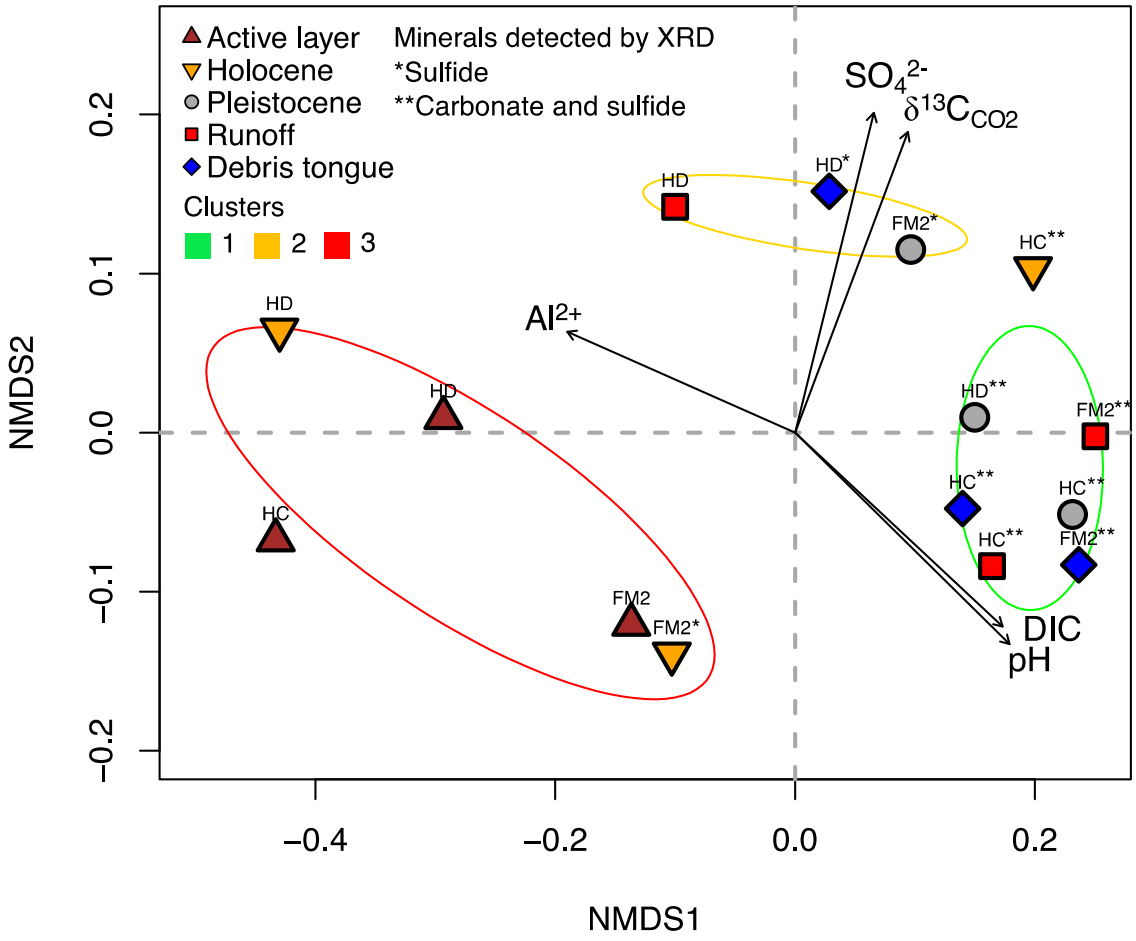

Figure 4-5. *metaMDS* results showing similarities between measurements (proximate = more similar) and correlations between measurement and original observations (black text). Note RTS IDs included above measurements. Ellipses constrain statistical clusters in Fig. A4-2 (see Sec. 4.3 in main text).

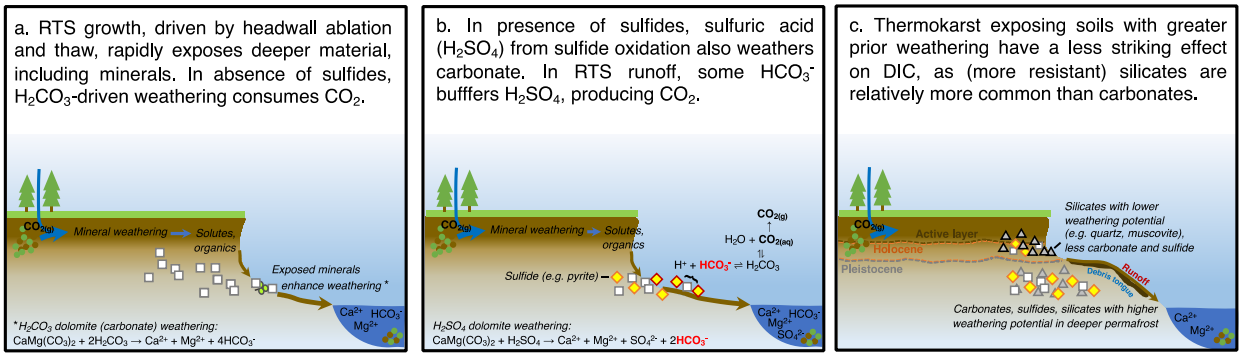

Figure 4-6. Refined conceptual model of RTS effects on inorganic carbon cycling on the Peel Plateau. Panel C depicts how this paper builds on previous understanding. Adapted from Zolkos et al. (2018).

CH. 5: Thermokarst Effects on Inorganic Carbon Cycling and Export Across Watershed Scales (Peel Plateau, Canada)

Summary

The transformation of thawed permafrost substrate into CO_2 and its release into the atmosphere is among the most significant climate feedbacks in northern ecosystems. Terrain subsidence following thaw (thermokarst) can release large amounts of permafrost substrate into fluvial networks, yet there is limited understanding of how this material transforms downstream. These effects are unstudied in relatively mineral-rich permafrost terrains, where mineral weathering may reshape inorganic carbon cycling and fluvial CO_2. Here, we determine the importance and effects of permafrost thaw on downstream inorganic carbon cycling and export within a relatively mineral-rich thermokarst terrain (Peel Plateau, Canada). Our work occurred along transects spanning three nested watersheds (~2 to 1000 km^2) with varying intensities of retrogressive thaw slump (RTS) thermokarst activity: a 500 m transect along a first-order thaw stream within an RTS; a 14 km transect along a stream which directly received RTS inputs; and a 70 km transect along an RTS-affected stream. Concentrations and stable isotopes of DIC and CO_2 revealed shifting drivers of inorganic carbon cycling across gradients of thermokarst disturbance. In the thaw stream, rapid weathering of carbonate tills amplified CO_2 efflux to the atmosphere and downstream HCO_3^- export from headwaters. Along the intermediate transect, DIC concentrations were ten times higher in the RTS-affected reach than in the undisturbed headwaters, despite some CO_2 loss to the atmosphere and downstream dilution from undisturbed inflowing streams. Along the largest transect, RTS activity in tributaries was a primary driver of increasing HCO_3^- export across watershed scales, which buffered some CO_2 and masked isotopic signals of downstream biotic CO_2 production. Constraining these effects in carbonate-bearing thermokarst-susceptible terrains across the circumpolar north is a clear priority for improving abilities to quantify and trace the effects of permafrost thaw on Arctic freshwater carbon cycling.

5.1. Introduction

Global inland waters are a critical nexus in the global carbon cycle because they receive, transform, and transport terrestrial organic carbon (5 PgC y^{-1}; Drake et al., 2017) at a magnitude comparable with CO_2 release associated with human activities (nearly 10 PgC y^{-1}; Stocker et al., 2013). The role of inland waters in carbon-climate feedbacks is of particular interest at northern

latitudes, where rapid climate warming (Serreze & Barry, 2011) is thawing large stores of organic carbon (800 PgC) (Hugelius et al., 2014) contained in perennially frozen (permafrost) soils and strengthening land-water linkages (Walvoord & Kurylyk, 2016). Consequently, constraining the rate and magnitude of freshwater carbon cycling has emerged as a priority in thermokarst terrains, where permafrost subsidence following thaw (Kokelj & Jorgenson, 2013) can release large amounts (up to millions of cubic meters; van der Sluijs et al., 2018) of readily-processed organic and inorganic substrate into fluvial networks (Vonk, Tank, Mann, et al., 2015; Zolkos et al., 2018). In relatively organic-rich thermokarst terrains, biotic processes are known to rapidly transform permafrost dissolved organic carbon (DOC) upon thaw (Drake et al., 2015; Littlefair & Tank, 2018; Vonk et al., 2013) and amplify CO_2 efflux from headwater streams to the atmosphere (Drake, Guillemette, et al., 2018). Working in relatively organic-rich permafrost regions, efforts to quantify the downstream evolution and fate of permafrost organic carbon indicate that biolabile permafrost DOC is rapidly transformed in headwaters (Drake, Guillemette, et al., 2018; Spencer et al., 2015) and that particulate carbon shows promise for tracing thermokarst effects on carbon cycling across broader scales (Wild et al., 2019). While relatively inorganic and mineral-rich thermokarst-susceptible terrains are thought to span the circumpolar north (Zolkos et al., 2018), thermokarst effects on the magnitude and drivers of fluvial inorganic carbon cycling across watershed scales remain unconstrained within emerging models of the Arctic freshwater carbon cycle (but see Drake et al., 2018b).

At the pan-Arctic scale, riverine fluxes of dissolved inorganic carbon (DIC = $\Sigma[CO_2, HCO_3^-, CO_3^{2-}]$; 57 TgC y^{-1}) are nearly 1.5 times greater than total (particulate and dissolved) organic carbon (Holmes et al., 2012; McClelland et al., 2016; Tank et al., 2012). The balance between DIC species is driven by variability in the pH continuum and processes which produce DIC, with key implications for linkages between CO_2 in freshwater and the atmosphere (Stumm & Morgan, 1996):

$$H_2O + CO_{2(g)} \rightleftharpoons H_2CO_3^* \rightleftharpoons H^+ + HCO_3^- \rightleftharpoons 2H^+ + CO_3^{2-} \quad (5\text{-}1)$$

From a mineral weathering perspective, the degree to which riverine DIC represents a CO_2 source or sink depends on the acid responsible for weathering. For instance, carbonic acid ($H_2CO_3^*$, including dissolved CO_2) weathering of carbonate (equation 5-2) and silicate (equation

5-3) renders CO_2 less susceptible to atmospheric exchange by converting it into bicarbonate (HCO_3^-), whereas sulfuric acid (H_2SO_4) carbonate weathering produces HCO_3^- without consuming CO_2 (equation 5-4):

$$H_2CO_3 + (Ca,Mg)CO_3 \rightarrow (Ca^{2+},Mg^{2+}) + 2HCO_3^- \quad (5\text{-}2)$$

$$2H_2CO_3 + 3H_2O + (Ca,Mg)Al_2Si_2O_8 \rightarrow (Ca^{2+},Mg^{2+}) + 2HCO_3^- + 2Al_2Si_2O_5(OH)_4 \quad (5\text{-}3)$$

$$H_2SO_4 + 2(Ca,Mg)CO_3 \rightarrow 2(Ca^{2+},Mg^{2+}) + SO_4^{2-} + 2HCO_3^- \quad (5\text{-}4)$$

Within the marine carbon cycle, precipitation reactions sequester half of this HCO_3^- as carbonate and release half as CO_2 (Calmels et al., 2007), rendering these weathering sources CO_2 neutral (equation 5-2), a sink (equation 5-3), and a source (equation 5-4) over geological timescales. Over shorter timescales, variability in pH and the transformation of HCO_3^- along the aquatic continuum may also generate CO_2 (Stumm & Morgan, 1996) (equation 5-1). Given observations of increasing HCO_3^- export in large northern rivers during recent decades (Drake, Tank, et al., 2018; Tank et al., 2016), determining how the effects from thermokarst and mineral weathering propagate from headwaters through fluvial networks is a priority for constraining inorganic carbon cycling and potential climate feedbacks.

The composition of ions and stable DIC isotopes ($\delta^{13}C_{DIC}$) in streams are useful indicators of fluvial inorganic carbon cycling. The proportions of solutes and $\delta^{13}C_{DIC}$ values can reflect sources of mineral weathering (e.g. equations 5-2–5-4) (Lehn et al., 2017), while $\delta^{13}C_{DIC}$ provides additional information about various biotic and abiotic processes which influence DIC (Kendall et al., 2014). $\delta^{13}C_{DIC}$ values reflect the $\delta^{13}C$ of source material (e.g. carbonate rock, organic carbon) to varying degrees, as DIC concentrations and thus isotopic values are readily altered within stream environments by CO_2 efflux to the atmosphere (Doctor et al., 2008; Drake, Guillemette, et al., 2018), calcite precipitation (Turner, 1982), methanogenesis (Campeau et al., 2018), photosynthesis (Descolas-Gros & Fontungne, 1990). Sampling ions and $\delta^{13}C_{DIC}$ along transects is thus a useful approach for tracing the downstream evolution of inorganic carbon cycling in fluvial networks. Working in a relatively organic-rich permafrost terrain, (Drake, Guillemette, et al., 2018) showed that strong $\delta^{13}C_{DIC}$ signals of biotic CO_2 production in headwater permafrost thaw streams were lost via degassing with increasing stream order. In relatively mineral-rich terrains including glacial environments, where high rates of physical

erosion increase mineral surface area, carbonate weathering, and HCO_3^- fluxes (Anderson, 2007), $\delta^{13}C_{DIC}$ values can primarily reflect carbonate weathering while isotopic signals of biotic CO_2 production may not be discernible in streams (Striegl et al., 2007). In environments with more intense carbonate rock weathering, $\delta^{13}C_{CO2}$ can thus elucidate the sources and transformation of CO_2 and DIC in fluvial networks. Yet, to our knowledge, no research to-date has explored the utility of dual DIC-CO_2 stable isotopes for constraining thermokarst effects on downstream fluvial inorganic carbon cycling in a relatively mineral-rich permafrost terrain.

Here, we build on recent research which documented intensified weathering of carbonate- and sulfide-bearing tills in association with accelerating retrogressive thaw slump (RTS) thermokarst activity on the Peel Plateau (NWT, Canada) (Zolkos et al., 2018). RTSs on the Peel Plateau are known to increase HCO_3^- immediately downstream (Zolkos et al., 2018) and solutes and sediments throughout fluvial networks (Kokelj et al., 2013; Malone et al., 2013). To determine how RTS effects on inorganic carbon cycling propagate through fluvial systems and the fate of inorganic permafrost constituents, we evaluate trends in major ions, and DIC and CO_2 concentrations and stable isotopes along transects which span gradients of thermokarst disturbance across three nested watersheds: (i) a 550 m permafrost runoff stream within a retrogressive thaw slump (RTS FM2 runoff); (ii) a 14 km transect in a creek which originated in undisturbed headwaters, was directly affected by RTS FM2 farther downstream, and, downstream of RTS FM2, received inputs from RTS-affected and undisturbed tributaries (Dempster Creek); and (iii) a 70 km transect in a stream which received inputs from multiple large RTS-affected tributaries and was itself a major tributary of the 70,000 km^2 Peel River watershed (Stony Creek) (Fig. 5-1). Our nested watershed approach and comparisons of stream chemistry between thermokarst-affected transects and undisturbed headwaters enabled us to explore the degree to which thermokarst effects on DIC cycling persist in fluvial networks. By pairing our geochemical measurements with geospatial analyses of landscape drivers of carbon cycling we further determine the importance of RTSs in fluvial DIC export and to develop a conceptual model of inorganic carbon cycling on the Peel Plateau. These results help to characterize carbon cycling in relatively inorganic-rich permafrost environments, which span the circumpolar north (Zolkos et al., 2018) yet are underrepresented within emerging models of the Arctic carbon cycle.

5.2. Methods

5.2.1. Study Area

The Stony Creek watershed (1100 km^2) is located southwest of the hamlet of Fort McPherson, in the northern section of the Peel River watershed (Fig. 5-1). Stony Creek, a major tributary of the Peel River, originates in the Richardson Mountains, where the slopes are sparsely vegetated and mainly consist of colluvium from exposed marine shale and sandstone bedrock (Duk-Rodkin & Hughes, 1992a; Norris, 1985). From its relatively undisturbed mountainous headwaters, Stony Creek flows through gravel bed streams incised within hummocky moraine on the Peel Plateau, where retrogressive thaw slump (RTS) thermokarst features in tributary watersheds enable the release of large amounts of sediment and solutes into streams (Kokelj, Tunnicliffe, et al., 2017). RTS growth is driven by the thaw and ablation of exposed ground ice and is perpetuated by the downslope removal of collapsed material via debris flows, which can accumulate in stream valleys (Fig. 5-1). RTS sediments and solutes are transported to streams via channelized rill runoff channels in the debris flow and can persist for tens of kilometers downstream (Malone et al., 2013). Accelerating RTS activity in the Stony Creek watershed in recent decades is associated with increasing solutes in the Peel River (Kokelj et al., 2013; Zolkos et al., 2018). The ~60 km^2 Dempster Creek watershed, which is a primary tributary of Stony Creek, originates in willow and open spruce taiga without RTS activity, but receives large inputs of sediments and solutes from the RTS FM2 (see also Kokelj et al., 2013; Malone et al., 2013; van der Sluijs et al., 2018) within several kilometers of the headwaters. Many small, non-RTS affected streams and several larger RTS-affected tributaries flow into Dempster Creek before it reaches Stony Creek.

5.2.2. Stream Sampling

In late July, 2017, we sampled DIC and CO_2 concentration, and stable isotopes of dissolved CO_2 ($\delta^{13}C_{CO2}$) at five locations along a 550 m-long transect within the RTS FM2 rill runoff channel (Fig. 5-1a). One day prior, additional parameters were sampled at runoff site five, for comparison with the full suite of chemistry parameters collected along the larger Dempster Creek transect. To characterize the downstream propagation of RTS FM2 inputs and effects on DIC cycling, we sampled the Dempster Creek in the undisturbed headwaters; from the RTS FM2 runoff near its confluence with Dempster Creek; and, along the RTS-affected reach of Dempster

Creek mainstem, upstream of three major tributaries and from the tributaries near their mouths (Fig. 5-1, Table A4-1). To determine RTS effects on DIC cycling across broader spatial scales, we further sampled the Stony Creek headwaters, the mainstem upstream of seven major tributaries, and the associated tributaries near their mouths. While the Dempster and Stony Creek headwater sites were not affected by RTSs, all other mainstem and tributary sites were (Table A4-1). At all sampling sites, stream temperature and pH were measured using a pre-calibrated YSI Professional-Plus water quality meter. Water samples for solutes and gases (see below) were collected from the center of the stream where possible, as an integrated sample from ~15 cm below the surface to ~1 m depth. An additional sample for total suspended sediments (TSS) was collected in a 1 L HDPE in the same fashion, following Gray and Landers (2014).

Water samples were filtered using sample-rinsed 0.45 µm polyethersulfone (PES, ThermoFisher) or cellulose-acetate (CA, Sartorius) membranes. Samples for DIC were collected without headspace in airtight syringes. Ions, DOC, and UV-visible absorbance were collected in acid washed (24h, 10% v/v HCl), DI rinsed all-plastic syringes. Syringes were triple sample-rinsed, sealed with a stopcock or luer plug, and stored cool and dark until processing within 10h. Water for DIC was filtered (PES) into precombusted (5h, 500˚C) glass vials without headspace and sealed with a butyl rubber septum for DIC concentration or two silicone-teflon septa for DIC stable isotopes ($\delta^{13}C_{DIC}$). Cations were filtered (CA) into acid-washed bottles and acidified with trace metal-grade HNO_3, while anions were filtered (CA) but not acidified. DOC was filtered (PES) into precombusted glass vials and acidified to pH < 2 using trace metal-grade HCl (Vonk, Tank, Mann, et al., 2015). UV-visible absorbance was filtered (PES) into non-acid washed 30 mL HDPE bottles. Samples were refrigerated (4˚C, dark) until analysis.

Dissolved CO_2 was collected following the headspace equilibration method (Hesslein et al., 1991) and stored in airtight 60 mL syringes (CO_2 concentration) or over-pressurized in pre-evacuated serum bottles sealed with pre-baked (60˚C, 12h), gas-inert butyl rubber stoppers ($\delta^{13}C_{CO2}$) (Spawn et al., 2015). One atmospheric CO_2 sample was collected at each site and stored in an airtight syringe. Gas samples were stored in the dark and at ~20˚C prior to analysis within 10h (CO_2) or two months ($\delta^{13}C_{CO2}$). Water and air temperature, atmospheric pressure, and the volumetric ratio of sample to atmospheric headspace was recorded for correcting later calculations of CO_2 partial pressure (pCO_2) and $\delta^{13}C_{CO2}$ (Hamilton & Ostrom, 2007; Tank et al., 2009).

5.2.3. Stream Flow

Discharge was calculated from measurements of stream flow (RedBack Model RB1, PVD100) and cross-sectional area made at increments equal to 10% of stream width (Gordon, 2004; Lurry & Kolbe, 2000). Where stream flow could not be measured across the entire width (W) of the Stony Creek tributaries, we estimated discharge (Q) from a hydraulic geometry model (Gordon, 2004) that we developed using measurements made during 2015-2017 (n = 20) across diverse stream morphologies (W = 0.4–6.6 m) and flow conditions (Q = 0.005–0.91 $m^3\ s^{-1}$) on the Peel Plateau:

$$W = 6.258Q^{0.661}\ (p < 0.01,\ R^2 = 0.89) \quad (5\text{-}4)$$

Q was first averaged for sites with multiple measurements and W was derived from on-site measurements or photos with a known scale.

5.2.4. Geochemical Analyses

Upon returning from the field each day, CO_2 was measured using an infrared gas analyzer (PP Systems EGM-4). The EGM-4 was checked monthly for drift using a commercial standard (Scotty Gases). We calculated the partial pressure of CO_2 (pCO_2) using Henry's constants corrected for stream water temperature (Weiss, 1974) and accounting for the ratio of water volume to headspace during sample equilibration. DIC samples were measured by infrared CO_2 detection (LiCOR 7000) following acidification within a DIC analyzer (Apollo SciTech model AS-C3). Calibration curves were made daily using certified reference material (CRM) from the Scripps Institution of Oceanography. Samples with DIC concentrations < 400 µM were analyzed using solutions prepared from a 1000 ppm TIC stock (ACCUSPEC) that were calibrated with the CRM. DIC species (CO_2, HCO_3^-, CO_3^{2-}) were calculated from DIC concentration and pCO_2 using CO2sys (v.2.3) (Pierrot et al., 2006), using field temperature and pressure at the time of sample collection, and the freshwater constants for K1 and K2 (Millero, 1979).

Cations and trace elements were measured by optical emission spectrometry (Thermo ICAP-6300) and anions by ion chromatography (Dionex DX-600) at the University of Alberta Biogeochemical Analytical Services Laboratory (BASL, ISO/EIC accreditation #17025). DOC

was measured using a total organic carbon analyzer (Shimadzu 5000A). DOC standard curves were made daily with a 1000 ppm KHP solution (ACCUSPEC) and an in-house caffeine standard (10 mg L^{-1}) was run every 20 samples to monitor instrument drift. Absorbance spectra were analyzed using an Ocean Optics UV-VIS instrument with a Flame spectrometer module, following details in Stubbins et al. (2017). To evaluate potential organic carbon reactivity, we used specific ultraviolet absorbance at 254 nm ($SUVA_{254}$) to infer DOC source (Weishaar et al., 2003).

$\delta^{13}C_{DIC}$ was determined using an isotope ratio mass spectrometer (Finnigan Mat DeltaPlusXP) interfaced to a total organic carbon analyzer (OI Analytical Aurora Model 1030W) at the University of Ottawa Stable Isotope Laboratory. $\delta^{13}C_{CO2}$ was analyzed within two months by a Picarro isotope analyzer (G2201-*i*; <0.2‰ precision) equipped with an injection module for discrete samples (SSIM). Commercial $\delta^{13}C_{CO2}$ standards were used to check for drift during each run. We used mass balance to correct $\delta^{13}C_{CO2}$ values for the $\delta^{13}C$ and mass of atmospheric CO_2 used for equilibration (Hamilton & Ostrom, 2007). To evaluate potential effects from calcite precipitation on the fractionation of CO_2 stable isotopes (Turner, 1982) in FM2 runoff, we calculated the saturation index (SI) using the hydrochemical software Aqion version 6.7.0 (http://www.aqion.de), which uses the U.S. Geological Survey software PHREEQC (Parkhurst & Appelo, 2013) as the internal numerical solver.

TSS samples were filtered onto muffled (450˚C, 4h) and pre-weighed glass fiber filters (Whatman GF/F; 0.7 µm nominal pore size) upon returning from the field, stored frozen, and dried (60˚C, 24h) for gravimetric analysis following a modified version of United States Geological Survey Method I-3765.

5.2.5. Geospatial Analyses

To determine landscape controls on DIC cycling in the major tributaries of Stony Creek, we derived RTS abundance, watershed slope (reflecting terrain relief), and vegetation distribution from geospatial data. Here, we use terrain relief as a proxy for potential physical erosion, as the denudation of shale regolith from mountainous terrains in the Peel River watershed has been shown to promote sulfide oxidation (Calmels et al., 2007) and may therefore influence DIC cycling. Active RTSs that were connected to streams were manually delineated within a pan-sharpened image created from orthorectified SPOT Panchromatic (1.6 m resolution) and

multispectral imagery (6.6 m resolution). The imagery was collected September 9–25, 2016, and pan-sharpened using the Image Analysis tool. The area of active RTSs was normalized to watershed area to calculate the proportional area disturbed by RTSs (RTS_{area}). Stream networks and watershed areas were delineated from the gridded (30 m) Canadian Digital Elevation Model (CDEM) and quality-checked following St. Pierre et al. (2018). Mean slope was derived from the non-conditioned CDEM data using Spatial Analyst tools in ArcGIS 10.5. For the Stony Creek tributary watersheds, the mean slope and enhanced vegetation index (EVI) were calculated using the Zonal Statistics tool. EVI can be useful for characterizing vegetation productivity (Loranty et al., 2014; Rocha & Shaver, 2011) and was used to broadly evaluate potential relationships between vegetation and DIC (Berner, 1999). We used the United States National Aeronautics and Space Administration EVI product (Didan, 2015), which is derived from gridded (250 m) moderate resolution imaging spectroradiometer (MODIS). The MODIS data were collected on July 28, 2017.

5.2.6. Mineral Weathering Sources and Controls on DIC Cycling and Tributary Yields

We used a Piper diagram (Piper, 1944) – which reflects the proportional equivalent concentrations of ions in a sample relative to mineral weathering end-members – to constrain the sources of mineral weathering and HCO_3^-. In addition to carbonate weathering by H_2SO_4 (equation 5-4), silicate weathering by H_2SO_4 (equation 5-6), sulfate salt (e.g. gypsum) dissolution (equation 5-7), and sulfide (e.g. pyrite) oxidation (equation 5-8) are thought to contribute to SO_4^{2-} in streams on the Peel Plateau (Kokelj et al., 2013; Malone et al., 2013; Zolkos et al., 2018):

$$H_2SO_4 + H_2O + (Ca,Mg)Al_2Si_2O_8 \rightarrow (Ca^{2+},Mg^{2+}) + SO_4^{2-} + Al_2Si_2O_5(OH)_4 \quad (5\text{-}6)$$

$$(Ca,Mg)SO_4 \rightarrow (Ca^{2+},Mg^{2+}) + SO_4^{2-} \quad (5\text{-}7)$$

$$FeS_2 + 15/4O_2 + 7/2H_2O \rightarrow Fe(OH_3) + 2H^+ + SO_4^{2-} \quad (5\text{-}8)$$

The products of equations 5-2, 5-4, 5-6, and 5-7 defined the mineral weathering end-members in the Piper diagram. Because the end-member space in a Piper diagram for gypsum dissolution (equation 5-7) can also reflect SO_4^{2-} from sulfide oxidation in excess of carbonate and/or silicate weathering, we used $\delta^{13}C_{DIC}$ and pH to further constrain the sources of mineral weathering and

DIC. To evaluate controls on cycling of the bulk DIC pool, end-member $\delta^{13}C_{DIC}$ values for equilibrium processes (mixing with atmospheric and/or biogenic CO_2) and kinetic reactions (mineral weathering) were derived following Jin et al. (2009) and Lehn et al. (2017) and compared with observed $\delta^{13}C_{DIC}$ values.

To evaluate potential effects on $\delta^{13}C_{CO2}$ from DIC speciation along the pH continuum (Clark & Fritz, 1997), we compared theoretical and observed $\delta^{13}C_{CO2}$ values in the Stony Creek mainstem. Theoretical $\delta^{13}C_{CO2}$ values were calculated using mass balance to obtain $\delta^{13}C_{HCO3}$ from measurements of DIC, CO_2, HCO_3^-, $\delta^{13}C_{DIC}$, and $\delta^{13}C_{CO2}$. We then used measurements of stream temperature (T) to calculate the equilibrium fractionation between CO_2 and HCO_3^- ($\varepsilon = -9.483 \times 10^3/T + 23.89‰$; Mook et al., 1974). Finally, ε was subtracted from $\delta^{13}C_{HCO3}$ to obtain theoretical $\delta^{13}C_{CO2}$. Similarity between observed and theoretical $\delta^{13}C_{CO2}$ values was interpreted as $\delta^{13}C_{CO2}$ variability driven by DIC speciation, whereas dissimilarity was taken to reflect effects from CO_2 degassing (Zhang et al., 1995) and/or microbial oxidation of organic matter (Kendall et al., 2014).

We tested for downstream change in HCO_3^- and pCO_2 along the Stony Creek mainstem using the non-parametric Mann-Kendall test from the R software (R Core Team, 2018) package *zyp* (Bronaugh & Werner, 2013), following the trend pre-whitening approach detailed by Yue et al. (2002) to account for serial autocorrelation. To characterize landscape controls on DIC cycling, we normalized instantaneous HCO_3^- flux (concentration*discharge) and discharge (Q) to watershed area, and scaled them from instantaneous to daily HCO_3^- yield (μmol m^{-2} d^{-1}) and water yield (cm d^{-1}) in the Stony Creek tributaries. We developed a predictive model of HCO_3^- yields in Stony Creek sub-watershed tributaries using the landscape measurements derived from geospatial data:

$$HCO_3^- \text{ yield} = \text{Water yield} + RTS_n + RTS_{area} + \text{Slope} + \text{EVI} \quad (5\text{-}9)$$

Where water yield is in cm d^{-1}; RTS_n is the number of active RTSs in the tributary watershed; RTS_{area} (proportion from 0 to 1; see above); slope is the mean sub-watershed slope (in degrees); and EVI is the mean sub-watershed EVI (–1 to 1). The multiple linear regression was trimmed using the *step* function in the R package *lmerTest* (Kuznetsova et al., 2018) to eliminate covariates which did not improve the model. The Variance Inflation Factor (VIF) was then used

to identify highly collinear covariates (VIF > 3; Zuur et al., 2010), which were removed from the trimmed models. Model fits were inspected visually with residual plots and covariates were transformed as needed to meet assumptions of independent and homoscedastic residuals (Zuur, 2009). All statistics were performed in the R programming environment (v.3.4; R Core Team, 2018) and significance was interpreted at $\alpha = 0.05$.

5.3. Results and Discussion

5.3.1. Signals of Rapid Inorganic Carbon Cycling within a Permafrost Thaw Stream

HCO_3^- concentrations were up to two orders of magnitude greater in the runoff of RTS FM2 (~1500 µM) than in the Dempster and Stony Creek headwaters (1–115 µM), where RTSs were absent (Table 5-1, Fig. 5-2). In the RTS FM2 runoff, the high proportion of SO_4^{2-} relative to other ions (Fig. 5-3) reflected sulfate salt (e.g. gypsum) dissolution and ^{13}C-enriched DIC ($\delta^{13}C_{DIC} = –1.0‰$) further revealed that sulfide oxidation coupled with carbonate weathering was a primary source of HCO_3^- (Fig. 5-4). These results align with previous findings that RTS activity on the Peel Plateau enhances the chemical weathering of tills and fluvial export of solutes (Kokelj et al., 2013; Malone et al., 2013; Zolkos et al., 2018). Further, the increase in conductivity along the RTS FM2 runoff transect (from 1370 to 1990 µS cm^{-1}) demonstrates that minerals within regional tills readily weather during fluvial transport. Mineral weathering along the runoff transect occurred in concert with a decrease in HCO_3^- (from 1510 to 1386 µM), an increase in pCO_2 within the first ~200 m (from 1050 to 1530 µatm) followed by a decrease (to 740 µatm) thereafter, and variability in pH opposite that of pCO_2 (Table 5-1). These trends are consistent with observations of some HCO_3^- conversion to CO_2 within RTS runoff (Zolkos et al., 2018) and reflect a strong coupling between mineral weathering and CO_2 following the thaw and exposure of tills by thermokarst.

The relatively ^{13}C-enriched CO_2 in RTS FM2 runoff (–9.4 to –14.3‰; Table 5-1, Fig. 5-5) aligned with $\delta^{13}C_{CO2}$ values expected from H_2SO_4 weathering of regional carbonate (–0.7 to –5.6‰) (Hitchon & Krouse, 1972), accounting for isotopic fractionation of ~9‰ between carbonate and CO_2 at the temperature of FM2 runoff (17.2˚C) (Clark & Fritz, 1997). In agreement with the other geochemical signals (see above), increasing pCO_2 and $\delta^{13}C_{CO2}$ values (from –12 to –10‰) along the upper 400 m of the runoff transect are consistent with abiotic CO_2 production. In contrast, the large decrease in pCO_2 and increasing $\delta^{13}C_{CO2}$ along the lower 100 m

of the transect indicated stronger effects from CO_2 efflux to the atmosphere, which aligns with the preferential loss of ^{12}C in the CO_2 phase via DIC fractionation and degassing (Doctor et al., 2008; Drake, Guillemette, et al., 2018; Finlay, 2003). ^{13}C enrichment of the CO_2 pool by methanogenesis (Campeau et al., 2018), photosynthesis (Descolas-Gros & Fontungne, 1990), and/or calcite precipitation (Turner, 1982) was unlikely, as CH_4 in FM2 runoff was relatively low (pCH_4 = 7.6 ± 3.9 µatm, mean ± SD, n = 6; Zolkos et al., 2019), the high turbidity of FM2 runoff likely impeded light penetration, and calcite was below saturation (SI = –0.79).

Together, these trends in DIC, mineral weathering sources, and $\delta^{13}C_{CO2}$ indicate that rapid transformation of thawed permafrost substrate generates substantial HCO_3^- and some geogenic CO_2 (e.g. Zolkos et al., 2018) during fluvial transport. Evidently, the majority of DIC generated within RTS runoff is exported laterally as HCO_3^-, while a smaller proportion is rapidly effluxed to the atmosphere (e.g. Zolkos et al., 2019). In agreement with research in relatively organic-rich permafrost (yedoma) regions (Drake, Guillemette, et al., 2018), these results from a relatively inorganic-rich terrain demonstrate that thermokarst can promote rapid inorganic carbon cycling in close proximity to thaw (i.e. RTS FM2 runoff) and during fluvial transport in thaw streams.

5.3.2. Reshaping the Inorganic Carbon Cycle: Thermokarst Effects at Intermediate Scales

The trends in HCO_3^- concentration and pCO_2, mineral weathering sources, and stable isotopes along the 14 km Dempster Creek transect reveal that inputs of thawed permafrost substrate from RTS FM2 runoff reshaped DIC cycling far downstream. HCO_3^- concentrations downstream of RTS FM2 were ten-fold greater than in the Dempster Creek headwaters (115 µM), where high pCO_2 (Fig. 5-2b) and ^{13}C-depleted $\delta^{13}C_{CO2}$ values are consistent with DIC cycling driven by biotic-organic interactions (Campeau et al., 2018; Kendall et al., 2014) and some atmospheric mixing (Fig. 5-4, Fig. 5-5). Along the entire RTS-affected reach of the Dempster Creek, the high proportion of SO_4^{2-} relative to other ions (Fig. 5-3) and relatively ^{13}C-enriched DIC values (Fig. 5-4) indicated that carbonate weathering by H_2SO_4 in excess was a primary source of DIC. Yet, the decrease in HCO_3^- (from 1321 to 946 µM), conductivity (950 to 416 µS cm^{-1}), and pCO_2 (685 to 600 µatm) along the transect show that the effects from RTS FM2 slightly diminished downstream (Table 5-1, Fig. 5-2, 5-4). The decrease in HCO_3^- coincided with inputs from dozens of small, non RTS-affected streams that were characterized by lower HCO_3^-, conductivity, $\delta^{13}C$ (both DIC and CO_2), and TSS than the Dempster Creek

mainstem (Table 5-1), suggesting that dilution was partly responsible for tempering the signals of thermokarst activity along the transect. Yet, relative to the headwaters, the high concentrations of HCO_3^- near the mouth of the Dempster Creek indicate that RTS increased DIC export far downstream.

In contrast to HCO_3^-, pCO_2 decreased to near-atmospheric values along the Dempster Creek mainstem (Fig. 5-2), consistent with observations that substantial CO_2 is lost in headwaters via efflux to the atmosphere (Butman & Raymond, 2011; Crawford et al., 2013; Drake, Guillemette, et al., 2018). While H_2CO_3 weathering of carbonate tills during fluvial transport is known to consume CO_2 (Striegl et al., 2007), the downstream decrease in HCO_3^- and pH along the Dempster Creek (Fig. 5-2, 5-4) suggest that dilution likely had stronger effects on CO_2 loss than did H_2CO_3 carbonate weathering. Thus, carbonate weathering during fluvial transport is most pronounced within RTS runoff and appears to be relatively less pronounced in mid-order streams like the Dempster Creek, where DIC transformation is more strongly influenced by dilution during export to larger rivers. Along the RTS-affected reach of the Dempster Creek mainstem, decreasing pCO_2 (Fig. 5-1) reflected degassing – which would increase $\delta^{13}C_{CO2}$ values (see above) – yet relatively depleted and decreasing $\delta^{13}C_{CO2}$ values (Table 5-1, Fig. 5-5) suggest that additional processes were driving the downstream changes in pCO_2. The decreasing $\delta^{13}C_{CO2}$ values coincided with increasing DOC concentrations and $SUVA_{254}$ values, which became more similar to the tributary streams (Table 5-1, Fig. 5-6), suggesting that tributary streams perhaps stimulated microbial activity and some biotic CO_2 production and/or delivered ^{13}C-depleted CO_2 to the mainstem Dempster Creek. Consistent with previous studies on the Peel Plateau (Littlefair et al., 2017), these findings indicate that inputs from undisturbed streams may counterbalance potential inhibitions to microbial oxidation imposed by the adsorption of DOC to RTS sediments (Gentsch et al., 2015) by diluting TSS and increasing DOC in the Dempster Creek mainstem (Table 5-1, Fig. 5-6).

Provided RTS activity on the Peel Plateau continues to accelerate (Segal et al., 2016a) and promote the thaw and weathering of carbonate tills (Kokelj et al., 2013; Malone et al., 2013; Zolkos et al., 2018), thermokarst effects on regional DIC cycling can be expected to intensify in the future. In contrast to downstream trends in fluvial carbon cycling in organic-rich permafrost environments (e.g. Drake et al., 2018b), elevated HCO_3^- and $\delta^{13}C_{DIC}$ along the Dempster Creek reveal that the geochemical signals of thermokarst can persist far downstream in carbonate-

bearing permafrost terrains. In the absence of pulses of fresh substrate directly from RTSs, inorganic carbon cycling downstream of RTS FM2 reflected equilibration with the surrounding environment via some dilution of DIC by inputs from undisturbed tributaries, and also some degassing and biotic production of CO_2. Evaluating the downstream balance of HCO_3^- and CO_2 and the broad-scale drivers of DIC transformation can help to understand the persistence of thermokarst effects across watershed scales.

5.3.3. Thermokarst Effects on Inorganic Carbon Cycling Across a Major Watershed

In the mountainous, non-RTS affected headwaters of the Stony Creek (mainstem and tributary Site 1), the low concentrations of HCO_3^- coupled with pCO_2 near atmospheric equilibrium (Fig. 5-2) suggest that fluvial inorganic carbon cycling was mainly controlled by mixing with atmospheric and biogenic CO_2 (Fig. 5-4). The Ca^{2+}–Mg^{2+}–SO_4^{2-}-type waters (Fig. 5-3a), low HCO_3^- concentration (33 µM), and limited $\delta^{13}C_{DIC}$ evidence for carbonate weathering (Fig. 5-4) reflected the denudation of sulfide- and gypsum-bearing lithologies exposed in this part of the Richardson Mountains (Norris, 1985). HCO_3^- increased along Stony Creek to ~460 µM near the Peel River (Table 5-1, Fig. 5-2a), in concert with strengthening geochemical signals of H_2SO_4 carbonate weathering (Fig. 5-3, 5-4) and also inputs from RTS-affected tributaries. Together, these trends reflect amplified HCO_3^- export associated with intensified carbonate weathering across watershed scales. To determine the importance of RTS activity on carbon cycling relative to hydrology, vegetation, and terrain relief across the Stony Creek watershed, we paired HCO_3^- and stream flow measurements in the major tributaries (Fig. 5-1) with GIS data for terrain relief and vegetation productivity (EVI) in a linear mixed effects model (see Sec. 5.2.6). To account for varying tributary watershed areas, we used tributary HCO_3^- yields in the model, which we calculated using discharge (Q) estimated from the hydraulic geometry relationship between Q and stream width ($p < 0.01$, $R^2 = 0.89$; Sec. 5.2.3). The linear mixed effects model indicated that water yield was a strong predictor of HCO_3^- yield ($F_3 = 23$, $p = 0.01$, $R^2 = 0.92$). The area of RTS disturbance in each tributary watershed and EVI, despite having relatively minor importance, were retained during automated model selection because they improved the final model (Table A4-2). This aligns with observations in the RTS-affected tributaries, where HCO_3^- yields (1,070 ± 985 µmol m^{-2} d^{-1}, mean ± SD, $n = 6$) were several orders of magnitude higher than in the non-RTS affected headwaters (1.6 µmol m^{-2} d^{-1}) (Table 5-2) and approached

summertime HCO_3^- yields in watersheds with carbonate rock weathering by glacial activity (2700 to 3300 μmol m^{-2} d^{-1}) (Lafrenière & Sharp, 2005; Striegl et al., 2007). These findings aligns with the understanding that, on the Peel Plateau, RTSs enhance mineral weathering by unearthing large amounts of till (van der Sluijs et al., 2018; Zolkos et al., 2018) and by providing flowing surface waters with direct access to the carbonate- and sulfide-bearing sediments which were previously protected by permafrost (e.g. Striegl et al., 2005; Walvoord and Kurylyk, 2016; Walvoord and Striegl, 2007).

While inputs from RTS-affected tributaries drove increasing HCO_3^- concentrations and $\delta^{13}C_{DIC}$ values along the Stony Creek mainstem (Table 5-1, Fig. 5-5), pCO_2 was consistently saturated and showed modest variability (479 ± 35 μatm, mean ± SD). Despite relatively stable pCO_2 levels along the Stony Creek, $\delta^{13}C_{CO2}$ values decreased downstream (from –13.8 to –18.1‰) (Fig. 5-5). This indicated firstly that biotic CO_2 production increased downstream and secondly that – owing to $\delta^{13}C_{DIC}$ values which primarily reflected the high proportion of DIC comprised of (^{13}C-enriched, geogenic) HCO_3^- relative to CO_2 – the biogenic (^{13}C-depleted) CO_2 was not discernible in $\delta^{13}C_{DIC}$ values (i.e. masked). Elsewhere, H_2CO_3 weathering of glacial carbonate flour during fluvial transport has been shown to increase $\delta^{13}C_{DIC}$, consume CO_2 to below atmospheric levels, and mask signals of biotic CO_2 production (Sharp et al., 1995; Striegl et al., 2007; Tranter & Wadham, 2014). To assess the controls on DIC cycling along Stony Creek, we compared our measurements of $\delta^{13}C_{CO2}$ with theoretical values reflecting DIC speciation along the pH continuum (see details in Sec. 5.2.6). From ~5 to 35 km downstream, the good agreement between decreasing measured and theoretical $\delta^{13}C_{CO2}$ values reflected equilibrium fractionation (ε = 9.7‰ at 9˚C; Mook et al., 1974) associated with pH buffering, suggesting that DIC speciation was a primary control on CO_2 (Fig. 5-7). Farther down the Stony Creek mainstem, $\delta^{13}C_{CO2}$ values were slightly lower than expected from DIC speciation alone (Fig. 5-7) and aligned with rising DOC concentrations (Fig. 5-6), indicating that increased carbon availability stimulated some biotic CO_2 production and sustained modest pCO_2 (Fig. 5-3b).

These observations reveal that the drivers and intensity of DIC cycling shifted downstream along gradients of thermokarst disturbance. Within a permafrost thaw stream (RTS FM2 runoff), high concentrations of HCO_3^- and rapid CO_2 production and efflux to the atmosphere across relatively short distances reflected relatively fast DIC cycling associated with mineral

weathering. Over broader geographic extents, DIC cycling was characterized by relatively slower processes associated with HCO_3^- export across watershed scales (Fig. 5-8). The influence of these processes on inorganic carbon cycling across the circumpolar north is strongly coupled to regional variability in glacial history, geology, and the mineral composition of permafrost, which remain understudied in the context of permafrost carbon climate feedbacks.

5.3.4. Inorganic Carbon Cycling in Thermokarst-Affected Fluvial Networks

Our assessment of the importance and effects of thermokarst on inorganic carbon cycling shows that pulses of inorganic substrate from thermokarst activity increased DIC and reshaped inorganic carbon cycling across watershed scales. These findings align with the paradigm that fluvial networks actively process and transport terrestrial substrate (Cole et al., 2007) and they are among the first to evaluate downstream carbon cycling in thermokarst-affected fluvial networks (e.g. Drake et al., 2018b) within a relatively inorganic-rich permafrost terrain (see also Kokelj et al., 2013; Malone et al., 2013). The striking DIC production and CO_2 degassing that we documented in RTS FM2 runoff indicates that rapid carbon cycling can be expected where thermokarst releases inorganic and/or organic substrate with limited prior modification. Across watershed scales on the Peel Plateau, HCO_3^- export was a primary fate of carbonate tills unearthed by thermokarst and reached magnitudes comparable to watersheds with carbonate denudation by glacial activity (see above). These findings directly link accelerating thermokarst activity on the Peel Plateau (Segal et al., 2016a) with signals of intensifying carbon weathering across the broader Peel and Mackenzie River watersheds (Tank et al., 2016; Zolkos et al., 2018) and indicate that future intensification of inorganic carbon cycling can be expected in thermokarst terrains across the circumpolar north (Zolkos et al., 2018). Regional differences in the mineral composition of permafrost – which are broadly related to geology and glacial history (Amiotte Suchet et al., 2003; Hartmann & Moosdorf, 2012; Zolkos et al., 2018) – will have fundamental implications for carbon cycling and climate feedbacks.

The degree to which carbonate weathering is coupled with sulfide oxidation will determine if mineral weathering is a CO_2 sink or source, and thus the strength of abiotic components of the permafrost carbon-climate feedback (Schuur et al., 2015; Zolkos et al., 2018). Current models suggest that mineral weathering across the Peel River watershed is a modest source of CO_2 to the atmosphere, owing to widespread sulfide oxidation coupled with carbonate weathering (Beaulieu

et al., 2011). Yet these models are based on relatively coarse lithologic data which under-represent the abundance of carbonate in exposed bedrock in the southern Richardson and Mackenzie Mountains (Norris, 1985). In the Eurasian north, increasing alkalinity fluxes in recent decades are thought to reflect enhanced H_2CO_3 carbonate weathering coincident with a suite of environmental changes including intensifying permafrost thaw, precipitation, and vegetation activity (Drake, Guillemette, et al., 2018). Investigating the effects of regional variability in thermokarst, geology, hydrology, and vegetation on aquatic inorganic carbon cycling is a clear priority for constraining climate feedbacks across broad and diverse permafrost terrains (Li Yung Lung et al., 2018; Tank et al., 2012; Zolkos et al., 2018).

5.4. Conclusions

On the Peel Plateau, the downstream evolution of DIC species and stable isotopes in three nested watersheds revealed shifting drivers of inorganic carbon cycling and export across gradients of thermokarst disturbance. In headwaters, rapid inorganic carbon cycling during fluvial transport was strongly coupled with carbonate weathering and sulfide oxidation, resulting in enhanced CO_2 efflux to the atmosphere and substantial HCO_3^- export downstream. The downstream persistence of high HCO_3^- concentrations prompted DIC transformation which masked some downstream biotic CO_2 production. As thermokarst activity accelerates (Lewkowicz & Way, 2019; Segal et al., 2016a) and reshapes land-freshwater linkages (Vonk, Tank, Bowden, et al., 2015) in ice-rich, carbonate-bearing terrains cross the circumpolar north (Kokelj, Lantz, et al., 2017; Zolkos et al., 2018), tracing the effects on DIC cycling across watershed scales will be imperative for constraining the fate of permafrost carbon and potential climate feedbacks.

Table 5-1. Geochemical characteristics of tributary and mainstem sites along the Dempster and Stony Creeks. *Site was not affected by retrogressive thaw slumps. †Sampled on July 30, 2017, while other FM2 runoff samples were collected on July 31, 2017. FM2 runoff site #5 was nearest the confluence with the Dempster Creek.

Creek	Type	Site	pH	pCO_2 (µatm)	CO_2 (µM)	HCO_3^- (µM)	CO_3^{2-} (µM)	DIC (uM)	Cond (µS cm^{-1})	$\delta^{13}C_{DIC}$ (‰VPDB)	$\delta^{13}C_{CO2}$ (‰VPDB)	DOC (µM)	$SUVA_{254}$ (L mgC^{-1} m^{-1})	TSS (mg L^{-1})	Watershed area (km^2)
FM2	Runoff	1	7.72	1046	43	1510	5	1559	1370	–	-12.1	758	1.85	–	–
FM2	Runoff	2	7.51	1534	60	1439	4	1502	1816	–	-11.4	–	–	–	–
FM2	Runoff	3	7.71	914	37	1420	5	1462	1920	–	-10.3	–	–	–	–
FM2	Runoff	4	7.73	877	38	1391	5	1433	1903	–	-10.0	–	–	–	–
FM2	Runoff	5	7.80	741	33	1386	6	1424	1986	–	-11.2	–	–	–	–
FM2	Runoff	5†	7.82	690	29	1450	7	1487	1653	-1.0	-11.6	726	1.84	15805	–
Dempster	Mainstem	1*	5.82	2463	124	115	0	239	52	-15.0	-21.6	960	3.66	5	2
Dempster	Mainstem	2	7.55	685	35	1321	5	1361	958	-4.2	-16.1	790	2.53	11795	16
Dempster	Mainstem	3	7.54	656	31	1073	4	1107	655	-5.3	-15.6	823	2.93	9165	24
Dempster	Mainstem	4	7.35	599	30	946	3	978	416	-5.7	-16.8	1156	3.28	2797	57
Dempster	Tributary	2	7.56	834	50	1233	3	1286	390	-10.5	-21.3	1053	3.46	26	2
Dempster	Tributary	3	7.32	477	23	561	1	586	171	-7.2	-18.1	1241	3.65	985	11
Dempster	Tributary	4	7.30	551	27	697	2	726	236	-8.0	-18.5	922	3.61	223	168
Stony	Mainstem	1*	5.66	542	33	33	0	65	406	-11.6	-13.8	102	1.29	3	83
Stony	Mainstem	2	6.37	447	25	69	0	94	396	-8.0	-15.1	124	1.58	920	136
Stony	Mainstem	3	7.01	473	27	112	0	139	334	-6.9	-15.3	202	2.16	799	176
Stony	Mainstem	4	6.69	444	25	248	0	273	283	-8.9	-17.6	306	2.77	462	479
Stony	Mainstem	5	7.20	482	27	325	0	353	279	-8.4	-17.6	364	3.09	507	490
Stony	Mainstem	6	7.33	461	25	382	1	408	290	-7.8	-18.1	385	3.01	665	626
Stony	Mainstem	7	7.30	461	25	409	1	435	293	-8.1	-18.1	390	2.99	761	689
Stony	Mainstem	8	7.30	518	27	461	1	489	279	-7.8	-18.1	551	3.19	1073	995
Stony	Tributary	1*	5.00	451	25	1	0	26	524	-15.6	-12.3	101	0.73	5	26
Stony	Tributary	2	6.71	501	28	449	1	478	226	-5.0	-15.9	437	2.22	39568	7

Stony	Tributary	3	7.11	448	26	338	0	365	148	-9.3	-18.0	458	3.12	10	59
Stony	Tributary	4	6.53	572	32	375	0	407	245	-8.5	-19.4	550	3.31	704	194
Stony	Tributary	5	7.00	494	26	601	1	628	479	-7.0	-18.0	596	2.88	1270	104
Stony	Tributary	6	7.37	498	27	633	1	661	260	-8.0	-18.3	1142	3.34	1936	38
Stony	Tributary	7	7.32	475	26	570	1	597	230	-10.7	-18.0	1078	3.56	1258	227

Table 5-2. Characteristics of Stony Creek tributary watersheds. *Site was not affected by retrogressive thaw slumps (RTS). Coordinates reported in decimal degrees. EVI = enhanced vegetation index. †Denotes mean values for the watershed.

Tributary	HCO_3^- yield ($\mu M\ m^{-2}\ d^{-1}$)	Water yield ($cm\ d^{-1}$)	RTS (% area)	RTS (*n*)	Slope (°)†	EVI†
1*	1.6	0.20	0.03	1	14.9	0.28
2	2721	0.61	3.5	6	6.5	0.48
3	616	0.18	0.16	3	8.7	0.45
4	155	0.04	0.67	50	6.5	0.45
5	742	0.12	0.13	10	7.2	0.46
6	1791	0.28	0.2	8	4.8	0.47
7	397	0.07	0.6	14	5.7	0.45

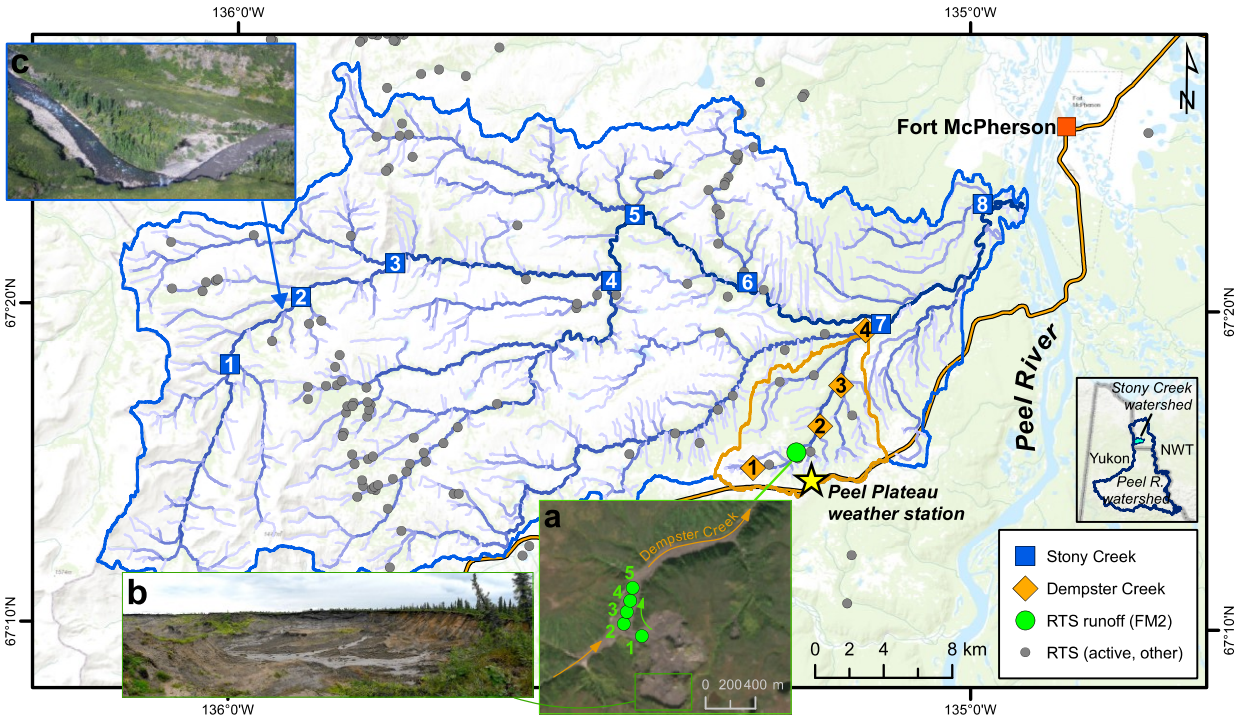

Figure 5-1. Sampling sites on the Peel Plateau (NWT, Canada). Water samples were collected along the mainstem Dempster and Stony Creeks (n = 12) and major tributaries (n = 10), and from the rill runoff at retrogressive thaw slump (RTS) FM2. Site numbers given within symbols (Table A4-1). Basemap from Esri ArcGIS Online. (a) RTS FM2 runoff transect sampling scheme. Satellite image of RTS FM2 in September 2017 obtained from Copernicus Sentinel data (European Space Agency, https://sentinel.esa.int/). (b) A portion of the RTS FM2 headwall (see location in (a)). RTS FM2 spans ~40 ha and its headwall reaches ~25 m in height. (c) Aerial photograph of the Stony Creek where it was first impacted by RTS activity. Locations of other active RTS features modified from the literature (Segal et al., 2016b).

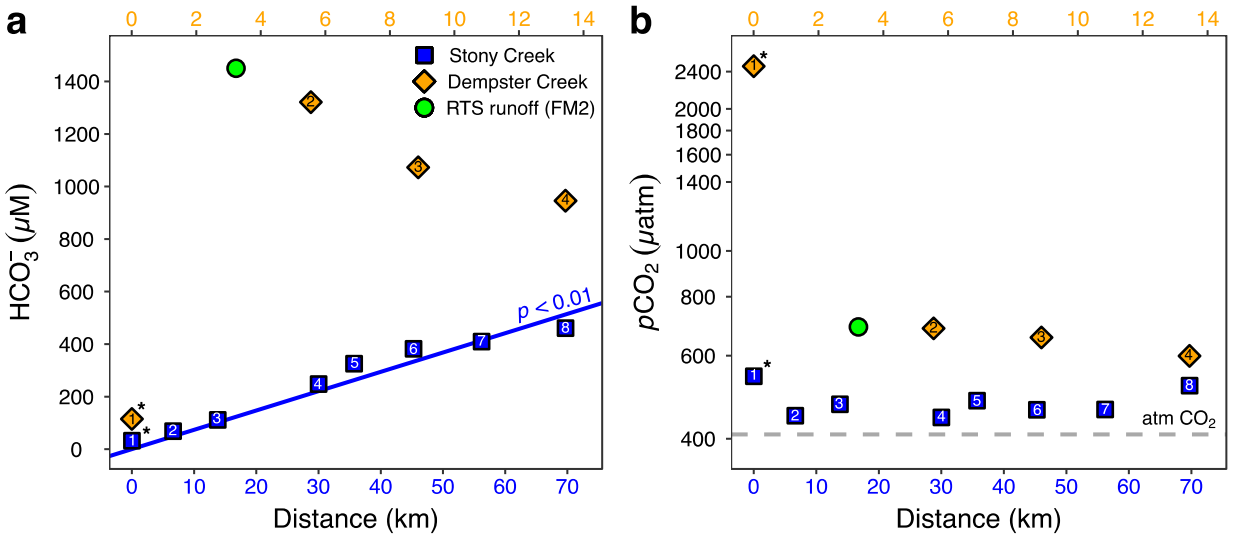

Figure 5-2. (a) HCO_3^- and (b) pCO_2 trends along the mainstem Stony and Dempster Creeks (see locations in Fig. 5-1). The retrogressive thaw slump (RTS) FM2 runoff is a tributary to the Dempster Creek. Note different x-axis scales for the two transects. Regression line in (a) is from the Mann-Kendall test (see text for details). The Dempster Creek enters the Stony Creek at Site 7. *Site was not affected by retrogressive thaw slumps. Site numbers given within symbols (Table A4-1).

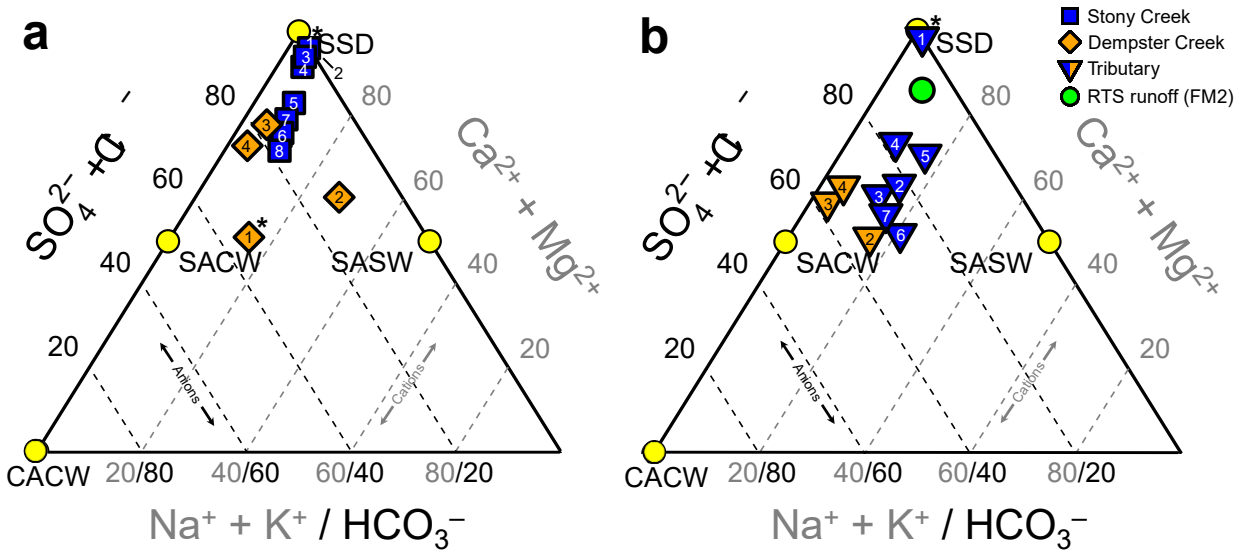

Figure 5-3. Piper diagrams (Piper, 1944) (modified to show the upper half of the diamond plot) showing stream chemistry of the (a) mainstem sites and (b) tributary and RTS FM2 runoff sites. Axes and corresponding text in gray and black reflect the proportions of cations and anions, respectively. Mineral weathering end-members were derived from the proportional concentration (meq L^{-1}) of solutes generated by H_2CO_3 carbonate weathering (CACW, equation 5-2 in text), H_2SO_4 carbonate weathering (SACW, equation 5-4), H_2SO_4 silicate weathering (SASW, equation 5-6), and sulfate salt (gypsum) dissolution (SSD, equation 5-7). *Site was not affected by retrogressive thaw slumps. Site numbers given within symbols (Table A4-1).

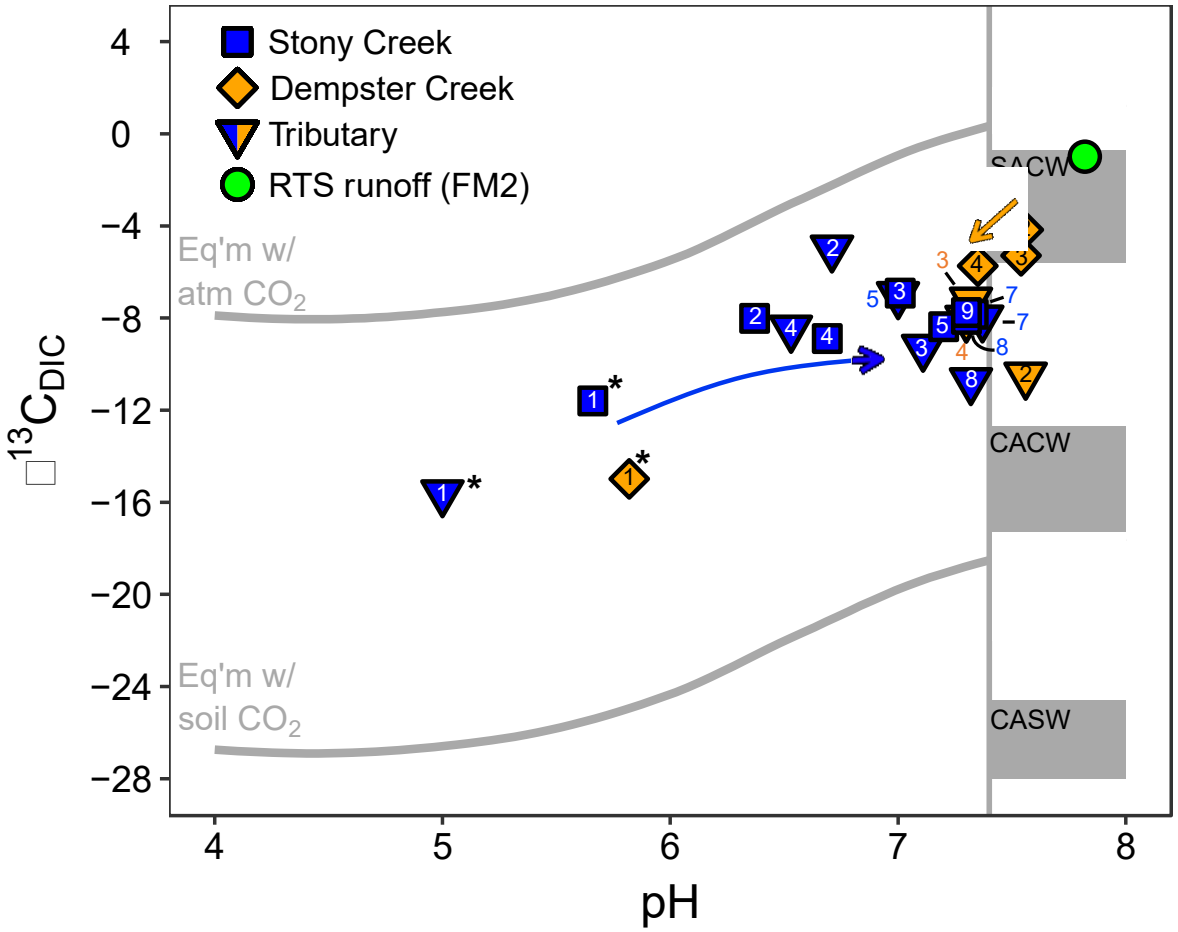

Figure 5-4. The pH and composition of dissolved inorganic carbon stable isotopes ($\delta^{13}C_{DIC}$) in streams. The upper and lower reference lines depict theoretical end-members for equilibrium reactions (mixing with atmospheric and biogenic CO_2, respectively). Gray boxes span theoretical end-member values for kinetically controlled mineral weathering reactions (SACW = H_2SO_4 carbonate weathering, CACW = H_2CO_3 carbonate weathering, CASW = H_2CO_3 silicate weathering). The vertical line corresponds to the pH at which ≥ 90% of DIC is HCO_3^-, for the mean observed stream water temperature (11.7˚C). At pH < 7.4, $\delta^{13}C_{DIC}$ values primarily reflect equilibrium (rather than kinetic) controls on DIC cycling. Arrows reflect increasing downstream distance from the headwaters in the Stony Creek and from the first RTS-affected site in the Dempster Creek. *Site was not affected by retrogressive thaw slumps. Site numbers given within symbols (Table A4-1).

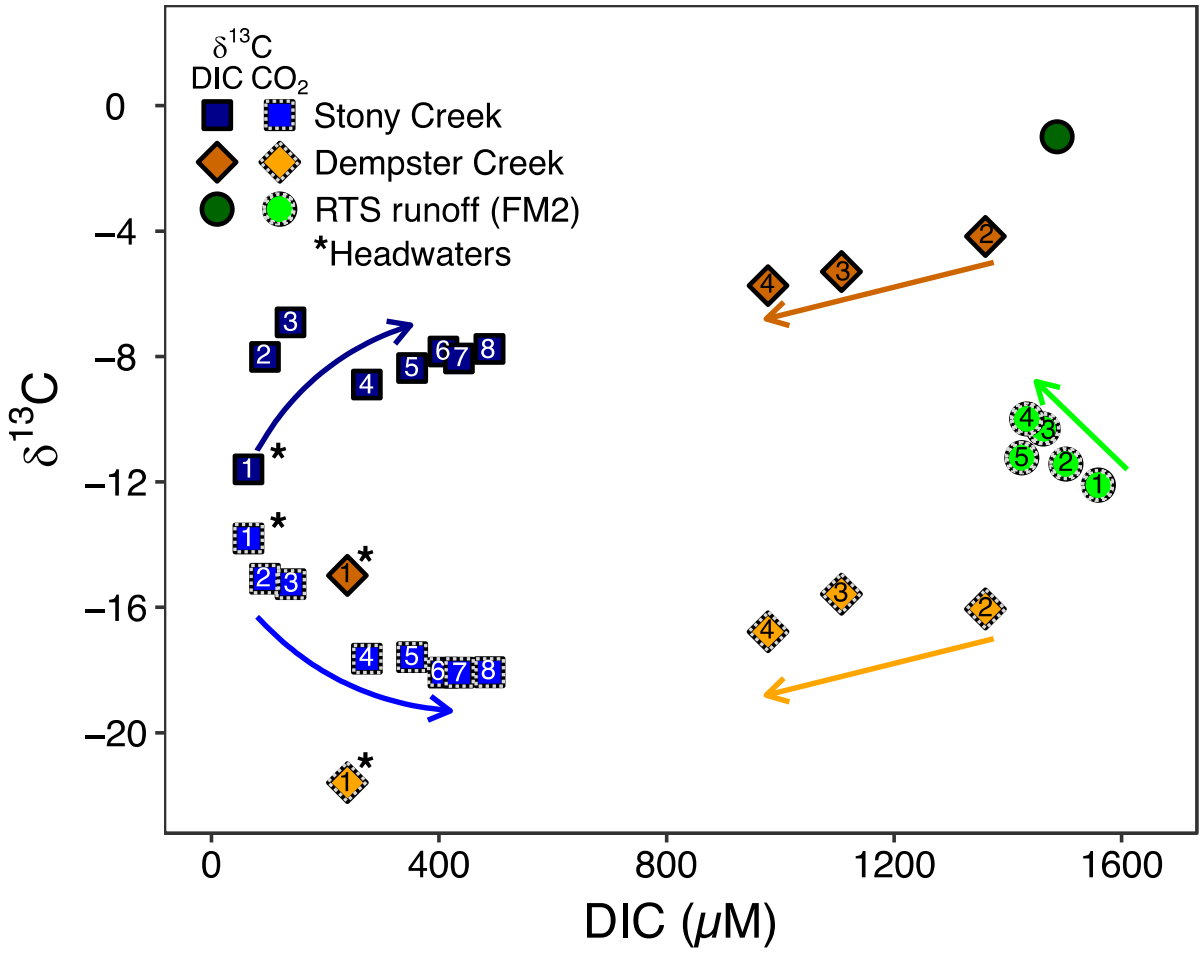

Figure 5-5. The composition of DIC and CO_2 stable isotopes at varying DIC concentrations along the Dempster and Stony Creek mainstems, and in the rill runoff of retrogressive thaw slump (RTS) FM2. Arrows reflect increasing downstream distance from headwaters in the Stony Creek, from the first RTS-affected site in the Dempster Creek, and from the start of the FM2 runoff transect. *Site was not affected by retrogressive thaw slumps. Site numbers given within symbols (Table A4-1).

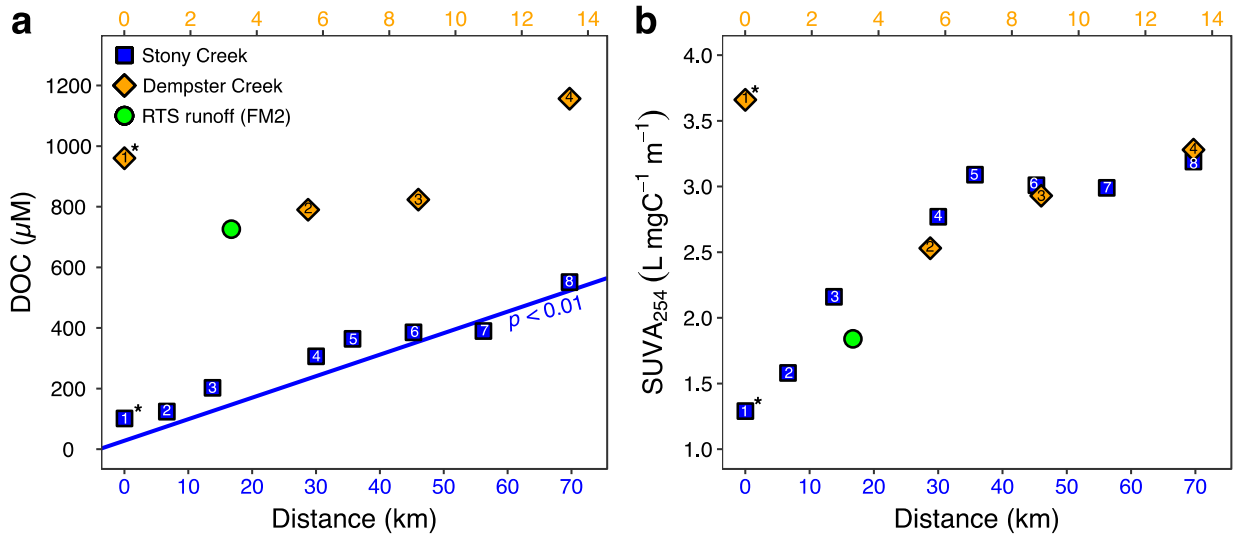

Figure 5-6. Trends in (a) DOC and (b) $SUVA_{254}$ along the mainstem Stony and Dempster Creeks (see locations in Fig. 5-1). Retrogressive thaw slump (RTS) FM2 runoff is a tributary to the Dempster Creek. Note different x-axis scales for the two transects. Regression line in (a) is from the Mann-Kendall test (see text for details). The Dempster Creek enters the Stony Creek at 58.5 km downstream. Site numbers given within symbols (Table A4-1). *Site was not affected by retrogressive thaw slumps.

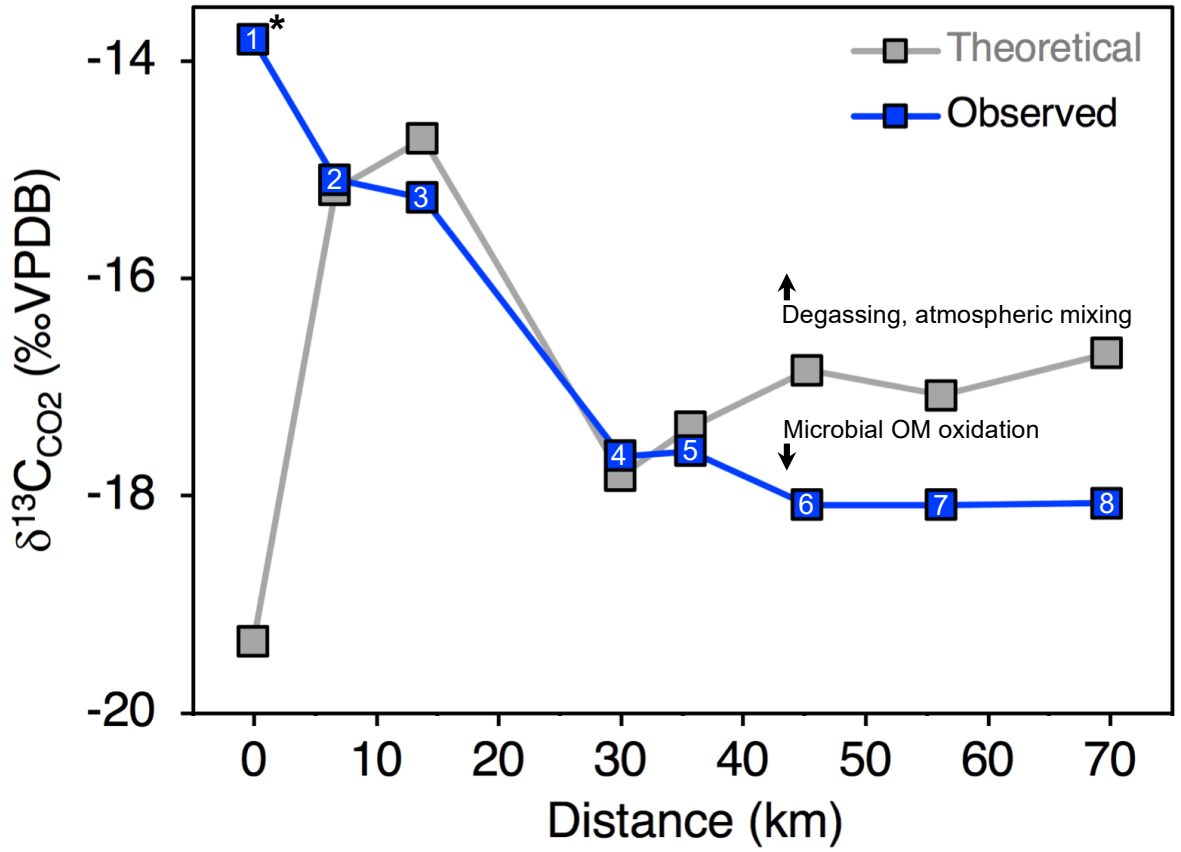

Figure 5-7. Observed and expected $\delta^{13}C_{CO2}$ values along the Stony Creek mainstem. Theoretical $\delta^{13}C_{CO2}$ values were calculated as detailed in Sec. 5.2.6 and reflect changes in CO_2 due to DIC speciation (i.e. $H_2CO_3^* \rightleftharpoons H^+ + HCO_3^-$, equation 5-1). Deviation from theoretical $\delta^{13}C_{CO2}$ values by observed values thus indicates isotopic effects from degassing and/or microbial oxidation of organic matter (OM), as indicated by the arrows. *Site was not affected by retrogressive thaw slumps. Site numbers given within symbols (Table A4-1).

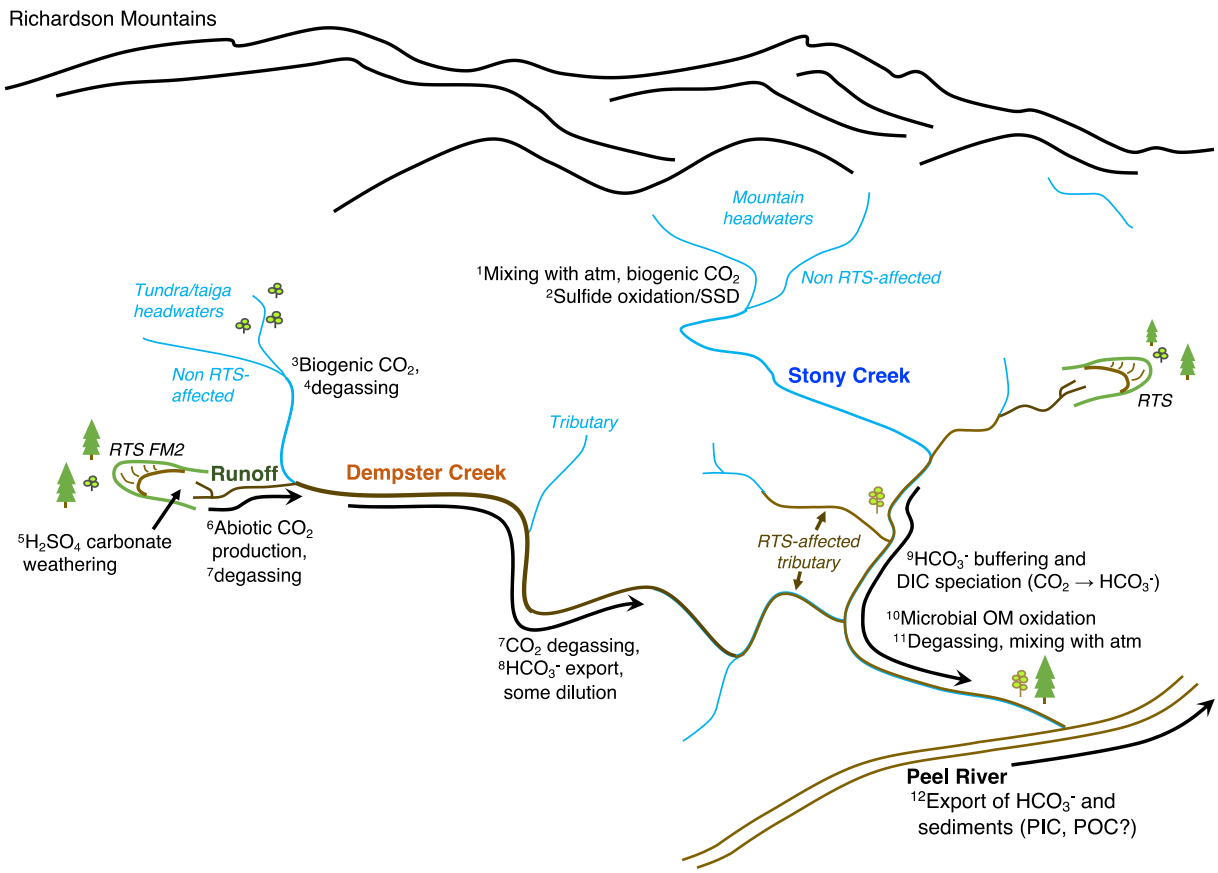

Figure 5-8. Conceptual model of fluvial inorganic carbon cycling in a glaciated thermokarst terrain (Peel Plateau, NWT). Evidence for processes in the diagram are discussed in the main text: [1]Low CO_2, intermediate $\delta^{13}C_{CO2}$; [2]High SO_4^{2-} and ^{13}C-enriched $\delta^{13}C_{DIC}$; [3]Low $\delta^{13}C_{CO2}$; [4]decreasing CO_2; [5]High HCO_3^-, pH, and $\delta^{13}C_{DIC}$; [6,7]Relatively ^{13}C-enriched and increasing $\delta^{13}C_{CO2}$; [8]high but decreasing HCO_3^- and conductivity; [9]Increasing HCO_3^-, pH, and $\delta^{13}C_{DIC}$, and $\delta^{13}C_{CO2}$ reflective of DIC speciation; [10]$\delta^{13}C_{CO2}$ reflective of microbial organic matter (OM) oxidation; [11]Saturated and stable pCO_2; [12]Kokelj et al. (2013), Zolkos et al. (2018).

CH. 6: Divergent Landscape Evolution Shapes Fluvial Chemistry and Carbon Balance in the Western Canadian Arctic

Summary

Global inland waters are a critical nexus in the global carbon (C) cycle because they receive, transport, and transform large amounts of terrestrial C. The fate of fluvial C is of particular interest in northern environments, where C release from thawing permafrost and strengthening land-freshwater linkages are reshaping watershed C cycling. Characterizing fluvial C species balance and export across diverse permafrost landscapes provides an opportunity to constrain the magnitude and drivers of northern C cycling and assess terrain responses to permafrost thaw. Working in a suite of watersheds across permafrost terrains with varying geology, topography, hydrology, vegetation, and thermokarst, we quantified the magnitude and proportions of C species exported in fluvial networks, characterized the hydrochemical and landscape drivers of fluvial C cycling, and estimated fluvial C contributions to ecosystem C balance. Our measurements of stream chemistry and C export (lateral flux and gas efflux to the atmosphere) paired with geospatial analyses revealed gradients of C cycling driven by contrasting landscape conditions. A primary gradient was coupled to terrain relief and broadly separated inorganic from organic processes. In higher-elevation watersheds with more exposed bedrock, bicarbonate dominated fluvial C export (70% of total). In lower elevation and low-relief watersheds, lateral DOC flux (50%) and CO_2 efflux to the atmosphere (25%) dominated, reflecting stronger biotic controls on C cycling across the relatively organic-rich terrains. Watersheds underlain by ice-rich permafrost were intermediate in this gradient, except where thermokarst enhanced carbonate weathering and sediment release by mobilizing mineral-rich tills, revealing a strong gradient across a former glacial margin. From an ecosystem C balance perspective, fluvial C export was equivalent to 8% of CO_2 uptake by terrestrial vegetation, except in the watersheds affected by thermokarst (~1% by area), where fluvial C export was equivalent to nearly 40% of CO_2 uptake by vegetation. Constraining the effects of environmental change on the balance and fate of fluvial C species is a priority for refining models of C cycling across the diversity of landscape types that contribute to the variability in the circumpolar permafrost environment.

6.1. Introduction

Global inland waters are a critical nexus in the global carbon cycle because they receive, transport, and transform large amounts of terrestrial carbon (Drake et al., 2017). Freshwater carbon cycling is of particular interest at northern latitudes, where rapid warming is thawing perennially frozen ground (permafrost) (Biskaborn et al., 2019), increasing vegetation productivity (Myers-Smith et al., 2011; Pearson et al., 2013), intensifying hydrologic cycles (Bring et al., 2016; Rawlins et al., 2010), and strengthening land-freshwater linkages (Vonk, Tank, Bowden, et al., 2015; Walvoord & Kurylyk, 2016). Together, these changes are reshaping the carbon cycle across the circumpolar north. In recent decades, increasing solute fluxes in major northern rivers reflect a thickening of the seasonally-thawed active layer, deepening hydrologic flow paths, and enhanced mineral weathering occurring in concert with climate warming and intensifying precipitation (Drake, Tank, et al., 2018; Tank et al., 2016; Toohey et al., 2016). Coincident changes in the magnitude and drivers of fluvial carbon export thus have profound implications for the role of freshwaters in the northern carbon cycle.

Among the most significant implications of rapid northern warming is the thaw and biogeochemical transformation of large stores of organic carbon contained in permafrost (1,307 ± 170 PgC) (Hugelius et al., 2014) into the greenhouse gases carbon dioxide (CO_2) and methane (CH_4) (Schuur et al., 2015). Recent experiments and measurements in the field show that permafrost dissolved organic carbon (DOC) can be rapidly transformed into CO_2 within fluvial network headwaters (Drake et al., 2015; Drake, Guillemette, et al., 2018; Littlefair & Tank, 2018; Vonk et al., 2013; Ward et al., 2017). Yet, understanding of Arctic fluvial carbon cycling is largely driven by studies in relatively organic-rich terrains. Northern permafrost landscapes show considerable regional variability with respect to the composition of permafrost – including ground ice content (Brown et al., 1997), organic carbon content (Hugelius et al., 2014), and sediments (Schuur et al., 2015) – and also landscape factors which are known to influence fluvial carbon cycling, including hydrology (Walvoord & Kurylyk, 2016), geology (Tank et al., 2012), and vegetation productivity (Berner, 1992; Campeau et al., 2019). For instance, observations of increasing riverine export of alkalinity (includes bicarbonate, HCO_3^-) and DOC in major Arctic rivers (Drake, Tank, et al., 2018; Tank et al., 2016; Toohey et al., 2016) indicate an acceleration of both inorganic and organic carbon cycling across the pan-Arctic watershed. Such changes in riverine carbon export are expected to have strong effects in the Arctic Ocean (AMAP, 2018;

Tank et al., 2012), which contains 1% of the global ocean volume and receives more than 10% of global river discharge (Shiklomanov, 1998). However, the degree to which landscape conditions such as permafrost composition, geology, hydrology, and vegetation productivity influence the balance of inorganic and organic carbon species remains understudied in fluvial network headwaters, especially in relatively inorganic-rich permafrost terrains.

Variability in the composition of permafrost across the circumpolar north is, to a degree, influenced by glacial history (Brown et al., 1997; Hugelius et al., 2014; Zolkos et al., 2018). In North America, the Richardson Mountains in the Yukon and Northwest Territories (Canada) demarcate the western limit of the former Laurentide Ice Sheet (LIS) (Clark et al., 2009; Ehlers et al., 2011). In contrast to the western slopes of the Richardson Mountains, glaciated terrains in the Mackenzie River delta region host ice-and sediment-rich permafrost (Kokelj, Tunnicliffe, et al., 2017) and represent a relatively inorganic-rich end-member on the spectrum of permafrost composition (Hugelius et al., 2014). From the Yukon to the Northwest Territories, glacial history and diverse topographies (i.e. terrain relief) have enabled the divergent evolution of regional landscapes with respect to hydrology and vegetation (Ecosystem Classification Group, 2009, 2010; Smith et al., 2004). Rapid warming and intensifying precipitation are accelerating permafrost thaw-induced terrain subsidence (thermokarst) along glacial margins (Kokelj, Lantz, et al., 2017; Segal et al., 2016a). The gradient of environmental conditions across these diverse terrains provides an ideal setting to determine how contrasting glacial legacies and the divergent evolution of regional permafrost landscapes since the last glacial maximum have given rise to trends in modern-day fluvial chemistry, carbon cycling, and ecosystem carbon balance.

6.2. Methods

6.2.1. Study Sites

We studied four regions along a ~300 km transect from the Richardson Mountains (Yukon Territory) to Inuvik (Northwest Territories): the Richardson Mountains, Peel Plateau, Mackenzie Lowlands, and Travaillant Uplands (Table A5-1, Fig. 6-1). These regions align with previously classified ecoregions which span nearly 150,000 km^2 (Ecosystem Classification Group, 2009, 2010; Smith et al., 2004) and cover an environmental gradient across landscapes with varying glacial history and terrain relief (Kokelj, Tunnicliffe, et al., 2017) and terrain relief (Ecosystem Classification Group, 2009, 2010; Smith et al., 2004).

Unlike the other study regions, the Richardson Mountains region was unglaciated during the last glacial maximum (Slaymaker, 2017) and contains landscapes shaped primarily by mass wasting and weathering during the Pleistocene (Smith et al., 2004). This region has the greatest range in terrain relief (450 to 900 masl), with peaks that reach 1600 masl and exposed outcrops of shale, carbonate, and sandstone bedrock (Norris, 1985; Smith et al., 2004). The Dempster Highway follows a structural and topographic depression which separates uplifted shales in the northern study watersheds (BB-6 to BB-8; Table A5-1) from folded and exposed limestone and sandstone in the southern watersheds (BB-1 to BB-5) (Norris, 1985; Smith et al., 2004). Upper mountain slopes are blanketed by a veneer of mostly unvegetated colluvium which transitions into tussock- and shrub-tundra on pediment surfaces at lower elevations, with stands of white spruce in sheltered environments in larger river valleys (Smith et al., 2004). The soils in this region are relatively acidic and generally high in organic matter and silt, and are associated with continuous permafrost and a seasonally-thawed active layer that extends to roughly 0.5 m (Smith et al., 2004). Air temperatures average 10˚C in the summertime (mean annual = –7.5˚C), when precipitation is heaviest (total annual = 250–400 mm) (Smith et al., 2004).

The Peel Plateau demarcates the western limit of the former LIS and contains permafrost up to 50 m in thickness underlain by sandstone and siltstone bedrock (Kokelj, Tunnicliffe, et al., 2017; Norris, 1985). Following the last glacial maximum in this region (18.5 kybp) (Lacelle et al., 2013), retreat of the LIS emplaced ice- and sediment-rich tills via the burial of glacier ice and development of segregated ground ice (Kokelj, Tunnicliffe, et al., 2017). These tills contain carbonates, sulfides, and silicates (Zolkos et al., 2018) that were likely incorporated into the LIS during its westward expansion across regional carbonate and shale bedrock (Norris, 1985; Stott, 1991). Early Holocene warming (12–8.5 kybp) promoted surficial thaw, mineral weathering, and the accumulation of solutes and organic matter in the upper few meters of soil (Burn, 1997; Kokelj, Tunnicliffe, et al., 2017; Lacelle, 2004; Malone et al., 2013), which were preserved in aggrading permafrost by a cooler climate 7–5.5 kybp (Kokelj, Tunnicliffe, et al., 2017; Lacelle et al., 2013). The modern-day Peel Plateau contains ice-rich hummocky moraine, glaciofluvial, glaciolacustrine, and colluvial deposits (Duk-Rodkin & Hughes, 1992a). Incised valleys and sloping terrain host hundreds of thermokarst features (Kokelj et al., 2013; Lacelle et al., 2015) which evacuate a sediment- and solute-rich slurry of thawed permafrost substrate through rill channels and into streams (Kokelj et al., 2013). While many headwater streams are not

thermokarst-affected, the affected streams propagate thawed materials across watershed scales (Kokelj et al., 2013; Malone et al., 2013). Elevations on the Peel Plateau ranges from 750 masl at the eastern base of the Richardson Mountains to 100 masl west of the Peel River (Kokelj, Tunnicliffe, et al., 2017). The mountain slopes are sparsely vegetated and mainly consist of colluvium from exposed marine shale and sandstone bedrock (Duk-Rodkin & Hughes, 1992a; Norris, 1985), and transition into tussock- and shrub-tundra on the plateau and open spruce forest at lower elevations (Kokelj, Tunnicliffe, et al., 2017).

The Mackenzie Lowlands (elsewhere, "Arctic Red Plain high subarctic ecoregion"; Ecosystem Classification Group, 2009) consist of thousands of small thermokarst lakes and ponds connected by streams across a gently rolling till plain ranging from 25 to 350 masl (Ecosystem Classification Group, 2009). These tills overlie sandstone and shale bedrock (Norris, 1985) and are mantled by organic deposits associated with widespread peatlands and fenlands (Duk-Rodkin & Hughes, 1992a, 1992b), black spruce forest, and willowy fens (Ecosystem Classification Group, 2009). In the nearby hamlet of Fort McPherson, the 1981–2010 mean annual and summer (June-August) air temperatures were –7.3˚C and 13.3˚C, respectively, and total annual precipitation was 298 mm, roughly half of which was rainfall (146 mm) (http://climate.weather.gc.ca/climate_normals).

The Travaillant Uplands contain hummocky till plains and open spruce forest overlying sandstone and shale bedrock (Ecosystem Classification Group, 2009; Norris, 1985). Compared with the Mackenzie Lowlands, the Travaillant Uplands are characterized by slightly higher elevations (50 to 450 masl) and generally better drainage in the focal watersheds across this relatively organic-rich peatland and fenland terrain (Duk-Rodkin & Hughes, 1992b), resulting from lake-fed streams which develop across a stronger elevational gradient. In the nearby town of Inuvik, the 1981–2010 mean annual and summer (June-August) air temperatures were –8.2˚C and 12.2˚C, respectively, and total annual precipitation was 241 mm, roughly half of which was rainfall (115 mm) (http://climate.weather.gc.ca/climate_normals).

Study streams were chosen to represent a range of Strahler stream orders (from 1 to 5, in most regions) and to reflect the diverse environmental conditions in each region. To characterize the summertime climate in each region, we calculated the mean summer air temperature (MSAT, ˚C) and total summer precipitation (TSP, mm) for each region as the daily mean and sum, respectively, for June to August, 2016 from data provided by Environment Canada

(http://climate.weather.gc.ca/) and a Government of Northwest Territories meteorological station located on the Peel Plateau (Fig. 6-1).

6.2.2. Stream Sampling

Streams were visited up to three times each from June to August, 2016 (Table A5-1). During each site visit, water temperature, conductivity, and pH were measured using a pre-calibrated YSI Professional-Plus water quality meter. During each visit, water samples were collected for dissolved inorganic carbon (DIC = $\Sigma[CO_2, HCO_3^-, CO_3^{2-}]$) and dissolved organic carbon (DOC). We additionally sampled for optical analyses of chromophoric dissolved organic matter (CDOM) (specific UV absorbance at 254 nm [$SUVA_{254}$] and slope ratio [S_R]) to characterize organic matter, for dissolved Fe^{3+} to correct $SUVA_{254}$ measurements (detailed below), and for cations (Ca^{2+}, Mg^{2+}, Na^+, K^+) and anions (SO_4^{2-}, Cl^-) to constrain sources of mineral weathering. During each site visit, we also sampled a subset of streams for particulate carbon, to more fully constrain carbon export across these various landscapes, and total dissolved nitrogen (TDN) and dissolved inorganic nitrogen (DIN, $\Sigma[NH_3^+, NO_3^-, NO_2^-]$) to characterize nutrients (Table A5-1). The same subset of streams was also sampled for stable isotopes of DIC and DOC ($\delta^{13}C_{DIC}$, $\delta^{13}C_{DOC}$) to characterize carbon sources. Stable water isotopes ($\delta^{18}O_{H2O}$, $\delta^{2}H_{H2O}$) were sampled at the end of the summer to characterize water sources. While dissolved CO_2 and CH_4 concentrations were sampled during each site visit, CO_2 and CH_4 efflux from streams to the atmosphere was measured twice at each site, at the beginning and end of the summer.

DIC was filtered in the field (0.45 µm polyethersulfone [PES], ThermoFisher) into sealed and pre-evacuated 30 mL glass bottles. Bottles contained 2 g KCl to inhibit microbial activity (Striegl et al., 2001) and were partially back-filled with N_2 to achieve neutral pressure with sample. DIC samples were stored inverted at 20˚C and measured within four months.

Samples for dissolved CO_2 and CH_4 concentrations were collected following the headspace equilibration method (Hesslein et al., 1991) and stored in airtight 60 mL syringes (CO_2) or over-pressurized in pre-evacuated 30 mL glass bottles sealed with baked (60˚C, 12h), gas-inert butyl rubber stoppers (CH_4) (Spawn et al., 2015). Atmospheric gas samples were collected at each site and stored in either an airtight syringe (CO_2) or glass bottle (CH_4). Samples were stored at 20˚C, and analyzed within 10h (CO_2) or nine months (CH_4). The temperature of stream water and air,

atmospheric pressure, and volumetric ratio of sample to atmospheric headspace was recorded for correcting later calculations of CO_2 and CH_4 partial pressures (Tank et al., 2009).

Water samples for DOC, CDOM, ions, nitrogen, and sediments were collected in sample-rinsed 1L HDPE bottles from the center of the stream, as an integrated sample from ~15 cm below the surface to ~1 m depth (Gray & Landers, 2014). Water samples were refrigerated (4˚C, dark) until filtering within 24h through precombusted (450˚C, 4h) and pre-weighed 0.7 µm glass fiber filters (Whatman GF/F), which were saved and stored frozen (–15˚C) for particulate organic carbon (POC) analysis. Filtered subsamples were stored in filtrate-rinsed, acid-washed bottles (10% HCl v/v, 24h), except for anions and optical properties, which were stored in non-acid-washed bottles. DOC subsamples were acidified to pH < 2 with 8M trace metal-grade HCl (Vonk, Tank, Mann, et al., 2015). Subsamples were refrigerated prior to analysis, except for DIN, which was stored frozen.

Water for $\delta^{13}C_{DIC}$ and $\delta^{13}C_{DOC}$ was filtered in the field (0.45 µm PES) into precombusted (5h, 500˚C) glass vials without headspace and sealed with two silicone-teflon septa. $\delta^{13}C$ was refrigerated until analysis within two months. On the rare occasion when sediments prevented filtering water for DIC and $\delta^{13}C$ in the field, samples were collected without headspace in air-tight syringes and stored inverted at 4˚C for 1h, to allow sediments to settle prior to filtering in the laboratory. Stable water isotopes were filtered in the field (0.45µm cellulose-acetate, Sartorius) into 2 mL glass vials without headspace and refrigerated until analysis.

6.2.3. Geochemical Analyses

DIC was measured by gas chromatography following published methods (Stainton, 1973; Zolkos et al., 2018). Briefly, samples were acidified with 1.5 mL of 1 N sulfuric acid and shaken vigorously to convert DIC to CO_2. The concentration of CO_2 was measured in duplicate by gas chromatography (Varian CP3800) and DIC concentration was calculated based on five-point calibration curves (0-40 mg L^{-1}, $R^2 \geq 0.99$) prepared daily using in-house $NaHCO_3$ standards. Standards were prepared in the same fashion as water samples and were run every 10 samples to monitor instrument drift. Peak areas were normalized by the volume of filtrate of each sample and standard.

CO_2 concentration was measured by infrared gas analyzer (PP Systems EGM-4) each day upon returning from the field. The EGM-4 was checked monthly for drift using a 1010 ppm

standard (Scotty Gases). CH_4 was measured in duplicate using a gas chromatograph (Varian CP-3800) equipped with a flame ionization detector. CH_4 concentration was calculated from a four-point calibration curve made daily using commercial standards (Praxair). A CH_4 standard was analyzed every 10 samples to monitor for instrument drift. CO_2 partial pressure (pCO_2) was calculated using Henry's constants corrected for stream water temperature (Weiss, 1974) and CH_4 partial pressure (pCH_4) was calculated following Wiesenburg & Guinasso (1979), each accounting for the ratio of sample volume to headspace during equilibration.

POC concentration was measured by CHN analyzer (Exeter Analytical Inc. CE-440 Elemental Analyzer) at the University of Alberta Biogeochemical Analytical Services Laboratory (BASL, ISO/EIC 17025). Prior to analysis, samples were dried (60˚C, 24h) and fumigated with 12M HCl at room temperature to remove carbonates (Lorrain et al., 2003). POC samples from thermokarst-affected streams (PP-2 and PP-8; Table 6-1) were subject to a more stringent fumigation at 60˚C to remove the dolomite (Whiteside et al., 2011) known to exist within till sediments transported from retrogressive thaw slump (RTS) runoff into streams (Zolkos et al., 2018). Particulate inorganic carbon (PIC) was estimated from particulate samples collected in the same fashion on the Peel Plateau in 2015 (n = 36). For this subset, total carbon and POC were each measured in duplicate by elemental analyzer (Elementar Vario EL Cube or Micro Cube, Analysensysteme GmbH) at the University of California Davis Stable Isotope Facility. PIC was calculated as the difference between total carbon and POC.

DOC was measured by a total organic carbon analyzer using high-temperature combustion (Shimadzu TOC-V). DOC concentration was calculated from a four-point standard curve prepared from a 1,000 ppm KHP solution (ACCUSPEC). A 10 mg L^{-1} caffeine standard was prepared in-house and run every 20 samples to monitor instrument drift.

$\delta^{13}C$ (DIC, DOC) was analyzed by isotope ratio mass spectrometry (Finnigan Mat DeltaPlusXP IRMS) interfaced to a total organic carbon analyzer (OI Analytical Aurora Model 1030W) at the University of Ottawa Stable Isotope Laboratory. To evaluate DIC sources and cycling, we calculated end-member $\delta^{13}C_{DIC}$ values for equilibrium processes (e.g. mixing with atmospheric, biogenic CO_2) and kinetic reactions (mineral weathering) following the literature (Jin et al., 2009; Lehn et al., 2017). Stable water isotopes were analyzed by cavity ringdown spectroscopy (Picarro L2130-i) at the University of Alberta BASL. Calibration curves for stable water isotopes were made from U.S. Geological Survey (USGS) secondary standards (USGS45

and USGS46) and calibrated by an International Atomic Energy Agency standard as a quality control. We used stable water isotopes to calculate d-excess (d-excess = $\delta^2H - 8 \times \delta^{18}O$), which indicates isotopic enrichment by evaporation as a deviation from the global meteoric water line (GMWL) (Hutchins et al., 2019; Tondu et al., 2013; Turner et al., 2014) and thus reflects hydrology and climate effects on water sources and cycling.

Cations and Fe^{3+} were analyzed by optical emission spectrometry (Thermo ICAP-6300) and anions by ion chromatography (Dionex DX-600) at the University of Alberta BASL. TDN and DIN were analyzed at the BASL by flow injection analysis (Lachat QuickChem QC8500), using automated colorimetry to measure NO_3^- and NO_2^-. Dissolved organic nitrogen (DON) was calculated as the difference between TDN and DIN.

UV-visible absorbance was analyzed in duplicate at room temperature using a 1 cm quartz cuvette. Absorbance at 254 and 750 nm was measured within two weeks using a Genesys 10 UV spectrophotometer and absorbance from 200-800 nm was measured within four months using a Horiba Scientific Aqualog-UV-800, to calculate the spectral slope ratio (S_R). MilliQ water blanks were analyzed every ten samples to monitor machine drift. Absorbance at 750 nm and the mean absorbance from 700-800 nm was used to correct each sample for offset due to scattering (Stubbins et al., 2017) for samples measured using the Genesys and Aqualog, respectively. Potential effects from storage time were assessed by comparing the measurements of absorbance at 254 nm from the two instruments. $SUVA_{254}$ (L mgC^{-1} m^{-1}) was calculated as the decadic absorption coefficient at 254 nm (m^{-1}) divided by DOC concentration (Weishaar et al., 2003), using spectra corrected for Fe^{3+} interference (Poulin et al., 2014). The slopes of log-transformed absorbance from 275-295 and 350-400 nm were used to calculate S_R (Helms et al., 2008). $SUVA_{254}$ and S_R can provide useful inference on carbon source. For instance, $SUVA_{254}$ is positively correlated with DOM aromaticity (Weishaar et al., 2003) and higher S_R values reflect relatively lower molecular weight organic matter (Helms et al., 2008). In northern aquatic environments, more biolabile DOM has been shown to have lower $SUVA_{254}$ and higher S_R values (Littlefair & Tank, 2018; Wickland et al., 2012). Photochemical degradation of DOM is also known to increase S_R (Helms et al., 2008; Ward & Cory, 2016).

6.2.4. Fluvial CO_2 and CH_4 Fluxes

During each site visit, we measured stream velocity (RedBack Model RB1, PVD100) and cross-sectional area (Gordon, 2004) to calculate discharge (Q). Measurements were made at increments equal to 10% of stream width (Lurry & Kolbe, 2000). Instantaneous constituent fluxes (concentration*Q) and Q were normalized to watershed area (Sec. 6.2.6) to estimate daily constituent yields (μmol m^{-2} d^{-1}) and water yields (cm d^{-1}). Upscaling from instantaneous to daily estimates assumes constant fluxes and yields over the course of 24h. To constrain uncertainty in our daily flux and yield estimates, we report the site means and standard errors for each parameter.

CO_2 efflux from streams to the atmosphere was measured using an EGM-4 connected to a stationary streamlined chamber (Crawford et al., 2013). The chamber was lowered 2 cm into the stream and connected to the EGM-4 via inert Bev-a-line tubing. CO_2 concentration within the chamber headspace was measured every 15 s for five min and efflux was calculated from the net change in concentration upon reaching a constant rate of increasing CO_2, which typically occurred within the first minute. Prior to each measurement of CO_2 efflux, the concentration of atmospheric CO_2 was measured with the chamber suspended above the stream. Discrete CH_4 samples were collected every five minutes for twenty minutes from a port in the Bev-a-line tubing, and stored and later analyzed in the same fashion as dissolved CH_4 samples (Sec. 6.2.2). Atmospheric CH_4 was collected and stored in 10 mL vials, which were prepared in the same fashion as vials for dissolved CH_4. The efflux (J) of CO_2 (μmol m^{-2} s^{-1}) and CH_4 (nmol m^{-2} s^{-1}) was derived from triplicate and single measurements, respectively (Duc et al., 2013):

$$J = PH\Delta C / RT\Delta t \times c \quad (6\text{-}1)$$

Where P is atmospheric pressure (atm); H is flux chamber height (m); ΔC is the change in headspace gas (ppmv); R is the ideal gas constant (82.0562 mL atm K^{-1} mol^{-1}); T is air temperature (˚K); Δt is measurement duration (s); and c converts from mol to μmol (CO_2) or nmol (CH_4). Gas transfer velocities (k, m d^{-1}) for CO_2 and CH_4 were calculated using J and the concentrations of dissolved gas (mol m^{-3}) in the stream (c_{water}) and in equilibrium with the atmosphere (c_{sat}) (Cole & Caraco, 2001). CO_2 and CH_4 efflux data were quality-checked and 11

CH_4 efflux measurements were omitted, owing to poor linearity (n = 8) and CH_4 loss from the chamber (n = 3) (Table A5-2).

To upscale CO_2 and CH_4 efflux from streams to the atmosphere, we summed the product of J_{CO2} or J_{CH4} and fluvial surface area for each stream order in each watershed (Campeau et al., 2014; Zolkos et al., 2019). Fluvial surface area in each watershed was estimated as the product of mean stream width from field measurements and total stream length from geospatial modeling (Sec. 6.2.5) for each stream order. To constrain the effects of varying J_{CO2}, J_{CH4}, and stream width on upscaled efflux, we report the mean, minimum, and maximum upscaled J_{CO2} and J_{CH4}. For instance, minimum upscaled J_{CO2} was determined by summing the product of minimum observed J_{CO2} and minimum observed fluvial surface area (i.e. the product of minimum observed stream width and total stream length) for each stream order in each watershed.

6.2.5. Geospatial Analyses

To determine landscape controls on C cycling, we characterized watershed hydrology, topography, and surficial and bedrock geology using ArcGIS 10.5, and vegetation productivity (gross primary productivity, GPP) using Google Earth Engine (Gorelick et al., 2017). Geospatial data for lake and pond distribution was obtained from the Natural Resources Canada (NRCan; https://open.canada.ca) National Hydro Network (NHN). ArcHydro tools were used to delineate stream networks and watershed areas for each site from the NRCan gridded (30 m) Canadian Digital Elevation Model (CDEM). CDEM data were first reconditioned using the NHN stream vectors. Prior to reconditioning, the NHN was modified as needed to align with streams visible in Copernicus Sentinel-2 remote sensing imagery (2017; European Space Agency, https://sentinel.esa.int/). Spatial Analyst tools were used to calculate the mean elevation and slope from the (non-conditioned) CDEM. Geospatial data for surficial geology were obtained from Côté et al. (2013) for the Northwest Territories and from Lipovsky & Bond (2014) for the Yukon Territory. To unify the classifications of surficial geology units between the territories, data were reclassified to the highest common categorical resolution, resulting in five units (alluvial, colluvial, fluvial, moraine, and organic deposits). The distribution of bedrock lithologies within each watershed was delineated from a published geological map (Norris, 1985), which was first georeferenced in ArcGIS 10.5. Geological units were categorized as carbonate-bearing (containing limestone, dolomite) and silicate (primarily shale, sandstone, and

siltstone). We quantified lakes/ponds and surficial and bedrock geology units as the percent distribution in each watershed. Soil organic carbon content (SOCC) in the top 100 cm (kgC m^{-2}) (Hugelius et al., 2013) was calculated as the area-weighted mean for each watershed.

To characterize relationships between vegetation productivity and aquatic carbon cycling (e.g. Campeau et al., 2019; Hutchins et al., 2019), we used the gridded (500 m) 16-day GPP (Running et al., 2015) product derived from data collected by the United States National Aeronautics and Space Administration (NASA) moderate resolution imaging spectroradiometer (MODIS). For each watershed (derived in ArcHydro), GPP was calculated as the mean of all collection dates during the summer sampling period which matched our field sampling dates. For instances when MODIS data were not collected on the day we sampled, we calculated GPP for the sampling date using a simple linear regression between the consecutive MODIS samples which bounded our sampling date. Prior to calculating mean GPP, we applied the NHN data as a mask to omit GPP data which overlapped with lakes and ponds from the calculation.

Daily terrestrial net ecosystem exchange (NEE) in our study watersheds was obtained from the NASA EASE-Grid (Kimball et al., 2018) using the USGS AppEEARS online data extraction tool (https://lpdaacsvc.cr.usgs.gov/appeears/). The EASE-Grid provides global gridded (9 km) daily estimates of net ecosystem carbon (CO_2) exchange derived using a terrestrial carbon flux model informed by satellite measurements of ecosystem properties including soil moisture, land cover, and vegetation, and a NASA Earth-observing system model (GEOS-5) (Kimball et al., 2018). We evaluated the performance of mean summertime (June to August 2016) EASE-Grid NEE via comparison with NEE measurements from six AmeriFlux towers located in northern Canada (SCB) and Alaska within environments similar to our field sites (Table A5-3). EASE-Grid NEE data, which have a resolution similar to the scale of our larger watersheds, were extracted for the centroids of our watersheds, which we determined in ArcGIS. For each watershed, we calculated the mean of daily EASE-Grid NEE values within the sampling period (June to August). For comparison with fluvial carbon fluxes (Sec. 6.2.4), we converted NEE in each watershed to kgC d^{-1}, accounting for the surface area of streams and lakes/ponds.

6.2.6. Statistics

To characterize drivers of carbon cycling across the regional environmental gradients, we performed a redundancy analysis (RDA). We included our measurements of gas efflux (J_{CO2},

J_{CH4}) and carbon yield (CO_2, HCO_3^-, PIC, DOC, POC) as dependent variables, and water chemistry (d-excess, temperature, S_R, TDN) and landscape conditions (elevation, slope, GPP, SOCC, percent distribution of carbonate and colluvial surficial geology units, percent distribution of lakes and ponds; Sec. 6.2.5) as explanatory variables. Prior to performing the RDA, values were transformed as needed to improve normality. To simplify the RDA, we performed automated stepwise model selection using the *ordistep* function from the R software (R Core Team, 2018) package *vegan* (Oksanen et al., 2018), which constrains the most parsimonious model via *n* permutations of iterative model covariate selection. We used 5000 permutations and determined the significance of RDA axes and each explanatory variable using the constrained ordination variant of analysis of variance, which is automatically chosen by the *anova* function in R. When linear regression models were used to evaluate relationships between parameters, model fits were first inspected visually using residual and quantile-quantile plots and variables were transformed as needed to meet assumptions of independent and homoscedastic residuals (Zuur, 2009). Data below the detection limit (DL) were analyzed as DL/2 (EPA, 2000). Statistics were performed using R software v.3.4.4 (R Core Team, 2018). Unless noted, values for individual sites are reported as summertime mean ± standard error; values for study regions (n = 4) are reported as the means of individual sites ± standard error; and values across all sites (n = 33) as mean ± one standard deviation (1σ).

6.3. Results

6.3.1. Landscape Characteristics and Stream Chemistry

The 33 focal watersheds in the four study regions captured diverse conditions reflective of the broad environmental gradient across glacial limits and varying terrain relief. Mean watershed slope ranged from 1˚ in the Mackenzie Lowlands to 15˚ in the Richardson Mountains and was positively associated with elevation (Table 6-1). The composition of bedrock and its exposure via surficial geology varied across and within regions. Bedrock consisted mostly of silicate lithologies (Table 6-1) except for the southern sites in the Richardson Mountains (BB-1 to BB-5), where bedrock was primarily carbonate (Table A5-4). Compared with the other study regions, the watersheds in the Richardson Mountains and most on the Peel Plateau had a larger distribution of colluvial surficial deposits. All three study regions east of the Richardson Mountains were dominated by till moraine, with a greater proportion of organic surficial deposits

in the Mackenzie Lowlands and Travaillant Uplands. Lakes and ponds covered, on average, 10 to 20% of the study regions, with varying coverage when comparing between individual watersheds (0 to 41%; Table A5-4). Watersheds in the Travaillant Uplands and Mackenzie Lowlands generally had greater SOCC (30 and 71 kgC m^{-2}, respectively) and GPP (5.8 and 5.7 gC m^{-2} d^{-1}, respectively) than the Peel Plateau and Richardson Mountains (Table 6-1). NEE ranged from –0.60 ± 0.09 gC m^{-2} d^{-1} in the Travaillant Uplands to –0.82 ± 0.02 gC m^{-2} d^{-1} in the Mackenzie Lowlands. Estimates of NEE from EASE-Grid showed good correspondence with measurements from AmeriFlux field towers located in similar environments (Fig. A5-1).

These diverse environmental conditions were reflected by divergent stream water quality and chemistry across a gradient spanning only 300 km. Streams in the Travaillant Uplands and Mackenzie Lowlands were warmer (11.6 ± 0.6 and 13.0 ± 0.6˚C, respectively) and had lower conductivity (82 ± 7 and 95 ± 13 µS cm^{-1}) than streams on the Peel Plateau (7.1 ± 0.7˚C, 149 ± 76 µS cm^{-1}) and Richardson Mountains (5.6 ± 0.6˚C, 255 ± 51 µS cm^{-1}) (Table 6-1). pH was generally highest in the Richardson Mountains (6.86 ± 0.4 pH units), slightly lower in the Mackenzie Lowlands (6.68 ± 0.2) and Travaillant Uplands (6.65 ± 0.2), and lowest on the Peel Plateau (5.31 ± 0.4) (Table A5-5). Across stream sites, Ca^{2+} and HCO_3^- generally comprised a greater proportion of the major ions (Fig. 6-2). SO_4^{2-} was an intermediate proportion of ions in most watersheds of the Richardson Mountains, Peel Plateau, and Travaillant Uplands, and a major proportion in watersheds with greater silicate bedrock coverage in the Richardson Mountain (RM-6, RM-8) and on the Peel Plateau (PP-1) and in RTS-affected sites (PP-2, PP-8). Similar to SOCC and GPP, TDN – which was primarily DON (DON:TDN = 0.85 ± 0.17, mean ± 1σ) – was anticorrelated with mean watershed elevation ($p < 0.00$, $df = 18$, $R^2 = 0.85$), and increased from the Richardson Mountains (18 ± 1 µM) to the Mackenzie Lowlands (52 ± 6 µM).

6.3.2. Carbon Concentration and Quality

Our analysis of a subset of filters from the Peel Plateau for total carbon allowed for an estimate of PIC. For all streams, PIC was determined by analysis of duplicate filters for total carbon and POC concentrations (Sec. 6.2.3) at eight sites sampled two to three times each during summer 2015. Negative PIC values ($n = 4$) and outliers in a plot of PIC versus POC ($n = 3$) were removed. Following this quality-check, we calculated the PIC:POC ratio (0.154 ± 0.08, mean ± 1σ; $n = 36$). We acknowledge that poor carbonate combustion may result in underestimation of

PIC, but use of these ratios enables a first-order estimate of the carbon balance in a region where this has not been previously examined.

Total carbon concentrations (Σ[DIC, PIC, DOC, POC]) were greatest in streams on the Peel Plateau (4400 ± 1970 µM), yet relatively variable owing to RTS-affected streams (Table 6-1, Table A5-3). Excluding the RTS-affected streams, mean total carbon concentrations on the Peel Plateau (1360 µM) were slightly lower than in the other regions (1770 to 4210 µM). The relative importance of individual carbon species varied across the study regions. For instance, HCO_3^- was the dominant carbon species in the Richardson Mountains (1730 ± 450 µM) and around three times greater than in the other regions (Table 6-1). In contrast, DOC was the primary carbon species in the Mackenzie Lowlands (1900 ± 300 µM) and Travaillant Uplands (1510 ± 100 µM). DOC concentrations were anticorrelated with mean watershed elevation ($p < 0.00$, $df = 31$, $R^2 = 0.79$). pCO_2 was consistently supersaturated and greatest in the Mackenzie Lowlands (2700 ± 680 µatm) and roughly half as high in the Richardson Mountains (1300 ± 200 µatm), Peel Plateau (1540 ± 330 µatm), and Travaillant Uplands (1550 ± 390 µatm) (Table 6-1). pCH_4 was typically supersaturated and greatest in the Mackenzie Lowlands (150 ± 30 µatm), but also relatively high and variable on the Peel Plateau (130 ± 60 µatm). Both pCO_2 and pCH_4 varied considerably between individual watersheds within regions (Table A5-5).

Measurements of the gas transfer velocity (k) and efflux (J_{CO2}, J_{CH4}) showed varying rates and magnitudes of gas release from streams to the atmosphere. Mean k_{CO2} ranged from 1.52 to 14.1 m d^{-1} and k_{CH4} from –4.6 to 15.5 m d^{-1} (all sites, $n = 33$). Both k_{CO2} and k_{CH4} were generally greatest in the Richardson Mountains (7.8 ± 1.0 m d^{-1}) and smallest on the Peel Plateau (5.6 ± 0.8 m d^{-1}), but varied between sites in the same region (Table A5-5). J_{CO2} was lowest on the Peel Plateau (3.7 ± 1.3 µmol m^{-2} s^{-1}) and highest in the Mackenzie Lowlands (5.6. ± 1.0 µmol m^{-2} s^{-1}). J_{CH4} was lowest in the Richardson Mountains (14.1 ± 12.6 nmol m^{-2} s^{-1}) and highest on the Peel Plateau (33.1 ± 12.4 nmol m^{-2} s^{-1}), and similarly high but less variable in the Mackenzie Lowlands (30.1 ± 5.4 nmol m^{-2} s^{-1}).

Measurements of absorbance at 254 nm made in the field laboratory using the Genesys 10 UV spectrophotometer and four months later using the Horiba Scientific Aqualog-UV-800 showed strong correspondence (Fig. S2), providing confidence that effects from storage time were minimal. Across all study sites, S_R (0.85 ± 0.05, mean ± 1σ) and $\delta^{13}C_{DOC}$ values (–27.3 ± 0.3‰) were relatively consistent, while $SUVA_{254}$ (3.77 ± 0.58 L mgC^{-1} m^{-1}) and $\delta^{13}C_{DIC}$ (–13.0 ±

4.4‰) values showed greater variability. $\delta^{13}C_{DIC}$ values increased with pH (Fig. 6-3). $\delta^{13}C_{DIC}$ in the RTS-affected site PP-8 (–5.9‰) was more ^{13}C-enriched than in the non-RTS affected headwater site PP-7 (range = –23.1 to 23.6‰). $\delta^{13}C_{DIC}$ values showed a similar degree of variability in the Mackenzie Lowlands (–9.5 to –17.5‰) and Travaillant uplands (–6.1 to –18.4‰), and less in the Richardson Mountains (–8.3 to –11.7‰). d-excess reflected regional variability in water cycling across gradients of climate and hydrology. Relative to the GMWL (slope = 8.0), d-excess showed relatively little deviation in the Richardson Mountains (mean regional d-excess ± standard error = 7.0 ± 0.3) and on the Peel Plateau (8.7 ± 0.1), where MSAT was 11.8˚C and 12.8˚C, respectively (Fig. 6-1). d-excess deviated more strongly from the GMWL in the relatively lake-rich Mackenzie Lowlands (–1.3 ± 1.6) and Travaillant Uplands (1.4 ± 1.7), where MSAT was 14.5˚C and 13.2˚C, respectively. Stream *Q* varied across regions, from 0.16 ± 0.1 $m^3\ s^{-1}$ on the Peel Plateau to 0.53 ± 0.4 $m^3\ s^{-1}$ in the Travaillant Uplands (Table 6-1), and varied between sites in the same region (Table A5-5).

6.3.3. Carbon Cycling Across Regional Environmental Gradients

To facilitate comparisons of carbon cycling across sites with varying *Q* and watershed areas, we calculated yields for total carbon and for individual carbon species (Sec. 6.2.4). For DIC, we focus on CO_2 and HCO_3^- yields to assess variability in DIC species and because CO_3^{2-} was a minor component of DIC (maximum CO_3^{2-}:DIC = 0.003). The regional variability in yields of carbon species followed similar trends as concentrations (Fig. 6-4a,b). In the Richardson Mountains, HCO_3^- accounted for 80% of the total carbon yields, with DOC accounting for most of the remainder (Fig. 6-4). Total carbon yields on the Peel Plateau (12700 ± 4200 μmol $m^{-2}\ d^{-1}$) were more than two times greater and more variable than in the other regions (Table A5-5). In the Peel Plateau streams, organic carbon accounted for 80% of the total carbon yields, most of which was DOC. The Mackenzie Lowlands and Travaillant Uplands were characterized by organic carbon ≥ 75% of the total carbon yields, with HCO_3^- accounting for most of the remainder.

The trimmed (i.e. most parsimonious) redundancy analysis (RDA) retained mean watershed slope, the distribution of carbonate bedrock and colluvium, TDN, GPP, and stream temperature as significant variables. RDA axes one (RDA1) and two (RDA2) were both significant (Table 6-2). Gaseous, dissolved, and particulate carbon species – and, to a degree, the study regions – were generally separated along RDA1 (Fig. 6-5). The Mackenzie Lowlands and Travaillant

Uplands plotted in a cluster of negative values with CO_2 and CH_4 efflux and were associated with greater dissolved carbon yields, warmer water temperatures, more nutrients (TDN), and greater GPP values. In comparison, the Peel Plateau sites plotted with more positive RDA1 values and were more strongly associated with particulate carbon export. Compared with RDA1, RDA2 showed separation between relatively more inorganic (positive values) and organic conditions (negative values). HCO_3^- yields plotted with positive RDA2 values and were associated with carbonate bedrock and greater slope in the Richardson Mountains. The Mackenzie Lowlands and Travaillant Uplands had negative RDA2 values and were associated with greater GPP and SOCC (Table 6-1). Peel Plateau streams plotted with intermediate RDA2 values.

6.3.4. Fluvial Carbon Fluxes in Total and by Species Relative to Net Ecosystem Exchange

The proportional fluxes of individual carbon species (p = species flux / total flux, where total = vertical + horizontal) shows how the types of carbon comprising fluvial fluxes varied across regions. Proportional fluxes were generally greatest for DOC (DOC_p = 0.11–0.51), HCO_3^- ($HCO_3^-{}_p$ = 0.07–0.72), and J_{CO2} (J_{CO2p} = 0.10–0.29), but varied within and across regions (Fig. 6-6a, Table A5-6). The total fluvial carbon flux (ΣJ_{CO2}, J_{CH4}, DIC, DOC, PIC, POC) was equivalent to 3–25% of NEE (Fig. 6-6b, Table A5-6). Lateral carbon fluxes (2–24% of NEE) were greater than vertical fluxes (i.e. upscaled J_{CO2} and J_{CH4}), which were roughly equal to 1% of NEE across watersheds (Table A5-6).

On a regional basis, total fluvial carbon fluxes in the Richardson Mountains (1451 ± 905 kgC d^{-1}) were equivalent to ~10% of NEE (0.12 ± 0.02) (Table A5-6). Lateral fluxes were greatest for DIC ($HCO_3^-{}_p$ = 0.71 ± 0.03), with a smaller proportion from CO_2 efflux (J_{CO2p} = 0.14 ± 0.05) and DOC (DOC_p = 0.11 ± 0.03).

On the Peel Plateau, total fluvial carbon fluxes (1778 ± 1667 kgC d^{-1}) were generally low relative to NEE, except in a first-order watershed (PP-7, 37%) with relatively high DOC flux and for both of the RTS-affected streams, where lateral carbon fluxes were equivalent to ~37–39% of NEE (Table A5-6). Considering all sites on the Peel Plateau, total fluvial carbon fluxes were equivalent to ~25% of NEE (0.25 ± 0.08). For all streams on the Peel Plateau, roughly three quarters of the total carbon flux occurred as lateral fluxes of organic carbon (DOC_p = 0.47 ± 0.15, POC_p = 0.30 ± 0.16), whereas lateral fluxes of inorganic carbon (combined CO_{2p}, $HCO_3^-{}_p$,

$PIC_p \cong 0.15$) and vertical efflux of CO_2 and CH_4 were smaller (combined J_{CO2p} and $J_{CH4p} \cong 0.10$) (Table A5-6). In RTS-affected streams, lateral fluxes of POC were roughly ten times greater ($POC_p \cong 0.68$) than in non-RTS affected streams, where DOC dominated carbon fluxes (DOC_p range = 0.60–0.86) (Table A5-6).

The total fluvial carbon fluxes in the Travaillant Uplands (1963 ±1327 kgC d^{-1}) and Mackenzie Lowlands (1678 ±1003 kgC d^{-1}) were equivalent to ~3% and 6% of NEE, respectively (Table A5-6). In the Travaillant Uplands, DOC accounted for roughly half of the total fluvial carbon flux ($DOC_p = 0.52 \pm 0.03$, mean ± standard error) and CO_2 efflux to the atmosphere for one-fourth ($J_{CO2p} = 0.23 \pm 0.04$) (Fig. 6-6a, Table A5-6). The Mackenzie Lowlands showed similar trends ($DOC_p = 0.48 \pm 0.08$, $J_{CO2p} = 0.29 \pm 0.05$) and, in both regions, HCO_3^- was a larger component ($HCO_3^-{}_p \cong 0.17$) than particulate carbon and methane efflux (ΣPOC_p, PIC_p, $J_{CH4p} \lesssim 0.05$).

6.4. Discussion

Glaciated landscapes in northwestern Canada have evolved considerably since the last glacial maximum (Kokelj, Tunnicliffe, et al., 2017). Our measurements of carbon export paired with stream chemistry and geospatial measurements of terrain conditions reveal how the divergent evolution of regional landscapes has shaped modern-day fluvial chemistry and carbon balance. These findings help to constrain the role of fluvial carbon cycling in ecosystem carbon balance and indicate that future warming and intensifying precipitation at northern latitudes (Rawlins et al., 2010; Stocker et al., 2013) will likely enhance the divergence of fluvial carbon cycling in northwestern Canada and across the circumpolar north.

6.4.1. Regional Sources and Drivers of Carbon Cycling

The RDA revealed associations between carbon yields and landscape characteristics across the regional environmental gradients (Fig. 6-5). RDA1 broadly reflected a gradient of the species of carbon exported from watersheds along the x-axis, from gaseous to dissolved and particulate carbon, whereas RDA2 reflected a gradient of terrain controls on C cycling from high to low relief. This gradient aligned with a greater proportion of carbonate lithologies in the higher-elevation Richardson Mountains region and also broadly corresponded with a greater proportion of colluvium, reflecting greater physical erosion where terrain relief (slope) was greater.

The trends in ions, $\delta^{13}C_{DIC}$, and pH aligned with the RDA results and reflected contributions from biotic and abiotic processes to DIC across the study regions. Major ions indicated that carbonate weathering was generally more prevalent than silicate weathering, and that sulfide oxidation and/or sulfate salt dissolution were relatively stronger in the subset of streams in the Richardson Mountains and on the Peel Plateau which lay north of the structural depression (shale-dominated RM-6, RM-8) and in thermokarst-affected streams (PP-2, PP-8) (Fig. 6-2). In the southern watersheds of the Richardson Mountains study region, $\delta^{13}C_{DIC}$ values and high HCO_3^- yields relative to the other carbon species indicate that carbon cycling was driven by H_2CO_3 weathering of exposed carbonate bedrock (Fig. 6-3). In the Richardson Mountains, HCO_3^- yields alone were nearly double the total carbon yields in the Mackenzie Lowlands and Travaillant Uplands, suggesting that CO_2 consumption via H_2CO_3 weathering of exposed carbonate bedrock across similar terrains in the southern Peel River watershed (e.g. Beaulieu et al., 2012) may, to some degree, counterbalance CO_2 release in other regions of the watershed.

In contrast, ions on the Peel Plateau reflected HCO_3^- production from H_2SO_4 carbonate weathering, which is a CO_2 source over geological timescales (Calmels et al., 2007). $\delta^{13}C_{DIC}$ further revealed contributions from biotic CO_2 to DIC. Relative to the other study regions, contributions of particulate carbon from RTS-affected streams accounted for a large proportion of the total carbon concentrations and yields. Thermokarst on the Peel Plateau, which can increase fluvial sediment fluxes by orders of magnitude (Kokelj et al., 2013), was reflected by the high particulate carbon concentrations in RTS-affected PP-2 and PP-8 and the strong thermokarst-driven gradient along RDA1. While particulate carbon yields in both of the RTS-affected streams on the Peel Plateau were nearly two orders of magnitude greater than in the other (i.e. non RTS-affected) sites, only RTS-affected site PP-8 had much greater HCO_3^- yields. This aligns with the understanding that shallow thermokarst on the Peel Plateau (e.g. upstream of PP-2) mobilize a greater proportion of surficial organics from the Holocene permafrost and active layer compared with deeper thermokarst (e.g. upstream of PP-8), which unearth carbonate-bearing tills and thus amplify carbonate weathering and HCO_3^- production (Zolkos et al., 2018). These results further indicate that, regardless of thaw depth, RTSs on the Peel Plateau simply mobilize large amounts of carbon sediments into fluvial networks.

Ions indicate that H_2CO_3 drove carbonate weathering in the Mackenzie Lowlands, likely in association with acid production from soil organic matter oxidation and plant root respiration

(Berner, 1992) activity in this more biologically active region (e.g. high GPP). $\delta^{13}C_{DIC}$ values in the Mackenzie Lowlands also indicate contributions from a ^{13}C-depleted (biotic) CO_2 source (Fig. 6-3) and, together with the high DOC, pCO_2, TDN, and SOCC, support the interpretation that strong soil-stream linkages (e.g. Campeau et al., 2018) fuel summertime carbon cycling in this relatively carbon- and nutrient-rich landscape. Higher S_R values and lower Q relative to the Richardson Mountains and Peel Plateau suggest that greater residence time in the slower-moving waters across this lake-rich landscape promote relatively more photodegradation of CDOM. Together, these factors likely drove higher pCO_2 and thus J_{CO2} (e.g. Rocher-Ros et al., 2019) in the Mackenzie Lowlands.

Similar to the Mackenzie Lowlands, trends in stream chemistry in the Travaillant Uplands indicated that carbon cycling in this relatively lake- and organic carbon-rich terrain was driven by biotic processes. However, compared with the Mackenzie Lowlands, the lower SOCC and low abundance of carbonate lithologies coupled with low runoff in this region suggest that interactions between terrestrial carbon and flowing waters are currently relatively more limited in this terrain, as reflected by the lower total carbon concentrations (Table 6-1) and yields (Table A5-5).

6.4.2. Implications for Ecosystem Carbon Balance in a Changing Arctic

This work builds on current understanding of the role of northern freshwaters (e.g. Humborg et al., 2010; Striegl et al., 2007, 2012) and thermokarst effects (Abbott & Jones, 2015) on ecosystem carbon balance. Our measurements of fluvial carbon flux combined with estimates of NEE reveal that vegetation productivity in all watersheds assimilated more carbon than was effluxed from streams to the atmosphere or was exported laterally via fluvial networks. Our estimate that fluvial carbon flux across our study regions was equivalent to 3–25% of carbon uptake by terrestrial vegetation encompasses estimates for Sweden (10%) (Humborg et al., 2010) and the Yukon River basin (~15%) (Striegl et al., 2007, 2012), where CO_2 efflux to the atmosphere accounts for roughly 20 and 50% of total fluvial carbon export, respectively. In our study regions, the ratio of vertical (efflux) to lateral carbon export were generally higher in the Travaillant Uplands (0.36 ± 0.1) and Mackenzie Lowlands (0.43 ± 0.1) than on the Peel Plateau (0.13 ± 0.1) and in the Richardson Mountains (0.17 ± 0.1) (Table A5-5). Future changes in the magnitude of fluvial carbon export, the proportion of fluvial carbon effluxed to the atmosphere,

and the degree to which carbon exported laterally through fluvial networks represents a carbon sink or source have profound implications for the regional carbon balance.

In the Richardson Mountains study region, the relatively high HCO_3^- yields indicate that H_2CO_3 carbonate weathering is a significant regional CO_2 sink over millennial timescales (e.g. Beaulieu et al., 2012). Across the circumpolar north, intensified denudation is likely to enhance abiotic CO_2 consumption where carbonate weathering is not coupled with sulfide oxidation. For instance, regions where accelerating bedrock erosion, permafrost thaw, and glacial retreat expose carbonates are likely to be particularly strong CO_2 sinks (St. Pierre et al., 2019; Zolkos et al., 2018). While DIC accounts for the majority of Arctic riverine carbon export (Tank et al., 2012), studies on organic carbon dynamics have driven research on Arctic freshwater carbon cycling. Bringing abiotic processes into our conceptualization of permafrost carbon-climate feedback will be particularly important for constraining ecosystem carbon balance, particularly in glaciated environments across the circumpolar north (Zolkos et al., 2018).

Consistent with previous studies (e.g. Humborg et al., 2010; Striegl et al., 2007, 2012), our results suggest that vegetation productivity in northern environments counterbalances fluvial carbon export. Yet, biomass production is not expected to offset future carbon release associated with permafrost thaw and wildfire (Abbott et al., 2016). Our measurements of fluvial carbon export on the Peel Plateau offer a striking glimpse of this expectation: in watersheds affected by thermokarst (~1% by area), particulate carbon export was equivalent to nearly 40% of net CO_2 uptake by vegetation. While particulate carbon is considered a long-term carbon sink (Bröder et al., 2018, 2019; Galy et al., 2015; Hemingway et al., 2019; Hilton et al., 2015), there is limited understanding of its transformation within Arctic fluvial networks. The degree to which particulate carbon export increases with thermokarst activity has largely untested ramifications for ecosystem carbon balance on the Peel Plateau and in glacial margins across northern Canada, where rapid warming and intensifying precipitation are renewing widespread deglaciation (Kokelj et al., 2013; Lantz & Kokelj, 2008; Lewkowicz & Way, 2019; Rudy et al., 2017; Segal et al., 2016a). Investigating particulate carbon export (e.g. Wild et al., 2019) and biogeochemical transformation (e.g. microbial oxidation of POC, chemical weathering of PIC; Striegl et al., 2012) across a range of watershed scales – and its fate in deltaic (Vonk et al., 2016) and marine environments (Bröder et al., 2018, 2019; Martens et al., 2018) – is a clear priority for constraining the effects of thermokarst on ecosystem carbon balance.

In the Mackenzie Lowlands and Travaillant Uplands, where DOC and J_{CO2} were greatest, coupling between biotic-organic processes and changing landscape conditions will likely drive the evolution of carbon cycling in these relatively low-relief, organic- and lake-rich terrains. Northern lakes are generally considered to be sources of carbon to the atmosphere, yet the degree to which thermokarst enhances permafrost carbon oxidation in lacustrine environments varies across circumpolar landscapes (Bogard et al., 2019; Serikova et al., 2019; Walter Anthony et al., 2016). For instance, in the Mackenzie River delta, substantial macrophyte photosynthesis results in a summertime CO_2 sink in lakes not affected by thermokarst (Tank et al., 2009). This regional lacustrine CO_2 sink may be counteracted somewhat by increased organic matter respiration and delivery of allocthonous organic carbon from surrounding soils into streams (e.g. Wauthy et al., 2018). Yet, streams in these regions comprise a relatively small proportion of the aquatic surface area. Including lacustrine and ebullitive fluvial CO_2 and CH_4 efflux and direct field measurements of NEE, and constraining effects of seasonality would help future efforts to refine our estimates of fluvial contributions to ecosystem carbon balance.

6.5. Conclusions

In northwestern Canada, the development of terrain relief and continental glaciation over geological timescales preconditioned the divergent Holocene evolution of regional landscapes. Our observations of regional variability in the drivers and magnitude of carbon cycling reflect the culmination of this change and suggest that constraining the magnitude of fluvial carbon export in warming northern permafrost regions (e.g. Plaza et al., 2019) and the transformation of permafrost carbon across the terrestrial-freshwater-marine continuum (Vonk, Tank, Bowden, et al., 2015) are top research priorities for refining estimates of northern ecosystem carbon balance.

Table 6-1. Watershed Characteristics, Water Quality and Chemistry, Discharge, and CO_2 and CH_4 Efflux in the Four Study Regions (Regional Mean ± Standard Error).

Parameter	Units	Richardson Mountains	Peel Plateau	Mackenzie Lowlands	Travaillant Uplands
Slope	˚	14.8 (2.1)	5.7 (1.4)	0.8 (0.1)	1.2 (0.2)
Elevation	masl	815 (35)	503 (68)	88 (12)	156 (14)
Area	km^2	27.6 (16)	6.0 (5)	61.7 (24)	101.5 (74)
Carbonate	%	60 (18)	0 (0)	0 (0)	0 (0)
Silicate	%	40 (18)	100 (0)	100 (0)	100 (0)
Colluvial	%	93 (3)	40 (18)	0 (0)	0 (0)
Fluvial	%	6 (3)	0 (0)	0 (0)	0 (0)
Moraine	%	0 (0)	60 (18)	60 (9)	92 (4)
Organic	%	1 (1)	0 (0)	39 (9)	7 (4)
Lakes/ponds	%	0 (0)	0 (0)	18 (7)	7 (2)
SOCC	$kgC\ m^{-2}$	16.3 (3.9)	21.4 (0.2)	70.5 (2.1)	29.8 (5.2)
GPP	$gC\ m^{-2}\ d^{-1}$	3.3 (0.2)	5.5 (0.2)	5.7 (0.3)	5.8 (0.2)
NEE	$gC\ m^{-2}\ d^{-1}$	-0.65 (0.02)	-0.70 (0.03)	-0.82 (0.02)	-0.60 (0.09)
Stream temp.	˚C	5.6 (0.6)	7.1 (0.7)	13.0 (0.6)	11.6 (0.6)
Conductivity	$\mu S\ cm^{-1}$	255 (51)	149 (76)	95 (13)	82 (7)
pH	pH units	6.86 (0.4)	5.31 (0.4)	6.68 (0.2)	6.65 (0.2)
DIC	µM	1816 (456)	298 (102)	776 (85)	578 (39)
CO_2	µM	82 (14)	90 (19)	131 (34)	81 (21)
HCO_3^-	µM	1728 (451)	207 (109)	644 (90)	497 (48)
PIC	µM	4 (1)	382 (255)	9 (2)	15 (10)
DOC	µM	325 (75)	1051 (198)	1899 (303)	1507 (104)
POC	µM	24 (8)	2483 (1654)	56 (16)	99 (62)
Total carbon	µM	3268 (174)	4389 (1973)	2948 (383)	2171 (244)
S_R	–	0.83 (0.02)	0.83 (0.01)	0.90 (0.01)	0.86 (0.01)
TDN	µM	18.4 (1.4)	29.4 (5.1)	52.4 (5.8)	37.0 (4.4)
$\delta^{13}C_{DIC}$	‰VPDB	-9.8 (0.9)	-14.8 (2.4)	-13.4 (1.4)	-13.7 (1.9)
$\delta^{13}C_{DOC}$	‰VPDB	-27.3 (0.0)	-27.1 (0.1)	-27.5 (0.1)	-27.4 (0.0)
d-excess	–	7.0 (0.3)	8.7 (0.1)	-1.3 (1.6)	1.4 (1.7)
Runoff	$cm\ d^{-1}$	0.26 (0.05)	0.45 (0.10)	0.05 (0.01)	0.05 (0.01)
pCO_2	µatm	1298 (202)	1535 (325)	2699 (680)	1554 (389)
k_{CO2}	$m\ d^{-1}$	7.8 (1.0)	5.6 (0.8)	6.0 (1.2)	6.6 (1.3)
J_{CO2}	$\mu mol\ m^{-2}\ s^{-1}$	4.3 (0.6)	3.7 (1.3)	5.6 (1.0)	4.5 (1.9)

pCH_4	µatm	42 (38)	132 (57)	151 (29)	92 (60)
k_{CH4}	m d^{-1}	4.2 (2.3)	0.8 (0.2)	0.8 (0.2)	2.5 (1.6)
J_{CH4}	nmol m^{-2} s^{-1}	15.5 (12.5)	51.1 (22.6)	30.1 (5.4)	20.4 (6.1)

See Table A5-5 for means ± standard error for each site. RM = Richardson Mountains, PP = Peel Plateau, ML = Mackenzie Lowlands, TU = Travaillant Uplands. Elevation, Slope, and Area = watershed elevation, slope, and area. Carbonate and Silicate = distribution of carbonate and silicate bedrock, respectively (Norris, 1985). Colluvial, Fluvial, Moraine, Organic = distribution of surficial geology deposits (Côté et al., 2013; Lipovsky & Bond, 2014). Distribution of lakes and ponds from Natural Resources Canada (https://open.canada.ca). SOCC = soil organic carbon content (Hugelius et al., 2013). GPP = gross primary productivity (Running et al., 2015). NEE = net ecosystem exchange (Kimball et al., 2018). See Methods for details.

Table 6-2. Summary of the Significance of Landscape Covariates and Redundancy Analysis (RDA) Axes from the RDA of Carbon Export, Stream Chemistry, and Landscape Characteristics.

	p	***F***	**Variance**
Covariate			
Carbonate	0.001	20.0	5.14
Stream temperature	0.001	10.1	2.59
Slope	0.003	6.0	1.55
GPP	0.005	6.2	1.58
TDN	0.049	3.0	0.77
Colluvial	0.105	2.3	0.60
Residual	–	–	2.82
RDA axis			
RDA1	0.001	33.5	8.60
RDA2	0.001	9.7	2.49
RDA3	0.215	3.4	0.88
RDA4	0.912	1.0	0.25
RDA5	1.000	0.0	0.01
RDA6	1.000	0.0	0.00
Residual	–	–	2.82

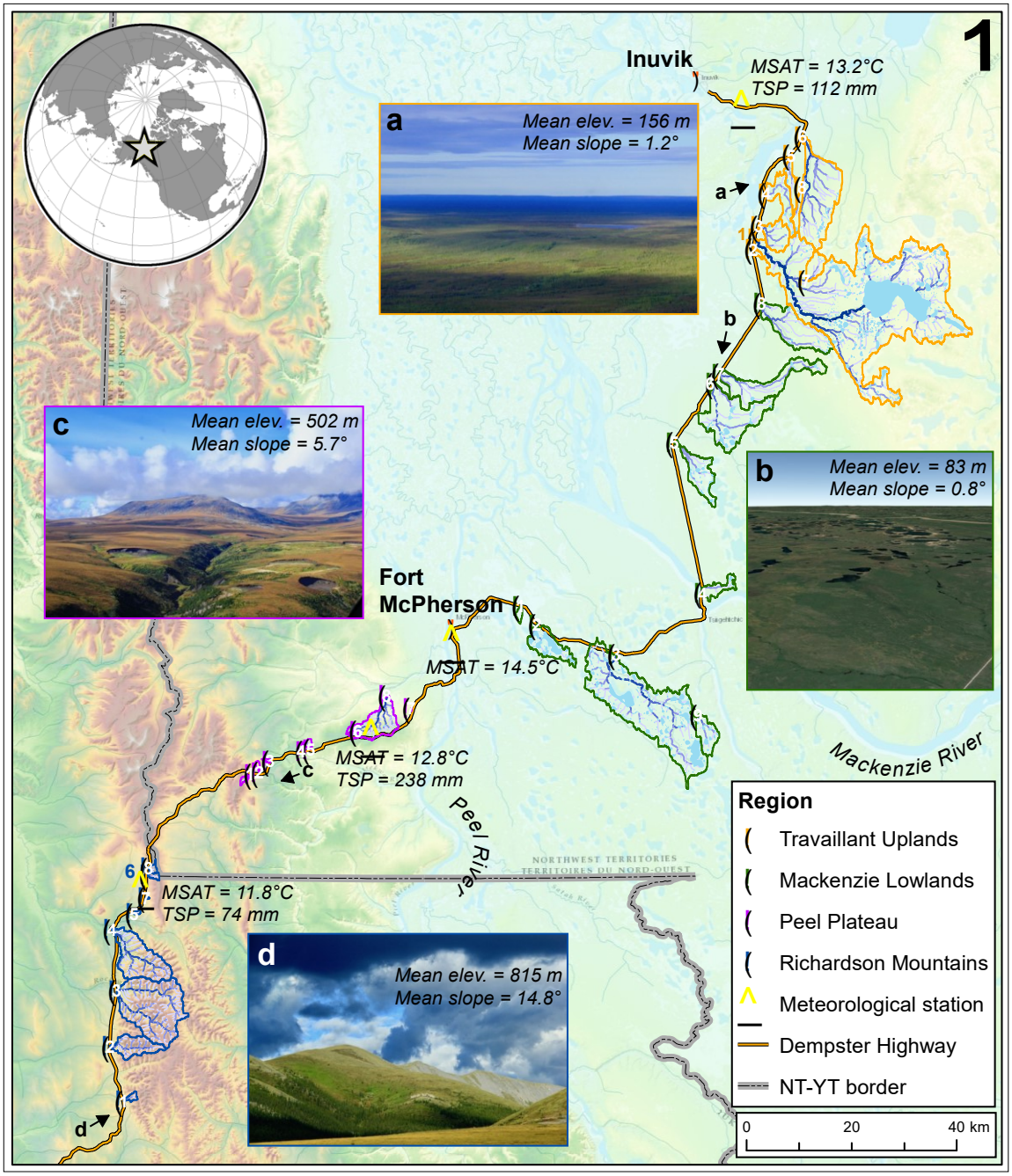

Figure 6-1. Map of study regions and sites. Site numbers are shown within or adjacent to symbols. Approximate locations and directions of inset photos indicated by corresponding letters and arrows. Inset (b) taken from Google Earth. MSAT = mean summer air temperature and TSP = total summer precipitation (summer = June, July, August). See Methods for sources of climate and topography data. Base map from ESRI ArcGIS Online.

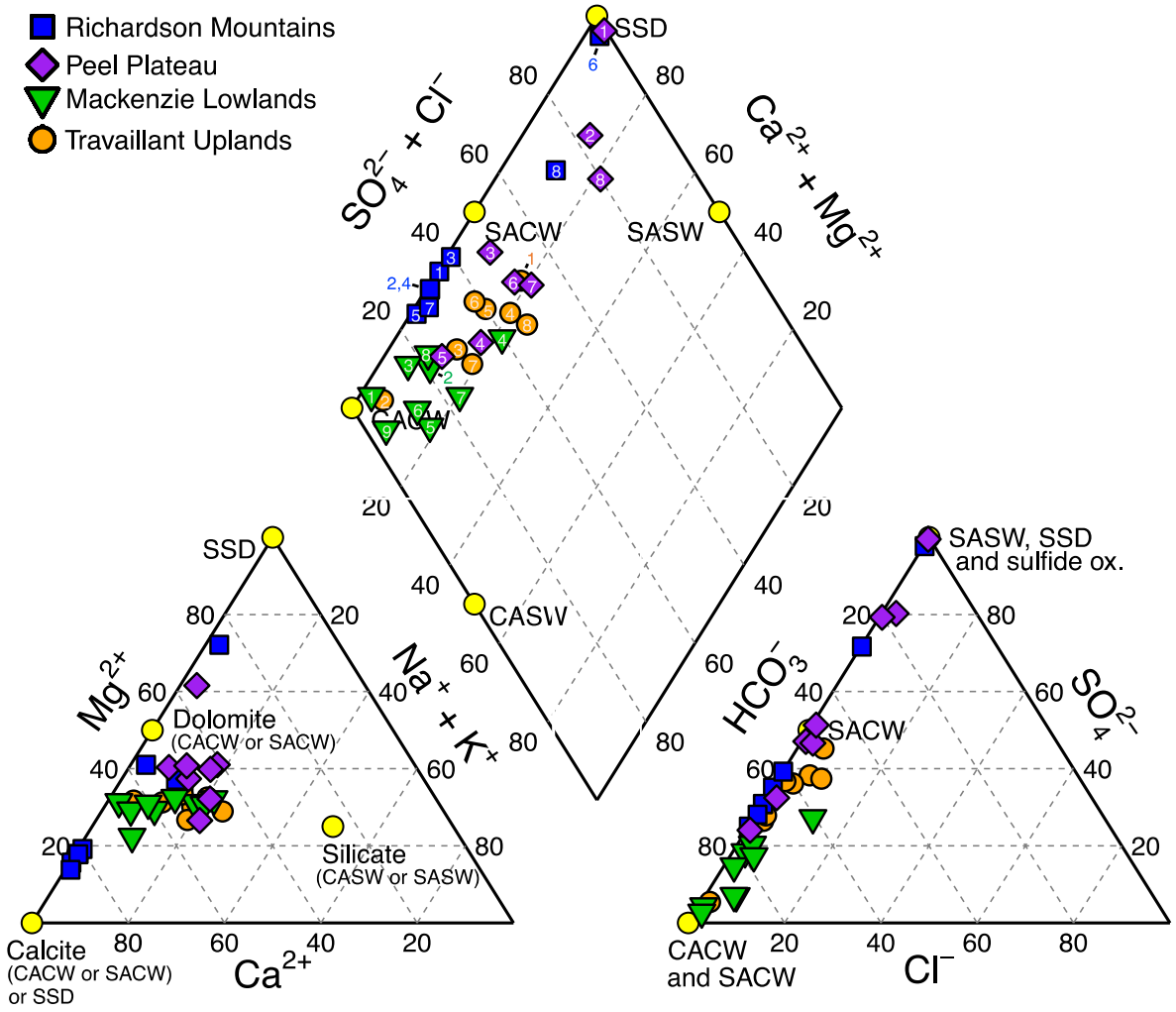

Figure 6-2. Piper diagram showing stream geochemistry (as proportions of ion equivalent concentrations). CACW = H_2CO_3 carbonate weathering, SACW = H_2SO_4 carbonate weathering, CASW = H_2CO_3 silicate weathering, SASW = H_2SO_4 silicate weathering, SSD = sulfate salt (gypsum) dissolution. End members determined from equations in the text. Site numbers shown within symbols of upper diamond plot (Table A5-1).

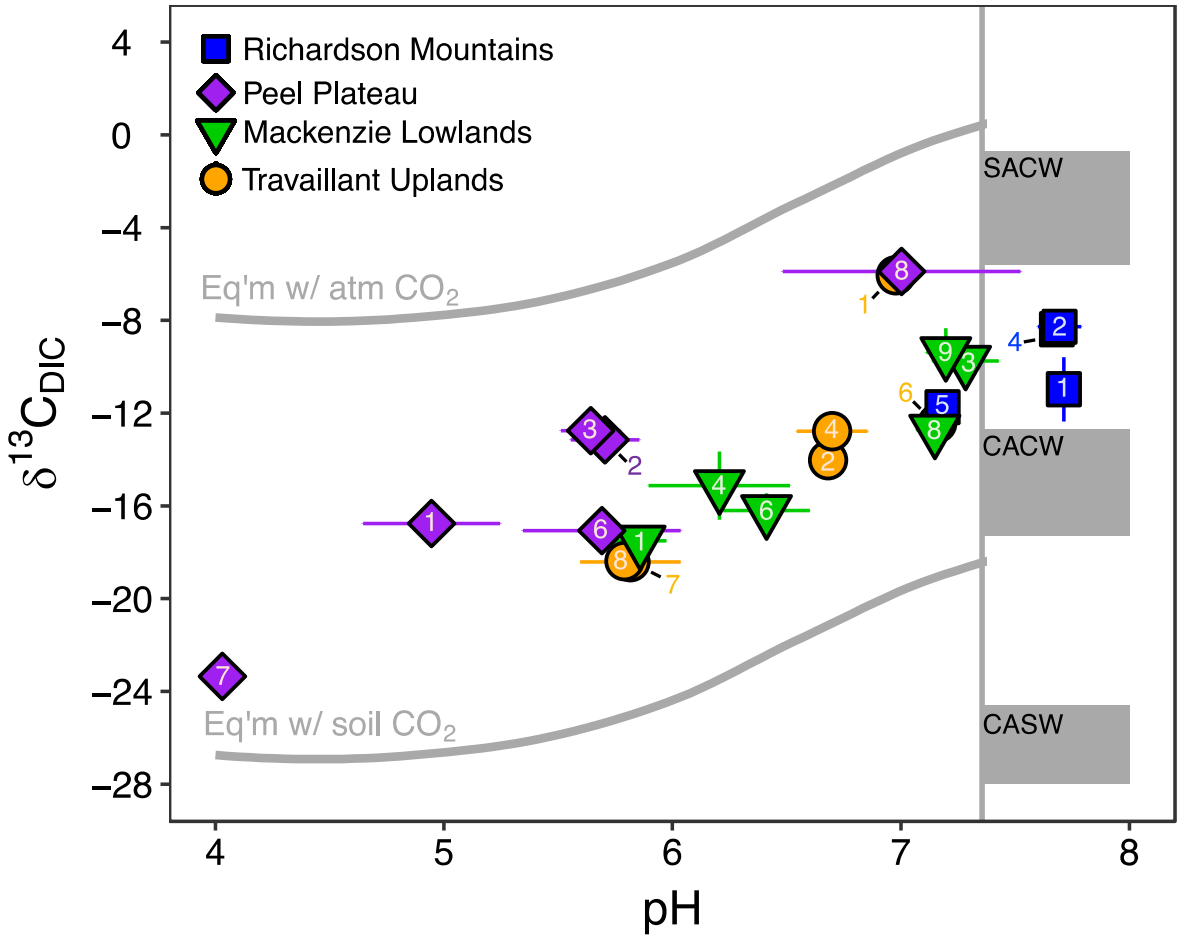

Figure 6-3. The mean pH and composition of stable dissolved inorganic carbon isotopes ($\delta^{13}C_{DIC}$) in streams. Error bars represent range and in some cases are smaller than the symbol (*n* = 2 for most points). Reference lines depict theoretical end-members for equilibrium reactions with atmospheric and biogenic CO_2. Gray areas span theoretical end-member values (Sec. 6.2.3) for kinetically controlled mineral weathering reactions. SACW = H_2SO_4 carbonate weathering; CACW = H_2CO_3 carbonate weathering; CASW = H_2CO_3 silicate weathering. Site numbers shown within points (Table A5-1).

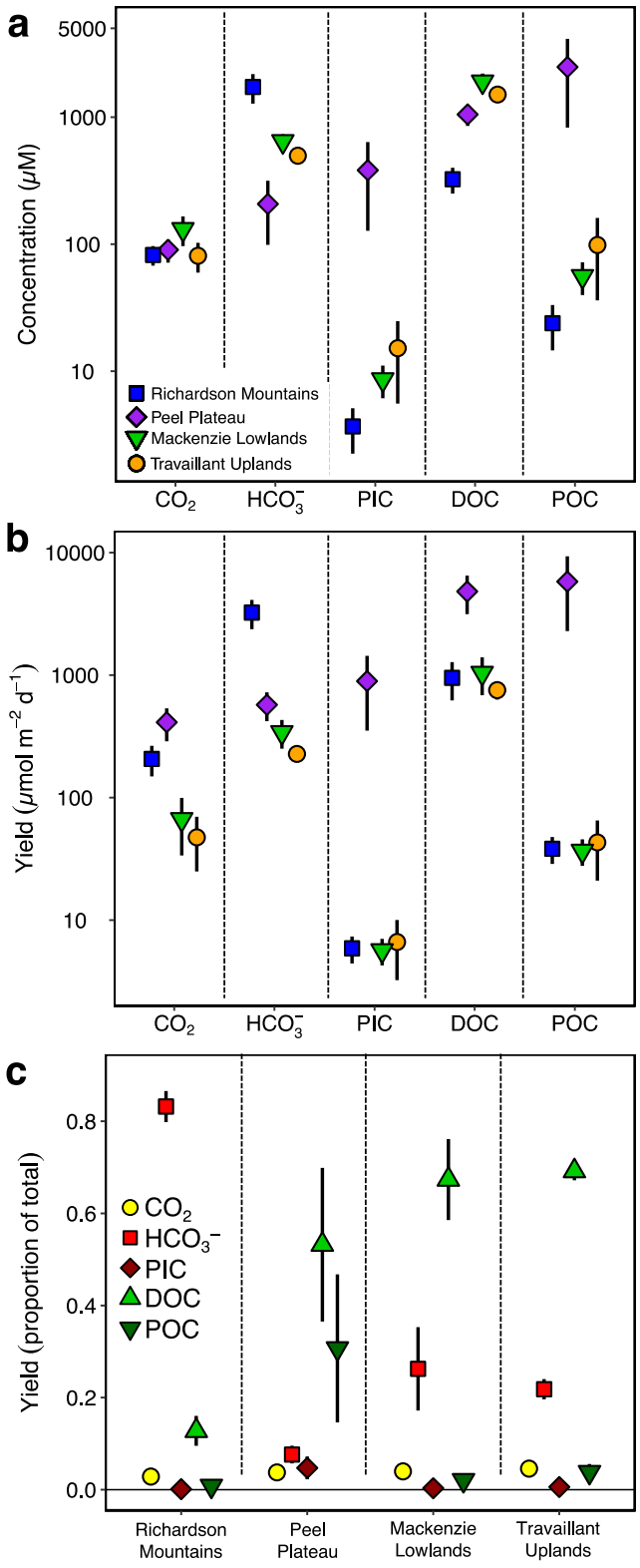

Figure 6-4. (a) Concentrations and (b) yields of fluvial carbon species. Note the legend for (a) also applies to (b). (c) Yields of carbon species as a proportion of total fluvial carbon flux. All plots show means ± standard error.

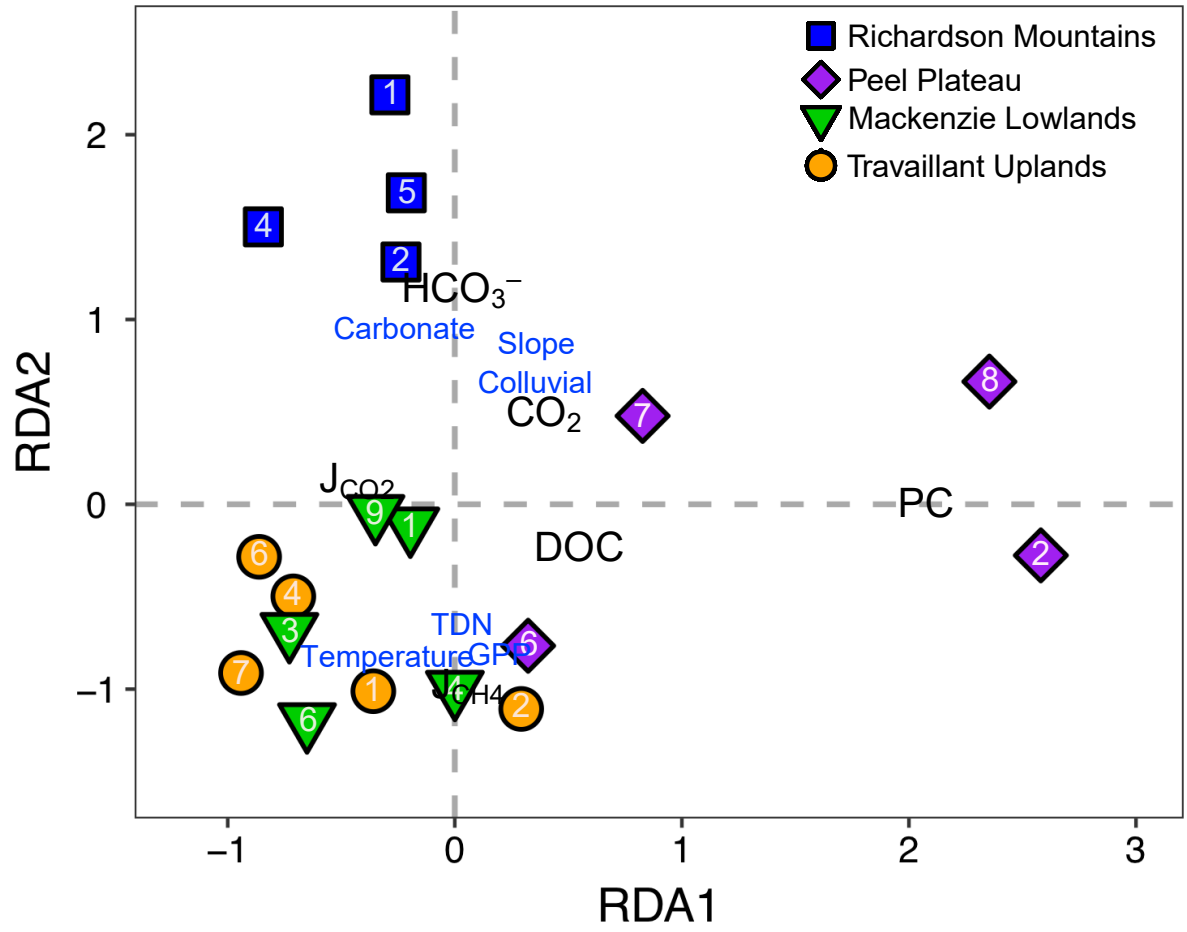

Figure 6-5. Ordination plot of redundancy analysis (RDA) of mean summertime carbon yields (black text) and landscape and water chemistry variables (blue text). Site numbers shown within points (Table A5-1). Sites PP-2 and PP-8 were affected by thermokarst, while all other sites were not. DOC = dissolved organic carbon. PC = particulate organic and inorganic carbon. J_{CO2} and J_{CH4} = CO_2 and CH_4 efflux. Temperature = stream temperature. TDN = total dissolved nitrogen. GPP = gross primary productivity. For all variables, see units and details in text and Table 6-1.

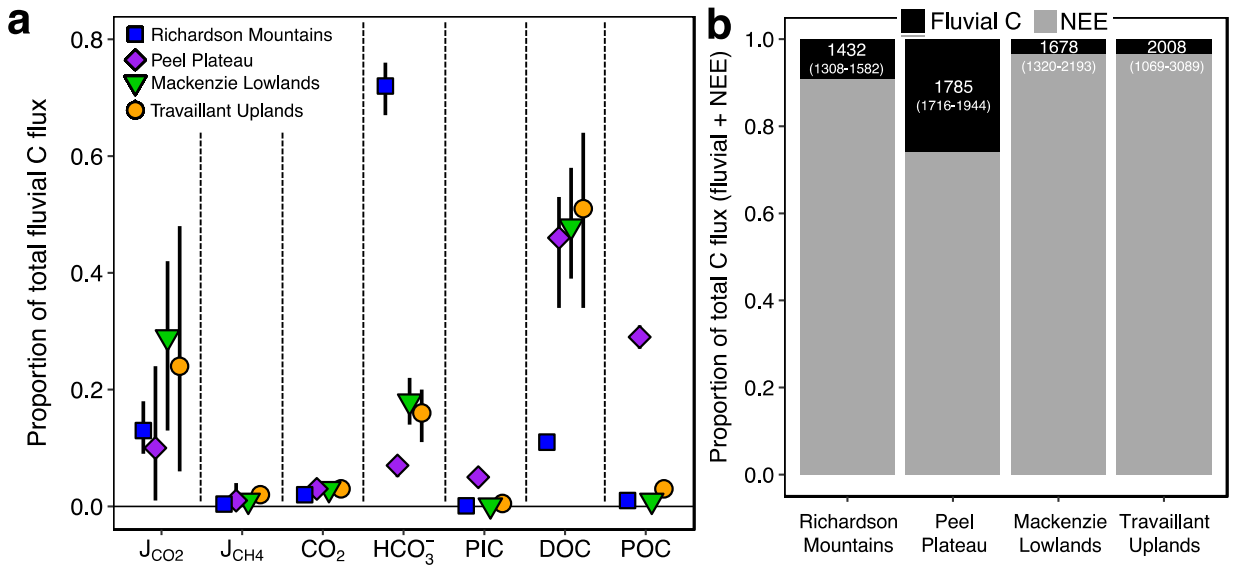

Figure 6-6. Mean daily regional fluvial carbon fluxes shown (a) as a proportion for each fluvial carbon species. Values in (a) reflect the proportion of fluvial carbon fluxes (mean ± range) in each region and in (b) the proportion of total fluvial plus terrestrial carbon flux (uptake by net ecosystem exchange, NEE).

7.1. Summary of Findings

This research investigated the effects of thermokarst on fluvial inorganic carbon cycling, which is largely unconstrained within models of the Arctic carbon cycle. The results broadly reveal that thermokarst can reshape fluvial carbon cycling across watershed scales.

The results in Chapter 2 reveal that RTSs thaw and expose carbonate- and sulfide-bearing tills to mineral weathering, resulting in intensified carbonate weathering by sulfuric acid (H_2SO_4), some abiotic CO_2 production within RTSs, and greater bicarbonate concentrations immediately downstream of RTSs. Changes in Peel River chemistry indicate a long-term (ca. 1980–2010) increase in H_2SO_4 carbonate weathering across its 70,000 km^2 watershed and without a significant increase in river discharge, suggesting that regional intensification of thermokarst activity is likely contributing to increased bicarbonate export. While thermokarst-enhanced H_2SO_4 carbonate weathering on the Peel Plateau will be a net CO_2 source over geological timescales, we conclude that carbonate weathering driven by carbonic acid (H_2CO_3*) – and thus the mineral composition of permafrost – at broad scales will determine the role of mineral weathering in permafrost carbon-climate feedbacks.

Given the high concentrations of CO_2 we observed in rill runoff streams within RTSs in Chapter 2, an objective of Chapter 3 was to quantify the magnitude of CO_2 efflux. We found that CO_2 efflux RTSs was four times higher than in adjacent streams, whereas CH_4 efflux was more variable. Both CO_2 and CH_4 were a small component of watershed-scale fluvial efflux (< 1%). While RTS activity was a primary driver of the variability in pCO_2 between streams, pCH_4 was highly variable and more strongly associated with conditions reflecting biological activity. High CO_2 concentrations were sustained along a short (200 m) transect downstream of a large RTS feature exposing deeper permafrost, but not a smaller feature exposing a greater proportion of active layer, perhaps indicating that stratigraphic variability in the composition of permafrost – and prior exposure to thaw – may influence downstream inorganic carbon cycling.

The results in Chapter 4 experimentally corroborated our conclusion from Chapter 2 that the intensity of sulfide oxidation in thawing tills is a primary abiotic control on the degree to which carbonate weathering consumes CO_2 in regional thermokarst environments. During the abiotic mineral weathering experiment, trends in ions and CO_2 stable isotopes revealed that carbonate

weathering consumed ~30% of dissolved CO_2 for unthawed and recently-thawed sediments with carbonate > sulfide, but weathering did not consume abiotic CO_2 where sulfide oxidation occurred in excess of carbonate weathering. Greater prior exposure to thaw mostly eradicated carbonates and sulfides from modern and paleo active layer sediments, indicating that the regional intensification of thermokarst and exposure of deeper, more mineral-rich tills can be expected to amplify DIC cycling.

In Chapter 5, the striking and sustained increase in DIC concentrations and isotopic signals of H_2SO_4 carbonate weathering from RTS-affected headwaters to near the Peel River clearly showed intensified fluvial inorganic carbon cycling across scales in the Stony Creek watershed, a moderately-sized tributary watershed of the Peel River. Predictive models supported the interpretation that RTS activity and water yields were primary drivers of bicarbonate export in major tributaries of the Stony Creek. Additionally, trends in $\delta^{13}C_{CO2}$ reflected stronger signals of biotic CO_2 production downstream than in headwaters. Together, these results suggest that increasing precipitation and accelerating thermokarst activity will intensify regional inorganic cycling across the land to freshwater continuum.

To provide context for trends in fluvial inorganic carbon cycling on the Peel Plateau, Chapter 6 investigated the magnitude and drivers of fluvial carbon cycling and export, and the implications for ecosystem carbon balance in a series of watersheds across diverse permafrost terrains in the Yukon and Northwest Territories. Regional variability in carbon cycling broadly followed gradients of terrain relief and thermokarst, whereby bicarbonate export dominated in mountainous terrain with carbonate bedrock, dissolved organic carbon export and CO_2 and CH_4 efflux dominated in organic-rich low-relief terrains, and the Peel Plateau was intermediate except where thermokarst enhanced sediment export. Fluvial carbon export was equivalent to ~8% of CO_2 uptake by terrestrial vegetation and greatest in thermokarst-affected terrains (nearly 40%). These results suggest that northern fluvial systems are an important component of the ecosystem carbon balance, particularly in terrains where thermokarst affects even a small portion of the landscape.

7.2. Future Research

These findings help to refine emerging models of the Arctic carbon cycle by revealing that intensifying climate change and thermokarst activity will reshape fluvial inorganic carbon

cycling across broad swaths of the circumpolar north. Thus, a clear research priority is to constrain the effects of thermokarst on carbon cycling in fluvial network headwaters in northern permafrost terrains. Previous research has concluded that studying headwaters of Arctic fluvial networks is needed to improve understanding of organic carbon cycling and CO_2 dynamics (Drake et al., 2015; Spencer et al., 2015), which is unequivocally coupled with inorganic carbon cycling (DIC = $\Sigma[CO_2, HCO_3^-, CO_3^{2-}]$). Given this coupling and the challenges of studying carbon dynamics in headwater streams across broad spatial scales, quantifying both organic and inorganic processes simultaneously will benefit future efforts to constrain carbon cycling in Arctic fluvial networks. In support of these ongoing efforts, I conclude by offering potential directions for future research.

In Chapter 2, trends in pH, CO_2, ions, and stable DIC and CO_2 isotopes indicated that H_2SO_4 carbonate weathering in RTS runoff produced abiotic CO_2. The ^{14}C-dead signature of ancient marine carbonates (Clark & Fritz, 1997) would be reflected in abiotic CO_2 produced from H_2SO_4 weathering, as observed in other environments where these processes are known to occur (Soulet et al., 2018). Importantly, $\Delta^{14}C_{CO2}$ may be less useful for discriminating between biogenic and geogenic CO_2 sources in certain environments where permafrost exposes organic carbon ≳50 ky old at the land surface (Froese et al., 2008; Murton et al., 2017). Therefore, measurements of $\Delta^{14}C_{CO2}$ would help to constrain the proportion of abiotic versus biotic CO_2 produced within RTSs on the Peel Plateau. Related, direct measurements of CO_2 efflux within RTS runoff would help to constrain estimates of CO_2 loss to the atmosphere documented in Chapter 3. Extending measurements of CO_2 efflux across the diversity of exposed surfaces within RTSs would improve understanding of thermokarst effects on CO_2 exchange across watershed scales. While few studies have quantified CO_2 exchange across the surface of thermokarst features (Abbott & Jones, 2015; Cassidy et al., 2016), measurements indicate that thermokarst may shift tundra from a net CO_2 sink to source (Cassidy et al., 2016). Measurements of terrestrial CO_2 exchange within RTSs on the Peel Plateau would help to provide context for the fluvial component of inorganic carbon cycling.

The results in Chapter 4 experimentally revealed how the chemical weathering of thawed tills may drive the evolution of fluvial inorganic carbon cycling in thermokarst-affected streams. Making frequent measurements of ions, $\delta^{13}C_{DIC}$ and $\delta^{13}C_{CO2}$ in RTS-affected streams on the Peel Plateau would complement the findings of this experiment and help to validate our conclusion

that the exposure of stratigraphic layers with varying mineral compositions is a primary control on fluvial inorganic carbon cycling. Diurnal cycles of RTS activity associated with changes in solar radiation (Kokelj et al., 2013) provide an opportunity to quantify hourly changes in the sources and concentration of DIC downstream of large RTSs, and would broadly improve understanding of fluvial inorganic carbon cycling in thermokarst-affected streams.

As indicated by the results in Chapter 5 and in previous research, precipitation and air temperature are primary drivers of RTS activity (Kokelj et al., 2015; Segal et al., 2016a) and thus the intensification of mineral weathering and DIC dynamics. Therefore, early, mid, and late summertime measurements of DIC and stable isotopes along stream transects would help to constrain the effects of climate on fluvial inorganic carbon cycling across watershed scales. Additional meteorological measurements along the elevation gradient between the mountainous headwaters and low-lying mouths of the major watersheds on the Peel Plateau (Kokelj et al., 2017) would be imperative for helping to constrain climate effects on inorganic carbon dynamics.

Chapters 2–5 clearly demonstrate that thermokarst enhances mineral weathering and, on the Peel Plateau, produces some abiotic CO_2. Chapter 6 demonstrates that thermokarst can substantially increase the fluvial component of ecosystem carbon balance, which varies considerably across diverse terrains. Together, these findings suggest that a logical evolution of dynamic numerical models of regional CO_2 exchange (e.g. Beaulieu et al., 2012) would include mineral-weathering mediated CO_2 exchange associated with regional variability in thermokarst and aquatic CO_2 and CH_4 efflux. Ultimately, multidisciplinary, collaborative efforts are required to advance understanding of climate feedbacks across the diversity of landscapes that contribute to variability in northern permafrost environments.

BIBLIOGRAPHY

Abbott, B. W., & Jones, J. B. (2015). Permafrost collapse alters soil carbon stocks, respiration, CH_4, and N_2O in upland tundra. *Global Change Biology*, *21*(12), 4570–4587. https://doi.org/10.1111/gcb.13069

Abbott, B. W., Jones, J. B., Godsey, S. E., Larouche, J. R., & Bowden, W. B. (2015). Patterns and persistence of hydrologic carbon and nutrient export from collapsing upland permafrost. *Biogeosciences*, *12*(12), 3725–3740. https://doi.org/10.5194/bg-12-3725-2015

Abbott, B. W., Jones, J. B., Schuur, E. A. G., Chapin III, F. S., Bowden, W. B., Bret-Harte, M. S., et al. (2016). Biomass offsets little or none of permafrost carbon release from soils, streams, and wildfire: an expert assessment. *Environmental Research Letters*, *11*(3), 034014. https://doi.org/10.1088/1748-9326/11/3/034014

Ali, H. N., & Atekwana, E. A. (2011). The effect of sulfuric acid neutralization on carbonate and stable carbon isotope evolution of shallow groundwater. *Chemical Geology*, *284*(3–4), 217–228. https://doi.org/10.1016/j.chemgeo.2011.02.023

AMAP. (2017). *Snow, Water, Ice and Permafrost in the Arctic (SWIPA) 2017*. Oslo, Norway: Arctic Monitoring and Assessment Programme (AMAP).

AMAP. (2018). *Arctic Ocean Acidification - Summary for Policymakers*.

AMAP. (2019). *Arctic Climate Change Update 2019 – An Update to Key Findings of Snow, Water, Ice and Permafrost in the Arctic (SWIPA) 2017*.

Amiotte Suchet, P., Probst, J.-L., & Ludwig, W. (2003). Worldwide distribution of continental rock lithology: Implications for the atmospheric/soil CO_2 uptake by continental weathering and alkalinity river transport to the oceans. *Global Biogeochemical Cycles*, *17*(2), 1–13. https://doi.org/10.1029/2002GB001891

Anderson, S. P. (2007). Biogeochemistry of Glacial Landscape Systems. *Annual Review of Earth and Planetary Sciences*, *35*(1), 375–399. https://doi.org/10.1146/annurev.earth.35.031306.140033

Anderson, S. P., Drever, J. I., Frost, C. D., & Holden, P. (2000). Chemical weathering in the foreland of a retreating glacier. *Geochimica et Cosmochimica Acta*, *64*(7), 1173–1189.

Bates, D., Mächler, M., Bolker, B., & Walker, S. (2015). Fitting Linear Mixed-Effects Models Using lme4. *Journal of Statistical Software*, *67*(1). https://doi.org/10.18637/jss.v067.i01

Beaulieu, E., Goddéris, Y., Donnadieu, Y., Labat, D., & Roelandt, C. (2012). High sensitivity of the continental-weathering carbon dioxide sink to future climate change. *Nature Climate Change*, *2*(5), 346–349. https://doi.org/10.1038/nclimate1419

Beaulieu, E., Goddéris, Y., Labat, D., Roelandt, C., Calmels, D., & Gaillardet, J. (2011). Modeling of water-rock interaction in the Mackenzie basin: Competition between sulfuric and carbonic acids. *Chemical Geology*, *289*(1–2), 114–123. https://doi.org/10.1016/j.chemgeo.2011.07.020

Berner, R. A. (1992). Weathering, plants, and the long-term carbon cycle. *Geochimica et Cosmochimica Acta*, *56*(8), 3225–3231.

Berner, R. A. (1998). The carbon cycle and carbon dioxide over Phanerozoic time: the role of land plants. *Philosophical Transactions of the Royal Society of London B: Biological Sciences*, *353*(1365), 75–82.

Berner, R. A. (1999). A new look at the long-term carbon cycle. *GSA Today*, *9*(11), 1–6.

Billett, M. F., & Moore, T. R. (2008). Supersaturation and evasion of CO_2 and CH_4 in surface waters at Mer Bleue peatland, Canada. *Hydrological Processes*, *22*(12), 2044–2054. https://doi.org/10.1002/hyp.6805

Biskaborn, B. K., Herzschuh, U., Bolshiyanov, D. Y., Schwamborn, G., & Diekmann, B. (2013). Thermokarst Processes and Depositional Events in a Tundra Lake, Northeastern Siberia. *Permafrost and Periglacial Processes*, *24*(3), 160–174. https://doi.org/10.1002/ppp.1769

Biskaborn, B. K., Smith, S. L., Noetzli, J., Matthes, H., Vieira, G., Streletskiy, D. A., et al. (2019). Permafrost is warming at a global scale. *Nature Communications*, *10*(1). https://doi.org/10.1038/s41467-018-08240-4

Bjornson, J. (2003). *Les glissements rétrogressifs de fonte de la rivière Willow, Territoires du Nord-Ouest, Canada: Caractéristiques sédimentologiques, distribution spatiale et temporelle* (Unpublished MSc Thesis). University of Ottawa.

Blum, J. D., Gazis, C. A., Jacobson, A. D., & Chamberlain, C. P. (1998). Carbonate versus silicate weathering in the Raikhot watershed within the High Himalayan Crystalline Series. *Geology*, *26*(5), 411–414.

Bogard, M. J., Kuhn, C. D., Johnston, S. E., Striegl, R. G., Holtgrieve, G. W., Dornblaser, M. M., et al. (2019). Negligible cycling of terrestrial carbon in many lakes of the arid circumpolar landscape. *Nature Geoscience*. https://doi.org/10.1038/s41561-019-0299-5

Bowden, W. B., Gooseff, M. N., Balser, A., Green, A., Peterson, B. J., & Bradford, J. (2008). Sediment and nutrient delivery from thermokarst features in the foothills of the North Slope, Alaska: Potential impacts on headwater stream ecosystems. *Journal of Geophysical Research: Biogeosciences*, *113*(G2), 1–12. https://doi.org/10.1029/2007JG000470

Brand, W. A., Coplen, T. B., Vogl, J., Rosner, M., & Prohaska, T. (2014). Assessment of international reference materials for isotope-ratio analysis (IUPAC Technical Report). *Pure and Applied Chemistry*, *86*(3). https://doi.org/10.1515/pac-2013-1023

Bring, A., Fedorova, I., Dibike, Y., Hinzman, L., Mård, J., Mernild, S. H., et al. (2016). Arctic terrestrial hydrology: A synthesis of processes, regional effects, and research challenges. *Journal of Geophysical Research: Biogeosciences*, *121*(3), 621–649. https://doi.org/10.1002/2015JG003131

Bröder, L., Andersson, A., Tesi, T., Semiletov, I., & Gustafsson, Ö. (2019). Quantifying Degradative Loss of Terrigenous Organic Carbon in Surface Sediments Across the Laptev and East Siberian Sea. *Global Biogeochemical Cycles*. https://doi.org/10.1029/2018GB005967

Bröder, L., Tesi, T., Andersson, A., Semiletov, I., & Gustafsson, Ö. (2018). Bounding cross-shelf transport time and degradation in Siberian-Arctic land-ocean carbon transfer. *Nature Communications*, *9*(1). https://doi.org/10.1038/s41467-018-03192-1

Bronaugh, & Werner. (2013). zyp: Zhang + Yue-Pilon trends package (Version 0.10-1). Pacific Climate Impacts Consortium. Retrieved from https://CRAN.R-project.org/package=zyp

Brooker, A., Fraser, R. H., Olthof, I., Kokelj, S. V., & Lacelle, D. (2014). Mapping the Activity and Evolution of Retrogressive Thaw Slumps by Tasselled Cap Trend

Analysis of a Landsat Satellite Image Stack. *Permafrost and Periglacial Processes*, *25*(4), 243–256. https://doi.org/10.1002/ppp.1819

Brown, J., Ferrians Jr., O. J., Heginbottom, J. A., & Melnikov, E. S. (1997). Circum-Arctic map of permafrost and ground-ice conditions. U.S. Geological Survey. Retrieved from https://pubs.er.usgs.gov/publication/cp45

Burke, A., Present, T. M., Paris, G., Rae, E. C. M., Sandilands, B. H., Gaillardet, J., et al. (2018). Sulfur isotopes in rivers: Insights into global weathering budgets, pyrite oxidation, and the modern sulfur cycle. *Earth and Planetary Science Letters*, *496*, 168–177. https://doi.org/10.1016/j.epsl.2018.05.022

Burke, K. D., Williams, J. W., Chandler, M. A., Haywood, A. M., Lunt, D. J., & Otto-Bliesner, B. L. (2018). Pliocene and Eocene provide best analogs for near-future climates. *Proceedings of the National Academy of Sciences*, 6.

Burn, C. R. (1997). Cryostratigraphy, paleogeography, and climate change during the early Holocene warm interval, western Arctic coast, Canada. *Canadian Journal of Earth Sciences*, *34*(7), 912–925.

Burn, C. R., Michel, F. A., & Smith, M. W. (1986). Stratigraphic, isotopic, and mineralogical evidence for an early Holocene thaw unconformity at Mayo, Yukon Territory. *Canadian Journal of Earth Sciences*, *23*(6), 794–803. https://doi.org/10.1139/e86-081

Butman, D., & Raymond, P. A. (2011). Significant efflux of carbon dioxide from streams and rivers in the United States. *Nature Geoscience*, *4*(12), 839–842. https://doi.org/10.1038/ngeo1294

Calmels, D., Gaillardet, J., Brenot, A., & France-Lanord, C. (2007). Sustained sulfide oxidation by physical erosion processes in the Mackenzie River basin: Climatic perspectives. *Geology*, *35*(11), 1003–1006. https://doi.org/10.1130/G24132A.1

Campeau, A., & del Giorgio, P. A. (2014). Patterns in CH_4 and CO_2 concentrations across boreal rivers: Major drivers and implications for fluvial greenhouse emissions under climate change scenarios. *Global Change Biology*, *20*(4), 1075–1088. https://doi.org/10.1111/gcb.12479

Campeau, A., Bishop, K., Amvrosiadi, N., Billett, M. F., Garnett, M. H., Laudon, H., et al. (2019). Current forest carbon fixation fuels stream CO_2 emissions. *Nature Communications*, *10*(1), 1876. https://doi.org/10.1038/s41467-019-09922-3

Campeau, A., Bishop, K., Nilsson, M. B., Klemedtsson, L., Laudon, H., Leith, F. I., et al. (2018). Stable Carbon Isotopes Reveal Soil-Stream DIC Linkages in Contrasting Headwater Catchments. *Journal of Geophysical Research: Biogeosciences*, *123*(1), 149–167. https://doi.org/10.1002/2017JG004083

Campeau, A., Lapierre, J.-F., Vachon, D., & del Giorgio, P. A. (2014). Regional contribution of CO_2 and CH_4 fluxes from the fluvial network in a lowland boreal landscape of Québec. *Global Biogeochemical Cycles*, *28*(1), 57–69. https://doi.org/10.1002/2013GB004685

Cassidy, A. E., Christen, A., & Henry, G. H. R. (2016). The effect of a permafrost disturbance on growing-season carbon-dioxide fluxes in a high Arctic tundra ecosystem. *Biogeosciences*, *13*(8), 2291–2303. https://doi.org/10.5194/bg-13-2291-2016

Chin, K. S., Lento, J., Culp, J. M., Lacelle, D., & Kokelj, S. V. (2016). Permafrost thaw and intense thermokarst activity decreases abundance of stream benthic macroinvertebrates. *Global Change Biology*, *22*(8), 2715–2728. https://doi.org/10.1111/gcb.13225

Ciais, P., Sabine, C., Bala, G., Bopp, L., Brovkin, V., Canadell, J., et al. (2013). Carbon and other biogeochemical cycles. In T. F. Stocker, D. Qin, G.-K. Plattner, M. Tignor, S. K. Allen, J. Boschung, et al. (Eds.). Cambridge, United Kingdom and New York, USA: Cambridge University Press.

Clark, I. D., & Fritz, P. (1997). *Environmental isotopes in hydrogeology*. Boca Raton, FL: CRC Press/Lewis Publishers.

Clark, P. U., Dyke, A. S., Shakun, J. D., Carlson, A. E., Clark, J., Wohlfarth, B., et al. (2009). The Last Glacial Maximum. *Science*, *325*(5941), 710–714. https://doi.org/10.1126/science.1172873

Clarke, F. W. (1924). *The Data of Geochemistry*. US Government Printing Office.

Cole, J. J., & Caraco, N. F. (2001). Carbon in catchments: connecting terrestrial carbon losses with aquatic metabolism. *Marine and Freshwater Research*, *52*(1), 101–110.

Cole, J. J., Prairie, Y. T., Caraco, N. F., McDowell, W. H., Tranvik, L. J., Striegl, R. G., et al. (2007). Plumbing the Global Carbon Cycle: Integrating Inland Waters into the Terrestrial Carbon Budget. *Ecosystems*, *10*(1), 172–185. https://doi.org/10.1007/s10021-006-9013-8

Cooper, H. K., Duke, M. J. M., Simonetti, A., & Chen, G. (2008). Trace element and Pb isotope provenance analyses of native copper in northwestern North America: results of a recent pilot study using INAA, ICP-MS, and LA-MC-ICP-MS. *Journal of Archaeological Science*, *35*(6), 1732–1747. https://doi.org/10.1016/j.jas.2007.11.012

Côté, M. M., Duchesne, C., Wright, J. F., & Ednie, M. (2013). *Digital compilation of the surficial sediments of the Mackenzie Valley corridor, Yukon Coastal Plain, and the Tuktoyaktuk Peninsula* (No. 7289). https://doi.org/10.4095/292494

Crawford, J. T., Loken, L. C., West, W. E., Crary, B., Spawn, S. A., Gubbins, N., et al. (2017). Spatial heterogeneity of within-stream methane concentrations. *Journal of Geophysical Research: Biogeosciences*, *122*(5), 1036–1048. https://doi.org/10.1002/2016JG003698

Crawford, J. T., Stanley, E. H., Dornblaser, M. M., & Striegl, R. G. (2017). CO_2 time series patterns in contrasting headwater streams of North America. *Aquatic Sciences*, *79*(3), 473–486. https://doi.org/10.1007/s00027-016-0511-2

Crawford, J. T., Striegl, R. G., Wickland, K. P., Dornblaser, M. M., & Stanley, E. H. (2013). Emissions of carbon dioxide and methane from a headwater stream network of interior Alaska. *Journal of Geophysical Research: Biogeosciences*, *118*(2), 482–494. https://doi.org/10.1002/jgrg.20034

Denfeld, B. A., Frey, K. E., Sobczak, W. V., Mann, P. J., & Holmes, R. M. (2013). Summer CO_2 evasion from streams and rivers in the Kolyma River basin, north-east Siberia. *Polar Research*, *32*(1), 19704. https://doi.org/10.3402/polar.v32i0.19704

Descolas-Gros, C., & Fontungne, M. (1990). Stable carbon isotope fractionation by marine phytoplankton during photosynthesis. *Plant, Cell and Environment*, *13*(3), 207–218. https://doi.org/10.1111/j.1365-3040.1990.tb01305.x

Didan, K. (2015). MOD13Q1 MODIS/Terra Vegetation Indices 16-Day L3 Global 250m SIN Grid V006 [Data set]. *NASA EOSDIS LP DAAC*. https://doi.org/doi: 10.5067/MODIS/MOD13Q1.006

Doctor, D. H., Kendall, C., Sebestyen, S. D., Shanley, J. B., Ohte, N., & Boyer, E. W. (2008). Carbon isotope fractionation of dissolved inorganic carbon (DIC) due to outgassing of carbon dioxide from a headwater stream. *Hydrological Processes*, *22*(14), 2410–2423. https://doi.org/10.1002/hyp.6833

Dornblaser, M. M., & Striegl, R. G. (2015). Switching predominance of organic versus inorganic carbon exports from an intermediate-size subarctic watershed. *Geophysical Research Letters*, *42*(2), 386–394. https://doi.org/10.1002/2014GL062349

Drake, T. W., Guillemette, F., Hemingway, J. D., Chanton, J. P., Podgorski, D. C., Zimov, N. S., & Spencer, R. G. M. (2018). The Ephemeral Signature of Permafrost Carbon in an Arctic Fluvial Network. *Journal of Geophysical Research: Biogeosciences*. https://doi.org/10.1029/2017JG004311

Drake, T. W., Raymond, P. A., & Spencer, R. G. M. (2017). Terrestrial carbon inputs to inland waters: A current synthesis of estimates and uncertainty. *Limnology and Oceanography Letters*. https://doi.org/10.1002/lol2.10055

Drake, T. W., Tank, S. E., Zhulidov, A. V., Holmes, R. M., Gurtovaya, T., & Spencer, R. G. M. (2018). Increasing Alkalinity Export from Large Russian Arctic Rivers. *Environmental Science & Technology*, *52*(15), 8302–8308. https://doi.org/10.1021/acs.est.8b01051

Drake, T. W., Wickland, K. P., Spencer, R. G. M., McKnight, D. M., & Striegl, R. G. (2015). Ancient low–molecular-weight organic acids in permafrost fuel rapid carbon dioxide production upon thaw. *Proceedings of the National Academy of Sciences*, *112*(45), 13946–13951. https://doi.org/10.1073/pnas.1511705112

Dubois, K. D., Lee, D., & Veizer, J. (2010). Isotopic constraints on alkalinity, dissolved organic carbon, and atmospheric carbon dioxide fluxes in the Mississippi River. *Journal of Geophysical Research: Biogeosciences*, *115*(G2). https://doi.org/10.1029/2009JG001102

Duc, N. T., Silverstein, S., Lundmark, L., Reyier, H., Crill, P., & Bastviken, D. (2013). Automated Flux Chamber for Investigating Gas Flux at Water–Air Interfaces. *Environmental Science & Technology*, *47*(2), 968–975. https://doi.org/10.1021/es303848x

Duk-Rodkin, A., & Hughes, O. L. (1992a). Surficial geology, Fort McPherson-Bell River, Yukon-Northwest Territories. Geological Survey of Canada.

Duk-Rodkin, A., & Hughes, O. L. (1992b). Surficial geology, Arctic Red River, District of Mackenzie, Northwest Territories. Geological Survey of Canada.

Eberl, D. D. (2003). *User's guide to RockJock - a program for determining quantitative mineralogy from powder X-ray diffraction data* (No. 03–78) (p. 45). Boulder, Colorado, USA: U.S. Geological Survey.

Ecosystem Classification Group. (2009). *Ecological regions of the Northwest Territories: Taiga Plains*. Yellowknife, NWT: Dept. of Environment and Natural Resources, Govt. of the Northwest Territories. Retrieved from 978-0-7708-0161-8

Ecosystem Classification Group. (2010). *Ecological regions of the Northwest Territories: Cordillera*. Yellowknife, NWT: Dept. of Environment and Natural Resources, Govt. of the Northwest Territories. Retrieved from 978-0-7708-0188-5

Ehlers, J., Gibbard, P. L., & Hughes, P. D. (2011). *Quaternary Glaciations - Extent and Chronology A Closer Look* (Vol. 15). Elsevier. https://doi.org/10.1016/B978-0-444-53447-7.00001-5

EPA. (2000). *Guidance for Data Quality Assessment* (No. EPA QA/G-9 QA00 Version). Environmental Protection Agency.

Finlay, J. C. (2003). Controls of streamwater dissolved inorganic carbon dynamics in a forested watershed. *Biogeochemistry*, *62*(3), 231–252.

Foster, G. L., & Vance, D. (2006). Negligible glacial–interglacial variation in continental chemical weathering rates. *Nature*, *444*(7121), 918–921. https://doi.org/10.1038/nature05365

French, H. M. (2018). *The periglacial environment* (Fourth edition). Hoboken, NJ: Wiley, Blackwell.

Fritz, M., Wetterich, S., Schirrmeister, L., Meyer, H., Lantuit, H., Preusser, F., & Pollard, W. H. (2012). Eastern Beringia and beyond: Late Wisconsinan and Holocene landscape dynamics along the Yukon Coastal Plain, Canada. *Palaeogeography, Palaeoclimatology, Palaeoecology*, *319–320*, 28–45. https://doi.org/10.1016/j.palaeo.2011.12.015

Froese, D. G., Westgate, J. A., Reyes, A. V., Enkin, R. J., & Preece, S. J. (2008). Ancient permafrost and a future, warmer Arctic. *Science*, *321*(5896), 1648–1648.

Froese, D. G., Zazula, G. D., Westgate, J. A., Preece, S. J., Sanborn, P. T., Reyes, A. V., & Pearce, N. J. G. (2009). The Klondike goldfields and Pleistocene environments of Beringia. *GSA Today*, *19*(8), 4. https://doi.org/10.1130/GSATG54A.1

Fuchs, M., Grosse, G., Strauss, J., Günther, F., Grigoriev, M., Maximov, G. M., & Hugelius, G. (2018). Carbon and nitrogen pools in thermokarst-affected permafrost landscapes in Arctic Siberia. *Biogeosciences*, *15*(3), 953–971. https://doi.org/10.5194/bg-15-953-2018

Gaillardet, J., Dupré, B., Louvat, P., & Allegre, C. J. (1999). Global silicate weathering and CO_2 consumption rates deduced from the chemistry of large rivers. *Chemical Geology*, *159*(1), 3–30. https://doi.org/10.1016/S0009-2541(99)00031-5

Galy, V., Peucker-Ehrenbrink, B., & Eglinton, T. (2015). Global carbon export from the terrestrial biosphere controlled by erosion. *Nature*, *521*(7551), 204–207. https://doi.org/10.1038/nature14400

Gardner, A. S., Moholdt, G., Wouters, B., Wolken, G. J., Burgess, D. O., Sharp, M. J., et al. (2011). Sharply increased mass loss from glaciers and ice caps in the Canadian Arctic Archipelago. *Nature*, *473*(7347), 357–360. https://doi.org/10.1038/nature10089

Gentsch, N., Mikutta, R., Shibistova, O., Wild, B., Schnecker, J., Richter, A., et al. (2015). Properties and bioavailability of particulate and mineral-associated organic matter in Arctic permafrost soils, Lower Kolyma Region, Russia. *European Journal of Soil Science*, *66*(4), 722–734. https://doi.org/10.1111/ejss.12269

Gislason, S. R., Oelkers, E. H., Eiriksdottir, E. S., Kardjilov, M. I., Gisladottir, G., Sigfusson, B., et al. (2009). Direct evidence of the feedback between climate and weathering. *Earth and Planetary Science Letters*, *277*(1–2), 213–222. https://doi.org/10.1016/j.epsl.2008.10.018

Gordon, N. D. (Ed.). (2004). *Stream hydrology: an introduction for ecologists* (2nd ed). Chichester, West Sussex, England ; Hoboken, N.J: Wiley.

Gorelick, N., Hancher, M., Dixon, M., Ilyushchenko, S., Thau, D., & Moore, R. (2017). Google Earth Engine: Planetary-scale geospatial analysis for everyone. *Remote Sensing of Environment*, *202*, 18–27. https://doi.org/10.1016/j.rse.2017.06.031

Gray, J. R., & Landers, M. N. (2014). Measuring Suspended Sediment. In *Comprehensive Water Quality and Purification* (pp. 157–204). Elsevier. https://doi.org/10.1016/B978-0-12-382182-9.00012-8

Guo, J., Wang, F., Vogt, R. D., Zhang, Y., & Liu, C.-Q. (2015). Anthropogenically enhanced chemical weathering and carbon evasion in the Yangtze Basin. *Scientific Reports*, *5*(1). https://doi.org/10.1038/srep11941

Hamilton, S. K., & Ostrom, N. E. (2007). Measurement of the stable isotope ratio of dissolved N_2 in ^{15}N tracer experiments. *Limnology and Oceanography: Methods*, *5*(7), 233–240.

Harden, J. W., Koven, C. D., Ping, C.-L., Hugelius, G., David McGuire, A., Camill, P., et al. (2012). Field information links permafrost carbon to physical vulnerabilities of thawing. *Geophysical Research Letters*, *39*(15). https://doi.org/10.1029/2012GL051958

Harrison, X. A., Donaldson, L., Correa-Cano, M. E., Evans, J., Fisher, D. N., Goodwin, C. E. D., et al. (2018). A brief introduction to mixed effects modelling and multi-model inference in ecology. *PeerJ*, *6*, e4794. https://doi.org/10.7717/peerj.4794

Hartmann, J., & Moosdorf, N. (2012). The new global lithological map database GLiM: A representation of rock properties at the Earth surface. *Geochemistry, Geophysics, Geosystems*, *13*(12). https://doi.org/10.1029/2012GC004370

Heiri, O., Lotter, A. F., & Lemcke, G. (2001). Loss on ignition as a method for estimating organic and carbonate content in sediments: reproducibility and comparability of results. *Journal of Paleolimnology*, *25*, 101–110.

Helms, J. R., Stubbins, A., Ritchie, J. D., Minor, E. C., Kieber, D. J., & Mopper, K. (2008). Absorption spectral slopes and slope ratios as indicators of molecular weight, source, and photobleaching of chromophoric dissolved organic matter. *Limnology and Oceanography*, *53*(3), 955–969. https://doi.org/10.4319/lo.2008.53.3.0955

Hemingway, J. D., Rothman, D. H., Grant, K. E., Rosengard, S. Z., Eglinton, T. I., Derry, L. A., & Galy, V. V. (2019). Mineral protection regulates long-term global preservation of natural organic carbon. *Nature*, *570*(7760), 228–231. https://doi.org/10.1038/s41586-019-1280-6

Hercod, D. J., Brady, P. V., & Gregory, R. T. (1998). Catchment-scale coupling between pyrite oxidation and calcite weathering. *Chemical Geology*, *151*, 259–276.

Hesslein, R. H., Rudd, J. W. M., Kelly, C., Ramlal, P., & Hallard, K. A. (1991). Carbon dioxide pressure in surface waters of Canadian lakes. In S. C. Wilhelms & J. S. Gulliver (Eds.), *Air-Water Mass Transfer: Selected Papers from the Second*

International Symposium on Gas Transfer at Water Surfaces (pp. 413–431). New York, New York: American Society of Civil Engineers.

Hilton, R. G., Galy, V., Gaillardet, J., Dellinger, M., Bryant, C., O'Regan, M., et al. (2015). Erosion of organic carbon in the Arctic as a geological carbon dioxide sink. *Nature*, *524*(7563), 84–87. https://doi.org/10.1038/nature14653

Hindshaw, R. S., Heaton, T. H. E., Boyd, E. S., Lindsay, M. R., & Tipper, E. T. (2016). Influence of glaciation on mechanisms of mineral weathering in two high Arctic catchments. *Chemical Geology*, *420*, 37–50. https://doi.org/10.1016/j.chemgeo.2015.11.004

Hitchon, B., & Krouse, H. R. (1972). Hydrogeochemistry of the surface waters of the Mackenzie River drainage basin, Canada-III. Stable isotopes of oxygen, carbon and sulphur. *Geochimica et Cosmochimica Acta*, *36*, 1337–1357.

Hjort, J., Karjalainen, O., Aalto, J., Westermann, S., Romanovsky, V. E., Nelson, F. E., et al. (2018). Degrading permafrost puts Arctic infrastructure at risk by mid-century. *Nature Communications*, *9*(1). https://doi.org/10.1038/s41467-018-07557-4

Holmes, R. M., McClelland, J. W., Peterson, B. J., Tank, S. E., Bulygina, E., Eglinton, T. I., et al. (2012). Seasonal and Annual Fluxes of Nutrients and Organic Matter from Large Rivers to the Arctic Ocean and Surrounding Seas. *Estuaries and Coasts*, *35*(2), 369–382. https://doi.org/10.1007/s12237-011-9386-6

Hope, D., Palmer, S. M., Billett, M. F., & Dawson, J. J. C. (2004). Variations in dissolved CO_2 and CH_2 in a first-order stream and catchment: an investigation of soil-stream linkages. *Hydrological Processes*, *18*(17), 3255–3275. https://doi.org/10.1002/hyp.5657

Hopkins, D. M. (1982). *Paleoecology of Beringia*. (J. V. Jr. Matthews, C. E. Schweger, & S. B. Young, Eds.). New York: Academic Press.

Hotchkiss, E. R., Hall Jr, R. O., Sponseller, R. A., Butman, D., Klaminder, J., Laudon, H., et al. (2015). Sources of and processes controlling CO_2 emissions change with the size of streams and rivers. *Nature Geoscience*, *8*(9), 696–699. https://doi.org/10.1038/ngeo2507

Hugelius, G., Bockheim, J. G., Camill, P., Elberling, B., Grosse, G., Harden, J. W., et al. (2013). A new data set for estimating organic carbon storage to 3 m depth in soils of

the northern circumpolar permafrost region. *Earth System Science Data*, *5*(2), 393–402. https://doi.org/10.5194/essd-5-393-2013

Hugelius, G., Strauss, J., Zubrzycki, S., Harden, J. W., Schuur, E. A. G., Ping, C.-L., et al. (2014). Estimated stocks of circumpolar permafrost carbon with quantified uncertainty ranges and identified data gaps. *Biogeosciences*, *11*(23), 6573–6593. https://doi.org/10.5194/bg-11-6573-2014

Humborg, C., Mörth, C.-M., Sundbom, M., Borg, H., Blenckner, T., Giesler, R., & Ittekkot, V. (2010). CO_2 supersaturation along the aquatic conduit in Swedish watersheds as constrained by terrestrial respiration, aquatic respiration and weathering. *Global Change Biology*, *16*(7), 1966–1978. https://doi.org/10.1111/j.1365-2486.2009.02092.x

Hutchins, R. H. S., Prairie, Y. T., & del Giorgio, P. A. (2019). Large-Scale Landscape Drivers of CO_2, CH_4, DOC, and DIC in Boreal River Networks. *Global Biogeochemical Cycles*, *33*(2), 125–142. https://doi.org/10.1029/2018GB006106

Hyatt, J. A. (1992). Cavity development in ice-rich permafrost, Pangnirtung, Baffin Island, northwest territories. *Permafrost and Periglacial Processes*, *3*(4), 293–313.

IAEA/WMO. (2017). Global Network of Isotopes in Precipitation. The GNIP Database. Retrieved from https://nucleus.iaea.org/wiser

Jin, L., Ogrinc, N., Hamilton, S. K., Szramek, K., Kanduc, T., & Walter, L. M. (2009). Inorganic carbon isotope systematics in soil profiles undergoing silicate and carbonate weathering (Southern Michigan, USA). *Chemical Geology*, *264*(1–4), 139–153. https://doi.org/10.1016/j.chemgeo.2009.03.002

Jones, J. B., & Mulholland, P. J. (1998). Influence of drainage basin topography and elevation on carbon dioxide and methane supersaturation of stream water. *Biogeochemistry*, *40*(1), 57–72.

Jonsson, A., Algesten, G., Bergström, A.-K., Bishop, K., Sobek, S., Tranvik, L. J., & Jansson, M. (2007). Integrating aquatic carbon fluxes in a boreal catchment carbon budget. *Journal of Hydrology*, *334*(1–2), 141–150. https://doi.org/10.1016/j.jhydrol.2006.10.003

Keller, K., Blum, J. D., & Kling, G. W. (2007). Geochemistry of Soils and Streams on Surfaces of Varying Ages in Arctic Alaska. *Arctic, Antarctic, and Alpine Research*, *39*(1), 84–98. https://doi.org/10.1657/1523-0430(2007)39[84:GOSASO]2.0.CO;2

Keller, K., Blum, J. D., & Kling, G. W. (2010). Stream geochemistry as an indicator of increasing permafrost thaw depth in an arctic watershed. *Chemical Geology*, *273*(1–2), 76–81. https://doi.org/10.1016/j.chemgeo.2010.02.013

Kendall, C., Doctor, D. H., & Young, M. B. (2014). Environmental Isotope Applications in Hydrologic Studies. In H. D. Holland & K. K. Turekian (Eds.), *Treatise on Geochemistry* (2nd ed., Vol. 7, pp. 273–327). Oxford: Elsevier. https://doi.org/10.1016/B978-0-08-095975-7.00510-6

Kendall, Carol, & Caldwell, E. A. (1998). Fundamentals of Isotope Geochemistry. In *Isotope Tracers in Catchment Hydrology* (pp. 51–86). Amsterdam: Elsevier Science.

Kimball, J. S., Jones, L. A., Kundig, T., & Reichle, R. (2018). SMAP L4 Global Daily 9 km EASE-Grid Carbon Net Ecosystem Exchange, Version 4 [Data set]. Boulder, Colorado USA: NASA National Snow and Ice Data Center Distributed Active Archive Center. https://doi.org/10.5067/9831n0jgvaf6

Kling, G. W., Kipphut, G. W., & Miller, M. C. (1992). The flux of CO_2 and CH_4 from lakes and rivers in arctic Alaska. In *Toolik Lake* (pp. 23–36). Springer. Retrieved from http://link.springer.com/chapter/10.1007/978-94-011-2720-2_3

Kokelj, S. V., & Jorgenson, M. T. (2013). Advances in Thermokarst Research. *Permafrost and Periglacial Processes*, *24*(2), 108–119. https://doi.org/10.1002/ppp.1779

Kokelj, S. V., Lacelle, D., Lantz, T. C., Tunnicliffe, J., Malone, L., Clark, I. D., & Chin, K. S. (2013). Thawing of massive ground ice in mega slumps drives increases in stream sediment and solute flux across a range of watershed scales. *Journal of Geophysical Research: Earth Surface*, *118*(2), 681–692. https://doi.org/10.1002/jgrf.20063

Kokelj, S. V., Lantz, T. C., Tunnicliffe, J., Segal, R., & Lacelle, R. (2017). Climate-driven thaw of permafrost preserved glacial landscapes, northwestern Canada. *Geology*, *45*(4), 371–374. https://doi.org/10.1130/G38626.1

Kokelj, S. V., Tunnicliffe, J. F., & Lacelle, D. (2017). The Peel Plateau of Northwestern Canada: An Ice-Rich Hummocky Moraine Landscape in Transition. In O. Slaymaker (Ed.), *Landscapes and Landforms of Western Canada* (pp. 109–122). Cham: Springer International Publishing. https://doi.org/10.1007/978-3-319-44595-3_7

Kokelj, S. V., Tunnicliffe, J., Lacelle, D., Lantz, T. C., Chin, K. S., & Fraser, R. (2015). Increased precipitation drives mega slump development and destabilization of ice-rich

permafrost terrain, northwestern Canada. *Global and Planetary Change*, *129*, 56–68. https://doi.org/10.1016/j.gloplacha.2015.02.008

Kuznetsova, A., Brockhoff, P. B., & Christensen, R. H. B. (2018). Package 'lmerTest' (Version 3.0-1).

Lacelle, D. (2004). Segregated-intrusive ice of subglacial meltwater origin in retrogressive thaw flow headwalls, Richardson Mountains, NWT, Canada. *Quaternary Science Reviews*, *23*(5–6), 681–696. https://doi.org/10.1016/j.quascirev.2003.09.005

Lacelle, D., Bjornson, J., & Lauriol, B. (2010). Climatic and geomorphic factors affecting contemporary (1950-2004) activity of retrogressive thaw slumps on the Aklavik Plateau, Richardson Mountains, NWT, Canada. *Permafrost and Periglacial Processes*, *21*(1), 1–15. https://doi.org/10.1002/ppp.666

Lacelle, D., Brooker, A., Fraser, R. H., & Kokelj, S. V. (2015). Distribution and growth of thaw slumps in the Richardson Mountains–Peel Plateau region, northwestern Canada. *Geomorphology*, *235*, 40–51. https://doi.org/10.1016/j.geomorph.2015.01.024

Lacelle, D., Fontaine, M., Forest, A. P., & Kokelj, S. (2014). High-resolution stable water isotopes as tracers of thaw unconformities in permafrost: A case study from western Arctic Canada. *Chemical Geology*, *368*, 85–96. https://doi.org/10.1016/j.chemgeo.2014.01.005

Lacelle, D., Lauriol, B., Zazula, G., Ghaleb, B., Utting, N., & Clark, I. D. (2013). Timing of advance and basal condition of the Laurentide Ice Sheet during the last glacial maximum in the Richardson Mountains, NWT. *Quaternary Research*, *80*(02), 274–283. https://doi.org/10.1016/j.yqres.2013.06.001

Lafrenière, M. J., & Sharp, M. J. (2005). A comparison of solute fluxes and sources from glacial and non-glacial catchments over contrasting melt seasons. *Hydrological Processes*, *19*(15), 2991–3012. https://doi.org/10.1002/hyp.5812

Lamoureux, S. F., & Lafrenière, M. J. (2014). Seasonal fluxes and age of particulate organic carbon exported from Arctic catchments impacted by localized permafrost slope disturbances. *Environmental Research Letters*, *9*(4), 045002. https://doi.org/10.1088/1748-9326/9/4/045002

Lantz, T. C., & Kokelj, S. V. (2008). Increasing rates of retrogressive thaw slump activity in the Mackenzie Delta region, N.W.T., Canada. *Geophysical Research Letters*, *35*(6). https://doi.org/10.1029/2007GL032433

Laudon, H., & Slaymaker, O. (1997). Hydrograph separation using stable isotopes, silica and electrical conductivity: an alpine example. *Journal of Hydrology*, *201*(1–4), 82–101.

Lauriol, B., Lacelle, D., St-Jean, M., Clark, I. D., & Zazula, G. D. (2010). Late Quaternary paleoenvironments and growth of intrusive ice in eastern Beringia (Eagle River valley, northern Yukon, Canada). *Canadian Journal of Earth Sciences*, *47*(7), 941–955. https://doi.org/10.1139/E10-012

Lehn, G. O., Jacobson, A. D., Douglas, T. A., McClelland, J. W., Barker, A. J., & Khosh, M. S. (2017). Constraining seasonal active layer dynamics and chemical weathering reactions occurring in North Slope Alaskan watersheds with major ion and isotope ($\delta^{34}S_{SO4}$, $\delta^{13}C_{DIC}$, $^{87}Sr/^{86}Sr$, $\delta^{44/40}Ca$, and $\delta^{44/42}Ca$) measurements. *Geochimica et Cosmochimica Acta*, *217*, 399–420. https://doi.org/10.1016/j.gca.2017.07.042

Lewkowicz, A. G., & Way, R. G. (2019). Extremes of summer climate trigger thousands of thermokarst landslides in a High Arctic environment. *Nature Communications*, *10*(1). https://doi.org/10.1038/s41467-019-09314-7

Li Yung Lung, J. Y. S., Tank, S. E., Spence, C., Yang, D., Bonsal, B., McClelland, J. W., & Holmes, R. M. (2018). Seasonal and Geographic Variation in Dissolved Carbon Biogeochemistry of Rivers Draining to the Canadian Arctic Ocean and Hudson Bay. *Journal of Geophysical Research: Biogeosciences*, *123*(10), 3371–3386. https://doi.org/10.1029/2018JG004659

Li, S.-L., Calmels, D., Han, G., Gaillardet, J., & Liu, C.-Q. (2008). Sulfuric acid as an agent of carbonate weathering constrained by δ13CDIC: Examples from Southwest China. *Earth and Planetary Science Letters*, *270*(3–4), 189–199. https://doi.org/10.1016/j.epsl.2008.02.039

Lipovsky, P. S., & Bond, J. D. (2014). *Yukon digital surficial geology compilation, digital release 1*. Whitehorse, YT, Canada: Yukon Geological Survey. Retrieved from http://data.geology.gov.yk.ca/Compilation/8

Lique, C., Holland, M. M., Dibike, Y. B., Lawrence, D. M., & Screen, J. A. (2016). Modeling the Arctic freshwater system and its integration in the global system: Lessons learned

and future challenges. *Journal of Geophysical Research: Biogeosciences*, *121*(3), 540–566. https://doi.org/10.1002/2015JG003120

Littlefair, C. A., & Tank, S. E. (2018). Biodegradability of Thermokarst Carbon in a Till-Associated, Glacial Margin Landscape: The Case of the Peel Plateau, NWT, Canada. *Journal of Geophysical Research: Biogeosciences*. https://doi.org/10.1029/2018JG004461

Littlefair, C. A., Tank, S. E., & Kokelj, S. V. (2017). Retrogressive thaw slumps temper dissolved organic carbon delivery to streams of the Peel Plateau, NWT, Canada. *Biogeosciences*, *14*(23), 5487–5505. https://doi.org/10.5194/bg-14-5487-2017

Loranty, M. M., Natali, S. M., Berner, L. T., Goetz, S. J., Holmes, R. M., Davydov, S. P., et al. (2014). Siberian tundra ecosystem vegetation and carbon stocks four decades after wildfire. *Journal of Geophysical Research: Biogeosciences*, *119*(11), 2144–2154. https://doi.org/10.1002/2014JG002730

Lorrain, A., Savoye, N., Chauvaud, L., Paulet, Y.-M., & Naulet, N. (2003). Decarbonation and preservation method for the analysis of organic C and N contents and stable isotope ratios of low-carbonated suspended particulate material. *Analytica Chimica Acta*, *491*(2), 125–133. https://doi.org/10.1016/S0003-2670(03)00815-8

Lurry, D. L., & Kolbe, C. M. (2000). *Interagency Field Manual for the Collection of Water-Quality Data* (No. OFR 00-213). USGS.

MacIntyre, S., Wanninkhof, R., & Chanton, J. P. (1995). Trace gas exchange across the air-water interface in freshwater and coastal marine environments. In P. A. Matson & R. C. Harriss (Eds.), *Biogenic Trace Gases: Measuring Emissions from Soil and Water* (pp. 52–97). Oxford, U.K.: Blackwell Science Ltd.

Malone, L., Lacelle, D., Kokelj, S., & Clark, I. D. (2013). Impacts of hillslope thaw slumps on the geochemistry of permafrost catchments (Stony Creek watershed, NWT, Canada). *Chemical Geology*, *356*, 38–49. https://doi.org/10.1016/j.chemgeo.2013.07.010

Mandile, A. J., & Hutton, A. C. (1995). Quantitative X-ray diffraction analysis of mineral and organic phases in organic-rich rocks. *International Journal of Coal Geology*, *28*(1), 51–69.

Marion, G. M. (1995). *Freeze-thaw processes and soil chemistry* (Special Report No. 95–12). US Army Corps of Engineers CRREL.

Martens, J., Wild, B., Pearce, C., Tesi, T., Andersson, A., Bröder, L., et al. (2018). Remobilization of old permafrost carbon to Chukchi Sea sediments during the end of the last deglaciation. *Global Biogeochemical Cycles*. https://doi.org/10.1029/2018GB005969

Martin, A. F., Lantz, T. C., & Humphreys, E. R. (2017). Ice wedge degradation and CO_2 and CH_4 emissions in the Tuktoyaktuk Coastlands, NT. *Arctic Science*. https://doi.org/10.1139/AS-2016-0011

Matveev, A., Laurion, I., & Vincent, W. F. (2018). Methane and carbon dioxide emissions from thermokarst lakes on mineral soils. *Arctic Science*, 1–21. https://doi.org/10.1139/as-2017-0047

McClelland, J. W., Holmes, R. M., Peterson, B. J., Raymond, P. A., Striegl, R. G., Zhulidov, A. V., et al. (2016). Particulate organic carbon and nitrogen export from major Arctic rivers. *Global Biogeochemical Cycles*, *30*(5), 629–643. https://doi.org/10.1002/2015GB005351

Michel, F. A. (2011). Isotope characterisation of ground ice in northern Canada. *Permafrost and Periglacial Processes*, *22*(1), 3–12. https://doi.org/10.1002/ppp.721

Millero, F. J. (1979). The thermodynamics of the carbonate system in seawater. *Geochimica et Cosmochimica Acta*, *43*, 1651–1661.

Millero, F. J. (2010). Carbonate constants for estuarine waters. *Marine and Freshwater Research*, *61*(2), 139. https://doi.org/10.1071/MF09254

Mook, W. G., Bommerson, J. C., & Staverman, W. H. (1974). Carbon isotope fractionation between dissolved bicarbonate and gaseous carbon dioxide. *Earth and Planetary Science Letters*, *22*(2), 169–176.

Murphy, M. J., Porcelli, D., Pogge von Strandmann, P. A. E., Hirst, C. A., Kutscher, L., Katchinoff, J. A., et al. (2019). Tracing silicate weathering processes in the permafrost-dominated Lena River watershed using lithium isotopes. *Geochimica et Cosmochimica Acta*, *245*, 154–171. https://doi.org/10.1016/j.gca.2018.10.024

Murton, J. B., Edwards, M. E., Lozhkin, A. V., Anderson, P. M., Savvinov, G. N., Bakulina, N., et al. (2017). Preliminary paleoenvironmental analysis of permafrost deposits at Batagaika megaslump, Yana Uplands, northeast Siberia. *Quaternary Research*, *87*(2), 314–330. https://doi.org/10.1017/qua.2016.15

Myers-Smith, I. H., Forbes, B. C., Wilmking, M., Hallinger, M., Lantz, T., Blok, D., et al. (2011). Shrub expansion in tundra ecosystems: dynamics, impacts and research priorities. *Environmental Research Letters*, *6*(4), 045509. https://doi.org/10.1088/1748-9326/6/4/045509

Natali, S. M., Schuur, E. A. G., Mauritz, M., Schade, J. D., Celis, G., Crummer, K. G., et al. (2015). Permafrost thaw and soil moisture driving CO_2 and CH_4 release from upland tundra. *Journal of Geophysical Research: Biogeosciences*, *120*(3), 525–537. https://doi.org/10.1002/2014JG002872

Norris, D. K. (1985). Geology of the Northern Yukon and Northwestern District of Mackenzie. Ottawa, Canada: Geological Survey of Canada.

Obu, J., Westermann, S., Bartsch, A., Berdnikov, N., Christiansen, H. H., Dashtseren, A., et al. (2019). Northern Hemisphere permafrost map based on TTOP modelling for 2000–2016 at 1 km2 scale. *Earth-Science Reviews*, *193*, 299–316. https://doi.org/10.1016/j.earscirev.2019.04.023

Oksanen, J., Blanchet, F. G., Friendly, M., Kindt, R., Legendre, P., McGlinn, D., et al. (2018). *Package 'vegan.'*

Olefeldt, D., Goswami, S., Grosse, G., Hayes, D., Hugelius, G., Kuhry, P., et al. (2016). Circumpolar distribution and carbon storage of thermokarst landscapes. *Nature Communications*, *7*, 13043. https://doi.org/10.1038/ncomms13043

Overpeck, J., Hughen, K., Hardy, D., Bradley, R., Case, R., Douglas, M., Finney, B., Gajewski, K., Jacoby, G., Jennings, A., Lamoureux, S., Lasca, A., MacDonald, G., Moore, J., Retelle, M., Smith, S., Wolfe, A., & Zielinski, G. (1997). Arctic Environmental Change of the Last Four Centuries. Science, 278(5341), 1251–1256. https://doi.org/10.1126/science.278.5341.1251

Parkhurst, D. I., & Appelo, C. A. J. (2013). Description of input and examples for PHREEQC version 3 – A computer program for speciation, batch- reaction, one-dimensional transport, and inverse geochemical calculations (Vol. A43, p. 497). U.S. Geological Survey. Retrieved from http://pubs.usgs.gov/tm/06/a43

Pearson, R. G., Phillips, S. J., Loranty, M. M., Beck, P. S. A., Damoulas, T., Knight, S. J., & Goetz, S. J. (2013). Shifts in Arctic vegetation and associated feedbacks under climate change. *Nature Climate Change*, *3*(7), 673–677. https://doi.org/10.1038/nclimate1858

Pellerin, B. A., Wollheim, W. M., Feng, X., & Vörösmarty, C. J. (2007). The application of electrical conductivity as a tracer for hydrograph separation in urban catchments. *Hydrological Processes*, *22*(12), 1810–1818. https://doi.org/10.1002/hyp.6786

Pierrot, D., Lewis, E., & Wallace, D. W. R. (2006). *MS Excel program developed for CO_2 system calculations*. Retrieved from doi:10.3334/CDIAC/otg. CO2SYS_XLS_CDIAC105a

Piper, A. M. (1944). A graphic procedure in the geochemical interpretation of water-analyses. *Transactions, American Geophysical Union*, *25*(6), 914. https://doi.org/10.1029/TR025i006p00914

Plaza, C., Pegoraro, E., Bracho, R., Celis, G., Crummer, K. G., Hutchings, J. A., et al. (2019). Direct observation of permafrost degradation and rapid soil carbon loss in tundra. *Nature Geoscience*. https://doi.org/10.1038/s41561-019-0387-6

Pogge von Strandmann, P. A. E., Desrochers, A., Murphy, M. J., Finlay, A. J., Selby, D., & Lenton, T. M. (2017). Global climate stabilisation by chemical weathering during the Hirnantian glaciation. *Geochemical Perspectives Letters*, 230–237. https://doi.org/10.7185/geochemlet.1726

Post, E., Bhatt, U. S., Bitz, C. M., Brodie, J. F., Fulton, T. L., Hebblewhite, M., et al. (2013). Ecological Consequences of Sea-Ice Decline. *Science*, *341*(6145), 519–524. https://doi.org/10.1126/science.1235225

Post, E., Forchhammer, M. C., Bret-Harte, M. S., Callaghan, T. V., Christensen, T. R., Elberling, B., et al. (2009). Ecological Dynamics Across the Arctic Associated with Recent Climate Change. *Science*, *325*(5946), 1355–1358. https://doi.org/10.1126/science.1173113

Poulin, B. A., Ryan, J. N., & Aiken, G. R. (2014). Effects of Iron on Optical Properties of Dissolved Organic Matter. *Environmental Science & Technology*, *48*(17), 10098–10106. https://doi.org/10.1021/es502670r

Qu, B., Aho, K. S., Li, C., Kang, S., Sillanpää, M., Yan, F., & Raymond, P. A. (2017). Greenhouse gases emissions in rivers of the Tibetan Plateau. *Scientific Reports*, *7*(1). https://doi.org/10.1038/s41598-017-16552-6

R Core Team. (2015). *R: A Language and Environment for Statistical Computing*. Vienna, Austria: R Foundation for Statistical Computing. Retrieved from http://www.r-project.org/

R Core Team. (2018). *R: A Language and Environment for Statistical Computing*. Vienna, Austria: R Foundation for Statistical Computing. Retrieved from http://www.r-project.org/

Rawlins, M. A., Steele, M., Holland, M. M., Adam, J. C., Cherry, J. E., Francis, J. A., et al. (2010). Analysis of the Arctic System for Freshwater Cycle Intensification: Observations and Expectations. *Journal of Climate*, *23*(21), 5715–5737. https://doi.org/10.1175/2010JCLI3421.1

Raymond, P. A., Zappa, C. J., Butman, D., Bott, T. L., Potter, J., Mulholland, P., et al. (2012). Scaling the gas transfer velocity and hydraulic geometry in streams and small rivers: Gas transfer velocity and hydraulic geometry. *Limnology and Oceanography: Fluids and Environments*, *2*(1), 41–53. https://doi.org/10.1215/21573689-1597669

Richey, J. E., Melack, J. M., Aufdenkampe, A. K., Ballester, V. M., & Hess, L. L. (2002). Outgassing from Amazonian rivers and wetlands as a large tropical source of atmospheric CO_2. *Nature*, *416*(6881), 617–620.

Rocha, A. V., & Shaver, G. R. (2011). Burn severity influences postfire CO_2 exchange in arctic tundra. *Ecological Applications*, *21*(2), 477–489. https://doi.org/10.1890/10-0255.1

Rocher-Ros, G., Sponseller, R. A., Lidberg, W., Mörth, C., & Giesler, R. (2019). Landscape process domains drive patterns of CO_2 evasion from river networks. *Limnology and Oceanography Letters*, lol2.10108. https://doi.org/10.1002/lol2.10108

Ross, M. R. V., Nippgen, F., Hassett, B. A., McGlynn, B. L., & Bernhardt, E. S. (2018). Pyrite oxidation drives exceptionally high weathering rates and geologic CO_2 release in mountaintop-mined landscapes. *Global Biogeochemical Cycles*. https://doi.org/10.1029/2017GB005798

Rounds, S. A. (2012). Alkalinity and Acid Neutralizing Capacity (ver. 4.0). In *U.S. Geological Survey Techniques of Water-Resources Investigations, book 9, chap. A6., sec. 6.6, September 2012, accessed October 16, 2017, from http://pubs.water.usgs.gov/twri9A6/*. Retrieved from http://pubs.water.usgs.gov/twri9A6/

Rudy, A. C. A., Lamoureux, S. F., Kokelj, S. V., Smith, I. R., & England, J. H. (2017). Accelerating Thermokarst Transforms Ice-Cored Terrain Triggering a Downstream Cascade to the Ocean. *Geophysical Research Letters*, *44*(21), 11,080-11,087. https://doi.org/10.1002/2017GL074912

Runkel, R. L., Crawford, C. G., & Cohn, T. A. (2004). Load estimator (LOADEST): a FORTRAN program for estimating constituent loads in streams and rivers (p. 69). U.S. Geological Survey. Retrieved from http://pubs. water.usgs.gov/tm4a5

Running, S. W., Mu, Q., & Zhao, M. (2015). MOD17A2H MODIS/Terra Gross Primary Productivity 8-Day L4 Global 500m SIN Grid V006 [Data set]. https://doi.org/10.5067/MODIS/MOD17A2H.006

Schade, J. D., Bailio, J., & McDowell, W. H. (2016). Greenhouse gas flux from headwater streams in New Hampshire, USA: Patterns and drivers: Greenhouse gas flux from headwater streams. *Limnology and Oceanography*, *61*(S1), S165–S174. https://doi.org/10.1002/lno.10337

Schaefer, K., Lantuit, H., Romanovsky, V., Schuur, E., & others. (2012). *Policy implications of warming permafrost*. United Nations Environment Programme Special Report. Retrieved from http://epic.awi.de/33086/1/permafrost.pdf

Schirrmeister, L., Kunitsky, V., Grosse, G., Wetterich, S., Meyer, H., Schwamborn, G., et al. (2011). Sedimentary characteristics and origin of the Late Pleistocene Ice Complex on north-east Siberian Arctic coastal lowlands and islands – A review. *Quaternary International*, *241*(1–2), 3–25. https://doi.org/10.1016/j.quaint.2010.04.004

Schlesinger, W. H., & Bernhardt, E. S. (2013). *Biogeochemistry: an analysis of global change* (Third edition). Amsterdam ; Boston: Elsevier/Academic Press.

Scholze, M., Knorr, W., Arnell, N. W., & Prentice, I. C. (2006). A climate-change risk analysis for world ecosystems. *Proceedings of the National Academy of Sciences*, *103*(35), 13116–13120. https://doi.org/10.1073/pnas.0601816103

Schuur, E. A. G., & Mack, M. C. (2018). Ecological Response to Permafrost Thaw and Consequences for Local and Global Ecosystem Services. *Annual Review of Ecology, Evolution, and Systematics*, *49*, 279–301. https://doi.org/10.1146/annurev-ecolsys-121415- 032349

Schuur, E. A. G., McGuire, A. D., Schädel, C., Grosse, G., Harden, J. W., Hayes, D. J., et al. (2015). Climate change and the permafrost carbon feedback. *Nature*, *520*(7546), 171–179. https://doi.org/10.1038/nature14338

Segal, R. A., Lantz, T. C., & Kokelj, S. V. (2016a). Acceleration of thaw slump activity in glaciated landscapes of the Western Canadian Arctic. *Environmental Research Letters*, *11*(3), 034025. https://doi.org/10.1088/1748-9326/11/3/034025

Segal, R. A., Lantz, T. C., & Kokelj, S. V. (2016b). *Inventory of active retrogressive thaw slumps in the Peel Plateau, Northwest Territories*. Northwest Territories Geological Survey, NWT Open Report 2015-020, 7 pages.

Serikova, S., Pokrovsky, O. S., Ala-Aho, P., Kazantsev, V., Kirpotin, S. N., Kopysov, S. G., et al. (2018). High riverine CO_2 emissions at the permafrost boundary of Western Siberia. *Nature Geoscience*. https://doi.org/10.1038/s41561-018-0218-1

Serikova, S., Pokrovsky, O. S., Laudon, H., Krickov, I. V., Lim, A. G., Manasypov, R. M., & Karlsson, J. (2019). High carbon emissions from thermokarst lakes of Western Siberia. *Nature Communications*, *10*(1). https://doi.org/10.1038/s41467-019-09592-1

Serreze, M. C., & Barry, R. G. (2011). Processes and impacts of Arctic amplification: A research synthesis. *Global and Planetary Change*, *77*(1–2), 85–96. https://doi.org/10.1016/j.gloplacha.2011.03.004

Sharp, M., Tranter, M., Brown, G. H., & Skidmore, M. (1995). Rates of chemical denudation and CO_2 drawdown in a glacier-covered alpine catchment. *Geology*, *23*(1), 61–64.

Shiklomanov, I. A. (1998). World Water Resources: A New Appraisal and Assessment for the 21st Century, 40.

Singer, P. C., & Stumm, W. (1970). Acidic Mine Drainage: The Rate-Determining Step. *Science*, *167*(3921), 1121–1123. https://doi.org/10.1126/science.167.3921.1121

Skidmore, M., Sharp, M., & Tranter, M. (2004). Kinetic isotopic fractionation during carbonate dissolution in laboratory experiments: Implications for detection of microbial CO_2 signatures using δ^{13}C-DIC. *Geochimica et Cosmochimica Acta*, *68*(21), 4309–4317. https://doi.org/10.1016/j.gca.2003.09.024

Slaymaker, O. (Ed.). (2017). *Landscapes and Landforms of Western Canada*. Cham: Springer International Publishing. https://doi.org/10.1007/978-3-319-44595-3

Smith, C. A. S., Meikle, J. C., & Roots, C. F. (Eds.). (2004). *Ecoregions of the Yukon Territory: Biophysical properties of Yukon landscapes.* Summerland, British Columbia: Agriculture and Agri-Food Canada.

Soulet, G., Hilton, R. G., Garnett, M. H., Dellinger, M., Croissant, T., Ogrič, M., & Klotz, S. (2018). Technical note: In situ measurement of flux and isotopic composition of CO_2 released during oxidative weathering of sedimentary rocks. *Biogeosciences*, *15*(13), 4087–4102. https://doi.org/10.5194/bg-15-4087-2018

Spawn, S., Dunn, S., Fiske, G., Natali, S., Schade, J., & Zimov, N. (2015). Summer methane ebullition from a headwater catchment in Northeastern Siberia. *Inland Waters*, *5*(3), 224–230. https://doi.org/10.5268/IW-5.3.845

Spencer, R. G. M., Mann, P. J., Dittmar, T., Eglinton, T. I., McIntyre, C., Holmes, R. M., et al. (2015). Detecting the signature of permafrost thaw in Arctic rivers. *Geophysical Research Letters*, *42*(8), 2830–2835. https://doi.org/10.1002/2015GL063498

St. Louis, V. L., Kelly, C. A., Duchemin, É., Rudd, J. W., & Rosenberg, D. M. (2000). Reservoir Surfaces as Sources of Greenhouse Gases to the Atmosphere: A Global Estimate. *AIBS Bulletin*, *50*(9), 766–775.

St. Pierre, K. A., St. Louis, V. L., Lehnherr, I., Schiff, S. L., Muir, D. C. G., Poulain, A. J., et al. (2019). Contemporary limnology of the rapidly changing glacierized watershed of the world's largest High Arctic lake. *Scientific Reports*, *9*(1). https://doi.org/10.1038/s41598-019-39918-4

St. Pierre, K. A., St. Louis, V. L., Schiff, S. L., Lehnherr, I., Dainard, P. G., Gardner, A. S., et al. (2019). Proglacial freshwaters are significant and previously unrecognized sinks of atmospheric CO_2. *Proceedings of the National Academy of Sciences*, 201904241. https://doi.org/10.1073/pnas.1904241116

St. Pierre, K. A., Zolkos, S., Shakil, S., Tank, S. E., St. Louis, V. L., & Kokelj, S. V. (2018). Unprecedented Increases in Total and Methyl Mercury Concentrations Downstream of Retrogressive Thaw Slumps in the Western Canadian Arctic. *Environmental Science & Technology*, *52*(24), 14099–14109. https://doi.org/10.1021/acs.est.8b05348

Stainton, M. P. (1973). A Syringe Gas-Stripping Procedure for Gas-Chromatographic Determination of Dissolved Inorganic and Organic Carbon in Fresh Water and

Carbonates in Sediments. *Journal of the Fisheries Research Board of Canada*, *30*, 1441–1445.

Stallard, R. F., & Edmond, J. M. (1983). Geochemistry of the Amazon: 2. The Influence of Geology and Weathering Environment on the Dissolved Load. *Journal of Geophysical Research*, *88*(C14), 9671–9688.

Stanley, E. H., Casson, N. J., Christel, S. T., Crawford, J. T., Loken, L. C., & Oliver, S. K. (2016). The ecology of methane in streams and rivers: patterns, controls, and global significance. *Ecological Monographs*, *86*(2), 26.

Stocker, T., Qin, D., Plattner, G. K., Tignor, M. M. B., Allen, S. K., Boschung, J., et al. (Eds.). (2013). *IPCC, 2013: Climate Change 2013: The Physical Science Basis. Contribution of Working Group I to the Fifth Assessment Report of the Intergovernmental Panel on Climate Change*. Cambridge, United Kingdom and New York, NY, USA: Cambridge University Press.

Stott, D. F. (1991). Geotectonic correlation chart, Sheet 1, Northwest Territories and Yukon. In D. F. Stott & J. D. Aiken (Eds.), *Sedimentary Cover of the Craton in Canada*. Ottawa, Canada: Geological Survey of Canada.

Strauss, J., Schirrmeister, L., Grosse, G., Fortier, D., Hugelius, G., Knoblauch, C., et al. (2017). Deep Yedoma permafrost: A synthesis of depositional characteristics and carbon vulnerability. *Earth-Science Reviews*, *172*, 75–86. https://doi.org/10.1016/j.earscirev.2017.07.007

Strauss. (1997). The isotopic composition of sedimentary sulfur through time. *Palaeogeography, Palaeoclimatology, Palaeoecology*, *132*, 97–118.

Striegl, R. G., Aiken, G. R., Dornblaser, M. M., Raymond, P. A., & Wickland, K. P. (2005). A decrease in discharge-normalized DOC export by the Yukon River during summer through autumn. *Geophysical Research Letters*, *32*(21). https://doi.org/10.1029/2005GL024413

Striegl, R. G., Dornblaser, M. M., Aiken, G. R., Wickland, K. P., & Raymond, P. A. (2007). Carbon export and cycling by the Yukon, Tanana, and Porcupine rivers, Alaska, 2001-2005. *Water Resources Research*, *43*(2). https://doi.org/10.1029/2006WR005201

Striegl, R. G., Dornblaser, M. M., McDonald, C. P., Rover, J. R., & Stets, E. G. (2012). Carbon dioxide and methane emissions from the Yukon River system. *Global Biogeochemical Cycles*, *26*(4), 1–11. https://doi.org/10.1029/2012GB004306

Striegl, R. G., Kortelainen, P., Chanton, J. P., Wickland, K. P., Bugna, G. C., & Rantakari, M. (2001). Carbon dioxide partial pressure and ^{13}C content of north temperate and boreal lakes at spring ice melt. *Limnology and Oceanography*, *46*(4), 941–945.

Stubbins, A., Silva, L. M., Dittmar, T., & Van Stan, J. T. (2017). Molecular and Optical Properties of Tree-Derived Dissolved Organic Matter in Throughfall and Stemflow from Live Oaks and Eastern Red Cedar. *Frontiers in Earth Science*, *5*. https://doi.org/10.3389/feart.2017.00022

Stumm, W., & Morgan, J. J. (1996). *Aquatic Chemistry: Chemical Equilibria and Rates in Natural Waters* (3rd ed.). New York: John Wiley & Son, Inc.

Stutter, M. I., & Billett, M. F. (2003). Biogeochemical controls on streamwater and soil solution chemistry in a High Arctic environment. *Geoderma*, *113*(1–2), 127–146. https://doi.org/10.1016/S0016-7061(02)00335-X

Suzuki, R., & Shimodaira, H. (2015). Package 'pvclust' (Version 2.0-0).

Tank, S. E., Lesack, L. F. W., & Hesslein, R. H. (2009). Northern Delta Lakes as Summertime CO_2 Absorbers Within the Arctic Landscape. *Ecosystems*, *12*(1), 144–157.

Tank, S. E., Raymond, P. A., Striegl, R. G., McClelland, J. W., Holmes, R. M., Fiske, G. J., & Peterson, B. J. (2012). A land-to-ocean perspective on the magnitude, source and implication of DIC flux from major Arctic rivers to the Arctic Ocean. *Global Biogeochemical Cycles*, *26*(4), 1–15. https://doi.org/10.1029/2011GB004192

Tank, S. E., Striegl, R. G., McClelland, J. W., & Kokelj, S. V. (2016). Multi-decadal increases in dissolved organic carbon and alkalinity flux from the Mackenzie drainage basin to the Arctic Ocean. *Environmental Research Letters*, *11*(5), 054015. https://doi.org/10.1088/1748-9326/11/5/054015

Tanski, G., Lantuit, H., Ruttor, S., Knoblauch, C., Radosavljevic, B., Strauss, J., et al. (2017). Transformation of terrestrial organic matter along thermokarst-affected permafrost coasts in the Arctic. *Science of The Total Environment*, *581–582*, 434–447. https://doi.org/10.1016/j.scitotenv.2016.12.152

Teodoru, C. R., del Giorgio, P. A., Prairie, Y. T., & Camire, M. (2009). Patterns in pCO_2 in boreal streams and rivers of northern Quebec, Canada. *Global Biogeochemical Cycles*, *23*(2), n/a-n/a. https://doi.org/10.1029/2008GB003404

Tondu, J. M. E., Turner, K. W., Wolfe, B. B., Hall, R. I., Edwards, T. W. D., & McDonald, I. (2013). Using Water Isotope Tracers to Develop the Hydrological Component of a Long-Term Aquatic Ecosystem Monitoring Program for a Northern Lake-Rich Landscape. *Arctic, Antarctic, and Alpine Research*, *45*(4), 594–614. https://doi.org/10.1657/1938-4246-45.4.594

Toohey, R. C., Herman-Mercer, N. M., Schuster, P. F., Mutter, E. A., & Koch, J. C. (2016). Multidecadal increases in the Yukon River Basin of chemical fluxes as indicators of changing flowpaths, groundwater, and permafrost. *Geophysical Research Letters*, *43*(23), 12,120-12,130. https://doi.org/10.1002/2016GL070817

Torres, M. A., Moosdorf, N., Hartmann, J., Adkins, J. F., & West, A. J. (2017). Glacial weathering, sulfide oxidation, and global carbon cycle feedbacks. *Proceedings of the National Academy of Sciences*, *114*(33), 8716–8721. https://doi.org/10.1073/pnas.1702953114

Tranter, M., & Wadham, J. L. (2014). Geochemical Weathering in Glacial and Proglacial Environments. In *Treatise on Geochemistry* (pp. 157–173). Elsevier. https://doi.org/10.1016/B978-0-08-095975-7.00505-2

Turchyn, A. V., Tipper, E. T., Galy, A., Lo, J.-K., & Bickle, M. J. (2013). Isotope evidence for secondary sulfide precipitation along the Marsyandi River, Nepal, Himalayas. *Earth and Planetary Science Letters*, *374*, 36–46. https://doi.org/10.1016/j.epsl.2013.04.033

Turner, J. V. (1982). Kinetic fractionation of carbon-13 during calcium carbonate precipitation. *Geochimica et Cosmochimica Acta*, *46*, 1183–1191. https://doi.org/10.1016/0016-7037(82)90004-7

Turner, K. W., Edwards, T. W. D., & Wolfe, B. B. (2014). Characterising Runoff Generation Processes in a Lake-Rich Thermokarst Landscape (Old Crow Flats, Yukon, Canada) using $\delta^{18}O$, $\delta^{2}H$ and d-excess Measurements. *Permafrost and Periglacial Processes*, *25*(1), 53–59. https://doi.org/10.1002/ppp.1802

van der Sluijs, J., Kokelj, S. V., Fraser, R. H., Tunnicliffe, J., & Lacelle, D. (2018). Permafrost Terrain Dynamics and Infrastructure Impacts Revealed by UAV Photogrammetry and Thermal Imaging. *Remote Sensing*, 30.

van Everdingen, R. O., & Krouse, H. R. (1985). Isotope composition of sulphates generated by bacterial and abiological oxidation. *Nature*, *315*, 395–396.

Vonk, J. E., Mann, P. J., Davydov, S., Davydova, A., Spencer, R. G. M., Schade, J., et al. (2013). High biolability of ancient permafrost carbon upon thaw. *Geophysical Research Letters*, *40*(11), 2689–2693. https://doi.org/10.1002/grl.50348

Vonk, J. E., Tank, S. E., Bowden, W. B., Laurion, I., Vincent, W. F., Alekseychik, P., et al. (2015). Reviews and syntheses: Effects of permafrost thaw on Arctic aquatic ecosystems. *Biogeosciences*, *12*(23), 7129–7167. https://doi.org/10.5194/bg-12-7129-2015

Vonk, J. E., Tank, S. E., Mann, P. J., Spencer, R. G. M., Treat, C. C., Striegl, R. G., et al. (2015). Biodegradability of dissolved organic carbon in permafrost soils and aquatic systems: a meta-analysis. *Biogeosciences*, *12*(23), 6915–6930. https://doi.org/10.5194/bg-12-6915-2015

Vonk, J. E., Dickens, A. F., Giosan, L., Hussain, Z. A., Kim, B., Zipper, S. C., et al. (2016). Arctic Deltaic Lake Sediments As Recorders of Fluvial Organic Matter Deposition. *Frontiers in Earth Science*, *4*. https://doi.org/10.3389/feart.2016.00077

Wallin, M. B., Grabs, T., Buffam, I., Laudon, H., Ågren, A., Öquist, M. G., & Bishop, K. (2013). Evasion of CO_2 from streams - The dominant component of the carbon export through the aquatic conduit in a boreal landscape. *Global Change Biology*, *19*(3), 785–797. https://doi.org/10.1111/gcb.12083

Wallin, M. B., Löfgren, S., Erlandsson, M., & Bishop, K. (2014). Representative regional sampling of carbon dioxide and methane concentrations in hemiboreal headwater streams reveal underestimates in less systematic approaches. *Global Biogeochemical Cycles*, *28*(4), 465–479. https://doi.org/10.1002/2013GB004715

Walter Anthony, K., Daanen, R., Anthony, P., Schneider von Deimling, T., Ping, C.-L., Chanton, J. P., & Grosse, G. (2016). Methane emissions proportional to permafrost carbon thawed in Arctic lakes since the 1950s. *Nature Geoscience*, *9*(9), 679–682. https://doi.org/10.1038/ngeo2795

Walther, G.-R., Post, E., Convey, P., Menzel, A., Parmesan, C., Beebee, T. J. C., et al. (2002). Ecological responses to recent climate change. *Nature*, *416*(6879), 389–395. https://doi.org/10.1038/416389a

Walvoord, M. A., & Kurylyk, B. L. (2016). Hydrologic Impacts of Thawing Permafrost—A Review. *Vadose Zone Journal*, *15*(6), 0. https://doi.org/10.2136/vzj2016.01.0010

Walvoord, M. A., & Striegl, R. G. (2007). Increased groundwater to stream discharge from permafrost thawing in the Yukon River basin: Potential impacts on lateral export of carbon and nitrogen. *Geophysical Research Letters*, *34*(12). https://doi.org/10.1029/2007GL030216

Ward Jones, M. K., Pollard, W. H., & Jones, B. M. (2019). Rapid initialization of retrogressive thaw slumps in the Canadian high Arctic and their response to climate and terrain factors. *Environmental Research Letters*. https://doi.org/10.1088/1748-9326/ab12fd

Ward, C. P., & Cory, R. M. (2016). Complete and Partial Photo-oxidation of Dissolved Organic Matter Draining Permafrost Soils. *Environmental Science & Technology*, *50*(7), 3545–3553. https://doi.org/10.1021/acs.est.5b05354

Ward, C. P., Nalven, S. G., Crump, B. C., Kling, G. W., & Cory, R. M. (2017). Photochemical alteration of organic carbon draining permafrost soils shifts microbial metabolic pathways and stimulates respiration. *Nature Communications*, *8*(1). https://doi.org/10.1038/s41467-017-00759-2

Wauthy, M., Rautio, M., Christoffersen, K. S., Forsström, L., Laurion, I., Mariash, H. L., et al. (2018). Increasing dominance of terrigenous organic matter in circumpolar freshwaters due to permafrost thaw: Increasing allochthony in arctic freshwaters. *Limnology and Oceanography Letters*. https://doi.org/10.1002/lol2.10063

Weishaar, J. L., Aiken, G. R., Bergamaschi, B. A., Fram, M. S., Fujii, R., & Mopper, K. (2003). Evaluation of Specific Ultraviolet Absorbance as an Indicator of the Chemical Composition and Reactivity of Dissolved Organic Carbon. *Environmental Science & Technology*, *37*(20), 4702–4708. https://doi.org/10.1021/es030360x

Weiss, R. F. (1974). Carbon dioxide in water and seawater: the solubility of a non-ideal gas. *Marine Chemistry*, *2*(3), 203–215.

Whiteside, J. H., Olsen, P. E., Eglinton, T. I., Cornet, B., McDonald, N. G., & Huber, P. (2011). Pangean great lake paleoecology on the cusp of the end-Triassic extinction.

Palaeogeography, Palaeoclimatology, Palaeoecology, *301*(1–4), 1–17. https://doi.org/10.1016/j.palaeo.2010.11.025

Wickland, K. P., Aiken, G. R., Butler, K., Dornblaser, M. M., Spencer, R. G. M., & Striegl, R. G. (2012). Biodegradability of dissolved organic carbon in the Yukon River and its tributaries: Seasonality and importance of inorganic nitrogen. *Global Biogeochemical Cycles*, *26*(4), 1–14. https://doi.org/10.1029/2012GB004342

Wiesenburg, D. A., & Guinasso, N. L. (1979). Equilibrium solubilities of methane, carbon monoxide, and hydrogen in water and sea water. *Journal of Chemical and Engineering Data*, *24*(4), 356–360.

Wild, B., Andersson, A., Bröder, L., Vonk, J., Hugelius, G., McClelland, J. W., et al. (2019). Rivers across the Siberian Arctic unearth the patterns of carbon release from thawing permafrost. *Proceedings of the National Academy of Sciences*, 6.

Wolf, D. C., & Skipper, H. D. (1994). Soil sterilization. In *Methods of Soil Analysis: Part 2—Microbiological and Biochemical Properties* (pp. 41–51).

Yao, G., Gao, Q., Wang, Z., Huang, X., He, T., Zhang, Y., et al. (2007). Dynamics of CO_2 partial pressure and CO_2 outgassing in the lower reaches of the Xijiang River, a subtropical monsoon river in China. *Science of The Total Environment*, *376*(1–3), 255–266. https://doi.org/10.1016/j.scitotenv.2007.01.080

Yue, S., Pilon, P., Phinney, B., & Cavadias, G. (2002). The influence of autocorrelation on the ability to detect trend in hydrological series. *Hydrological Processes*, *16*(9), 1807–1829. https://doi.org/10.1002/hyp.1095

Zamanian, K., Pustovoytov, K., & Kuzyakov, Y. (2016). Pedogenic carbonates: Forms and formation processes. *Earth-Science Reviews*, *157*, 1–17. https://doi.org/10.1016/j.earscirev.2016.03.003

Zhang, J., Quay, P. D., & Wilbur, D. O. (1995). Carbon isotope fractionation during gas-water exchange and dissolution of CO_2. *Geochimica et Cosmochimica Acta*, *59*(1), 107–114.

Zimov, S. A., Schuur, E. A. G., & Chapin III, F. S. (2006). Permafrost and the Global Carbon Budget. *Science*, *312*(5780), 1612–1613. https://doi.org/10.1126/science.1126279

Zolkos, S., Tank, S. E., & Kokelj, S. V. (2018). Mineral Weathering and the Permafrost Carbon-Climate Feedback. *Geophysical Research Letters*, *45*(18), 9623–9632. https://doi.org/10.1029/2018GL078748

Zolkos, S., Tank, S. E., Striegl, R. G., & Kokelj, S. V. (2019). Thermokarst Effects on Carbon Dioxide and Methane Fluxes in Streams on the Peel Plateau (NWT, Canada). *Journal of Geophysical Research: Biogeosciences*, (2019JG005038). https://doi.org/10.1029/2019JG005038

Zuberer, D. A. (1994). Recovery and Enumeration of Viable Bacteria. In *Methods of Soil Analysis: Part 2—Microbiological and Biochemical Properties* (pp. 119–144).

Zuur, A. F. (Ed.). (2009). *Mixed effects models and extensions in ecology with R*. New York, NY: Springer.

Zuur, A. F., Ieno, E. N., & Elphick, C. S. (2010). A protocol for data exploration to avoid common statistical problems: Data exploration. *Methods in Ecology and Evolution*, *1*(1), 3–14. https://doi.org/10.1111/j.2041-210X.2009.00001.x

Appendix 1. Supporting information for Chapter 2

A1.1. Stream Sampling

Field sampling on the Peel Plateau was conducted from June-August 2015 at five retrogressive thaw slump (RTS) sites accessed by foot, within 5 km of the Dempster Highway, and at three sites accessed by helicopter. Sites accessed by foot were visited up to six times each and sites accessed by helicopter twice each. At each site, we sampled three locations along the stream: (i) the pristine (i.e. unaffected) upstream; (ii) directly from the highly turbid permafrost thaw stream flowing out of the RTS and into the stream ("runoff"); and (iii) the RTS-affected reach (i.e. downstream of the confluence of the pristine reach and runoff) (Fig. 2-1a). Temperature, pH, conductivity, and dissolved oxygen were measured using a YSI Professional-Plus water quality meter. pH was calibrated daily using a two-point calibration curve (7.01 and 10.01 pH, NIST), conductivity using a 1413 µS cm^{-1} standard, and dissolved oxygen in a wetted sensor cap to achieve a 100% O_2-saturated environment. Owing to temporary YSI failure partway through the sampling season, pH and temperature were measured with an Oakton pHTestr 30 (accuracy ± 0.01 pH units), and conductivity by Oakton TDSTestr3 with automatic temperature compensation until the YSI was restored.

Samples for cations (Ca^{2+}, Mg^{2+}, Na^{+}, K^{+}, Fe) and anions (SO_4^{2-}, Cl^{-}) were collected in 1L HDPE bottles, and stored at 4˚C and in the dark for 24h to allow sediments to settle prior to filtering (0.7-µm glass-fiber filter [GFF], precombusted at 450˚C for 5h). Filtered subsamples were stored in acid-washed HDPE bottles and kept cool (4˚C) and dark prior to analysis, unless noted.

Dissolved inorganic carbon (DIC) was collected as bubble-free whole water in 60 mL polypropylene syringes and sealed with a stopcock to prevent gas exchange with the atmosphere. DIC samples were transported in the dark to the laboratory and sediments were allowed to settle for 1h at 4˚C and in the dark prior to filtering (0.45-µm polyethersulfone [PES] filter). All DIC samples were filtered gently to minimize DIC alteration by CO_2 off-gassing from turbulence. 15 mL of water was filtered into acid-washed, precombusted (500˚C, 5h) 30 mL glass serum bottles treated with 2 g (± 0.1 g) of KCl, to inhibit microbial activity (Striegl et al., 2012). Bottles were sealed with silicone septa and aluminum crimp rings. When

necessary, DIC samples were gently pre-filtered (precombusted 0.7-µm GFF). Serum bottles were weighed before and after sample collection to determine the precise volume of filtrate and to correct later calculations of DIC concentration. Bottles for in-house DIC standards were prepared in the same fashion, using reagent grade $NaHCO_3$.

Stable isotopes of dissolved inorganic carbon ($\delta^{13}C_{DIC}$) and dissolved organic carbon ($\delta^{13}C_{DOC}$) were collected in acid-washed polycarbonate bottles with minimal headspace, and sulfate ($\delta^{34}S_{SO4}$, $\delta^{18}O_{SO4}$) in pre-cleaned 250 mL glass amber bottles. DIC and DOC isotopes were filtered (0.45-µm PES) into acid-washed, precombusted 40 mL glass vials, without headspace or air bubbles, and sealed with two silicone-teflon septa. Sulfate isotopes were filtered (0.45-µm cellulose-nitrate) into acid-washed 120 mL HDPE bottles. Isotope subsample bottles were tightly sealed to prevent exchange with the atmosphere and kept cool (4˚C) and dark until analysis.

Dissolved CO_2 (both partial pressure [pCO_2] and stable isotopes [$\delta^{13}C_{CO2}$]) was collected from an airtight bottle following the headspace equilibration method (Hesslein et al., 1991). Briefly, 60 mL of headspace was introduced to a bottle containing 1 L of stream water and equilibrated by vigorously shaking for two minutes. Headspace gas was extracted and stored in a 60 mL polypropylene syringe fitted with a stopcock for pCO_2, and in a pre-evacuated and pre-combusted 37 mL serum bottle fitted with a butyl rubber septum (baked 12h at 60˚C) for $\delta^{13}C_{CO2}$. When sediments occluded the air intake of the collection bottle, 30 mL of stream water was equilibrated with 30 mL of introduced headspace in a 60 mL polypropylene syringe and headspace gas was stored in a second syringe. In such rare instances, the ratio of water to atmosphere was adjusted accordingly in later calculations of pCO_2. One ambient atmospheric CO_2 sample was collected per site, in a 60 mL polypropylene syringe. Water and air temperatures, and atmospheric pressure were recorded for later calculations. CO_2 samples were stored in the dark prior to analysis.

A1.2. Geochemical and Mineralogical Analyses

Cations and anions were analyzed at the University of Alberta Biogeochemical Analytical Services Laboratory (U. Alberta BASL) by Inductively-Coupled Argon Plasma Optical Emission Spectrometer (Thermo ICAP-6300) and Ion Chromatography (Dionex DX-600), respectively.

DIC was converted to CO_2 and measured in duplicate injections by gas chromatography (GC) (Varian CP3800). Samples and standards were acidified with 1.5 mL 1N sulfuric acid (Stainton, 1973), and shaken vigorously for 20 seconds to convert all DIC to CO_2. DIC concentrations were calculated based on five-point calibration curves (0-100 mg L^{-1} $NaHCO_3$, $R^2 \geq 0.99$), analyzed at the beginning and end of each run. CO_2 standards (Praxair) and a DIC standard were run every 10 samples to monitor GC drift. Peak areas were normalized by the volume of filtrate of each sample and standard.

Dissolved CO_2 was measured using an infrared gas analyzer (IRGA, PP Systems EGM-4) immediately upon returning from the field (< 10h after collection). We calculated pCO_2 using Henry's constants corrected for *in situ* water temperature (Weiss, 1974) and accounting for the ratio of sample volume to headspace during equilibration. IRGA machine drift was checked every 4-6 weeks using a 60 mL injection of 1,010 ppm CO_2 standard (Scotty Gases). Checks stabilized after 30-40 mL of standard was injected and were within 20 ppm (≤ 2%) of the standard concentration. $\delta^{13}C_{CO2}$ was analyzed at the U. Ottawa G.G. Hatch Stable Isotope Laboratory (U. Ottawa SIL) by Isotope-Ratio Mass Spectrometry (IRMS) (GC-Isolink 7890A interfaced to a Delta V IRMS by a Conflo IV continuous flow device). $\delta^{13}C_{CO2}$ was corrected for atmospheric CO_2 introduced into the headspace of the equilibration bottle, assuming atmospheric $\delta^{13}C_{CO2} = –8‰$ (Kendall et al., 2014) (equation A1-1):

$$(\delta^{13}C_{CO2\text{-}eq} \times M_{CO2\text{-}eq}) = (\delta^{13}C_{CO2\text{-}h2o} \times M_{CO2\text{-}h2o}) + (\delta^{13}C_{CO2\text{-}atm} \times M_{CO2\text{-}atm}) \quad \text{(A1-1)}$$

where $\delta^{13}C_{CO2\text{-}eq}$ and $M_{CO2\text{-}eq}$ represent the $\delta^{13}C$ and mass of equilibrated headspace CO_2, respectively; and "h2o" and "atm" in the remaining terms represent CO_2 in the equilibrated headspace derived from the water sample and atmosphere, respectively. "$\delta^{13}C_{CO2\text{-}eq}$" is thus corrected for atmospheric CO_2 used for equilibration. We used a similar mass balance approach to determine $\delta^{13}C_{CO2}$ of the original water sample (i.e. prior to fractionation effects induced by the headspace equilibration) (equation A1-2) by correcting for fractionation between water and headspace during equilibration (equation A1-3) following Hamilton & Ostrom (2007):

$$(\delta^{13}C_{CO2\text{-}smpl} \times M_{CO2\text{-}smpl}) = (\delta^{13}C_{CO2\text{-}eq} \times M_{CO2\text{-}eq}) + (\delta^{13}C_{CO2\text{-}liq} \times M_{CO2\text{-}liq}) \quad \text{(A1-2)}$$

$$\delta^{13}C_{CO2\text{-}liq} = \delta^{13}C_{CO2\text{-}eq} - \varepsilon \quad \text{(A1-3)}$$

where $\delta^{13}C$ and M represent the $\delta^{13}C$ and mass of CO_2 (e.g. equation A1-1); "smpl" represents the original water sample; $\delta^{13}C_{CO2\text{-}eq}$ comes from equation A1-1; and "liq" represents the equilibrated water sample. $\delta^{13}C_{CO2\text{-}liq}$ was corrected for temperature-dependent isotopic fractionation (ε) following Mook et al. (1974) (equation A1-3).

$\delta^{13}C_{DIC}$ and $\delta^{13}C_{DOC}$ were analyzed at the U. Ottawa SIL by IRMS (OI Analytical Aurora Model 1030W Total Organic Carbon Analyzer interfaced to a Finnigan Mat DeltaPlusXP IRMS). Samples were acidified with 5% H_3PO_4 to release inorganic carbon and resulting gases were carried through traps to remove water before quantitative analysis by IR spectroscopy (2% analytical precision). Organic carbon was released from sample via addition of persulfate solution and analyzed by IR spectroscopy, and isotopes were measured from the purified CO_2 (± 0.2‰ analytical precision).

$\delta^{34}S$ of sulfide was prepared by grinding a sulfide-containing rock sample collected from the debris tongue of a RTS into a fine powder using an agate mortar and pestle. Prior to $\delta^{34}S$ analysis, the powder was submitted for mineralogical analysis by X-ray diffraction (XRD) at U. Alberta, to confirm only sulfide and no gypsum was present. All sulfur isotopes ($\delta^{34}S$, $\delta^{34}S_{SO4}$, and $\delta^{18}O_{SO4}$) were analyzed at the U. Waterloo Environmental Isotope Laboratory (UW-EIL) by IRMS.

The mineralogy of FM2 and SE runoff was analyzed by XRD at U. Alberta. Runoff was collected in 1L HDPE bottles during July 2016 (from both RTS) and from FM2 in July 2017, refrigerated (4˚C) for 24-48 h to facilitate settling of sediment, and dried (20˚C) and disaggregated. Visible organic matter was removed from samples, which were then sieved to < 0.63 µm (2016) and < 250 µm (2017) (accounting for the majority of runoff particles < 500 µm). Loss-on-ignition was determined following published methods (Heiri et al., 2001) to evaluate potential interference with XRD peaks by organic matter (Mandile & Hutton, 1995). As organic matter content was low (<5%), samples were not pre-treated to remove organics. Mineralogy was analyzed on finely-ground sediments by XRD (Rigaku Ultimate IV), using Cobalt radiation and set to 0.6 s/step at 0.02˚ steps. Intensities were converted to Cu-Kα radiation and relative mineral abundances were quantified using the Excel macro RockJock11

(Eberl, 2003). Patterns of converted peak intensities revealed no interference from organic matter.

A1.3. Inorganic Carbon Species Calculations and Chemical Weathering Reactions

Inorganic carbon species (CO_2, HCO_3^- [bicarbonate], CO_3^{2-}) were calculated from DIC concentrations and pCO_2 using CO2sys (v.2.3) (Pierrot et al., 2006), using field temperature and pressure at the time of sample collection. For some samples, from which IC species could not be calculated from DIC and pCO_2, pH and pCO_2 were used as the input data parameters. We used the freshwater constants for K1 and K2, as defined by Millero (1979).

To evaluate mineral weathering, we used cation-anion ratios from the products side of chemical weathering reactions. Ion concentrations were converted to milliequivalents and equivalent ratios were determined from weathering products of the reactions:

$$2CaCO_3 + H_2SO_4 \rightarrow 2Ca^{2+} + SO_4^{2-} + 2HCO_3^- \text{ (A1-4) (Calmels et al., 2007)}$$

$$CaMg(CO_3)_2 + H_2SO_4 \rightarrow Ca^{2+} + Mg^{2+} + SO_4^{2-} + 2HCO_3^- \text{ (A1-5)}$$

$$CaCO_3 + H_2CO_3 \rightarrow Ca^{2+} + 2HCO_3^- \text{ (A1-6) (Tank et al., 2012)}$$

$$CaMg(CO_3)_2 + 2H_2CO_3 \rightarrow Ca^{2+} + Mg^{2+} + 4HCO_3^- \text{ (A1-7) (Stallard \& Edmond, 1983)}$$

These reactions represent the chemical weathering of calcite ($CaCO_3$) and dolomite ($CaMg(CO_3)_2$) by sulfuric and carbonic acid (H_2SO_4 and H_2CO_3, respectively). From Environment Canada hydrochemical data, H_2SO_4-driven carbonate weathering across the Peel River watershed partly aligned with weathering by H_2SO_4 in excess:

$$CaMg(CO_3)_2 + 2H_2SO_4 \rightarrow Ca^{2+} + Mg^{2+} + 2SO_4^{2-} + 2H_2CO_3 \text{ (A1-8) (Stallard \& Edmond, 1983)}$$

Weathering reactions S5 and S8 represent complete and incomplete neutralization of sulfuric acid by carbonate, respectively (Li et al., 2008).

A1.4. Isotope End-Member Calculations

Dissolved inorganic carbon

We calculated theoretical ranges of $\delta^{13}C_{DIC}$ to derive DIC end-member source ranges (Fig. 2-3c), and to evaluate contributions to the DIC pool from theoretical equilibrium reactions (mixing with atmospheric and biogenic CO_2) and kinetically-controlled mineral weathering reactions (Jin et al., 2009; Lehn et al., 2017) (supporting information Fig. A2-2).

For theoretical equilibrium reactions, we calculated $\delta^{13}C_{DIC}$ values according to:

$$\delta^{13}C_{DIC} = (f_{CO2} \times \delta^{13}C_{CO2}) + (f_{HCO3} \times \delta^{13}C_{HCO3}) \quad \text{(A1-9)}$$

where f_{CO2} and f_{HCO3} are the proportions of DIC as CO_2 and bicarbonate, respectively; $\delta^{13}C_{CO2}$ represents atmospheric or biogenic CO_2 (supporting information Fig. A2-2 end-members 2 and 4, respectively; calculation of biogenic CO_2 discussed below); and $\delta^{13}C_{HCO3}$ is calculated from $\delta^{13}C_{CO2}$ using isotopic fractionation factors between CO_2 and bicarbonate (Zhang et al., 1995), accounting for the range of water temperatures observed across stream sites (2.0–19.3˚C). Equation A1-9 does not include carbonate, which was negligible at the pH of our streams (maximum pH = 7.98). The influence of pH on DIC speciation – and subsequently on $\delta^{13}C_{DIC}$ – was accounted for in f_{CO2} and f_{HCO3}. For instance, f_{HCO3} was derived by calculating DIC from a constant input CO_2 and published constants for CO_2 solubility and ionization (Millero, 1979; Millero, 2010; Stumm & Morgan, 1996; Weiss, 1974). These calculations were made for pH from 3 to 9, to encompass f_{HCO3} <1% and >99% (i.e. bicarbonate comprising <1% and >99% of DIC). Importantly, as DIC speciation shifts to proportionally more CO_2 at lower pH, $\delta^{13}C_{DIC}$ is increasingly susceptible to influence by unreacted H_2CO_3, or may reflect silicate weathering by carbonic acid. Therefore, effects from equilibrium processes between stream DIC and atmospheric or biogenic CO_2 must be considered along with interpretations of mineral weathering contributions to $\delta^{13}C_{DIC}$ at pH < ~7.3 (where DIC > 90% HCO_3^-; supporting information Fig. A2-2), given the range of stream temperatures we observed.

We also calculated $\delta^{13}C_{DIC}$ values for kinetically-controlled weathering reactions. To calculate $\delta^{13}C_{DIC}$ from carbonate weathering by carbonic acid (i.e. H_2CO_3 from biogenic CO_2), we first calculated the $\delta^{13}C$ of carbonic acid, accounting for isotopic fractionation during the hydration of CO_2 to carbonic acid (–1.1 to –1.2‰ (Mook et al., 1974)) ($\delta^{13}C_{CO2}$ = –24.6 to –

29.0‰). Weathering of regional carbonate bedrock (–0.7‰ to –5.6‰ PDB) (Hitchon & Krouse, 1972) by the resulting carbonic acid yields $\delta^{13}C_{DIC}$ with values roughly intermediate between the source rock and carbonic acid (Kendall et al., 2014) (–12.7‰ to –17.3‰; Fig. 2-3c end-member 2; supporting information Fig. A2-2 end-member 3). Accounting for fractionation effects (Clark & Fritz, 1997), carbonate weathering by sulfuric acid yields DIC with $\delta^{13}C$ similar to that of the carbonate rock (–3.5‰ to –8.9‰; Fig. 2-3c end-member 1 and supporting information Fig. A2-2 end-member 1). RTS runoff with $\delta^{13}C_{DIC}$ values more positive than this calculated range (e.g. RTS FM2 and HA; Fig. 1c) may reflect weathering of carbonates with $\delta^{13}C$ exceeding 0‰, which is not uncommon (Kendall et al., 2014). Unreacted biogenic H_2CO_3 and DIC from silicate weathering have $\delta^{13}C_{DIC}$ roughly equal to the biogenic CO_2 source (Fig. 2-3c end-member 3).

Carbon dioxide

To evaluate CO_2 sources in RTS runoff (Fig. 2-3f), we calculated theoretical $\delta^{13}C_{CO2}$ ranges for atmospheric, biogenic, and geogenic (i.e. carbonate-derived) end-members, using published equations to account for changes in $\delta^{13}C$ associated with isotopic fractionation (Clark & Fritz, 1997; Mook et al., 1974; Zhang et al., 1995). To calculate atmospheric CO_2 in streams ($\delta^{13}C_{CO2}$ = –8.8 to –9.0‰; Fig. 2-3f end-member 1), we used published factors to correct atmospheric CO_2 (–8‰) (Kendall et al., 2014) for fractionation during transfer across the air-water interface at water temperatures ranging from 5–21˚C (Zhang et al., 1995) (observed RTS runoff temperatures were 4.2 to 16.7˚C). CO_2 generated by organic matter (OM) respiration has an isotopic signature approximately equal to that of the OM source (Kendall et al., 2014). We used measurements of $\delta^{13}C_{DOC}$ in RTS runoff (–23.5 to –27.8‰), which were isotopically similar to organic carbon in regional permafrost soil (mean $\delta^{13}C_{TOC}$ = –26.3‰) (Fritz et al., 2012), to calculate $\delta^{13}C$ of biogenic CO_2.

We calculated geogenic CO_2 as $\delta^{13}C$ of CO_2 generated from the protonation of bicarbonate (equation 2-3). Starting with the range of $\delta^{13}C$ from regional carbonate bedrock (–0.7‰ to –5.6‰), we first calculated $\delta^{13}C$ of bicarbonate following carbonate dissolution using an isotopic fractionation factor of –2.8‰ to –3.3‰ (Clark & Fritz, 1997). The resulting range in $\delta^{13}C$ (–3.5‰ to –8.9‰) (for 5–15˚C; Clark & Fritz, 1997) reflects bicarbonate generated from weathering of regional carbonate bedrock by sulfuric acid (e.g. equations A1-4, A1-5, and A1-8). From this, we corrected for isotopic fractionation between bicarbonate and CO_2 (–8.8‰ to –

10.3‰) at RTS runoff temperatures (4.2 to 16.7˚C) (Mook et al., 1974) to derive geogenic $\delta^{13}C_{CO2}$ (–12.3‰ to –19.2‰; Fig. 2-3f end-member 2). We followed the same approach to estimate geogenic $\delta^{13}C_{CO2}$ from carbonic acid-driven carbonate weathering (equations A1-6 and A1-7), assuming carbonic acid derived from biogenic CO_2 (reverse of equation 2-3). Biogenic CO_2 (see values above) was first corrected for isotopic fractionation during CO_2 hydration (–1.1 to –1.2‰) (Mook et al., 1974). Interaction between the resulting carbonic acid (–24.6 to –28.9‰) and regional carbonate bedrock yields bicarbonate with $\delta^{13}C$ values of –12.7‰ to –17.3‰ and $\delta^{13}C_{CO2}$ of –21.5‰ to –27.6‰ (Fig. 2-3f end-member 3) once corrected for fractionation during bicarbonate protonation (see above).

Comparison to literature values; derivation of sulfate isotopes

In some instances, we compare our $\delta^{13}C$ and $\delta^{34}S$ measurements with corresponding isotopes from the literature that were not calibrated according to IAEA guidelines on normalized permil (‰) scales (e.g. Kendall & Caldwell, 1998). For instance, some $\delta^{13}C$ and $\delta^{34}S$ values for the Peel River were reported in PDB (Hitchon & Krouse, 1972) and CDT (Calmels et al., 2007), respectively, but we note these standards are virtually identical to VPDB (Kendall & Caldwell, 1998) and VCDT (Brand et al., 2014). The gypsum end-member we use (Fig. 2-3d) encompasses gypsum-bearing units in the Mackenzie Plains (e.g. Bear Rock, Saline River formations) (Stott, 1991), with $\delta^{18}O_{SO4}$ = +17.9 to +29.2‰ (SMOW) and $\delta^{34}S_{SO4}$ = +14.0 to +15.6‰ (CDT) (Strauss, 1997).

When deriving sulfate isotope source values, end-members for sulfide-derived $\delta^{34}S_{SO4}$ are associated with variability in $\delta^{34}S$ of the regional sulfide source. Isotopically, SO_4^{2-} from sulfide oxidation closely resembles $\delta^{34}S$ of the original sulfide (Clark & Fritz, 1997). Thus, following Calmels et al. (2007), we use riverine $\delta^{34}S_{SO4}$ and $\delta^{18}O_{SO4}$ values to constrain $\delta^{34}S$ of regional "Mountains" and "Plains" sulfides (Fig. 2-3d). We reasoned "Plateau" sulfides were eroded from the Mackenzie Plains by the Laurentide Ice Sheet and incorporated into till permafrost of the Plateau (see main text), and are thus sourced from "Plains" sulfides (Calmels et al., 2007). Therefore, we averaged our measured "Plateau" $\delta^{34}S$ with published "Plains" $\delta^{34}S_{SO4}$ (Calmels et al., 2007) to derive a "Plains and Plateau" end-member ($\delta^{34}S_{SO4}$ = –26.1 ± 6.1‰, mean ± range; Fig. 2-3d). We used values from the literature ($\delta^{34}S_{SO4}$ = –6.2 ± 5.2‰, mean ± range; $\delta^{18}O_{SO4}$ = –

10.8‰) (Calmels et al., 2007; Hitchon & Krouse, 1972) to characterize sulfur isotopes in the Peel River (Fig. 2-3d).

Variability in sulfide-derived $\delta^{18}O_{SO4}$ is imparted by varying contributions from the O_2 and Fe^{3+} oxidation pathways, and the corresponding enrichment factors from isotopic fractionation (Clark & Fritz, 1997; van Everdingen & Krouse, 1985). Through the Fe^{3+} pathway, SO_4^{2-} inherits oxygen from water molecules (equation A1-10). Sulfides may also be oxidized by a combination of atmospheric O_2 ($\delta^{18}O \sim +23.5‰$) and oxygen from water molecules (equation A1-11) (Calmels et al., 2007).

$$FeS_2 + 14Fe^{3+} + 8H_2O \rightarrow 15Fe^{2+} + 2SO_4^{2-} + 16\ H^+ \text{ (A1-10) (Calmels et al., 2007)}$$

$$FeS_2 + 7/2O_2 + H_2O \rightarrow Fe^{2+} + 2SO_4^{2-} + 2H^+ \text{ (A1-11) (Calmels et al., 2007)}$$

We followed van Everdingen & Krouse (1985) to calculate theoretical $\delta^{18}O_{SO4}$ values derived from sulfide oxidation ($\delta^{18}O_{SO4}$ = –28.4 to +6.3‰; Fig. 2-3d), accounting for fractionation effects, using published measurements of headwall ice $\delta^{18}O$ (Lacelle et al., 2013; Michel, 2011), rainwater, and snow $\delta^{18}O$. To calculate this range, we used values of $\delta^{18}O_{H2O}$ for rain (June-August; –17.5‰) and snow (December-February; –30.6‰) sourced from Inuvik, NWT (values for 1986–1989) (IAEA/WMO, 2017); values of $\delta^{18}O_{H2O}$ for ground ice from above the Holocene thaw unconformity ($\delta^{18}O_{H2O}$ = –22.0‰) (Lacelle et al., 2013) and Pleistocene-aged pore and massive ground ice ($\delta^{18}O_{H2O}$ = –31.0‰) (Michel, 2011) were also sourced for this region.

Constraining the range of $\delta^{18}O_{SO4}$ helps elucidate the environmental conditions in which sulfides may oxidize in RTS on the Plateau. To assess sulfide oxidation pathways, we calculated the range of theoretical $\delta^{18}O_{SO4}$ from sulfide oxidation to represent varying contributions from the Fe^{3+} and O_2 oxidation pathways (van Everdingen & Krouse, 1985). Relatively light $\delta^{18}O_{SO4}$ in RTS runoff (–5.9‰ to –21.4‰) suggests oxygen from relatively ^{18}O-depleted water molecules contributed to sulfide oxidation, likely during wetter conditions from rainfall or melting permafrost ice, with greater contribution from atmospheric O_2 under drier conditions. This suggests sulfide oxidation in RTS perhaps occurred when freshly-exposed minerals were subject to alternating wet and dry conditions during the summertime. This interpretation aligns with field

observations of standing waters within RTS scar zones, which were heavily tinted reddish-orange, likely by iron oxides.

A1.5. Peel and Mackenzie River Yield Comparison

We used long-term water chemistry collected by Environment Canada (wateroffice.ec.gc.ca/) and daily historical discharge data from the Water Survey of Canada to evaluate long-term trends in Ca^{2+}, Mg^{2+}, and SO_4^{2-}, and alkalinity loads in the Peel River. Hydrochemical observations spanned 1969–2015, except for alkalinity (1969–2014) and Mg^{2+} (1971–2015). Daily discharge data spanned 1969–2015, with some daily or monthly discharge measurements missing for 1974-1978, 1997–1998, 2004, 2016, and all of 1987. Consequently, only complete years of chemistry and discharge measurements from 1979–2015 were included. Following Tank et al. (2016), we used alkalinity as a proxy for bicarbonate, as the Mackenzie River system and its tributaries are bicarbonate rich and well-buffered. Total alkalinity (as $CaCO_3$, mg L^{-1}) was converted to milliequivalents (meq L^{-1}) (Rounds, 2012); concentrations of all ions were converted from mg L^{-1} to molar units. Mean chemistry concentrations and discharge were used when multiple measurements were made in one day. We paired chemistry and discharge data in the LoadRunner software package, which automates runs of the USGS program LOADEST (Runkel et al., 2004) to assist with estimating constituent loads in rivers. LOADEST uses the Aikaike information criterion (AIC) to determine the most suitable multiple linear regression from a suite of models. We inspected normal probability and residual plots from the most suitable model (lowest AIC) to confirm it met assumptions of normality and homoscedasticity, and used the adjusted maximum likelihood estimate, which is most suitable for non-censored data. We calculated total annual constituent loads by summing daily constituent loads for each month and evaluated long-term trends using the non-parametric Mann-Kendall test, following the trend pre-whitening approach (Yue et al., 2002) to account for serial autocorrelation, using the *zyp* package (Bronaugh & Werner, 2013) in the R programming environment (R Core Team, 2015).

To evaluate broad-scale effects of a relatively high proportion of thermokarst in the Peel River watershed, we compared historical trends in sulfide-induced carbonate weathering between the Peel and Mackenzie Rivers from 1975-2015. For both rivers, we calculated changes in SO_4^{2-} and Ca^{2+}-Mg^{2+} yields by normalizing total changes in our modeled loads for the Peel and published loads for the Mackenzie (Tank et al., 2016) to their respective watershed areas.

A1.6. Statistical and Geographic Information Systems (GIS) Analyses

We used linear mixed effects models in the R package *lme4* (Bates et al., 2015) to evaluate the impact of RTS on DIC, bicarbonate, and pCO_2 species in streams. Linear mixed effects regression is suitable for longitudinal, unbalanced (i.e. different *n*), nested study designs, because random effects in the model account for variability associated with repeat measurements of treatment levels (e.g. sampling location) for different treatments (e.g. sampling site), irrespective of *n*. In our model, we included sampling location (pristine, runoff, affected) as a fixed effect and a random slope term specifying an interaction between sampling location and RTS to account for variability in stream geochemistry between RTS.

To quantify the proportion of RTS runoff solutes in affected streams, we used conductivity in a two end-member mixing model defined by Malone et al. (2013) as the "fraction of slump runoff" (f_{SR}):

$$f_{SR} = (AF - UA) / (SR - UA) \quad \text{(S2-12)}$$

where "UA", "AF", and "SR" are conductivity (μS cm^{-1}) from pristine, RTS-affected, and runoff streams (Fig. 2-1a). f_{SR} assumes end-member conductivities remain constant across space and time (e.g. Pellerin et al., 2007). Therefore, this assumes minimal alteration to solute concentrations along a stream flow path (e.g. from water-mineral interactions or freshwater inputs) (e.g. Laudon & Slaymaker, 1997). Our f_{SR} calculations thus provide a first order estimate of RTS contribution to solutes in RTS-affected streams and may overestimate concentrations for RTS-affected stream sites more distant from their pristine counterpart, as stream water-mineral interactions may occur between the pristine and affected sites prior to RTS runoff entering the stream. Our sampling design aimed to minimize effects from chemistry changes prior to RTS runoff entering the affected stream.

To advance a broad understanding of inorganic carbon dynamics in the context of rapidly thawing permafrost, we used freely-available geospatial data for global lithology (Hartmann & Moosdorf, 2012); Pleistocene glacial maxima (Kokelj et al., 2017); regional coverage of hillslope thermokarst (Olefeldt et al., 2016); and direct (Biskaborn et al., 2013; Fritz et al., 2012; Hyatt, 1992; Lauriol et al., 2010; Schirrmeister et al., 2011; Stutter & Billett, 2003) and inferred

(Keller et al., 2007) observations of carbonates in permafrost to highlight regions in the circumpolar north where thermokarst and carbonate terrains coincide. Hillslope thermokarst included RTS, active layer detachment slides, thermo-erosional gullies, beaded streams, and thermokarst water tracks (Olefeldt et al., 2016). We focused our analysis on terrains with moderate to high hillslope thermokarst (10-60% regional coverage (Olefeldt et al., 2016)), and regions where carbonate lithologies are dominant or documented to be present (i.e. mixed sedimentary lithology) (Hartmann & Moosdorf, 2012). We acknowledge thermokarst-carbon dynamics in terrains identified here are likely different from those on the Plateau. However, this analysis provides a first-order characterization of where thermokarst may interact with carbonates, and where future research might occur to continue refining our understanding of thermokarst-freshwater interactions in the context of inorganic carbon cycling.

Table A1-1. Mineral abundances in RTS runoff, calculated from XRD intensities using the Excel macro RockJock (Eberl, 2003). 'ND' indicates not detected by XRD. Full pattern degree of fit reflects the fit between the measured pattern of XRD intensities and that calculated by RockJock, based on converted Co radiation (see text for details). Fits ≤ 0.10 are strong.

Mineral	**Abundance (weight %), or present/not detected**		
Sample	SE (07/25/16)	FM2 (07/06/16)	FM2 (07/12/17)
Quartz	84.91%	78.68%	Present
Albite	5.61%	7.55%	Present
Muscovite	4.65%	7.62%	Present
Chlorite	2.67%	3.13%	Present
Anatase	0.87%	ND	ND
Pyrite	0.67%	1.13%	Present
Dolomite	0.62%	1.89%	Present
Calcite	ND	ND	Present
Gypsum	ND	ND	Present
Sanidine	ND	ND	Present
Tot.	**100.00%**	**100.00%**	-
Full pattern degree of fit:	0.4311	0.3886	-

Table A1-2. Study site locations and morphological characteristics of RTS.

RTS	Lat (DD)	Lon (DD)	Headwall height† (~m, max)	Area§ (ha)	Growth rate§ (m y^{-1})	Age* (~yrs)
FM2	67.257	-135.236	25	48	15	< 25
SE	67.148	-135.718	23	ND	ND	~5
FM4	67.277	-135.159	17	20	9.4	> 25
FM3	67.253	-135.273	6.5	10	12.5	> 60
HA	67.150	-135.688	6-8	ND	ND	ND
HB	67.240	-135.823	6-8	14	15	ND
HD	67.400	-135.334	6-8	ND	ND	ND
SD	67.179	-135.726	2	< 1	ND	~5

†Headwall heights from the literature (FM2 (Kokelj et al., 2013); HA, HB, HD (Littlefair et al., 2017)), field measurements in 2015 (FM4, FM3, SD), and estimated from photo with known scale (SE). Headwall height of HA ≳ HB ≳ HD.
§RTS area and growth rate from the literature (Brooker et al., 2014), except for SD area (estimated from field observations). "ND" indicates no data.
*RTS age from the literature (FM2, FM3, FM4 (Brooker et al., 2014)), estimated from field observations and remote sensing imagery (SD, SE), and unknown (HA, HB, HD).

Table A1-3. RTS impacts on stream solutes. Parameters were compared between pristine streams, RTS runoff, and RTS-affected streams. Data were transformed, as indicated, to meet the assumptions of linear mixed effects regression. df = degrees of freedom, t and *p* represent t- and *p*-values from each model. For all, $\alpha = 0.05$.

	Runoff			*RTS-affected*		
Variable	**df**	**t**	***p***	**df**	**t**	***p***
$3\sqrt{}$ DIC	7.5	2.48	0.040	10.7	2.62	0.024
log pCO_2	7.5	5.60	0.001	15.2	-0.98	0.342
log HCO_3^-	7.4	2.03	0.080	8.2	2.72	0.026
log Ca^{2+}+Mg^{2+}	6.1	3.94	0.007	8.2	2.61	0.031
log SO_4^{2-}	5.6	6.32	0.001	7.4	4.34	0.003
pH	5.9	-0.76	0.475	7.2	1.77	0.118
log Conductivity	91.1	16.42	0.000	91.1	6.89	0.000

Table A1-4. Coefficients and goodness-of-fit metrics for linear models of bicarbonate concentrations in RTS-affected streams versus the fraction of slump runoff (f_{SR}) for the five foot-access RTS. $n = 27$. Bicarbonate was log-transformed for all sites. Regression lines are shown in Fig. 2-4b. For all, $\alpha = 0.05$.

RTS	df	t	*p*	Adj. R^2
FM2	5	3.1	0.04	0.62
SE	4	9.9	0.00	0.96
FM4	5	6.1	0.00	0.88
FM3	5	1.8	0.15	0.31
SD	3	2.3	0.15	0.59

Table A1-5. Summaries of constituent load trends for the Peel River (1979-2015) from the Mann-Kendall test, with pre-whitening treatment, as presented in Fig. 2-5. Loads were determined from Environment Canada hydrochemistry and hydrology data, using USGS LOADEST software. Intercept represents the value of the best-fit line for discharge (km^3) or load (Gmol for Ca^{2+}, Mg^{2+}, SO_4^{2-}; Geq for alkalinity) in 1979. Rate of change not calculated for non-significant (NS) trends.

Parameter	Intercept	τ	*p*	Total change	% total change	% change decade^{-1}
Ca^{2+}	19.0	0.50	0.000	6.14	32.2	7.8
Mg^{2+}	8.9	0.62	0.000	4.61	51.9	11.7
SO_4^{2-}	7.5	0.79	0.000	9.30	124.5	22.7
Alkalinity	41.6	0.23	0.088	4.12	9.9	NS
Discharge	21.6	0.10	0.427	0.71	3.3	NS
$(Ca^{2+} + Mg^{2+}) : 2SO_4^{2-}$	1.8	-0.35	0.000	-0.62	-33.3	-11.2

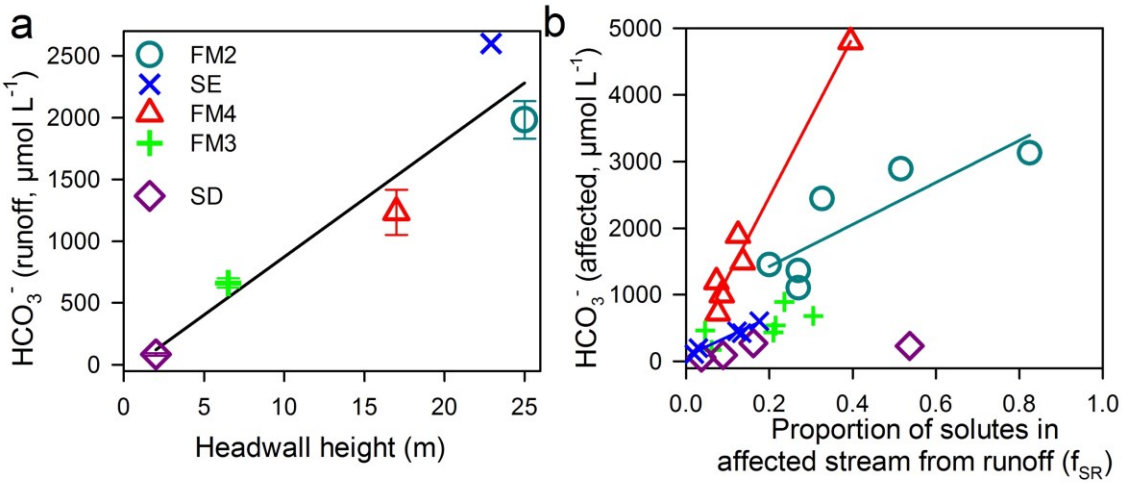

Figure A1-1. (a) HCO_3^- in RTS runoff vs. maximum headwall height (p = 0.02, t = 4.86, df = 3, R^2 = 0.85). Error bars represent standard error. (b) HCO_3^- in RTS-affected streams versus the proportion of solutes in the affected stream from RTS runoff (f_{SR}), where 1.0 = 100% of downstream solutes from RTS runoff. f_{SR} is based on conductivity, which increases with activity in larger RTS (Kokelj et al., 2013). Regression lines indicate a significant linear relationship (p < 0.05; Table A1-4).

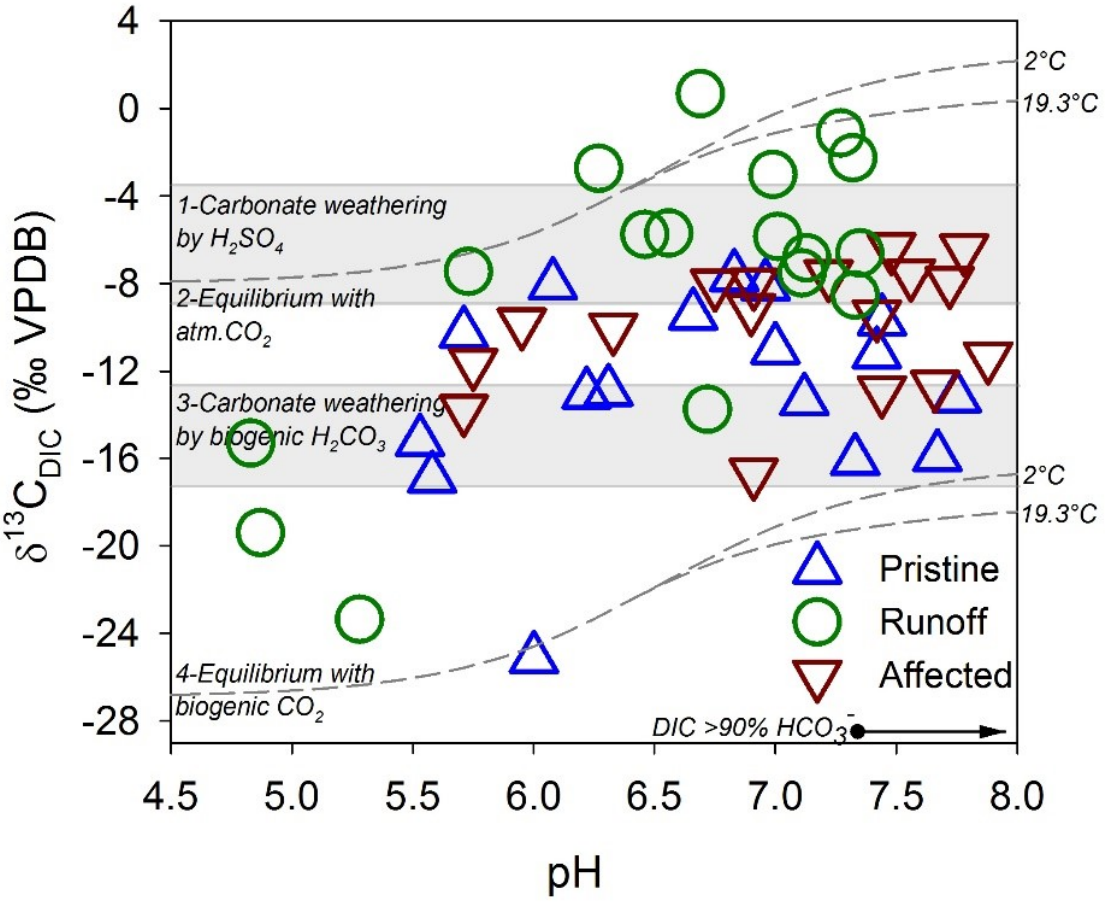

Figure A1-2. Composition of stable DIC isotopes in streams, compared to theoretical end-members for equilibrium (dashed lines, end-members 2 and 4) and kinetically-controlled (shaded, end-members 1 and 3) reactions. See supporting information text for derivation of end-members and the effect of pH on DIC end-member interpretation where HCO_3^- dominates (>90% of) the DIC pool, at pH ≥ 7.3 for this study.

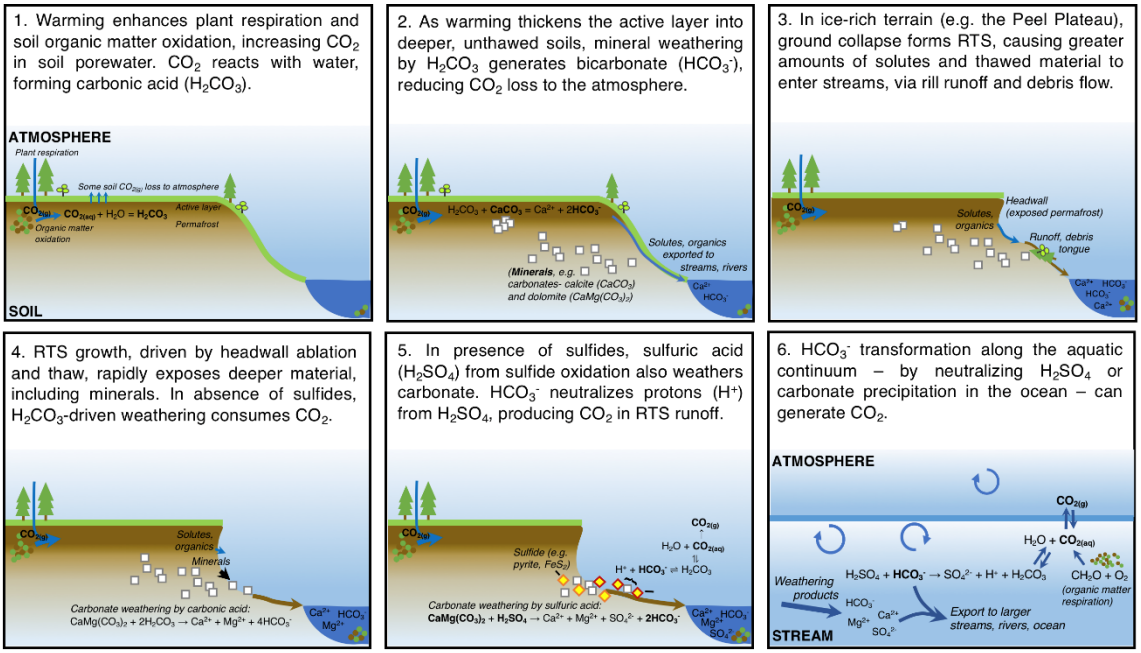

Figure A1-3. Thermokarst evolution and effects on inorganic carbon cycling in Arctic fluvial networks, in the context of this study (diagram format following Drake et al., 2015).

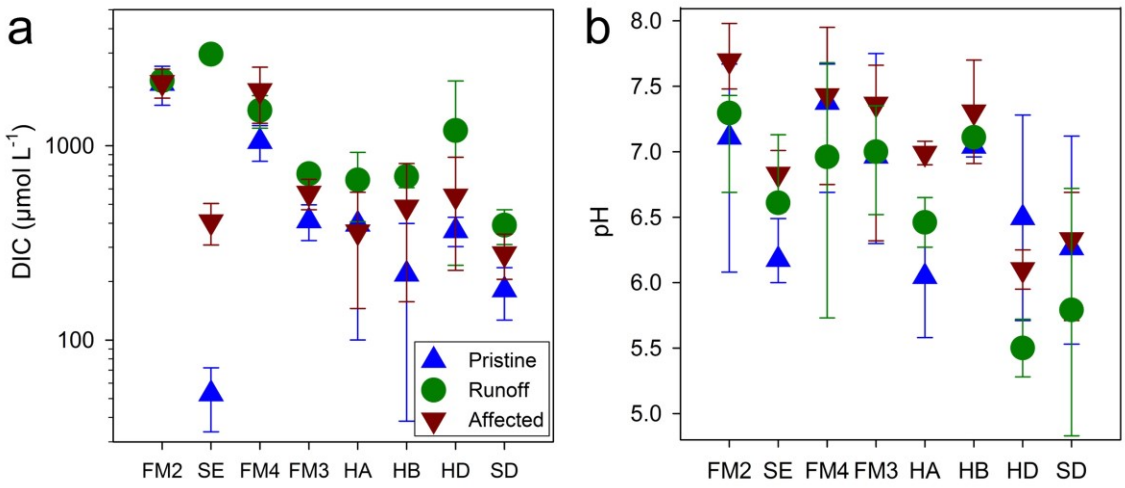

Figure A1-4. RTS impacts on (a) DIC and (b) pH. RTS are ordered from left to right by decreasing maximum headwall height. Values and error bars represent mean and standard error (a), and median and range (b).

Appendix 2. Supporting information for Chapter 3

Table A2-1. Linear regression trends from the flux chamber measurements of CO_2 and CH_4 used to derive *k* models. Sample IDs in the sample column contain measurement date (mm/dd/yy) - Site # - flux measurement replicate # for CO_2. Only one measurement was made for CH_4 flux for each site and date (see main text for details). df = degrees of freedom.

Sample ID	Gas	R^2	*p*-value	df	*t*
06/25/16-1-1	CO_2	0.9830	8.22E-15	15	30.0
06/25/16-1-2	CO_2	0.9900	1.29E-18	17	42.0
06/25/16-1-3	CO_2	0.9820	2.08E-17	18	32.4
06/25/16-2-1	CO_2	0.9880	6.70E-17	16	36.8
06/25/16-2-2	CO_2	0.9940	2.92E-18	15	51.2
06/25/16-2-3	CO_2	0.9880	3.91E-17	16	38.1
06/25/16-3-1	CO_2	0.9540	1.28E-09	12	16.5
06/25/16-3-2	CO_2	0.9870	7.21E-13	12	31.3
06/25/16-3-3	CO_2	0.9900	1.47E-15	14	38.2
06/28/16-4-1	CO_2	0.9800	4.55E-10	10	23.4
06/28/16-4-2	CO_2	0.9920	5.32E-13	11	37.8
06/28/16-4-3	CO_2	0.9890	2.10E-14	13	36.0
06/26/16-5-1	CO_2	0.9980	4.45E-21	14	95.0
06/26/16-5-2	CO_2	0.9960	4.62E-17	13	57.8
06/26/16-5-3	CO_2	0.9970	7.77E-21	15	76.2
06/27/16-6-1	CO_2	0.9940	1.31E-22	19	56.3
06/27/16-6-2	CO_2	0.9460	1.80E-10	14	16.2
06/27/16-6-3	CO_2	0.9810	1.29E-13	14	27.6
06/26/16-7-1	CO_2	0.9970	2.24E-20	15	71.0
06/26/16-7-2	CO_2	0.9700	2.41E-15	18	24.7
06/26/16-7-3	CO_2	0.9890	2.73E-18	17	40.2
06/14/16-8-1	CO_2	0.9360	1.00E-08	12	13.8
06/14/16-8-2	CO_2	0.9800	5.44E-17	18	30.7
06/14/16-8-3	CO_2	0.9820	1.53E-16	17	31.6
08/18/16-1-1	CO_2	0.9860	1.57E-14	14	32.2
08/18/16-1-2	CO_2	0.9890	2.33E-17	16	39.4
08/18/16-1-3	CO_2	0.9930	1.39E-14	12	43.6
08/18/16-2-1	CO_2	0.9960	1.13E-15	12	53.8

08/18/16-2-2	CO_2	0.9950	5.08E-19	15	57.6
08/18/16-2-3	CO_2	0.9930	1.43E-14	12	43.5
08/18/16-3-1	CO_2	0.9240	3.71E-11	17	14.8
08/18/16-3-2	CO_2	0.9910	7.10E-13	11	36.8
08/18/16-3-3	CO_2	0.9780	4.00E-14	15	27.0
08/18/16-4-1	CO_2	0.9560	3.88E-11	14	18.2
08/18/16-4-2	CO_2	0.9640	1.95E-12	15	20.7
08/18/16-4-3	CO_2	0.9970	7.75E-18	13	66.3
08/18/16-5-1	CO_2	0.9920	3.40E-15	13	41.4
08/18/16-5-2	CO_2	0.9980	4.14E-20	14	81.0
08/18/16-5-3	CO_2	0.9820	6.46E-13	13	27.6
08/17/16-6-1	CO_2	0.9710	8.66E-11	12	20.8
08/17/16-6-2	CO_2	0.9240	1.08E-07	11	12.1
08/17/16-6-3	CO_2	0.9810	9.95E-13	13	26.6
08/18/16-7-1	CO_2	0.9930	1.31E-14	12	43.8
08/18/16-7-2	CO_2	0.9990	7.07E-19	12	99.5
08/18/16-7-3	CO_2	0.9030	3.96E-07	11	10.6
08/02/16-8-1	CO_2	0.9850	2.28E-13	13	29.9
08/02/16-8-2	CO_2	0.9910	6.49E-15	13	39.4
08/02/16-8-3	CO_2	0.9670	1.68E-10	12	19.7
06/25/16-1 [L]	CH_4	0.096	0.61	3	-0.6
06/25/16-2	CH_4	0.836	0.03	3	3.9
06/25/16-3 [C]	CH_4	0.732	0.06	3	-2.9
06/28/16-4	CH_4	0.996	0.00	3	27.3
06/28/16-5	CH_4	0.767	0.05	3	3.1
06/27/16-6	CH_4	0.988	0.00	3	15.5
06/28/16-7	CH_4	0.675	0.18	2	2.0
08/18/16-1 [L]	CH_4	0.093	0.62	3	0.6
08/18/16-2	CH_4	0.628	0.11	3	2.3
08/18/16-3 [L]	CH_4	0.001	0.95	3	-0.1
08/18/16-4 [L]	CH_4	0.270	0.37	3	-1.1
08/18/16-5	CH_4	0.800	0.04	3	3.5
08/17/16-6	CH_4	0.925	0.01	3	6.1
08/18/16-7	CH_4	0.694	0.08	3	2.6

[L]For CH_4, sample excluded owing to poor linearity ($n = 4$).
[C]Sample excluded owing to CH_4 loss ($n = 1$).

Table A2-2. Stream characteristics and fluvial CO_2 flux upstream and downstream of RTS features (stream orders 1-3), and in RTS runoff in the Stony Creek and Vittrekwa River watersheds. Stream length derived from GIS and length (%) calculated for stream orders 1-6. Mean stream width from field measurements and mean flux from estimates upstream and downstream of eight RTS sites. Daily CO_2 and CH_4 mass flux in runoff (n = 5 each) reported as the mean values from flux calculations. See text for details.

Stream order	Stream length (m)	Length (%)	Stream width (m)	Area (m^2)	Area (%)	CO_2 flux ($\mu mol\ m^{-2}\ s^{-1}$)	CO_2 flux ($kmol\ d^{-1}$)	CH_4 flux ($nmol\ m^{-2}\ s^{-1}$)	CH_4 flux ($kmol\ d^{-1}$)
1	1,952,568	49.2	0.71	1,340,633	47.8	2.41	288	15.9	1.9
2	935,378	23.6	0.89	832,284	28.7	2.41	174	8.9	0.6
3	515,950	13.0	1.32	678,852	23.4	2.91	170	6.8	0.4
4	265,319	6.7	–	–	–	–	–	–	–
5	147,358	3.7	–	–	–	–	–	–	–
6	144,760	3.6	–	–	–	–	–	–	–
Runoff	6,450	0.2	0.3	1,935	0.07	8.3	0.6–1.8	1.41	$1x10^{-4}$–$3x10^{-4}$

Table A2-3. Measurements of mean stream velocity (V) and channel slope.

Site	Loc	V (m s^{-1})	Slope (m m^{-1})
FM2	UP	0.33	0.048
	DN	0.40	0.016
SE	UP	0.61	0.055
	DN	0.51	0.045
FM4	UP	0.31	0.034
	DN	0.62	0.084
FM3	UP	0.27	0.011
	DN	0.51	0.063
HA	UP	0.35	0.058
	DN	0.48	0.092
HB	UP	0.32	0.023
	DN	0.36	0.026
HD	UP	0.54	nd
	DN	0.54	0.000
SD	UP	0.25	0.054
	DN	0.30	0.024

UP = upstream, DN = downstream. nd = no data.

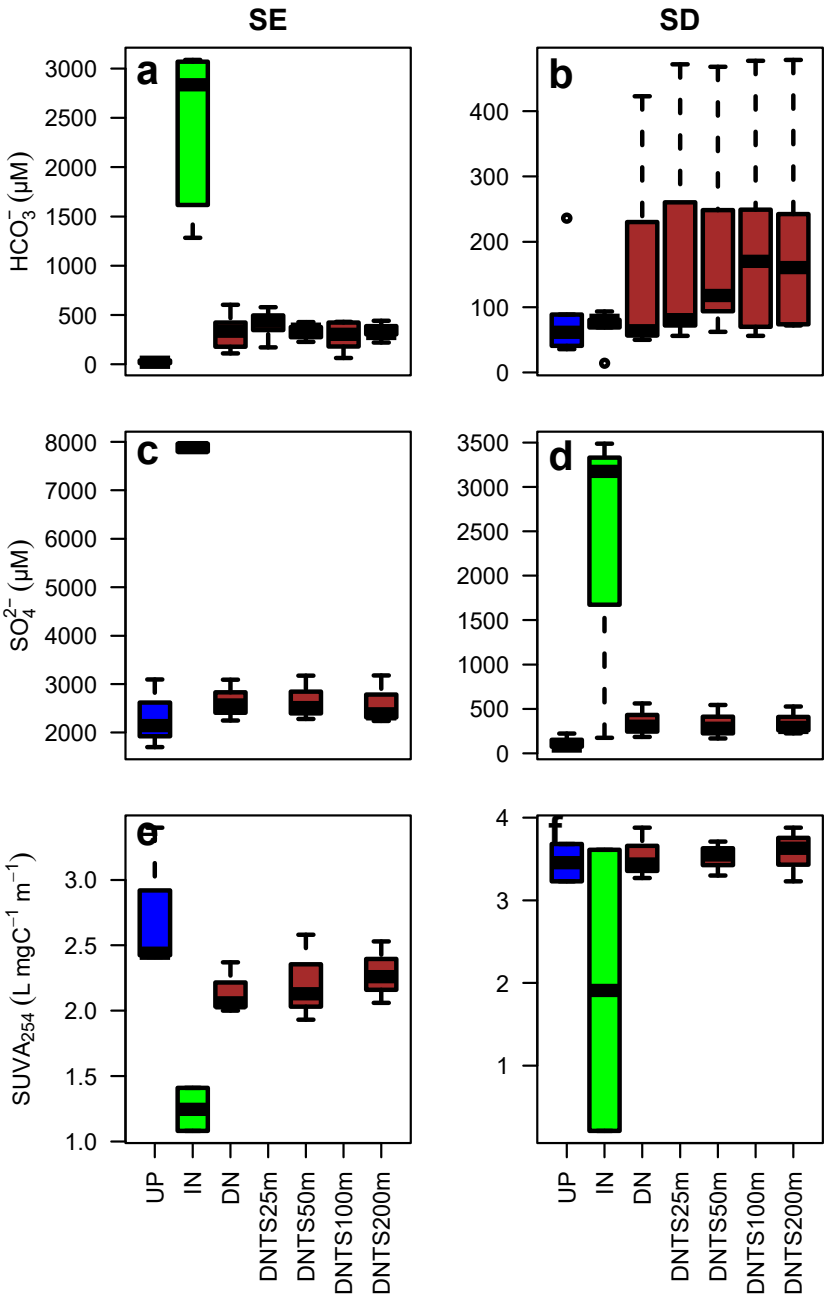

Figure A2-1. Box and whisker plots of downstream trends in selected geochemistry variables at RTS SE and SD. "UP" = upstream, "IN" = runoff, "DN" = downstream, "TS" = transect distance (e.g. "DNTS25m" = 25 m downstream). Whiskers depict range, boxes depict median (black line) and first and third quartiles. For both RTSs SE and SD, n = 5, 3, 3 for measurements of HCO_3^-, SO_4^{2-}, and $SUVA_{254}$, respectively.

Appendix 3. Supporting information for Chapter 4

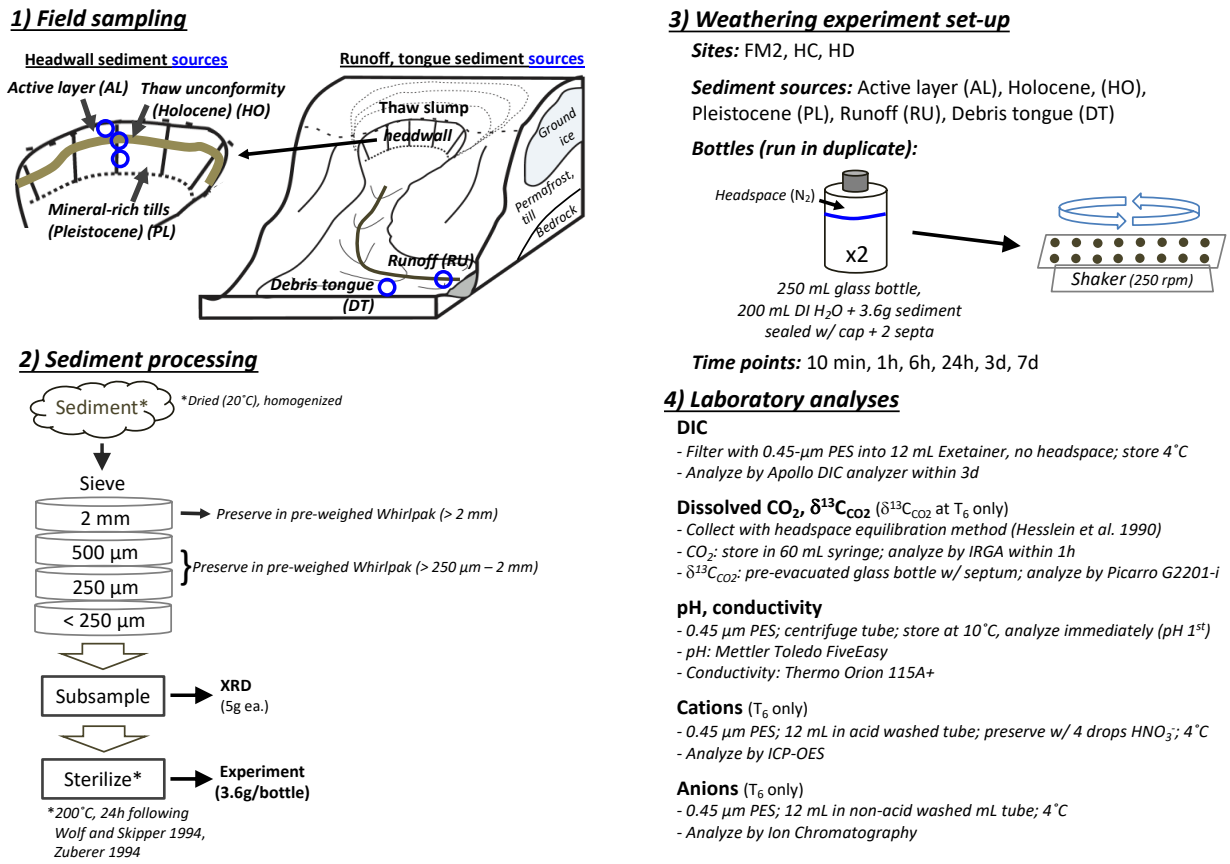

Figure A3-1. Diagram of field sampling, sediment processing, and set-up for the mineral weathering experiment.

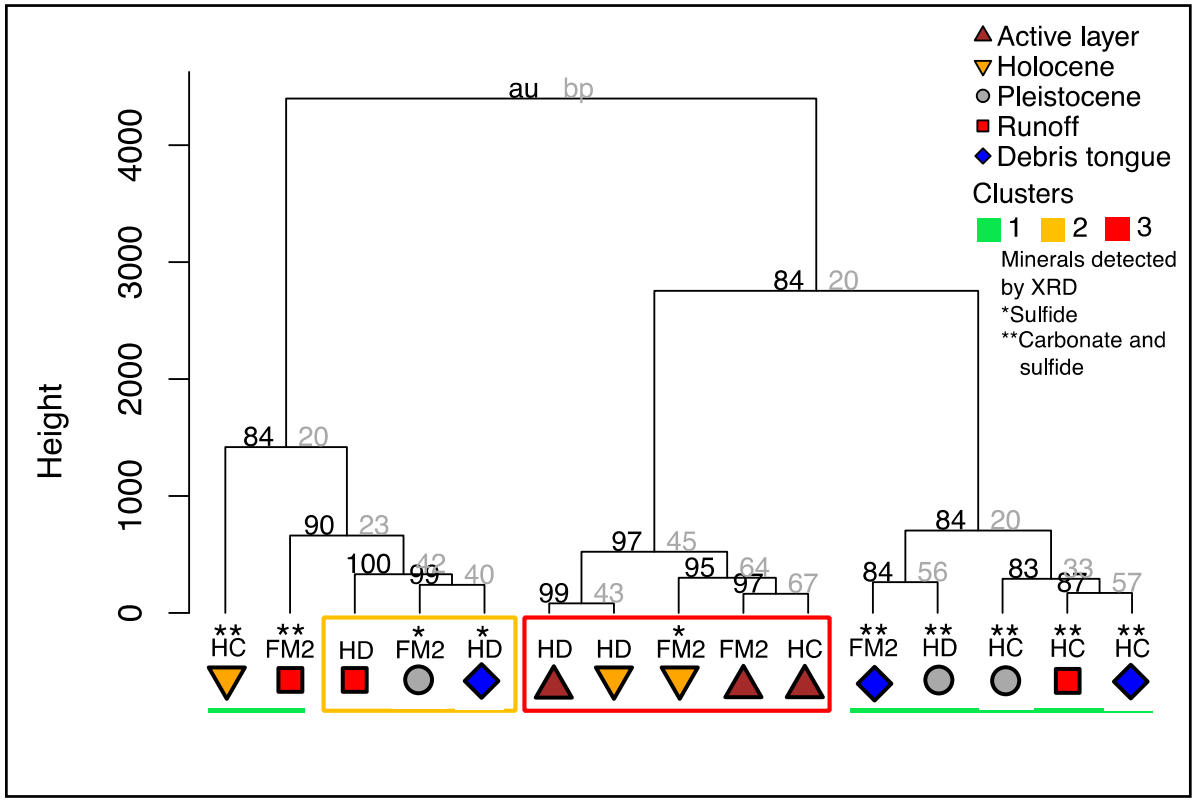

Figure A3-2. Geochemical clusters from the *pvclust* analysis. Rectangles denote clusters where $p < 0.05$. au = approximately unbiased p-value, bp = bootstrapped probability.

Appendix 4. Supporting information for Chapter 5

Table A4-1. Characteristics of mainstem sampling sites along the Dempster and Stony Creeks. Retrogressive thaw slump FM2 runoff was a tributary to the Dempster Creek (upstream of site 2) and Dempster Creek was a tributary to the Stony Creek (site 8). Coordinates reported in decimal degrees. *Site was not affected by retrogressive thaw slumps.[†]FM2 runoff distances in m.

Creek	Site	Type	Latitude (DD)	Longitude (DD)	Sampling date	Distance (km)[†]	Elevation (m)
FM2	1	Runoff	67.25639	-135.23422	7/31/17	0	–
FM2	2	Runoff	67.25726	-135.23756	7/31/17	220	–
FM2	3	Runoff	67.25813	-135.23700	7/31/17	330	–
FM2	4	Runoff	67.25894	-135.23636	7/31/17	440	–
FM2	5	Runoff	67.25986	-135.23595	7/31/17	550	–
FM2	5	Runoff	67.25981	-135.23587	7/30/17	–	271
Dempster	1*	Mainstem	67.25181	-135.29456	7/31/17	0	407
Dempster	2	Mainstem	67.27364	-135.20409	7/29/17	5.6	194
Dempster	3	Mainstem	67.29500	-135.17570	7/27/17	8.9	132
Dempster	4	Mainstem	67.32336	-135.14133	7/27/17	13.5	67
Dempster	2	Tributary	67.27364	-135.20367	7/29/17	–	–
Dempster	3	Tributary	67.29497	-135.17538	7/27/17	–	–
Dempster	4	Tributary	67.32414	-135.14252	7/27/17	–	–
Stony	1*	Mainstem	67.30280	-136.00468	7/27/17	0.0	575
Stony	2	Mainstem	67.33878	-135.90912	7/27/17	6.6	474
Stony	3	Mainstem	67.35704	-135.78165	7/25/17	13.8	382
Stony	4	Mainstem	67.34913	-135.48802	7/25/17	30.0	230
Stony	5	Mainstem	67.38380	-135.45747	7/25/17	35.7	184
Stony	6	Mainstem	67.34879	-135.30302	7/25/17	45.3	123
Stony	7	Mainstem	67.32732	-135.12160	7/25/17	56.2	57
Stony	8	Mainstem	67.39000	-134.98380	7/25/17	69.7	6
Stony	1*	Tributary	67.30367	-136.00421	7/27/17	–	–
Stony	2	Tributary	67.33933	-135.90836	7/27/17	–	–
Stony	3	Tributary	67.35719	-135.78311	7/25/17	–	–
Stony	4	Tributary	67.34860	-135.48773	7/25/17	–	–
Stony	5	Tributary	67.38467	-135.45607	7/25/17	–	–
Stony	6	Tributary	67.34882	-135.30196	7/25/17	–	–
Stony	7	Tributary	67.32703	-135.12213	7/25/17	–	–

Table A4-2. Results from the linear mixed effects model to determine the drivers of HCO_3^- yields in the Stony Creek tributary watersheds. Covariates eliminated during model selection (RTS_n, Slope) are not reflected in the table or final model: HCO_3^- yield = 832*ln*Water yield + 188*ln*RTS_{area} + 4689EVI + 656.

Covariate	**Estimate**	***t***	***p***
*ln*Water yield	832	6.3	0.01
lnRTS_{area}	188	1.7	0.19
EVI	4689	1.8	0.16

Appendix 5. Supporting information for Chapter 6

Table A5-1. Study Site Locations (Coordinates in Decimal Degrees) and Sampling Dates.

Region	Site	Latitude	Longitude	Sampling date(s)
Travaillant Uplands	1*	68.08756	-133.48795	June 20, July 16, Aug 6
Travaillant Uplands	2*	68.07018	-133.50121	June 20, July 17, Aug 6
Travaillant Uplands	3*	68.10948	-133.47348	June 20, July 16, Aug 7
Travaillant Uplands	4	68.16450	-133.43538	June 19, July 16, Aug 6
Travaillant Uplands	5	68.22931	-133.31763	June 19, July 16, Aug 7
Travaillant Uplands	6*	68.26068	-133.26173	June 19, July 16, Aug 6
Travaillant Uplands	7*	68.01468	-133.26311	June 14, Aug 2
Travaillant Uplands	8*	68.17418	-133.26973	June 14
Mackenzie Lowlands	1*	67.46526	-134.57455	June 24, July 19, Aug 12
Mackenzie Lowlands	2	67.43404	-134.50290	June 24, July 19, Aug 12
Mackenzie Lowlands	3*	67.38150	-134.15186	June 24, July 19, Aug 12
Mackenzie Lowlands	4*	67.48364	-133.76538	June 23, July 18, Aug 8
Mackenzie Lowlands	5	67.74252	-133.87836	June 23, July 18, Aug 8
Mackenzie Lowlands	6*	67.84227	-133.69276	June 21, July 17, Aug 7
Mackenzie Lowlands	7	67.85775	-133.66634	June 21, July 17, Aug 7
Mackenzie Lowlands	8*	67.97765	-133.46948	June 21, July 17, Aug 7
Mackenzie Lowlands	9*	67.27515	-133.79344	June 14, Aug 2
Peel Plateau	1*	67.17670	-135.75869	June 25, July 20, Aug 18
Peel Plateau	2*	67.17998	-135.72739	June 25, July 20, Aug 18
Peel Plateau	3*	67.19934	-135.68059	June 25, July 20, Aug 18
Peel Plateau	4	67.21668	-135.53216	June 28, July 20, Aug 18
Peel Plateau	5	67.22001	-135.50299	June 26, July 21, Aug 18
Peel Plateau	6*	67.25158	-135.29417	June 27, July 21, Aug 17
Peel Plateau	7*	67.29176	-135.06042	June 26, July 21, Aug 18
Peel Plateau	8*	67.31275	-135.16824	June 14, Aug 2
Richardson Mountains	1*	66.61338	-136.29329	July 1, July 23, Aug 19
Richardson Mountains	2*	66.70658	-136.35746	July 1, July 23, Aug 20
Richardson Mountains	3	66.80225	-136.33396	July 1, July 23, Aug 20
Richardson Mountains	4*	66.90668	-136.36131	June 29, July 23, Aug 20
Richardson Mountains	5*	66.93507	-136.26559	June 29, July 22, Aug 19
Richardson Mountains	6	67.00164	-136.20873	June 29, July 22, Aug 19
Richardson Mountains	7	66.96231	-136.21491	June 28, July 22, Aug 20
Richardson Mountains	8	67.01345	-136.20655	June 28, July 22, Aug 19

*Stream also sampled for stable isotopes of dissolved inorganic and organic carbon; particulate organic carbon; and dissolved nitrogen species.

Table A5-2. Linear Regression Parameters from CO_2 and CH_4 Flux Measurements.

	CO_2				CH_4			
Sample	R^2	*p*	df	*t*	R^2	*p*	df	*t*
TU-1-06/20/16-1	0.979	1.0E-16	18	29.6				
TU-1-06/20/16-2	0.927	1.9E-12	19	15.9				
TU-1-06/20/16-3	0.990	1.8E-13	12	35.1	0.56	0.14	3	2.0
TU-2-06/20/16-1	0.984	3.0E-13	13	29.2				
TU-2-06/20/16-2	0.937	4.9E-10	14	15.0				
TU-2-06/20/16-3	0.943	1.1E-09	13	15.3	0.85	0.03	3	4.1
TU-3-06/20/16-1	0.978	2.1E-17	19	29.8				
TU-3-06/20/16-2	0.993	6.6E-19	16	49.3				
TU-3-06/20/16-3[C]	0.989	1.9E-16	15	38.7	0.42	0.24	3	1.5
TU-4-06/19/16-1	0.996	1.6E-18	14	62.3				
TU-4-06/19/16-2	0.994	1.7E-22	19	55.5				
TU-4-06/19/16-3	0.996	2.1E-17	13	61.3	0.53	0.17	3	1.8
TU-5-06/19/16-1	0.985	4.2E-19	19	36.7				
TU-5-06/19/16-2	0.991	8.8E-15	13	38.5				
TU-5-06/19/16-3[L]	0.987	8.2E-16	15	35.1	0.05	0.71	3	-0.4
TU-6-06/19/16-1	0.996	4.1E-24	19	67.7				
TU-6-06/19/16-2	0.966	4.3E-14	17	22.5				
TU-6-06/19/16-3[L]	0.996	6.2E-25	19	74.7	0.33	0.31	3	1.2
TU-7-06/14/16-1	0.999	9.8E-31	18	179.4				
TU-7-06/14/16-2	0.999	1.0E-26	17	126.2				
TU-7-06/14/16-3	0.996	3.6E-21	16	68.3	0.80	0.04	3	3.5
TU-8-06/14/16-1	0.998	1.9E-26	18	103.8				
TU-8-06/14/16-2	0.997	2.9E-23	17	79.1				
TU-8-06/14/16-3	0.999	2.0E-27	17	138.9	0.46	0.21	3	1.6
TU-1-08/06/16-1	0.991	2.9E-21	19	47.8				
TU-1-08/06/16-2	0.991	5.8E-18	16	43.0				
TU-1-08/06/16-3	0.991	4.6E-18	16	43.6	0.78	0.05	3	3.2
TU-2-08/06/16-1	0.596	1.2E-03	11	4.3				
TU-2-08/06/16-2	0.999	5.6E-20	13	96.9				
TU-2-08/06/16-3	0.983	1.1E-07	7	21.8	0.63	0.11	3	2.2
TU-3-08/07/16-1	0.954	2.2E-14	19	20.4				
TU-3-08/07/16-2	0.969	7.9E-10	11	19.3				
TU-3-08/07/16-3	0.969	4.5E-09	10	18.5	0.29	0.35	3	1.1
TU-4-08/06/16-1	0.996	1.9E-18	14	61.7				
TU-4-08/06/16-2	0.999	2.0E-22	14	118.7				
TU-4-08/06/16-3[C]	0.998	3.9E-21	14	96.0	0.58	0.14	3	2.0

TU-5-08/07/16-1	0.889	2.8E-08	14	11.0				
TU-5-08/07/16-2	0.990	1.3E-12	11	34.8				
TU-5-08/07/16-3	0.992	4.9E-13	11	38.1	0.70	0.08	3	2.7
TU-6-08/06/16-1	0.905	2.8E-09	15	12.4				
TU-6-08/06/16-2	0.995	4.8E-19	15	57.8				
TU-6-08/06/16-3	0.959	2.4E-11	14	18.9	0.96	0.00	3	8.3
TU-7-08/02/16-1	0.997	6.0E-18	13	67.6				
TU-7-08/02/16-2	0.997	5.1E-18	13	68.5				
TU-7-08/02/16-3	0.999	1.7E-20	13	106.4	0.97	0.00	3	10.0
ML-1-06/24/16-1	0.935	2.6E-09	13	14.2				
ML-1-06/24/16-2	0.935	2.6E-09	13	14.2				
ML-1-06/24/16-3	0.947	6.9E-10	13	15.9	0.99	0.00	3	21.2
ML-2-06/24/16-1	0.999	2.1E-24	16	109.0				
ML-2-06/24/16-2	0.997	1.1E-23	17	83.8				
ML-2-06/24/16-3	0.993	4.2E-20	17	51.5	0.64	0.11	3	2.3
ML-3-06/24/16-1	0.986	1.1E-12	12	30.2				
ML-3-06/24/16-2	1.000	1.0E-29	17	189.8				
ML-3-06/24/16-3	0.989	2.1E-18	17	40.8	0.63	0.11	3	2.3
ML-4-06/23/16-1	0.965	8.6E-15	18	23.0				
ML-4-06/23/16-2	0.983	5.6E-14	14	29.4				
ML-4-06/23/16-3	0.927	6.9E-12	18	15.6	0.50	0.19	3	1.7
ML-5-06/23/16-1	0.938	3.4E-08	11	13.5				
ML-5-06/23/16-2	0.981	1.6E-14	15	28.7				
ML-5-06/23/16-3	0.920	2.7E-09	14	13.2	0.12	0.57	3	0.6
ML-6-06/21/16-1	0.998	4.3E-24	17	88.5				
ML-6-06/21/16-2	0.996	1.4E-19	15	62.9				
ML-6-06/21/16-3	0.995	2.9E-21	17	60.2	0.86	0.02	3	4.3
ML-7-06/21/16-1	0.999	5.0E-27	17	131.7				
ML-7-06/21/16-2	0.998	2.4E-24	17	91.7				
ML-7-06/21/16-3	0.996	2.7E-19	15	60.1	0.35	0.29	3	1.3
ML-8-06/21/16-1	0.998	5.5E-28	19	108.3				
ML-8-06/21/16-2	0.996	3.1E-22	17	68.7				
ML-8-06/21/16-3	0.998	1.0E-23	16	98.7	0.97	0.00	3	10.2
ML-9-06/14/16-1	0.998	1.9E-24	17	92.8				
ML-9-06/14/16-2	0.998	5.5E-24	17	87.2				
ML-9-06/14/16-3	0.998	4.0E-25	17	101.8	0.70	0.08	3	2.7
ML-1-08/12/16-1	0.998	5.0E-22	15	91.5				
ML-1-08/12/16-2	0.989	2.4E-17	16	39.3				
ML-1-08/12/16-3	0.995	8.7E-17	13	55.0	0.96	0.00	3	8.3
ML-2-08/12/16-1	0.996	4.4E-17	13	58.0				

ML-2-08/12/16-2	0.999	8.0E-22	14	107.5				
ML-2-08/12/16-3	0.998	5.0E-21	14	94.3	0.99	0.00	3	21.7
ML-3-08/12/16-1	0.998	5.6E-25	17	99.8				
ML-3-08/12/16-2	0.999	2.6E-25	16	124.1				
ML-3-08/12/16-3	0.995	3.2E-20	16	59.6	0.92	0.01	3	5.8
ML-4-08/08/16-1	0.918	1.1E-04	6	8.9				
ML-4-08/08/16-2	0.958	5.2E-07	8	14.4				
ML-4-08/08/16-3	0.971	5.4E-14	16	24.1	0.84	0.03	3	4.0
ML-5-08/08/16-1	0.976	7.9E-14	15	25.7				
ML-5-08/08/16-2	0.989	2.2E-15	14	37.1				
ML-5-08/08/16-3	0.992	5.1E-14	12	39.1	1.00	0.00	3	35.6
ML-6-08/07/16-1	0.994	4.5E-17	14	49.1				
ML-6-08/07/16-2	0.989	1.9E-13	12	34.9				
ML-6-08/07/16-3	0.987	8.3E-13	12	30.9	0.99	0.00	3	16.8
ML-7-08/07/16-1	0.993	5.3E-18	15	49.3				
ML-7-08/07/16-2	0.992	2.8E-15	13	42.0				
ML-7-08/07/16-3	0.977	2.3E-11	12	23.3	0.97	0.00	3	9.9
ML-8-08/07/16-1	0.992	5.0E-12	10	36.9				
ML-8-08/07/16-2	0.972	2.5E-09	10	19.7				
ML-8-08/07/16-3	0.994	6.3E-14	11	46.0	0.96	0.00	3	8.3
ML-9-08/02/16-1	0.999	8.4E-21	13	112.2				
ML-9-08/02/16-2	0.990	1.1E-13	12	36.6				
ML-9-08/02/16-3	0.990	1.4E-13	12	35.8	0.94	0.01	3	6.7
PP-1-06/25/16-1	0.983	8.2E-15	15	30.0				
PP-1-06/25/16-2	0.990	1.3E-18	17	42.0				
PP-1-06/25/16-3	0.982	2.1E-17	18	32.4	0.10	0.61	3	-0.6
PP-2-06/25/16-1	0.988	6.7E-17	16	36.8				
PP-2-06/25/16-2	0.994	2.9E-18	15	51.2				
PP-2-06/25/16-3	0.988	3.9E-17	16	38.1	0.78	0.05	3	3.3
PP-3-06/25/16-1	0.954	1.3E-09	12	16.5				
PP-3-06/25/16-2	0.987	7.2E-13	12	31.3				
PP-3-06/25/16-3[C]	0.990	1.5E-15	14	38.2	0.73	0.06	3	-2.9
PP-4-06/28/16-1	0.980	4.6E-10	10	23.4				
PP-4-06/28/16-2	0.992	5.3E-13	11	37.8				
PP-4-06/28/16-3	0.989	2.1E-14	13	36.0	1.00	0.00	3	27.3
PP-5-06/26/16-1	0.998	4.5E-21	14	95.0				
PP-5-06/26/16-2	0.996	4.6E-17	13	57.8				
PP-5-06/26/16-3	0.997	7.8E-21	15	76.2	0.77	0.05	3	3.1
PP-6-06/27/16-1	0.994	1.3E-22	19	56.3				
PP-6-06/27/16-2	0.946	1.8E-10	14	16.2				

PP-6-06/27/16-3	0.981	1.3E-13	14	27.6	0.99	0.00	3	19.6
PP-7-06/26/16-1	0.997	2.2E-20	15	71.0				
PP-7-06/26/16-2	0.970	2.4E-15	18	24.7				
PP-7-06/26/16-3	0.989	2.7E-18	17	40.2	0.06	0.70	3	0.4
PP-8-06/14/16-1	0.936	1.0E-08	12	13.8				
PP-8-06/14/16-2	0.980	5.4E-17	18	30.7				
PP-8-06/14/16-3	0.982	1.5E-16	17	31.6	0.18	0.48	3	0.8
PP-1-08/18/16-1	0.986	1.6E-14	14	32.2				
PP-1-08/18/16-2	0.989	2.3E-17	16	39.4				
PP-1-08/18/16-3^{L}	0.993	1.4E-14	12	43.6	0.09	0.62	3	0.6
PP-2-08/18/16-1	0.996	1.1E-15	12	53.8				
PP-2-08/18/16-2	0.995	5.1E-19	15	57.6				
PP-2-08/18/16-3	0.993	1.4E-14	12	43.5	0.63	0.11	3	2.3
PP-3-08/18/16-1	0.613	2.7E-05	18	5.6				
PP-3-08/18/16-2	0.991	7.1E-13	11	36.8				
PP-3-08/18/16-3^{L}	0.978	4.0E-14	15	27.0	0.00	0.95	3	-0.1
PP-4-08/18/16-1	0.956	3.9E-11	14	18.2				
PP-4-08/18/16-2	0.964	2.0E-12	15	20.7				
PP-4-08/18/16-3^{L}	0.997	7.7E-18	13	66.3	0.27	0.37	3	-1.1
PP-5-08/18/16-1	0.992	3.4E-15	13	41.4				
PP-5-08/18/16-2	0.998	4.1E-20	14	81.0				
PP-5-08/18/16-3	0.982	6.5E-13	13	27.6	0.80	0.04	3	3.5
PP-6-08/17/16-1	0.971	8.7E-11	12	20.8				
PP-6-08/17/16-2	0.924	1.1E-07	11	12.1				
PP-6-08/17/16-3	0.981	1.0E-12	13	26.6	0.93	0.01	3	6.1
PP-7-08/18/16-1	0.993	1.3E-14	12	43.8				
PP-7-08/18/16-2	0.999	7.1E-19	12	99.5				
PP-7-08/18/16-3	0.903	4.0E-07	11	10.6	0.69	0.08	3	2.6
PP-8-08/02/16-1	0.985	2.3E-13	13	29.9				
PP-8-08/02/16-2	0.991	6.5E-15	13	39.4				
PP-8-08/02/16-3	0.967	1.7E-10	12	19.7	0.69	0.08	3	2.6
RM-1-07/01/16-1	0.991	5.6E-17	15	42.0				
RM-1-07/01/16-2	0.987	7.2E-14	13	32.7				
RM-1-07/01/16-3	0.985	1.9E-12	12	28.8	0.00	0.95	3	-0.1
RM-2-07/01/16-1	0.972	1.7E-12	14	22.9				
RM-2-07/01/16-2	0.995	1.7E-16	13	52.4				
RM-2-07/01/16-3^{L}	0.985	1.4E-11	11	27.9	0.01	0.90	3	0.1
RM-3-07/01/16-1	0.995	5.4E-21	17	58.1				
RM-3-07/01/16-2	0.985	2.2E-15	15	32.8				
RM-3-07/01/16-3	0.989	3.7E-18	17	39.5	0.65	0.10	3	2.4

RM-4-06/29/16-1	0.998	2.7E-21	14	98.4				
RM-4-06/29/16-2	0.938	1.9E-09	13	14.6				
RM-4-06/29/16-3	0.998	2.5E-20	14	84.0	0.00	0.97	3	0.0
RM-5-06/29/16-1	0.963	4.7E-13	16	20.9				
RM-5-06/29/16-2	0.988	4.1E-10	9	28.4				
RM-5-06/29/16-3	0.974	1.9E-09	10	20.3	0.01	0.88	3	-0.2
RM-6-06/29/16-1	0.935	1.7E-10	15	15.2				
RM-6-06/29/16-2	0.958	4.6E-14	18	20.9				
RM-6-06/29/16-3	0.996	3.0E-17	13	59.8	0.00	0.94	3	0.1
RM-7-06/28/16-1	0.995	5.5E-18	14	57.1				
RM-7-06/28/16-2	0.997	6.4E-22	16	76.2				
RM-7-06/28/16-3	0.996	8.6E-19	14	65.2	0.76	0.05	3	3.1
RM-8-06/28/16-1	0.990	9.8E-15	13	38.2				
RM-8-06/28/16-2	0.997	5.7E-17	12	69.0				
RM-8-06/28/16-3[C]	0.980	1.8E-13	14	27.0	0.17	0.50	3	-0.8
RM-1-08/19/16-1	0.996	1.7E-12	9	52.4				
RM-1-08/19/16-2	0.981	3.5E-10	10	24.1				
RM-1-08/19/16-3	0.987	6.1E-13	12	31.7	0.00	0.96	3	0.1
RM-2-08/20/16-1	0.988	3.1E-11	10	30.7				
RM-2-08/20/16-2	0.979	5.7E-10	10	22.9				
RM-2-08/20/16-3	0.994	8.0E-13	10	44.4	0.11	0.59	3	0.6
RM-3-08/20/16-1	0.989	2.8E-16	15	37.7				
RM-3-08/20/16-2	0.982	5.4E-12	12	26.4				
RM-3-08/20/16-3	0.990	1.2E-15	14	38.8	0.00	0.99	3	0.0
RM-4-08/20/16-1	0.997	8.1E-18	13	66.1				
RM-4-08/20/16-2	0.996	2.3E-18	14	60.7				
RM-4-08/20/16-3	0.999	4.5E-20	13	98.6	0.11	0.60	3	0.6
RM-5-08/19/16-1	0.972	2.5E-13	15	23.8				
RM-5-08/19/16-2	0.991	7.8E-13	11	36.5				
RM-5-08/19/16-3	0.992	4.0E-13	11	38.8	0.02	0.85	3	0.2
RM-6-08/19/16-1	0.993	1.2E-15	13	44.8				
RM-6-08/19/16-2	0.991	4.6E-16	14	41.5				
RM-6-08/19/16-3[C]	0.995	8.3E-17	13	55.2	0.59	0.13	3	-2.1
RM-7-08/20/16-1	0.999	2.2E-21	14	100.0				
RM-7-08/20/16-2	0.998	3.1E-18	12	88.0				
RM-7-08/20/16-3	0.999	5.7E-23	14	129.7	0.96	0.00	3	8.2
RM-8-08/19/16-1	0.991	9.6E-11	9	33.4				
RM-8-08/19/16-2	0.983	3.1E-11	11	26.1				
RM-8-08/19/16-3	0.954	3.0E-10	13	17.0	1.00	0.00	3	24.8

TU = Travaillant Uplands, ML = Mackenzie Lowlands, PP = Peel Plateau, RM = Richardson Mountains. Sample IDs include sampling region – sampling site number – measurement date (mm/dd/yy) – efflux measurement replicate for CO_2. Only one efflux measurement was made for CH_4 for each site and date (see main text for details). df = degrees of freedom. $^{L}CH_4$ efflux sample excluded owing to poor linearity (n = 6). $^{C}CH_4$ efflux sample excluded owing to CH_4 loss (n = 5).

Table A5-3. Characteristics of AmeriFlux sites used for evaluating summertime NEE from the NASA EASE-Grid product.

AmeriFlux Station ID	Station name	Latitude	Longitude	Elevation (masl)	MAT (°C)	MAP (mm)	Vegetation
CA-DL1	Daring Lake - Mixed Tundra	64.86886	-111.57479	425	-9.0	250	Open shrublands; subarctic
CA-SCB	Scotty Creek Bog	61.30890	-121.29840	280	-2.8	388	Wetlands; subarctic
US-A10	ARM-NSA-Barrow	71.32420	-156.61490	4	-11.2	115	Barren sparse vegetation; tundra
US-EML	Eight Mile Lake Permafrost thaw gradient, Healy Alaska	63.87840	-149.25360	700	-1.0	378	Open shrublands; tundra
US-IVO	Ivotuk	68.48650	-155.75030	568	-8.28	304	Permanent wetlands; tundra
US-PRR	Poker Flat Research Range Black Spruce Forest	65.12367	-147.48756	210	-2.0	275	Evergreen needleleaf forest; subarctic
US-UAF	University of Alaska, Fairbanks	64.86627	-147.85553	155	-2.9	263	Evergreen needleleaf forest; subarctic

Table A5-4. Watershed Characteristics of the 33 Study Sites and the Means for Each of the Four Study Regions.

Region	Site	Strahler order	Elev. (m)	Slope (˚)	Area (km^2)	Carb. (%)	Sil. (%)	Colluvial (%)	Fluvial (%)	Moraine (%)	Organic (%)	Lakes/ ponds (%)	SOCC ($kgC\ m^{-2}$)	GPP ($gC\ m^{-2}\ d^{-1}$)	NEE ($gC\ m^{-2}\ d^{-1}$)
TU	1[a]	5	211	0.9	610.3	0	100	1	0	70	27	20	40.2	5.2 ± 2.1	-0.46
TU	2	1	87	1.9	1.8	0	100	0	0	100	0	0	50.0	6.6 ± 2.7	-0.75
TU	3	3	145	1.7	23.2	0	100	0	0	100	0	7	33.0	5.6 ± 2.1	-0.65
TU	4	2	138	1.7	27.8	0	100	0	0	98	2	7	15.8	5.9 ± 2.2	-0.63
TU	5	2	135	1.1	12.1	0	100	0	0	98	2	6	10.5	5.7 ± 2.1	-0.65
TU	6	4	161	0.9	115.1	0	100	0	0	96	4	4	19.0	5.3 ± 2.1	-0.68
TU	7	3	201	0.7	13.8	0	100	0	0	100	0	3	46.0	5.4 ± 1.8	-0.37
TU	8	2	166	0.4	8.2	0	100	0	0	75	25	10	24.1	6.7	–
Mean			156	1.2	102	0	100	0	0	92	7	7	30	5.8	-0.60 (0.09)
ML	1	1	41	0.7	2.7	0	100	0	0	72	28	1	69.2	5.9 ± 2.2	-0.74
ML	2	3	56	1.2	32.5	0	100	0	0	70	30	41	66.8	5.6 ± 2.4	-0.92
ML	3[l, a]	4	67	0.9	240.4	0	100	0	0	78	19	19	66.8	5.7 ± 2.1	-0.81
ML	4	2	87	1.7	13.0	0	100	3	0	90	7	8	65.1	7.2 ± 2.8	-0.84
ML	5	3	93	0.4	34.5	0	100	0	0	5	95	19	81.7	5.2 ± 2.0	-0.74
ML	6	3	92	0.4	85.8	0	100	0	0	44	56	10	78.6	5.8 ± 2.1	-0.86
ML	7	3	122	0.3	61.1	0	100	0	0	45	55	4	75.4	6.3 ± 2.5	-0.88
ML	8[a]	3	157	0.8	63.5	0	100	0	0	78	21	5	64.2	5.5 ± 2.2	-0.80
ML	9	3	81	0.4	21.9	0	100	0	0	59	41	60	66.8	4.1 ± 1.2	-0.75
Mean			88	0.8	62	0	100	0	0	60	39	18	71	5.7	-0.82 (0.02)
PP	1	2	863	14.4	1.8	0	100	100	0	0	0	0	20.1	4.2 ± 1.5	-0.71
PP	2	1	708	7.0	1.1	0	100	100	0	0	0	0	21.6	5.0 ± 1.7	-0.73
PP	3	1	540	6.1	0.8	0	100	100	0	0	0	0	21.6	5.6 ± 2.4	-0.73
PP	4	1	407	3.3	0.2	0	100	0	0	100	0	0	21.6	5.4 ± 1.6	-0.80
PP	5	2	376	2.3	2.3	0	100	0	0	100	0	0	21.6	5.9 ± 2.1	-0.68
PP	6	3	468	2.9	2.0	0	100	0	0	100	0	0	21.6	5.7 ± 1.8	-0.77
PP	7	1	324	3.5	0.1	0	100	0	0	100	0	0	21.6	6.3 ± 2.1	-0.59

PP	8	4	340	6.2	39.7	0	100	20	0	80	0	1	21.6	5.9 ± 1.9	-0.58
Mean			503	5.7	6	0	100	40	0	60	0	0	21	5.5	-0.70 (0.03)
RM	1	2	826	18.8	2.6	91	9	99	1	0	0	0	39.6	3.4 ± 0.4	-0.65
RM	2	3	878	22.9	27.5	96	4	90	10	0	0	0	16.2	2.2 ± 0.4	-0.62
RM	3	5	833	19.4	121.5	100	0	91	9	0	0	0	4.8	2.8 ± 0.5	-0.57
RM	4	4	736	17.2	64.4	93	7	88	6	0	6	0	5.5	3.5 ± 0.9	-0.61
RM	5	1	674	6.5	0.8	100	0	100	0	0	0	0	19.6	4.0 ± 0.7	-0.69
RM	6	2	956	14.2	2.1	0	100	76	24	0	0	0	12.7	3.0 ± 0.9	-0.69
RM	7	1	717	6.4	0.2	0	100	100	0	0	0	0	19.6	3.9 ± 1.5	-0.67
RM	8	2	899	12.7	2.1	0	100	100	0	0	0	0	12.7	3.4 ± 1.1	-0.69
Mean			815	14.8	28	60	40	93	6	0	1	0	16	3.3	-0.65 (0.02)

TU = Travaillant Uplands; ML = Mackenzie Lowlands; PP = Peel Plateau; RM = Richardson Mountains. Elev., Slope, and Area = watershed elevation, slope, and area. Carb. and Sil. = distribution of carbonate and silicate bedrock, respectively (Norris, 1985). Colluvial, Fluvial, Moraine, Organic = distribution of surficial geology deposits (sum to 100%, except where [l]2% lacustrine deposits and/or [a] ≤ 2% alluvial deposits) (Côté et al., 2013; Lipovsky & Bond, 2014). Distribution of lakes and ponds (Natural Resources Canada, https://open.canada.ca). SOCC = soil organic carbon content to 100 cm depth (Hugelius et al., 2013). GPP = gross primary productivity (Running et al., 2015). NEE = net ecosystem exchange (Kimball et al., 2018). Values are means (see Methods for details).

Table A5-5. Stream Water Quality and Carbon Concentration for the 33 Study Sites and the Means for Each of the Four Study Regions (Mean ± Standard Error).

Region	Site	Temp (˚C)	Cond (µS cm^{-1})	pH	DIC (µM)	CO_2 (µM)	HCO_3^- (µM)	DOC (µM)	POC (µM)
TU	1	14.8 (2.6)	105 (8)	6.98 (0.1)	528 (16)	37 (2)	490 (14)	1199 (201)	91 (21)
TU	2	9.4 (1.9)	73 (7)	6.68 (0.0)	739 (55)	85 (2)	653 (53)	2161 (122)	405 (49)
TU	3	11.3 (0.7)	89 (11)	7.17 (0.1)	662 (92)	39 (2)	622 (92)	1603 (130)	–
TU	4	12.9 (2.0)	80 (9)	6.72 (0.1)	461 (52)	46 (5)	414 (47)	1468 (192)	24 (7)
TU	5	12.1 (1.5)	84 (3)	6.83 (0.0)	531 (93)	53 (6)	477 (88)	1544 (242)	–
TU	6	11.4 (1.8)	107 (7)	7.17 (0.1)	663 (67)	36 (1)	626 (66)	1368 (202)	16 (6)
TU	7	11.2 (2.4)	59 (1)	5.87 (0.2)	617 (56)	170 (34)	446 (23)	1399 (278)	31 (27)
TU	8	9.3	56	5.79	426	180	246	1315	22
Mean		11.6 (0.6)	82 (7)	6.65 (0.2)	578 (39)	81 (21)	497 (48)	1507 (104)	99 (62)
ML	1	10.7 (0.8)	45 (4)	5.87 (0.1)	609 (103)	260 (42)	350 (65)	2755 (187)	34 (11)
ML	2	12.7 (1.3)	71 (3)	6.79 (0.1)	650 (51)	72 (13)	578 (56)	926 (137)	–
ML	3	14.5 (1.0)	137 (9)	7.30 (0.1)	1084 (69)	52 (6)	1030 (70)	1130 (21)	27 (5)
ML	4	10.2 (1.4)	63 (9)	6.28 (0.2)	323 (71)	44 (4)	279 (67)	3758 (392)	111 (22)
ML	5	12.2 (1.3)	77 (14)	6.08 (0.1)	822 (180)	338 (47)	483 (143)	1970 (200)	–
ML	6	14.5 (1.7)	75 (9)	6.44 (0.1)	687 (84)	134 (6)	553 (84)	1922 (189)	73 (17)
ML	7	13.9 (1.2)	119 (5)	6.96 (0.1)	888 (144)	85 (6)	802 (148)	1936 (320)	–
ML	8	13.0 (1.5)	98 (5)	7.15 (0.0)	760 (55)	53 (2)	706 (52)	1710 (161)	–
ML	9	15.4 (2.2)	171 (29)	7.21 (0.1)	1162 (147)	143 (58)	1019 (204)	986 (9)	34 (17)
Mean		13 (0.6)	95 (13)	6.68 (0.2)	776 (85)	131 (34)	644 (90)	1899 (303)	56 (16)
PP	1	6.3 (1.5)	523 (27)	5.03 (0.2)	56 (4)	32 (1)	24 (4)	156 (5)	–
PP	2	5.8 (1.6)	68 (10)	5.72 (0.1)	163 (14)	62 (5)	101 (10)	700 (49)	3800 (1188)
PP	3	5.1 (1.2)	27 (2)	5.66 (0.1)	182 (12)	56 (1)	126 (11)	818 (40)	78 (22)
PP	4	5.5 (0.7)	19 (0)	4.60 (0.0)	246 (24)	148 (23)	98 (10)	1200 (68)	–
PP	5	9.5 (1.3)	16 (0)	4.30 (0.1)	241 (15)	151 (8)	89 (22)	1277 (55)	–
PP	6	7.9 (1.3)	38 (1)	5.80 (0.2)	270 (17)	99 (12)	170 (9)	1143 (64)	70 (12)
PP	7	6.6 (1.8)	31 (2)	4.14 (0.2)	235 (12)	146 (9)	88 (21)	2114 (87)	33 (7)
PP	8	10.1 (0.8)	474 (142)	7.26 (0.5)	994 (159)	29 (2)	962 (156)	1003 (14)	8431 (2976)
Mean		7.1 (0.7)	149 (76)	5.31 (0.4)	298 (102)	90 (19)	207 (109)	1051 (198)	2483 (1654)
RM	1	4.4 (0.6)	400 (31)	7.72 (0.0)	2980 (118)	69 (5)	2899 (114)	553 (35)	12 (2)
RM	2	5.3 (0.3)	383 (25)	7.68 (0.0)	3068 (71)	78 (5)	2980 (74)	142 (31)	50 (22)
RM	3	6.1 (0.3)	344 (32)	7.82 (0.0)	2313 (101)	55 (5)	2249 (97)	138 (28)	–
RM	4	6.4 (0.6)	328 (31)	7.70 (0.1)	2501 (176)	67 (5)	2425 (172)	267 (60)	9 (1)
RM	5	2.5 (0.4)	325 (1)	7.19 (0.0)	2796 (230)	176 (15)	2617 (217)	656 (33)	25 (1)
RM	6	5.4 (0.5)	112 (31)	4.53 (0.1)	91 (15)	67 (9)	24 (8)	134 (13)	–
RM	7	8.7 (1.2)	51 (7)	6.01 (0.1)	475 (54)	98 (8)	377 (48)	500 (0)	–
RM	8	5.6 (0.7)	94 (17)	6.23 (0.1)	300 (32)	47 (2)	253 (29)	208 (25)	–

Mean	5.6 (0.6)	255 (51)	6.86 (0.4)	1816 (456)	82 (14)	1728 (451)	325 (75)	24 (8)

TU = Travaillant Uplands, ML = Mackenzie Lowlands, PP = Peel Plateau, RM = Richardson Mountains.

Table A5-5 (continued). Major Ion Concentrations for the 33 Study Sites and the Means for Each of the Four Study Regions (Mean ± Standard Error).

Region	Site	Ca^{2+} (µM)	Mg^{2+} (µM)	Na^{+} (µM)	K^{+} (µM)	SO_4^{2-} (µM)	Cl^{-} (µM)
TU	1	279 (14)	162 (12)	183 (20)	14.1 (1.5)	225 (36)	54.2 (6.5)
TU	2	293 (30)	147 (16)	44 (0)	5.0 (0.5)	19 (2)	12.5 (1.9)
TU	3	260 (32)	176 (24)	130 (22)	10.3 (0.6)	116 (18)	20.3 (2.1)
TU	4	207 (21)	143 (16)	167 (26)	10.1 (1.8)	143 (23)	45.2 (12.3)
TU	5	244 (15)	156 (10)	129 (9)	8.1 (1)	143 (32)	29.1 (2.4)
TU	6	334 (25)	182 (13)	123 (14)	10.0 (0.4)	187 (21)	17.7 (3.0)
TU	7	167 (15)	82 (6)	109 (17)	7.4 (1.8)	89 (44)	13.8 (1.7)
TU	8	134	85	140	7.4	86	40.9
Mean		240 (24)	142 (14)	128 (15)	9.1 (1)	126 (23)	29.2 (5.6)
ML	1	212 (21)	101 (9)	14 (0)	0.5 (0.1)	8 (4)	3.8 (1.6)
ML	2	232 (7)	114 (4)	68 (5)	15.4 (1.6)	67 (2)	18.9 (1.5)
ML	3	501 (33)	225 (15)	81 (1)	10.1 (1.9)	91 (16)	26.5 (3.1)
ML	4	198 (26)	138 (19)	178 (36)	8.0 (1.2)	63 (8)	56.5 (19.8)
ML	5	231 (49)	142 (32)	163 (29)	3.6 (0.5)	19 (7)	36.2 (6.5)
ML	6	238 (38)	143 (22)	113 (3)	5.8 (0.9)	22 (8)	38.1 (2.2)
ML	7	331 (31)	207 (20)	271 (12)	5.2 (0.6)	107 (59)	33.1 (3.2)
ML	8	343 (22)	176 (12)	91 (6)	7.1 (0.6)	79 (17)	44.8 (7.2)
ML	9	649 (107)	214 (32)	171 (30)	13.2 (0.4)	15 (3)	14.9 (2.5)
Mean		326 (51)	162 (15)	128 (25)	7.6 (1.6)	52 (12)	30.3 (5.4)
PP	1	945 (50)	1664 (105)	168 (10)	20.5 (2.2)	2740 (168)	1.6 (0.3)
PP	2	153 (23)	118 (18)	69 (10)	18.5 (3.3)	243 (54)	18.1 (6.6)
PP	3	67 (6)	52 (5)	18 (0)	3.3 (0.9)	57 (12)	2.1 (0.7)
PP	4	32 (2)	33 (2)	23 (1)	5.8 (1.3)	24 (2)	3.2 (0.3)
PP	5	33 (1)	28 (1)	14 (0)	1.9 (0.4)	14 (1)	0.9 (0.1)
PP	6	79 (1)	74 (1)	58 (2)	5.1 (1.6)	78 (15)	8.6 (1.3)
PP	7	55 (3)	38 (2)	46 (2)	3.1 (1.4)	47 (5)	1.7 (0.2)
PP	8	1267 (322)	649 (224)	1007 (438)	47.1 (5.4)	1896 (660)	29.9 (8.5)
Mean		329 (173)	332 (204)	175 (120)	13.2 (5.5)	637 (376)	8.3 (3.7)
RM	1	1900 (136)	354 (35)	16 (1)	1.8 (0.4)	784 (220)	1.9 (0.5)
RM	2	1736 (128)	381 (29)	26 (1)	7.1 (0.4)	664 (121)	3.7 (0.0)
RM	3	1516 (145)	364 (40)	27 (2)	7.8 (0.4)	728 (123)	3.5 (0.2)
RM	4	1494 (146)	327 (35)	19 (2)	7.2 (0.4)	543 (86)	3.8 (0.2)
RM	5	1563 (16)	253 (4)	38 (2)	4.0 (1.3)	437 (34)	2.1 (0.2)
RM	6	257 (76)	189 (57)	20 (3)	9.2 (1.2)	574 (106)	2.4 (0.4)
RM	7	123 (18)	354 (253)	21 (1)	7.0 (0.4)	74 (18)	1.7 (0.4)
RM	8	223 (39)	161 (33)	91 (11)	6.7 (0.4)	323 (80)	1.7 (0.2)

Mean	1102 (268)	298 (30)	32 (9)	6.4 (0.8)	516 (83)	2.6 (0.3)

TU = Travaillant Uplands, ML = Mackenzie Lowlands, PP = Peel Plateau, RM = Richardson Mountains.

Table A5-5 (continued). Optical Properties of CDOM and the Stable Isotopic Composition of Carbon and Water for the 33 Study Sites and the Means for Each of the Four Study Regions (Mean ± Standard Error).

Region	Site	$SUVA_{254}$ ($L\ mgC^{-1}\ m^{-1}$)	S_R	$\delta^{13}C_{DIC}$ (‰VPDB)	$\delta^{13}C_{DOC}$ (‰VPDB)	$\delta^{18}O_{H2O}$ (‰VSMOW)	$\delta^{2}H_{H2O}$ (‰VSMOW)	d-excess
TU	1	3.58 (0.2)	0.87 (0.00)	-6.1 (0.3)	-27.3 (0.2)	-16.8	-140.7	-6.7
TU	2	4.36 (0.0)	0.86 (0.00)	-14.0 (0.1)	-27.4 (0.1)	-19.9	-152.4	6.9
TU	3	4.00 (0.0)	0.87 (0.00)	–	–	-18.1	-145.1	-0.1
TU	4	4.25 (0.1)	0.87 (0.00)	-12.8 (0.4)	-27.4 (0.1)	-17.9	-143.1	0.0
TU	5	3.91 (0.1)	0.86 (0.00)	–	–	-18.7	-146.1	3.7
TU	6	3.83 (0.1)	0.87 (0.00)	-12.4 (0.2)	-27.4 (0.1)	-18.7	-145.0	4.9
TU	7	3.55 (0.2)	0.84 (0.00)	-18.4 (0.4)	-27.3 (0.2)	-18.1	-143.1	1.3
TU	8	4.20	0.83	-18.4	-27.3	–	–	–
Mean		3.96 (0.1)	0.86 (0.01)	-13.7 (1.9)	-27.4 (0)	-18.3 (0.4)	-145.1 (1.4)	1.4 (1.7)
ML	1	4.88 (0.1)	0.87 (0.00)	-17.5 (0.1)	-27.9 (0.1)	-19.8	-151.2	7.0
ML	2	3.13 (0.4)	0.95 (0.04)	–	–	-16.5	-138.0	-6.4
ML	3	3.48 (0.1)	0.95 (0.01)	-9.8 (0.9)	-27.3 (0.1)	-17.4	-145.6	-6.1
ML	4	4.72 (0.1)	0.86 (0.00)	-15.1 (1.5)	-27.8 (0.0)	-19.7	-155.2	2.2
ML	5	3.55 (0.1)	0.86 (0.00)	–	–	-18.3	-146.6	-0.5
ML	6	3.76 (0.1)	0.87 (0.00)	-16.2 (0.7)	-27.5 (0.0)	-17.8	-144.2	-2.0
ML	7	3.24 (0.1)	0.87 (0.00)	–	–	-18.3	-144.9	1.6
ML	8	4.06 (0.2)	0.88 (0.00)	-12.7 (0.0)	-27.6 (0.0)	-18.3	-145.4	0.9
ML	9	3.22 (0.0)	0.97 (0.01)	-9.4 (1.0)	-27 (0.2)	-16.8	-143.0	-8.3
Mean		3.78 (0.2)	0.90 (0.01)	-13.4 (1.4)	-27.5 (0.1)	-18.1 (0.4)	-146 (1.6)	-1.3 (1.6)
PP	1	2.64 (0.1)	0.80 (0.02)	-16.8 (0.0)	-27.4 (0.0)	-20.4	-155.1	8.4
PP	2	4.24 (0.2)	0.83 (0.00)	-13.2 (0.8)	-27.1 (0.1)	-20.2	-153.0	8.9
PP	3	3.95 (0.1)	0.80 (0.00)	-12.8 (0.1)	-26.8 (0.0)	-20.5	-154.8	8.9
PP	4	4.10 (0.1)	0.81 (0.00)	–	–	-20.7	-156.9	8.7
PP	5	4.25 (0.0)	0.84 (0.00)	–	–	-20.6	-156.5	8.3
PP	6	4.09 (0.1)	0.80 (0.00)	-17.1 (0.5)	-27.0 (0.0)	-20.4	-153.9	8.9
PP	7	4.85 (0.1)	0.85 (0.00)	-23.4 (0.3)	-27.3 (0.2)	-20.4	-153.7	9.3
PP	8	3.53 (0.1)	0.88 (0.03)	-5.9 (0.0)	-27.2 (0.1)	-20.8	-158.0	8.0
Mean		3.96 (0.2)	0.83 (0.01)	-14.8 (2.4)	-27.1 (0.1)	-20.5 (0.1)	-155.2 (0.6)	8.7 (0.1)
RM	1	3.65 (0.1)	0.87 (0.01)	-11 (1.4)	-27.3 (0.1)	-20.3	-156.4	5.8
RM	2	3.05 (0.2)	0.81 (0.04)	-8.4 (0.1)	-27.4 (0.3)	-20.8	-160.0	6.4
RM	3	3.13 (0.3)	0.87 (0.05)	–	–	-21.0	-159.9	7.9
RM	4	3.24 (0.2)	0.87 (0.02)	-8.3 (0.0)	-27.4 (0.4)	-21.0	-160.3	7.4
RM	5	3.43 (0.1)	0.87 (0.00)	-11.7 (0.1)	-27.2 (0.1)	-21.7	-165.6	8.0
RM	6	3.16 (0.3)	0.79 (0.03)	–	–	-20.1	-153.8	7.2

RM	7	3.68 (0.1)	0.78 (0.01)	–	–	-20.2	-154.4	6.9
RM	8	3.67 (0.2)	0.79 (0.02)	–	–	-20.1	-154.3	6.1
Mean		3.38 (0.1)	0.83 (0.02)	-9.8 (0.9)	-27.3 (0)	-20.6 (0.2)	-158.1 (1.4)	7.0 (0.3)

TU = Travaillant Uplands, ML = Mackenzie Lowlands, PP = Peel Plateau, RM = Richardson Mountains.

Table A5-5 (continued). Dissolved Nitrogen and Total Suspended Sediment Concentrations, Stream Flow Measurements, and Water Yield (Runoff) for the 33 Study Sites and the Means for Each of the Four Study Regions (Mean ± Standard Error).

Region	Site	TDN (µM)	DIN (µM)	DON (µM)	*V* (m s^{-1})	*Q* (m^3 s^{-1})	Runoff (cm d^{-1})
TU	1	29.7 (5.0)	1.0 (0.1)	28.7 (5.0)	0.535 (0.05)	2.927 (0.44)	0.041 (0.01)
TU	2	58.4 (3.2)	8.7 (1.1)	49.8 (2.2)	0.154 (0.06)	0.008 (0.00)	0.037 (0.00)
TU	3	–	–	–	0.382 (0.02)	0.104 (0.02)	0.039 (0.01)
TU	4	35.8 (3.4)	2.5 (0.7)	33.3 (3.9)	0.363 (0.08)	0.196 (0.07)	0.061 (0.02)
TU	5	–	–	–	0.163 (0.03)	0.032 (0.02)	0.023 (0.01)
TU	6	33.1 (4.9)	0.8 (0.0)	32.3 (4.8)	0.397 (0.07)	0.787 (0.24)	0.059 (0.02)
TU	7	32.5 (5.3)	0.8 (0.1)	31.7 (5.4)	0.299 (0.03)	0.052 (0.01)	0.032 (0.01)
TU	8	32.4	3.0	29.4	0.142	0.105	0.111
Mean		37 (4.4)	2.8 (1.2)	34.2 (3.2)	0.304 (0.05)	0.526 (0.35)	0.05 (0.01)
ML	1	61.8 (5.2)	1.6 (0.4)	60.1 (4.9)	0.065 (0.02)	0.042 (0.02)	0.135 (0.08)
ML	2	–	–	–	0.211 (0.03)	0.215 (0.08)	0.057 (0.02)
ML	3	41.1 (0.7)	0.7 (0.1)	40.4 (0.6)	0.661 (0.27)	1.580 (0.77)	0.057 (0.03)
ML	4	69.8 (7.2)	1.4 (0.1)	68.4 (7.1)	0.139 (0.04)	0.079 (0.04)	0.052 (0.02)
ML	5	–	–	–	0.072 (0.02)	0.023 (0.01)	0.006 (0.00)
ML	6	49.4 (4.9)	0.7 (0.1)	48.7 (4.7)	0.274 (0.07)	0.329 (0.14)	0.033 (0.01)
ML	7	–	–	–	0.664 (0.16)	0.225 (0.07)	0.032 (0.01)
ML	8	–	–	–	0.131 (0.04)	0.311 (0.09)	0.042 (0.01)
ML	9	40.2 (1.2)	1.9 (1)	38.3 (0.2)	0.417 (0.37)	0.190 (0.17)	0.075 (0.07)
Mean		52.4 (5.8)	1.3 (0.2)	51.2 (5.8)	0.293 (0.08)	0.333 (0.16)	0.054 (0.01)
PP	1	–	–	–	0.532 (0.08)	0.169 (0.03)	0.8 (0.15)
PP	2	21.9 (2.5)	6.0 (1.2)	15.8 (1.6)	0.399 (0.05)	0.064 (0.01)	0.508 (0.11)
PP	3	23.4 (1.6)	6.1 (0.9)	17.3 (0.7)	0.247 (0.03)	0.023 (0.00)	0.256 (0.05)
PP	4	–	–	–	0.189 (0.04)	0.014 (0.00)	0.639 (0.20)
PP	5	–	–	–	0.545 (0.09)	0.091 (0.03)	0.336 (0.11)
PP	6	21.5 (1.6)	1.8 (0.3)	19.7 (1.3)	0.312 (0.22)	0.049 (0.03)	0.209 (0.11)
PP	7	32.1 (1.4)	1.0 (0.1)	31.0 (1.4)	0.118 (0.04)	0.004 (0.00)	0.702 (0.29)
PP	8	48.4 (8.6)	19.5 (3.8)	28.8 (4.8)	0.685 (0.36)	0.827 (0.52)	0.18 (0.11)
Mean		29.4 (5.1)	6.9 (3.3)	22.6 (3.1)	0.378 (0.07)	0.155 (0.10)	0.454 (0.09)
RM	1	17.8 (0.8)	0.7 (0.3)	17.1 (0.9)	0.408 (0.07)	0.084 (0.03)	0.279 (0.11)
RM	2	15.3 (3.1)	8.2 (1.3)	7.1 (1.8)	0.266 (0.02)	0.330 (0.06)	0.104 (0.02)
RM	3	–	–	–	0.714 (0.1.0)	2.523 (0.80)	0.179 (0.06)
RM	4	17.5 (2.8)	8.7 (1.5)	8.8 (1.4)	0.512 (0.14)	1.064 (0.40)	0.143 (0.05)
RM	5	22.9 (3.9)	7.2 (3.5)	15.7 (0.5)	0.151 (0.09)	0.015 (0.01)	0.169 (0.07)
RM	6	–	–	–	0.342 (0.07)	0.074 (0.02)	0.302 (0.08)
RM	7	–	–	–	0.230 (0.03)	0.011 (0.00)	0.577 (0.12)

RM	8	–	–	–	0.410 (0.04)	0.078 (0.02)	0.319 (0.07)
Mean		18.4 (1.4)	6.2 (1.7)	12.2 (2.2)	0.379 (0.06)	0.522 (0.31)	0.259 (0.05)

TU = Travaillant Uplands, ML = Mackenzie Lowlands, PP = Peel Plateau, RM = Richardson Mountains.

Table A5-5 (continued). Partial Pressures, Transfer Velocities, and Instantaneous Effluxes of CO_2 and CH_4 for the 33 Study Sites and the Means for Each of the Four Study Regions (Mean ± Standard Error).

Region	Site	pCO_2 (µatm)	k_{CO2} (m d^{-1})	J_{CO2} (µmol m^{-2} s^{-1})	pCH_4 (µatm)	k_{CH4} (m d^{-1})	J_{CH4} (nmol m^{-2} s^{-1})
TU	1	809 (31)	7.4 (0.2)	1.6 (0.1)	40 (9)	1.6 (0.9)	23.1 (2.9)
TU	2	1565 (110)	2.7 (0.7)	1.9 (0.6)	506 (63)	0.2 (0.1)	53.2 (10.8)
TU	3	765 (25)	3.2 (1.8)	0.8 (0.4)	14 (3)	1.4	7.9
TU	4	945 (44)	14.1 (3.9)	3.7 (0.7)	4 (2)	13.4	8.2
TU	5	1065 (101)	4.6 (1.6)	1.6 (0.1)	12 (6)	0.6	4.7
TU	6	716 (43)	6.6 (2.2)	1.1 (0.2)	11 (5)	0.7	5.3
TU	7	3271 (390)	9.4 (0.6)	16.2 (2.3)	91 (45)	1.1 (0.7)	33.1 (8.2)
TU	8	3295	4.9	9.1	61	0.9	27.44
Mean		1554 (389)	6.6 (1.3)	4.5 (1.9)	92 (60)	2.5 (1.6)	20.4 (6.1)
ML	1	4977 (832)	3.1 (0.9)	7.5 (3.0)	320 (154)	0.3 (0.0)	22.2 (3.5)
ML	2	1458 (231)	13.1 (2.2)	9.8 (1.2)	82 (25)	1.2 (0.1)	32.6 (9)
ML	3	1118 (106)	9.2 (0.8)	4.2 (0.8)	159 (51)	0.7 (0.2)	47.6 (11.8)
ML	4	830 (103)	3.2 (2.2)	0.7 (0.3)	22 (10)	1.8 (1.6)	8.1 (4.1)
ML	5	6805 (990)	2.2 (0.2)	9.0 (0.9)	134 (38)	0.2 (0.0)	12.2 (4.2)
ML	6	2918 (269)	5.9 (2.3)	7.5 (3.2)	234 (50)	0.7 (0.4)	56 (23.5)
ML	7	1811 (178)	8.1 (0.6)	6.1 (1.4)	114 (18)	0.6 (0.3)	28.8 (15.8)
ML	8	1097 (34)	5.8 (2.9)	2.2 (0.9)	119 (10)	0.8 (0.4)	42.1 (23.8)
ML	9	3274 (1524)	3.5 (2.5)	3.4 (1.2)	173 (111)	0.6 (0.5)	21.5 (8.7)
Mean		2699 (680)	6 (1.2)	5.6 (1.0)	151 (29)	0.8 (0.2)	30.1 (5.4)
PP	1	518 (17)	8.0 (2.7)	0.9 (0.2)	1 (0.0)	0.6	0.3
PP	2	988 (64)	6.2 (0.6)	2.8 (0.2)	43 (12)	1.4 (0.0)	35 (16.1)
PP	3	876 (38)	5.3 (1.2)	1.9 (0.3)	2 (1.0)	–	–
PP	4	2362 (383)	3.5 (0.8)	5.7 (2.7)	289 (116)	0.6	165.3
PP	5	2796 (276)	7.9 (0.2)	12.0 (1.2)	143 (16)	1.1 (0.1)	79.4 (4.4)
PP	6	1751 (302)	5.1 (3.3)	3.9 (1.7)	442 (181)	0.5 (0.4)	68.7 (9.4)
PP	7	2451 (300)	1.5 (1.1)	1.9 (1.2)	134 (92)	0.1 (0)	6.3 (4.1)
PP	8	539 (51)	7.4 (2.2)	0.7 (0.4)	3 (0.0)	1.6 (0.4)	2.4 (0.6)
Mean		1535 (325)	5.6 (0.8)	3.7 (1.3)	132 (57)	0.8 (0.2)	51.1 (22.6)
RM	1	1061 (83)	7.0 (0.3)	3.2 (0.2)	3 (0)	-0.6 (0.8)	-0.8 (1.2)
RM	2	1233 (70)	6.9 (0.6)	4.1 (0.8)	2 (0)	1.6	2.4
RM	3	902 (96)	9.7 (4.0)	3.9 (1.0)	1 (0)	15.5 (16.4)	2.9 (3.6)
RM	4	1115 (102)	10.9 (1.9)	5.2 (1.5)	1 (0)	0.1 (1.4)	0.5 (0.8)
RM	5	2511 (247)	2.7 (0.0)	4.6 (0.7)	4 (2)	1.9 (1.9)	1.2 (1.3)
RM	6	1063 (124)	10.2 (4.8)	4.1 (1.7)	1 (0)	13.3	4.2
RM	7	1748 (88)	9.2 (1.6)	7.9 (2.4)	310 (55)	0.7 (0.1)	102.4 (7.6)

RM	8	753 (31)	5.6 (1.5)	1.5 (0.4)	14 (6)	0.8	11.4
Mean		1298 (202)	7.8 (1.0)	4.3 (0.6)	42 (38)	4.2 (2.3)	15.5 (12.5)

TU = Travaillant Uplands, ML = Mackenzie Lowlands, PP = Peel Plateau, RM = Richardson Mountains.

Table A5-5 (continued). Carbon Yields (Lateral [Fluvial] Export) for the 33 Study Sites and the Means for Each of the Four Study Regions (Mean ± Standard Error).

Region	Site	CO_2 yield (µmol m^{-2} d^{-1})	HCO_3^- yield (µmol m^{-2} d^{-1})	PIC yield (µmol m^{-2} d^{-1})	DOC yield (µmol m^{-2} d^{-1})	POC yield (µmol m^{-2} d^{-1})	TC yield (µmol m^{-2} d^{-1})
TU	1	15 (2)	203 (29)	6.6 (2.5)	521 (167)	40 (16)	785 (216)
TU	2	31 (4)	243 (40)	24.7 (4.7)	803 (121)	151 (29)	1252 (197)
TU	3	15 (2)	232 (42)	–	630 (153)	–	–
TU	4	27 (9)	246 (97)	2.9 (1.8)	942 (455)	18 (11)	1235 (573)
TU	5	11 (6)	108 (63)	–	399 (260)	–	–
TU	6	21 (6)	367 (126)	1.9 (1.2)	849 (366)	12 (7)	1251 (507)
TU	7	58 (26)	147 (46)	2.0 (1.9)	430 (32)	13 (11)	650 (117)
TU	8	200	272	4.1	1456	25	1957
Mean		47 (22)	227 (28)	7.0 (3.6)	754 (123)	43 (22)	1188 (187)
ML	1	326 (195)	494 (339)	6.4 (3.9)	3604 (2107)	39 (24)	4469 (2666)
ML	2	43 (19)	305 (84)	–	515 (180)	–	–
ML	3	29 (15)	548 (233)	2.9 (1.8)	651 (323)	18 (11)	1250 (583)
ML	4	21 (9)	115 (29)	11.2 (6.2)	1829 (674)	68 (38)	2044 (753)
ML	5	18 (3)	24 (5)	–	111 (29)	–	–
ML	6	45 (19)	160 (48)	3.5 (1.2)	592 (207)	22 (7)	821 (281)
ML	7	28 (10)	226 (31)	–	559 (101)	–	–
ML	8	22 (7)	293 (84)	–	753 (291)	–	–
ML	9	67 (53)	900 (845)	6.0 (5.8)	743 (677)	37 (36)	1753 (1618)
Mean		67 (33)	341 (90)	6.0 (1.5)	1040 (355)	37 (9)	2068 (636)
PP	1	250 (43)	206 (71)	–	1257 (267)	–	–
PP	2	304 (58)	516 (143)	2708 (330.7)	3525 (823)	16614 (2029)	23518 (1535)
PP	3	144 (33)	318 (57)	35.4 (14.7)	2138 (556)	217 (90)	2850 (741)
PP	4	873 (232)	604 (161)	–	7854 (2847)	–	–
PP	5	491 (133)	347 (177)	–	4383 (1486)	–	–
PP	6	185 (82)	342 (170)	20.8 (9.1)	2247 (1090)	128 (56)	2921 (1407)
PP	7	1000 (415)	686 (299)	40.6 (23.0)	15301 (6570)	249 (141)	17275 (7401)
PP	8	49 (29)	1554 (809)	1923 (684.3)	1789 (1111)	11796 (4198)	17010 (6797)
Mean		412 (124)	572 (151)	946 (572.9)	4812 (1672)	5801 (3515)	12715 (4178)
RM	1	183 (64)	7944 (3136)	5.9 (3.0)	1620 (741)	36 (18)	9821 (3976)
RM	2	79 (8)	3121 (618)	9.7 (5.8)	158 (59)	59 (36)	3438 (728)
RM	3	97 (29)	4077 (1404)	–	272 (138)	–	–
RM	4	92 (34)	3277 (1150)	2.3 (1.0)	413 (213)	14 (6)	3810 (1380)
RM	5	290 (132)	4533 (2226)	7.1 (3.3)	1159 (538)	43 (21)	6039 (2918)
RM	6	192 (33)	61 (13)	–	426 (156)	–	–
RM	7	574 (139)	2113 (329)	–	2886 (595)	–	–
RM	8	147 (29)	769 (106)	–	655 (139)	–	–

Mean	207 (58)	3237 (866)	6.2 (1.5)	949 (327)	38 (9)	5777 (1465)

TU = Travaillant Uplands, ML = Mackenzie Lowlands, PP = Peel Plateau, RM = Richardson Mountains.

Table A5-6. Total Fluvial Carbon Flux (kgC d^{-1}), Proportions of Flux by Carbon Species, Net Ecosystem Exchange (NEE; MgC d^{-1} where 1 Mg = 1000 kg)*, and Vertical Fluvial Efflux to the Atmosphere and Downstream Fluvial Flux as a Proportion of NEE for Each Study Site and Watershed (± Standard Error).

Region	Site	J_{CO2}	J_{CH4}	CO_2	HCO_3^-	PIC	DOC	POC	Total fluvial C	NEE	Lateral aq. export/NEE	Vertical aq. export/NEE	Total fluvial/NEE
TU	1	0.29	0.02	0.01	0.18	0.01	0.46	0.04	8337	-226.0	0.03	0.01	0.04
TU	2	0.05	0.01	0.02	0.18	0.02	0.60	0.11	29	-1.3	0.02	0.00	0.02
TU	3	–	–	–	–	–	–	–	–	-14.0	–	–	–
TU	4	0.21	0.01	0.02	0.15	0.00	0.59	0.01	531	-16.1	0.03	0.01	0.03
TU	5	–	–	–	–	–	–	–	–	-7.4	–	–	–
TU	6	0.28	0.01	0.01	0.21	0.00	0.48	0.01	2457	-75.3	0.02	0.01	0.03
TU	7	0.30	0.02	0.06	0.15	0.00	0.45	0.01	159	-4.9	0.02	0.01	0.03
TU	8	0.27	0.01	0.07	0.10	0.00	0.54	0.01	265	–	–	–	–
Mean		0.23 (0.04)	0.02 (0.00)	0.03 (0.01)	0.16 (0.01)	0.00 (0.00)	0.52 (0.03)	0.03 (0.02)	1963 (1327)	-65.0 (36.0)	0.02 (0.00)	0.01 (0.00)	0.03 (0.00)
ML	1	0.14	0.00	0.06	0.10	0.00	0.69	0.01	168	-2.0	0.07	0.01	0.08
ML	2	–	–	–	–	–	–	–	–	-17.7	–	–	–
ML	3	0.33	0.02	0.01	0.28	0.00	0.34	0.01	5572	-156.9	0.02	0.01	0.04
ML	4	0.27	0.01	0.01	0.04	0.00	0.64	0.02	442	-10.0	0.03	0.01	0.04
ML	5	–	–	–	–	–	–	–	–	-20.8	–	–	–
ML	6	0.45	0.02	0.03	0.10	0.00	0.38	0.01	1596	-66.8	0.01	0.01	0.02
ML	7	–	–	–	–	–	–	–	–	-51.7	–	–	–
ML	8	–	–	–	–	–	–	–	–	-47.9	–	–	–
ML	9	0.24	0.01	0.03	0.39	0.00	0.32	0.02	611	-6.5	0.07	0.02	0.09
Mean		0.29 (0.05)	0.01 (0.00)	0.03 (0.01)	0.18 (0.07)	0.00 (0.00)	0.48 (0.08)	0.01 (0.00)	1678 (1003)	-48.0 (22.0)	0.04 (0.01)	0.01 (0.00)	0.06 (0.02)
PP	1	–	–	–	–	–	–	–	–	-1.3	–	–	–

PP	2	0.01	0.00	0.01	0.02	0.11	0.15	0.69	313	-0.8	0.39	0.01	0.39
PP	3	0.15	0.03	0.04	0.09	0.01	0.61	0.06	32	-0.6	0.05	0.01	0.06
PP	4	–	–	–	–	–	–	–	–	-0.1	–	–	–
PP	5	–	–	–	–	–	–	–	–	-1.6	–	–	–
PP	6	0.21	0.03	0.05	0.09	0.01	0.59	0.03	92	-1.5	0.05	0.01	0.06
PP	7	0.03	0.01	0.06	0.04	0.00	0.85	0.01	12	-0.03	0.35	0.02	0.37
PP	8	0.04	0.00	0.00	0.09	0.10	0.10	0.67	8441	-22.7	0.36	0.01	0.37
Mean		0.09 (0.04)	0.01 (0.01)	0.03 (0.01)	0.07 (0.01)	0.05 (0.02)	0.46 (0.14)	0.29 (0.16)	1778 (1667)	-5.0 (3.0)	0.24 (0.08)	0.01 (0.00)	0.25 (0.08)
RM	1	0.05	0.00	0.02	0.77	0.00	0.16	0.00	321	-1.7	0.18	0.01	0.19
RM	2	0.18	0.00	0.02	0.74	0.00	0.04	0.01	1397	-17.0	0.07	0.02	0.08
RM	3	–	–	–	–	–	–	–	–	-68.9	–	–	–
RM	4	0.26	0.00	0.02	0.63	0.00	0.08	0.00	4024	-39.2	0.07	0.03	0.10
RM	5	0.06	0.00	0.04	0.70	0.00	0.18	0.01	61	-0.5	0.11	0.01	0.11
RM	6	–	–	–	–	–	–	–	–	-1.5	–	–	–
RM	7	–	–	–	–	–	–	–	–	-0.1	–	–	–
RM	8	–	–	–	–	–	–	–	–	-1.5	–	–	–
Mean		0.14 (0.05)	0.00 (0.00)	0.02 (0.01)	0.71 (0.03)	0.00 (0.00)	0.11 (0.03)	0.01 (.000)	1451 (905)	-15.0 (6.0)	0.11 (0.03)	0.01 (0.00)	0.12 (0.02)

*NEE was converted to kgC d^{-1} prior to calculating the proportions of vertical and lateral fluvial C export relative to NEE. For all sites, the proportion of CO_3^{2-} (not shown) was minor (maximum = 0.3% of DIC).

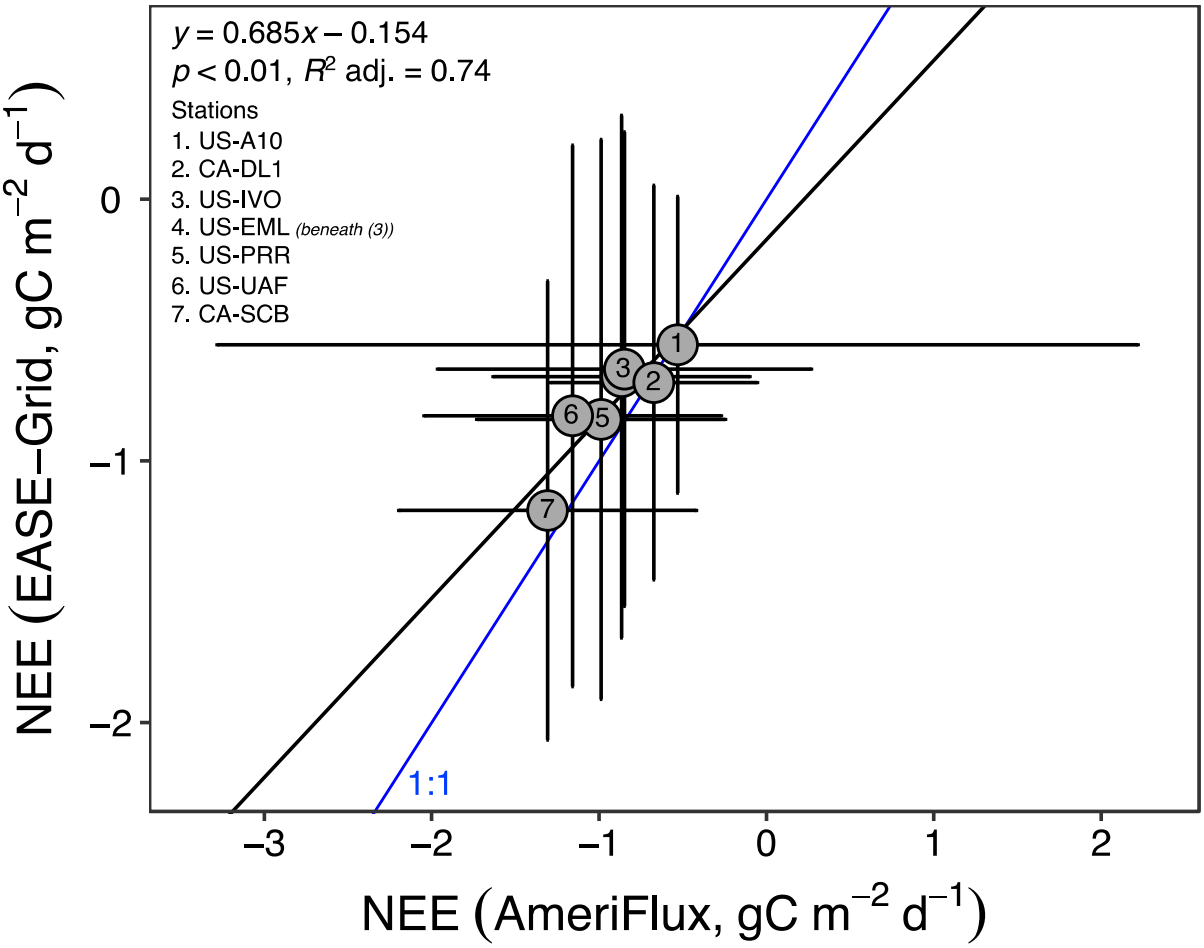

Figure A5-1. Comparison between mean (± 1σ) summertime (June–August 2016) net ecosystem exchange (NEE) from AmeriFlux field measurements and from values obtained from the NASA EASE-Grid NEE product. AmeriFlux sites with available data and similar ecosystems (taiga and tundra) as this study were used in the comparison (n = 6). AmeriFlux station IDs are provided adjacent to their data points.

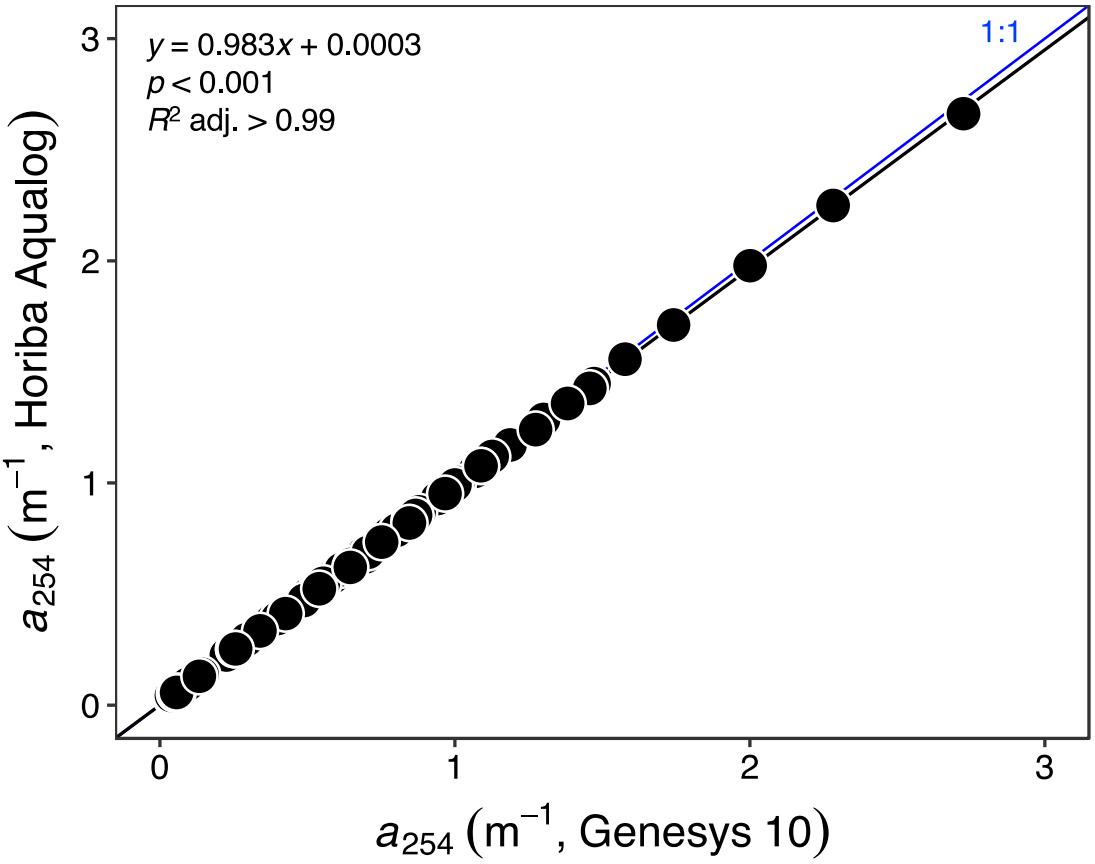

Figure A5-2. Comparison of measurements of absorbance at 254 nm (a_{254}) made using the Horiba Aqualog-UV-800 and Genesys 10 UV spectrophotometer.